Radio-frequency Transmit Coils and Imaging Techniques for TRASE MRI

by

Hongwei Sun

A thesis submitted in partial fulfillment of the requirements for the degree of

Doctor of Philosophy

in

Medical Physics

Department of Oncology

University of Alberta

Abstract

Magnetic Resonance Imaging (MRI) is a powerful diagnostic technique capable of revealing the internal structure and function of the human body. However, access to commercial MRI systems is restricted due to very high purchase, installation and running costs. These MRI scanners are generally confined to hospital suites, thus precluding mobile operation under many circumstances. Therefore, there is a growing interest in new MRI alternatives to mainstream MRI systems for affordable use by under-served patient populations, including those in smaller and remote centers, and in portable scenarios such as surgical intervention, triage, primary care suites, and even in space. An alternative MRI encoding principle known as Transmit Array Spatial Encoding (TRASE), which functions entirely without using magnetic field gradients was proposed in 2010. This is highly advantageous because much of the cost and complexity of MRI systems is associated with the generation of the switched magnetic field gradients needed for image encoding. TRASE is also particularly suitable for use in low-field magnets, enabling further cost savings. Compared with other novel MRI approaches, this method has the potential to generate sub-mm clinical image resolution, using the novel radio-frequency (RF) technology. TRASE has been very well received, most notably being featured in "Research Highlights" in Nature in 2013.

Up to the point where I started my research, 2D TRASE encoded *in vivo* MRI images of human wrist have been obtained, showing promise for its clinical use. However, the obtained *in vivo* image resolution was limited due to an inefficient RF system design, rendering a long scan duration vulnerable to tissue MR signal losses. Therefore, the goal of this project is to

1) design and optimize of a new RF transmit coil geometry, which allows an efficient MRI encoding using TRASE principles; 2) based on the new coil design, develop necessary RF and imaging techniques to combine multiple RF transmit coils, achieving a multi-dimensional TRASE encoding even for short T_2 samples.

A new twisted solenoid TRASE RF coil was first designed, optimized and constructed. This new type of coil is ideal for TRASE application due to its high efficiency, uniformity, and large usable imaging volume relative to its aperture. By rotating the coil former, this twisted solenoid is capable of encoding in any transverse direction, so a pair of such coils were combined with regular solenoids attached to accomplish geometric coil decoupling, obtaining high-resolution MRI images.

To achieve a 2D TRASE encoding, the geometrically-decoupled twisted solenoid pair was combined with a saddle coil, forming a 2D TRASE three-coil set. One main challenge for this combination is the effective enable/disable function of each coil, otherwise the strong interactions (coupling) among coils may, while transmitting with the primary coil, lead to cross-talk among other coil(s), causing severe MRI image distortions. Such image artifacts were indeed observed in MRI experiments with the geometrically-decoupled three-coil set, indicating that 2D TRASE is extremely sensitive to coil coupling, and to obtain a clean 2D TRASE image, additional coil decoupling capacity is required.

With such in-depth understanding, a low-field, inexpensive parallel transmit system was developed upon a waveform generator chip AD9106 and a controller Cyclone V System-on-Chip. In bench measurements such system can generate multiple independent RF drive signals with user-defined amplitudes and phases, being implemented as an active decoupling approach. This new RF transmit system is expected to be combined with the previous geometric decoupling techniques to significantly minimize interactions among the three-coil set, making a successful 2D TRASE MRI encoding.

Preface

A version of Chapter 4 has been published in the journal of *Journal of Magnetic Resonance:*

Hongwei Sun, Stephanie Yong, Jonathan C. Sharp (2019). *The Twisted Solenoid RF Phase Gradient Transmit Coil for TRASE Imaging*, Journal of Magnetic Resonance. 2019 Feb; 299:135-150. doi: 10.1016/j.jmr.2018.12.015

A version of Chapter 5 has been published in the journal of *Magnetic Resonance in Medicine:*

Hongwei Sun, Abbas AlZubaidi, Aaron Purchase, Jonathan C. Sharp (2019). *Geometrically-Decoupled Twisted Solenoid Pair for Single-axis TRASE Encoding*, Magnetic Resonance in Medicine. 2019 Aug; 83(4):1484-1498. doi: 10.1002/mrm.28003

For both published articles, I, Hongwei Sun, contributed to the majority of project conceptualization, and was responsible for data acquisition, analysis, and manuscript writing. Dr. Jonathan Sharp, the principal investigator, significantly contributed to the writing and editing process for both publications. Miss Stephanie Yong, contributed to the experimental setup design and manuscript review for the Chapter 4 article. Dr. Abbas AlZubaidi and Mr. Aaron Purchase were involved with the experimental approach and manuscript review for the Chapter 5 article.

The findings in Chapter 6 were split into one first-author manuscript (to be submitted) and one second-author manuscript which was submitted to the jounal of *Magnetic Resonance Imaging*. The Bloch simulations in Chapter 6 were performed by Miss Pallavi Bohidar, under the supervision and help of Dr. Gordon Sarty and Dr. Jonathan Sharp, while I, Hongwei Sun, conducted all the experiments and hardware instrumentations. For Chapter 7, I, Hongwei Sun, was responsible for electronics development, experiments and data analysis.

Acknowledgements

Stepping into a new and fascinating field of science, and acquiring new knowledge and personal growth, is what I have humbly experienced in the past four years. Many people have helped me with my journey in Edmonton, Canada, and I would like to take this great opportunity to express my sincerest gratitude to all of them.

Firstly, I would like to express my deepest thanks and love to my dearest parents, Chengquan Sun and Ke Li; as well as the rest of my family for caring and supporting me through my life. They showed me the true meaning of life and without their love, I could not have accomplished this doctoral research project. Thank you from the bottom of my heart, for allowing me to do what I enjoy to do!

I would like to express my greatest thanks to my supervisor, Dr. Jonathan Sharp for his continuous support and mentorship. During our countless meetings, his immense knowledge, and insightful advice never ceased to expand my vision of scientific research. He always enabled me to expand on my research and fostered my critical thinking abilities, all the while providing sufficient patience, efficient analysis, and supportive recommendations. Without his inspiration and guidance, this dissertation would not be possible. It has been a great pleasure working with him, and I sincerely appreciate him for inviting to join his research lab - a brilliant decision made!

I would like to thank all of the esteemed members of my supervisory committee, including Dr. Gino Fallone, Dr. Nicola De Zanche, and Dr. Boguslaw Tomanek. The expertise and constructive feedback provided throughout my graduate studies was invaluable and truly strengthened my research. Thank you also to Dr. Keith Wachowicz and Dr. Satyapal Rathee for being a part of my candidacy examination, and to Dr. Christopher Bidinosti for serving on my thesis defense.

I also want to express my appreciation to all my fellow students in the program: Mr. Aaron Purchase, Mr. Radim Barta who helped me tremendously when I first encountered the MRI techniques. I am grateful to the precious friendship over the past four years, with Andrei, Amanda, Bryson, Braden, Brennen, Clara, Cam, Dan Michael, Devin, Gawon, Hali, JD, Mark, Mike, Niri, Nick, Simon, Teresa, and all the ones that do not come to my mind right now. I also wish to extend special gratitude to Dr. Vyacheslav Volotovskyy, for his selfless sharing and helpful suggestions on all kinds of lab experiences.

I am also grateful to the faculty and staff of the entire Division of Medical Physics for their generous assistance. Special thanks goes out to Debbi and Brenda for their help with my graduate and administrative responsibilities, and the machine shop workers, including Mr. Ken Hennig and Mr. Curtis Osinchuck for their help and ideas in building various plastic formers and phantoms.

Importantly, I gratefully acknowledge the sources of student funding from Alberta Cancer Foundation, the University of Alberta, and the Government of Alberta.

Next I want to thank all my soccer teammates in RedForce Soccer FC for their generous supports whenever needed. I miss those days we hangout together after each game/practice. You guys made my life in Edmonton much happier and easier.

Finally, I owe a huge debt to Xiaofei Wang who made my entire Ph.D. journey unexpectedly fun. I am thankful that I got a chance to know you who took care of our cats, listened to me (good and bad) every day, constantly cheered me on, and always stand behind me for support. This would not have been possible without your help.

Contents

List of Tables

List of Figures

Chapter 1

Overview of the Thesis

1.1 Background

Magnetic Resonance Imaging (MRI) is a powerful diagnostic technique that is capable of revealing the internal structure and function of the human body for patients. In the past several decades, MRI has played a prominent and revolutionary role in the imaging industry by providing high-resolution medical images without the use of harmful ionizing radiations [1]. In comparison with other imaging modalities, MRI offers significant advantages including superior soft tissue contract and the capability of acquiring data in arbitrary orientations [2]. Further applications such as functional MRI and diffusion weighted imaging demonstrate significant values of MRI across a large number of areas (*e.g.*, visualization and mapping of neuronal networks' activity, functional neurosurgery, and psychiatry). Undeniably, MRI has gained remarkable recognition and become an indispensable tool in modern medical studies and diagnosis.

Briefly speaking, MRI produces images based on the recording and processing (*i.e.*, phase and frequency) in the absorption and emission of energy in the radiofrequency (RF) range of the electromagnetic spectrum, when strong magnetic fields are applied directly onto the nucleus (*e.g.*, protons) which are intrinsic parts of the body tissues being imaged. Despite considerable improvements in MR images quality and speed, the underlying technology re-

mains remarkably unchanged compared to the first-generation MR scanners developed several decades ago [3], [4], and for hardware requirements, a commercial MRI scanner typically consists of four main components: 1) Magnet; 2) Gradient System; 3) RF Transmit/Receive System; and 4) Control Console.

Although modern clinical MRI scanners, with an external main magnetic field (B_0) of 1.5 or 3.0 Tesla (T), can generate clinically useful images of very high quality, they are expensive (multi-million dollar), noisy and require bulky equipment. These factors severely limit access to MRI in comparison to more basic imaging technologies such as X-ray and ultrasound which are much more widely available. Worldwide only one-tenth of the population has access to MRI, and the distribution of sophisticated MRI system is extremely inhomogeneous. The highest accessibility to MRI is found in Japan, which owns 50 available scanners per million inhabitants, while in China and India, this number significantly reduces to about 0.89 [5]. These commercial MRI machines found in hospitals are filled with cryogenic helium, weigh several tons (*e.g.*, over 10 tonnes), and have stray magnetic field (although most MRI scanners nowadays have "active shielding" to cancel stray field) outside of the instrument, which as a whole, preclude mobile operation under many circumstances [6]. Although the costs of individual components of the MR system (*e.g.*, magnet, RF amplifier, etc) are considered proprietary information by manufacturers and are not readily available, a recent study [7] estimated the relative component group costs for a low-end 1.5 T superconducting magnet scanner, with the data shown in Figure 1.1.

In addition to the parts cost, the price of installation of the system and post-installation maintenance, as well as the complexity of operating an MR system, makes MRI techniques out of the financial reach for much of the world. Therefore, there is a growing interest in new MRI alternatives to mainstream MRI systems for affordable use by under-served patient populations, including those in smaller and remote centers, and in portable scenarios such as surgical intervention, triage, and primary care suites. A recent report [8] summarized that the access to MRI scanners is largely restricted to countries in upper-middle and high-

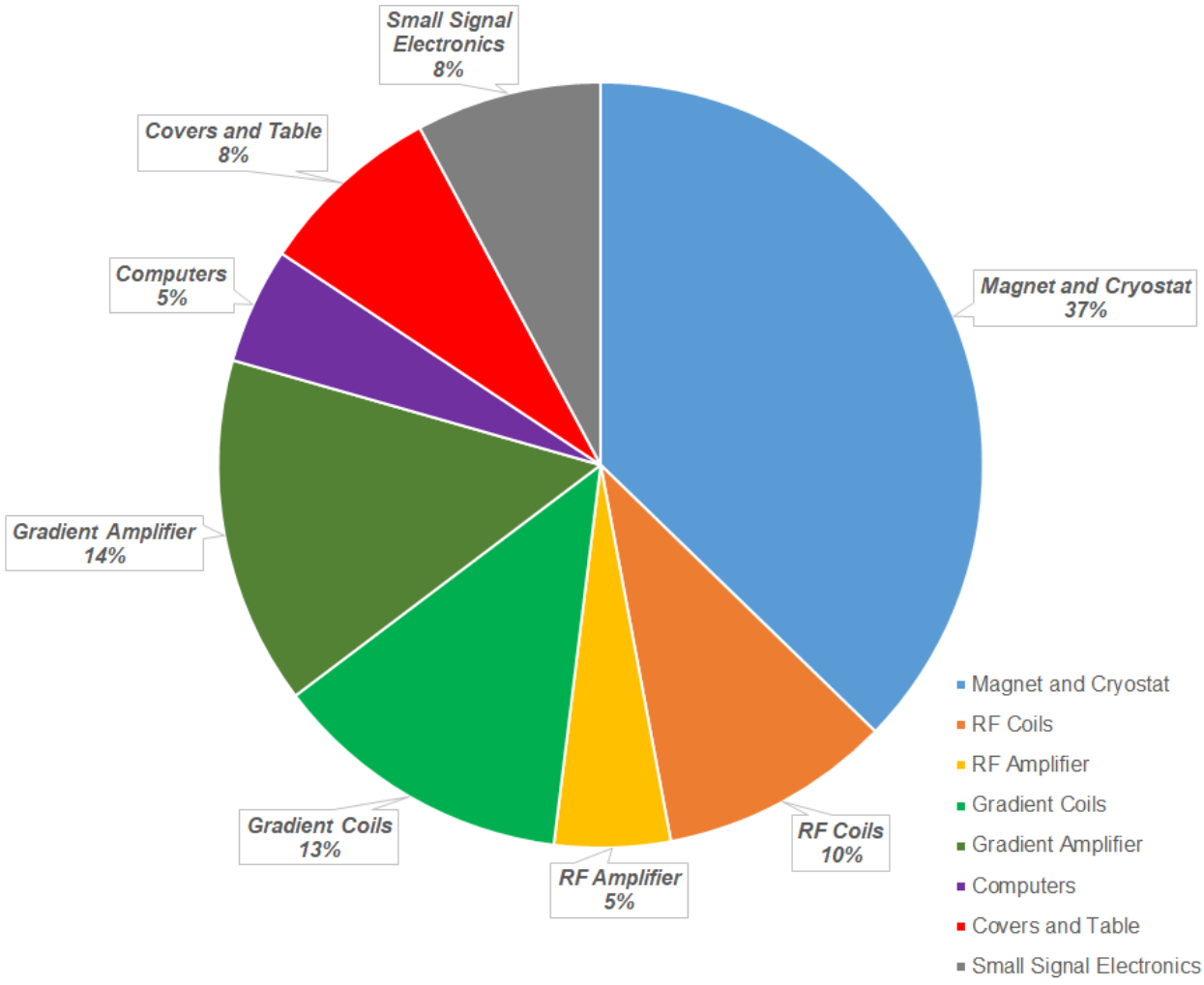

Figure 1.1: The estimation of the relative part costs for a low-end conventional 1.5T scanner. Note that a low-end system suggests a total components cost of 200,000 USD leaving a cost of about 76,000 USD for the magnet and cryostat, and 70,000 USD for gradient systems including gradient coils and amplifiers. However, it should be mentioned that these estimates are based on reporters' intuition [7], but not specific data in the publication.

income groups. People living in lower to lower-middle groups are reported to have lower MR scanner density, larger populations, life expectancies less than 70 years, of which all together represent the unmet need for accessible MRI. Based on the 2017 World Health Organization (WHO) report, some counties did not have a single MR machine, even though a significant increase of scanner density was found in emerging economies. A search survey shows that only eighty-four MRI units were found in the West Africa sub-region serving a combined population of over 370 million at the time of September 2017. Nigeria accounted for about 70% of the available units. Of these, nearly 80% of the units were low-field strength ($\leq$ 0.2 T) systems [9]. The huge deficit of neurosurgeons (1 per 7 million), and scanners (0.04 per million) in this region have prohibited access to MRI and its effective utilization [8]. Hydrocephalus, for example, is an excessive accumulation of fluid in the brain which affects the nervous system and can cause pain, brain damage, blindness and even death if not treated properly. This is a large problem for newborns in developing countries due to short of MRI techniques and nonsurgical care. As a consequence, medical practitioners in Africa have to expose children to numerous CT and X-ray scans, giving infant hydrocephalus unnecessary levels of radiation. This could be avoided, if an inexpensive, portable MRI scanner could be developed to help make the diagnosis and treatment of infant hydrocephalus available and affordable in these remote regions.

This possibility leads researches to rethink research in MRI technology. In comparison with the clear benefits gained by enabling MRI scanners to "see more" (new acquisition techniques, improved sensitivity, spatiotemporal resolution, and introduction of new biological contrasts and targets), extending the availability of MRI by reducing cost, siting, and operation burdens also directly benefits healthcare through increasing the number of patients with access to MRI examinations and tilting its cost–benefit equation to allow more frequent and varied use [7]. Additionally, advances in hardware and computational technology, together with burgeoning markets for MRI in the developing world, has created a resurgence of interest in low-cost and accessible MRI. Undeniably, dedicated solutions are needed to meet the

challenge of MRI access while maintaining quality at an affordable cost. The MRI community is now revisiting the approach of using low-field MRI, which, instead of producing the highest quality images, nevertheless focuses on providing diagnostically useful information [5].

This low-field accessible MRI direction has become an interesting field that attracts much attention, as reflected by a recent International Society for Magnetic Resonance in Medicine (ISMRM) workshop ("Accessible MRI for the World") in 2019. Now worldwide researchers are reporting their approaches to make a low-cost, high-performance MRI system [10]–[20]. In the market, *Hyperfine Inc.* just introduced an affordable, easy-to-use MRI system for the bedside in 2019, offering maneuver point-of-care scanner around the hospital. Their portable MRI (as claimed by Hyperfine) is 20 times less costly, 35 times lower power, and 10 times lighter than the most popular current MRI scanners.

1.2 Project Motivation

There is a growing interest in lower cost alternatives to mainstream MRI systems for use in smaller clinics and even in portable scenarios. Such designs often feature lower field and lower cost magnets [12], [21]. However, even with these novel techniques, a standard MRI system design is still, relatively speaking, expensive and complex, where much of the cost and complexity of MRI systems is associated with the generation of the switched magnetic field gradients needed for image encoding, as commonly seen in traditional commercialized MRI system. This main magnetic gradient system not only accounts for nearly 30% cost of parts, as illustrated in Figure 1.1, it also requires stable and high power supplies and adequate engineering support. In the early MRI literature a number of alternative image encoding approaches were investigated including some which make use of amplitude gradients in the transmit RF field (B_1), however clinical use was constricted by the need for extremely high RF power pulses [22], [23].

The principle investigator Dr. Jonathan Sharp is the co-inventor of an alternative MRI encoding principle, known as "Transmit Array Spatial Encoding" (TRASE), which functions entirely without gradient systems. Compared with many other novel MRI approaches, this method has the potential to generate sub-mm clinical image resolution [20], [24]. Using only the resonant RF transmit field B_1, Fourier spatial encoding equivalent to conventional MRI can be achieved. The concept relies upon the production of spatial phase gradients in the RF field and on echo-train pulse sequences. To encode a spatial axis, two different RF phase gradient transmit fields of opposite sign are applied as 180 degree refocusing pulses in alternation, resulting in progressively increasingly high-resolution data moving down the echo train. A long echo train therefore corresponds to high spatial resolution. The crucial discriminating feature of TRASE is that encoding is progressive, so image resolution is only limited by the length of the echo train, and in certain regimes very high-resolution imaging is possible. Image resolution is also proportional to phase gradient strength, which is dictated by transmit coil geometry. The high resolution capability makes this a standalone imaging technique which has been very well received, most notably being featured in 'Research Highlights' in Nature in 2013. [19]

TRASE promises the possibility of cheaper, portable, yet high-resolution MRI systems. Such MRI systems will increase the availability of MRI diagnostics to the world's population, enabling the provision of health care in remote regions like the Canadian north, rural locations and in developing countries. These MRI scanners will also find applications in the emergency room where a portable MRI is preferred to portable X-ray tomography because of the avoidance of ionizing radiation. The potential applicable scenarios are summarized in Figure 1.2.

The technical requirements for TRASE can be derived from the need to maintain adequate pulse refocusing action (hence image encoding). The need is for short ($\sim$ 100 μs) RF refocusing pulses on uniform magnitude (+/- 5%...10%) B_1 transmit fields, each possessing strong linear phase gradient ($\sim$ 5 deg/cm). Before I started my doctoral research, 2D en-

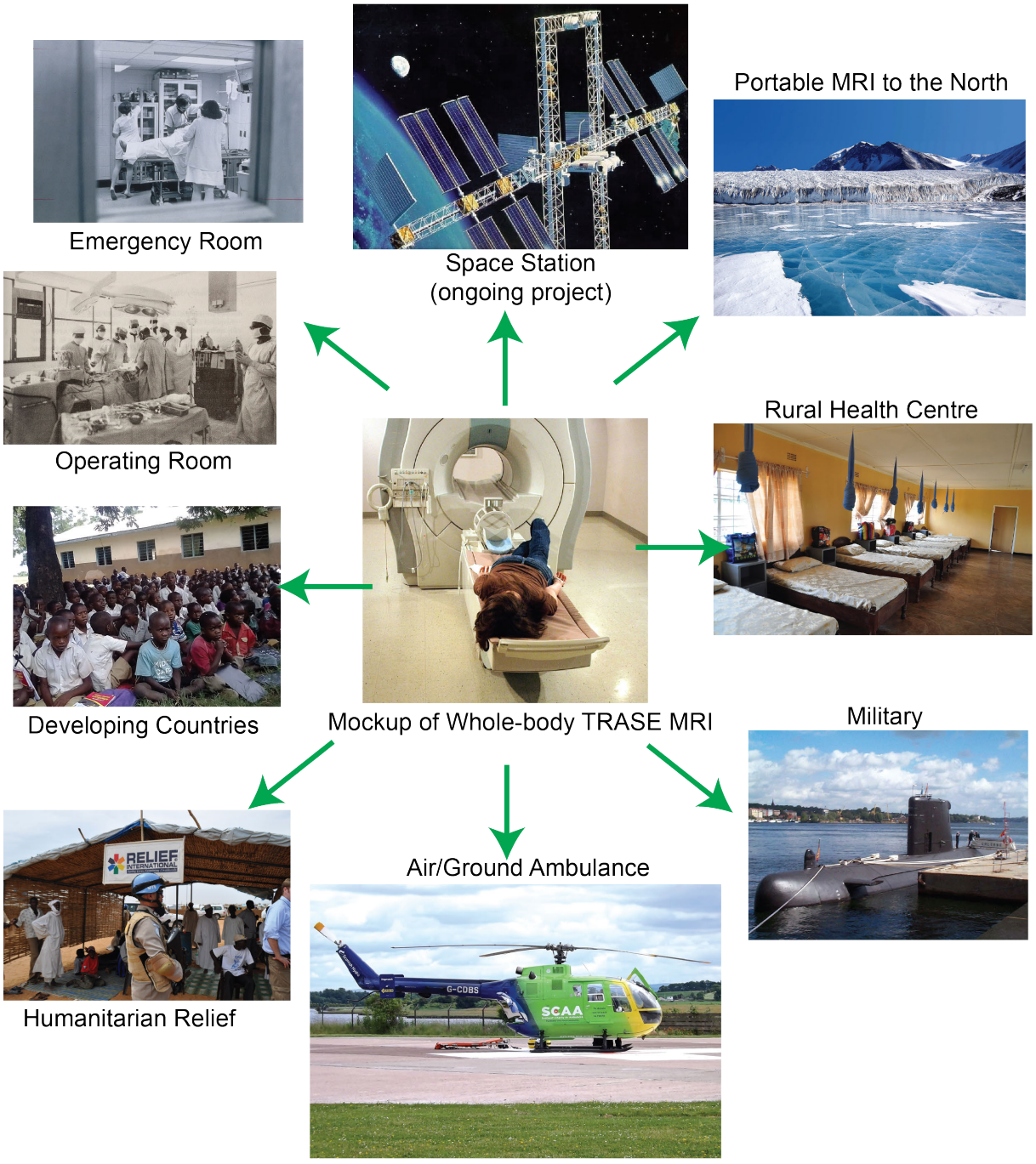

Figure 1.2: The potential applicable scenarios for TRASE MRI. All figures are from Wikimedia Commons with granted permissions.

coded *in vivo* TRASE MRI images of hand and wrist (see Figure 1.3) were obtained at a 0.2 T MRI system using a switched RF transmit Helmholtz-Maxwell coil array, driven by a single transmitter amplifier [25]. The array produces four phase gradient fields, which allows the encoding of two orthogonal spatial axes. Full 3D encoding using six fields has also been demonstrated in phantom experiments [24]. Moreover, this technological breakthrough may allow MRI to be transported into space for the first time. A TRASE-based wrist imager to study degenerative musculoskeletal changes in microgravity for the International Space Station has been researched over the last years, producing a 150+ page technical report [6].

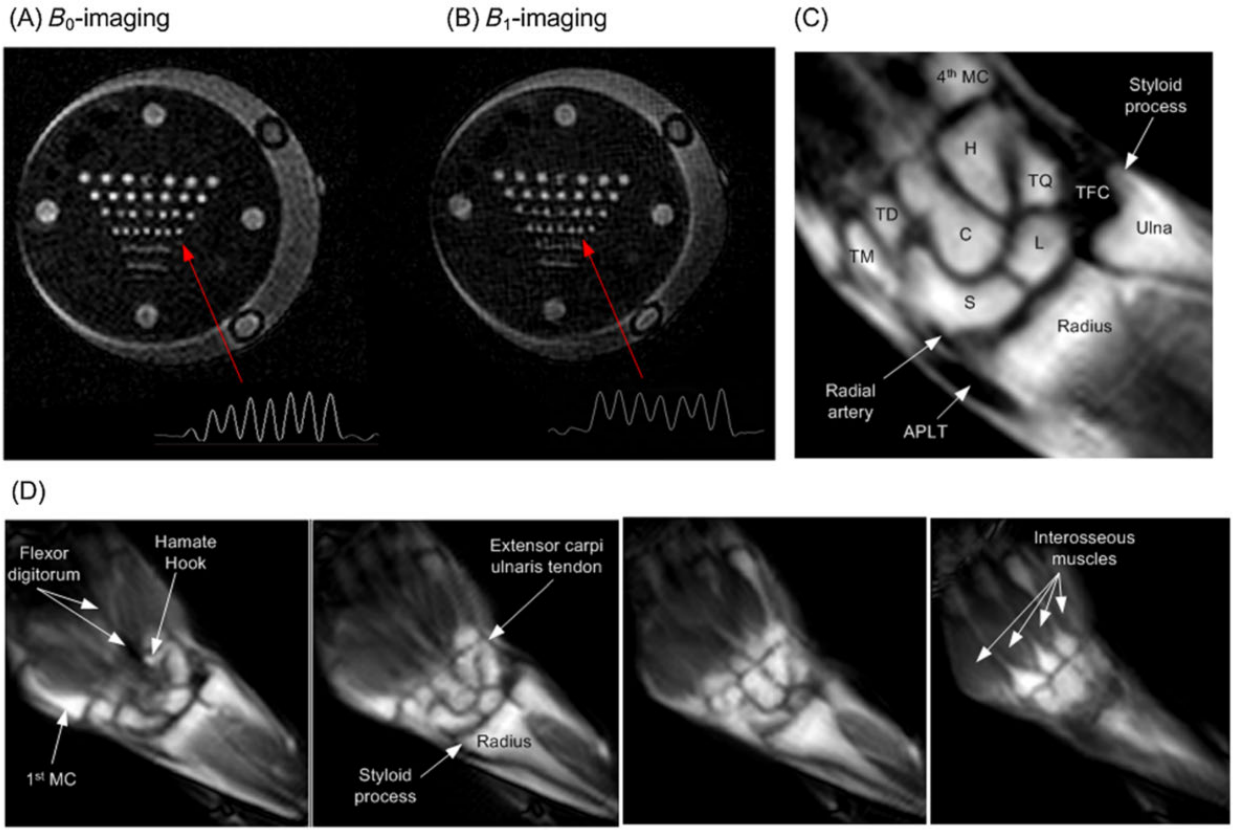

Figure 1.3: Wrist MR images show anatomical detail and contrast. A) and B): Comparison between conventional MRI (spin echo, TE = 14 ms, TR = 1000 ms), and TRASE encoding (pulse duration t_p = 500 μs, pulse spacing t_{sp} =700 μs, TR = 1000 ms, NA = 2) for a star phantom. C) and D) are 2D in vivo wrist images encoded using 4 phase gradients, where t_p = 500 μs, t_{sp} =1.1 ms, echo train length = 200. The third axis encoding was achieved by phase encoding. The figure is from the article [19], with permission granted from the rights owner (John Wiley and Sons) under license number 4841131295111.

The obtained 2D in vivo images show great promise for clinical application, however, further

improvement for *in vivo* image resolution is restricted to the RF coil efficiency. In current work, refocusing pulses are too long ($\sim 500\mu s$), and thus render the echo train sequence vulnerable to tissue T_2 relaxation losses. Additionally, the data acquisition of 3D TRASE MRI is slower than for ordinary clinical MRI.

In my Ph.D. work, I mainly focused on the design and verification of novel TRASE RF coils based upon new coil geometry, and reliable MRI control electronics. My co-author contributions can be found in projects involved with RF amplifier development [15], quad PIN diode driver for transmit switch [17], and TRASE pulse sequence design [14]. However, in this thesis, I will limit the scope of discussion to my main work on RF technologies only.

1.3 Introduction to Thesis

1.3.1 Thesis Hypothesis

Efficient TRASE MR encoding can be achieved by a new RF coil design, resulting in shorter refocusing pules and faster echo train. In addition, several such coils can be combined together with adequate decoupling techniques to accomplish multi-dimensional TRASE encoding, obtaining high resolution images even for short T_2 objects.

1.3.2 Thesis Organization

This thesis is organized into 6 main chapters, excluding Chapter 1 the overview (this chapter) and Chapter 8 for conclusions and future work.

Chapter 2 and 3 demonstrate the fundamental knowledge needed for this doctoral research. Specifically, Chapter 2 explains the basics of MRI and then covers the underlying theory of TRASE MR techniques, while Chapter 3 presents an introduction to radio-frequency design and several TRASE RF coil examples that were implemented prior to my work. The reader is expected to have some familiarity with basic MRI physics, such as the rotating reference

frame, RF pulses with different amplitude and phase, frequency and phase encoding, gradient systems, spin echoes, and the signal equation, etc. In this thesis, these topics will be repeatedly used, however, they will not be identified in details. The reader is encouraged to refer to other MRI resources such as [2], for clearer demonstrations of these common MRI concepts.

Chapter 4 is adapted from a journal article published in Journal of Magnetic Resonance, entitled:"*The twisted solenoid RF phase gradient transmit coil for TRASE imaging* [13]." It presents the design of a new family of phase gradient transmit coil based upon a solenoid twisted about a transverse axis. This design has many attractive geometric, electrical and magnetic characteristics, including the capability to spatially encode in the direction of the main static magnetic field without obstructing access to the bore. Analytical, numerical simulation and experimental results are presented, including demonstration of 1-dimensional TRASE encoding without the use of PIN diode switches.

Chapter 5 is based on a second publication that can be found in Magnetic Resonance in Medicine, entitled:"*A geometrically decoupled, twisted solenoid single-axis gradient coil set for TRASE* [16]." The new twisted solenoid coil can be rotated to generate a phase gradient in any transverse direction, therefore, combining two such coils would double k-space coverage for single-axis encoding, resulting in higher spatial resolution. This study demonstrates that a pair of twisted solenoid phase gradient RF coils can be geometrically decoupled, with added regular solenoid decoupling pair. Advantages over active PIN diode decoupling include faster switching, lower hardware complexity, and scalability.

Chapter 6 demonstrates the combination of three RF coils including two twisted solenoids and one saddle coil, for 2D TRASE encoding in the axial plane. The geometric decoupling techniques mentioned in Chapter 5 was fully exploited in this work, resulting in good decoupling capability on all three coils. However, since 2D TRASE imaging involves substantial use of RF pulses transmitted by three coils, the imaging result is extremely sensitive to the interactions among coils. To investigate the effects of residual coupling that are not captured

by geometric decoupling, TRASE MR experiments are performed, and the images are compared with Bloch simulation results from a collaborator, leading to a crucial understanding for users implementing practical TRASE coil arrays.

Chapter 7 presents the design of a quad parallel RF transmit system (PTx), which will be implemented together with geometric decoupling techniques to reduce the unwanted currents among coils. This new PTx is developed for low-field MRI scanners, based upon AD9106 quad DAC waveform generator chip and Altera Terasic Cyclone V System-on-Chip (SoC) board. Bench measurements indicated that four independent sine waveforms can be generated with this new PTx. As for RF pulse characteristics including waveform shape, duration, amplitude, phase, and start/end time, these can be elegantly specified and promptly updated ($\sim 12\mu s$), making a design of highly efficient MR sequence possible. The chosen Terasic Cyclone SoC board includes Analog-to-Digital converter, which makes MR receive functionality even possible. Based on this work, future developments on PTx and corresponding MR images will be demonstrated, possibly in the near future.

Chapter 2

Theory of MRI and TRASE Sequence

2.1 A Brief Overview of MRI Basics

2.1.1 Nuclear Spins

Magnetic Resonance (MR) is a measurement technique and may be performed on quantum particles possessing both spin and a magnetic moment. These include the electron, the neutron and many atomic nuclei. This thesis only focuses on nuclei and the use of MR techniques for their study. Recall that the nucleus is the location of the positively charged protons. Nuclei with net non-zero spin possess a local magnetic field, *i.e.*, a magnetic moment.

In clinical MRI lots of studies are performed upon hydrogen nucleus which is a single, positively charged proton, as shown in Figure 2.1. From quantum theory it is clear that the number of energy states of a nucleus is related to its spin quantum number S by number of energy states = $2S + 1$ [26]. Therefore, for a proton with a spin $S = 1/2$, the number of energy states is 2 (parallel and anti-parallel). Each proton spins about its axis, but there is no net magnetization present if an ensemble of protons are randomly oriented. However, when they are placed in an external magnetic field (referred to as B_0), they tend to line up with B_0, generatng a net magnetization M_0, as demonstrated in Figure 2.1. In this case, these protons not only spin about its own axis but also precess about the axis of B_0, with

the precess rate described by the Larmor equation:

$$\omega_0 = \gamma B_0 \tag{2.1}$$

where ω_0 is angular precessional frequency of proton, γ represents the gyromagnetic ratio.

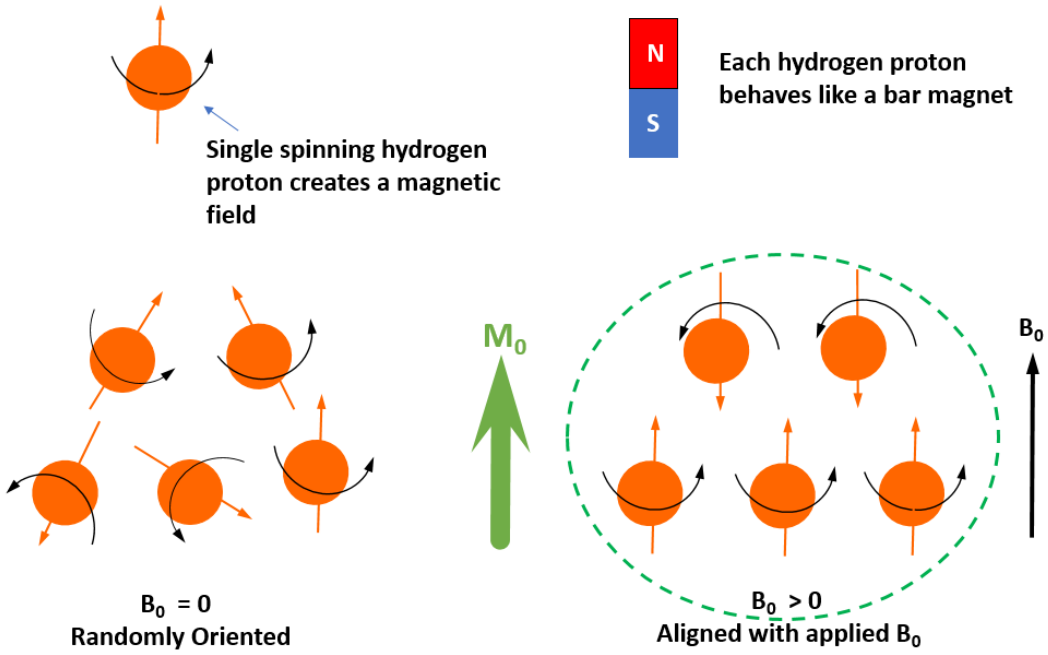

Figure 2.1: The schematic diagram of hydrogen nuclei and how a net magnetization (M_0) is created and aligned with an external magnetic field B_0.

2.1.2 The Bloch Equations and MR Relaxation

The nuclear magnetic resonance phenomenon is modeled on the macroscopic scale by a differential equation derived by Felix Bloch, and is characterized as the Bloch equations, shown as [26], [27]

$$\frac{d\mathbf{M}}{dt} = \gamma \mathbf{M} \times \mathbf{B} - \frac{M_x \hat{\mathbf{x}} + M_y \hat{\mathbf{y}}}{T_2} - \frac{(M_z - M_0)\hat{\mathbf{z}}}{T_1} \tag{2.2}$$

in which $\mathbf{M}$ and $\mathbf{B}$ represent the magnetization of the object and the magnetic field vec-

tors. The middle term describes transverse or spin-spin (T_2) relaxation, which represents interactions between individual spins causing coherence loss at a rate characterized by the T_2 relaxation time. The last term describes the longitudinal or spin-lattice (T_1) relaxation, a procedure where spins lose energy to the surrounding environment, at a rate characterized by the T_1 relaxation time. For simplicity, the Bloch's equation is usually written as

$$\begin{aligned} \frac{dM_x}{dt} &= \gamma M_y B_0 - \frac{M_x}{T_2} \\ \frac{dM_y}{dt} &= -\gamma M_x B_0 - \frac{M_y}{T_2} \\ \frac{dM_z}{dt} &= \frac{M_0 - M_z}{T_1} \end{aligned} \tag{2.3}$$

where the solutions are given by

$$\begin{aligned} M_x(t) &= [M_x(0)cos(\omega_0 t) + M_y(0)sin(\omega_0 t)]e^{-\frac{t}{T_2}} \\ M_y(t) &= [-M_x(0)sin(\omega_0 t) + M_y(0)cos(\omega_0 t)]e^{-\frac{t}{T_2}} \\ M_z(t) &= M_0 + [M_z(0) - M_0]e^{-\frac{t}{T_1}} \end{aligned} \tag{2.4}$$

2.1.3 RF (B_1) Pulse

In general MR literature, B_0 field points along the z-axis. By applying a transverse (*i.e.*, x or y direction) time-varying magnetic field B_1, the magnetization vector M can be rotated out of its equilibrium. The Bloch equations predict that a resonance condition will take place, reaching a maximum at a transmit frequency of $\omega_{rf} = \omega_0$, which is also said to be on resonance. In this case, the angle of rotation α is commonly called the *flip* or *tip* angle, and takes the form of

$$\alpha = \gamma \int_0^{\tau} B_1(t)dt \tag{2.5}$$

in which τ is the duration of B_1 RF pulse. Once the magnetization has been rotated away from its equilibrium, the transverse component of the magnetization M_{xy} can be detected by placing one or more receiver RF coils, generating time-dependent voltage/current signals. After the transmission of a single B_1 RF pulse, the signal detected is called the free-induction decay (FID), with the largest FID obtained for a flip angle of 90° excitation B_1 RF pulse.

2.1.4 T_2 and T_2^* Decay

According to the Bloch equations, one may expect the FID signal decays following T_2 relaxation. However, the actual signal decay occurs much faster due to the small spatial variations in B_0 field caused by local magnetic field inhomogeneity. These small field deviations cause the spins to precess at different Larmor frequencies, leading to a faster signal decay at a rate described by T_2^* [28]. The T_2^* is the shortened relaxation time, and is typically a combination of two effects: 1) The irreversible thermodynamic process characterized as T_2 decay; and 2) Inhomogeneity in the B_0 field and magnetic susceptibility differences cause reversible T_2' decay. This relationship is given as

$$\frac{1}{T_2^*} = \frac{1}{T_2} + \frac{1}{T_2'} \tag{2.6}$$

2.1.5 Spin Echo MR Sequence

The reason for naming T_2' as a reversible decay is because the effect of T_2' spin dephasing can be reversed by the formation of a spin echo, which, in the simplest case, consists of a 90° excitation RF pulse, followed by a 180° refocusing pulse. Based upon this idea, spin echo sequences have been widely used in MR imaging since they were developed decades ago. The acquisition of one train of spin echoes requires the sequence to have at least one

excitation pulse, and multiple refocusing pulses (preferably 180°). The excitation pulse(s) tip the magnetization vector from the longitudinal direction to the transverse plane, while the refocusing pulses rotate dispersing spin isochromats about an axis in the transverse plane to refocus the magnetization vectors subsequently [29]. The detailed description of spin echo formation, fast/turbo spin echo sequences, and use in conjunction with B_0 gradient systems to generate T_1-, T_2-, and proton- weighted images, etc., can be widely found in the literature [2], [28], [30]. However, for a standardized TRASE sequence which uses RF phase gradients in the B_1 fields, only long spin echo trains are needed. This will be introduced in the later sections.

2.1.6 Hardware of an MRI Scanner

A commercial MRI scanner consists of four main components, each of which plays an important role in MR images formation as summarized below. A schematic diagram of the whole MR system is shown in Figure 2.2.

- **Magnet** - To produce strong external magnetic field B_0. The magnets can be categorized depending on the field strength, or type of design (*i.e.*, permanent vs. superconducting).
- **Gradient System** - To produce an *intentional* perturbation in the B_0 field homogeneity (typically in a linear fashion), allowing one to decipher spatial information embedded in the received signal and localize it in space [30].
- **RF transmit/receive System** - To rotate the spin magnetization as a transmitter, or detect the magnetic flux created by the precession of the excited nuclear magnetization as a receiver.
- **Control Console** - To monitor and control the entire procedure such as manipulation of RF pulses and gradients necessary to acquire data, analysis to produce image, and data storage.

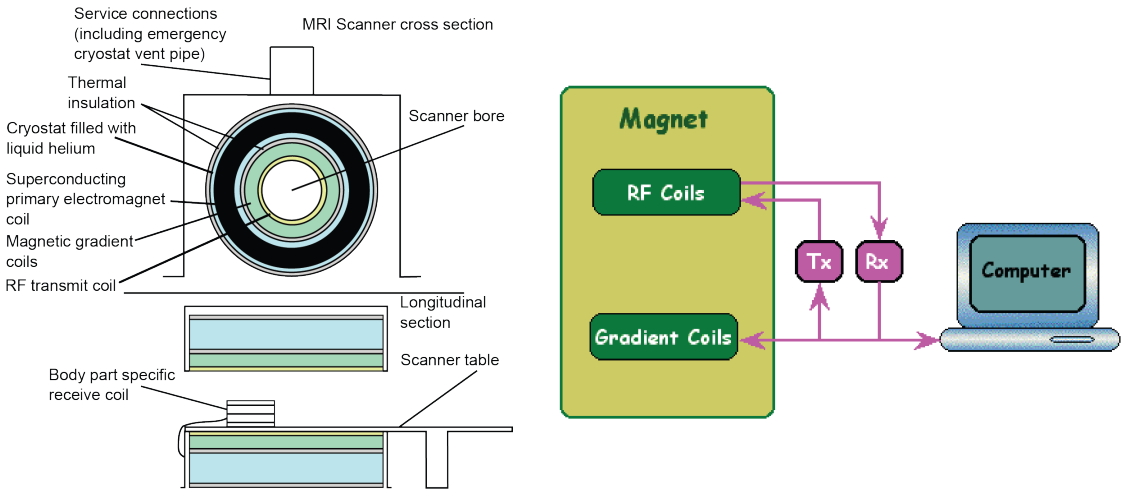

Figure 2.2: The schematic diagram of a commercial MRI scanner consisting of four main components. Figure source: `https://commons.wikimedia.org/wiki/File:MriScanner.gif`, and `https://en.wikipedia.org/wiki/File:Mri_scanner_schematic_labelled.svg` (Permissions granted)

2.2 MRI Data Collection in k-space

2.2.1 k-space and Filling Trajectories

The k-space is the data domain in MRI, and is mathematically described as the integral of B_0 magnitude gradient G over time t, as shown in the following equation in the unit of inverse distance, typically (cycles/m):

$$\mathbf{k}(t) = \frac{\gamma}{2\pi} \int_0^t \mathbf{G}(t')dt' \tag{2.7}$$

The real task of MR imaging can be simplified as to fill out the k-space in a designed manner - k-space trajectory. It is the path traced out by $\mathbf{k}(t)$, representing the acquisition strategy which affects both resulting artifacts and reconstruction algorithm to be applied. The k-space concept substantially simplifies the understanding of many pulse sequences which are rather cumbersome to analyze without it. Here, a simple example of ordinary Cartesian k-space trajectory is depicted, as shown in Figure 2.3.

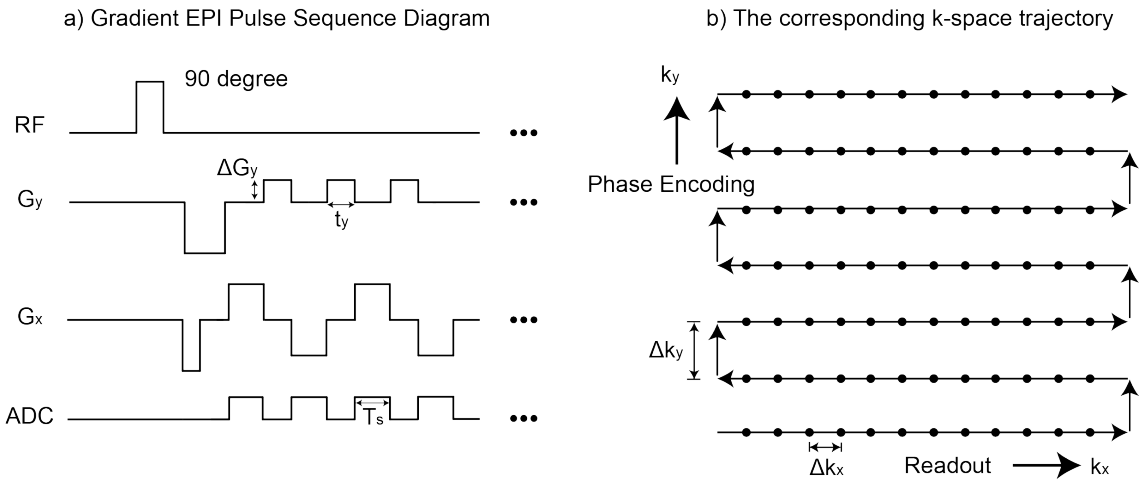

Figure 2.3: The schematic diagram of an ordinary Cartesian k-space trajectory using B_0 magnitude gradient. An example of gradient echo planar imaging (EPI) pulse sequence diagram and its corresponding k-space trajectory are shown. The k-space data collection starts at the bottom-left corner because large negative G_x and G_y gradients are applied before the first ADC. During each ADC, the readout gradient G_x is turned on, making a horizontal line of k-space points acquisition, followed by a small positive G_y gradient which causes a vertical movement in k-space.

The k-space corresponds to the data domain that is Fourier conjugate to the spatial/image domain, so image reconstruction involves with the direct Fourier Transform (FT). As a rule-of-thumb, the center of the k-space contains maximum signal and contributes to the contrast of the image, while the periphery of k-space contributes to the fine detail of the image, as illustrated in Figure 2.4.

2.2.2 B_1 Phase Gradient in k-space

A conventional MRI system is equipped with B_0 magnitude gradients, however, what makes TRASE unique is that it uses a different gradient for MR encoding. Specifically, TRASE MRI defines a linear phase gradient in the RF field (B_1), as given by:

$$\mathbf{B}_1 = |\mathbf{B}_1| e^{i\phi_1(\mathbf{r})}, \quad \phi_1(\mathbf{r}) = \mathbf{G}_1 \cdot \mathbf{r} = 2\pi \mathbf{k}_1 \cdot \mathbf{r} \tag{2.8}$$

The vector $\mathbf{k}_1$ represents the inherent phase variation in the RF field (B_1). For a conventional

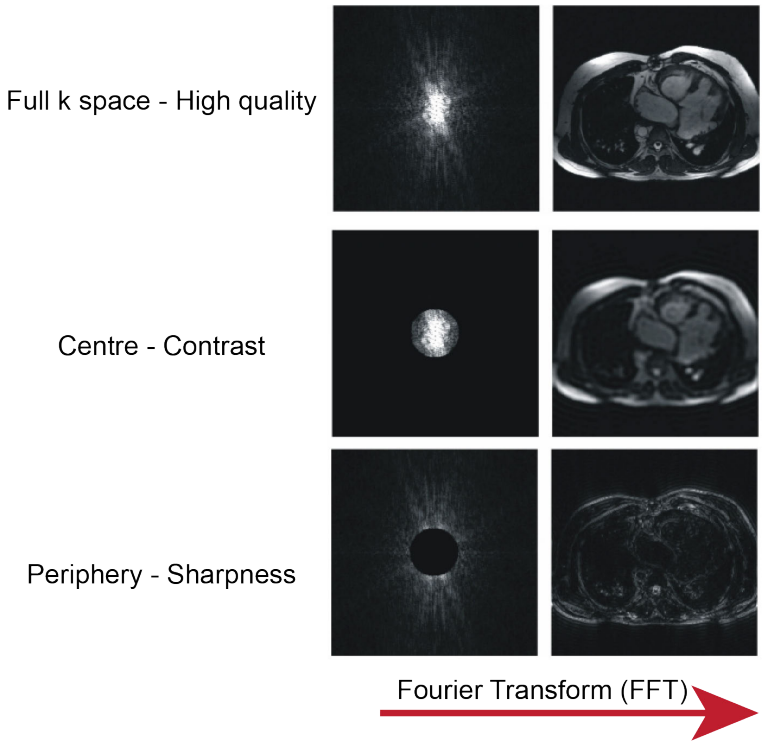

Figure 2.4: The Fourier Transform from k-space to spatial domain and different contribution of k-space points to MR image. (Reproduced with permission from Moratal et al. [31])

RF field with uniform phase distribution over space, $\mathbf{k}_1 = \mathbf{G}_1 = 0$. Since the B_1 amplitude is not needed for spatial encoding, it is preferably uniform. The generation of such RF phase gradient by either a dedicated coil design, or by the superposition of multiple fields will be explicitly discussed in the next chapter.

As mentioned previously, using k-space concept greatly simplifies the understanding of pulse sequences and image quality. By taking a look at the definition of $\mathbf{k}_1$ in Eq.2.8, it is an interesting fact that each $\mathbf{G}_1$ characterizes an RF field and corresponds to a unique $\mathbf{k}_1$ vector $\mathbf{k}_1 = (k_{1X}, k_{1Y}, k_{1Z})$ as follows:

$$\mathbf{k}_1 = \mathbf{G}_1/2\pi \tag{2.9}$$

This implies that, unlike conventional B_0 magnitude gradient, each RF phase gradient $\mathbf{G}_1$ can be represented as a single point in k-space, which is refereed to as the phase gradient

"k-space origin" [20]. For any non-zero phase gradient, it is an off-center point in k-space, as shown in Figure 2.5a).

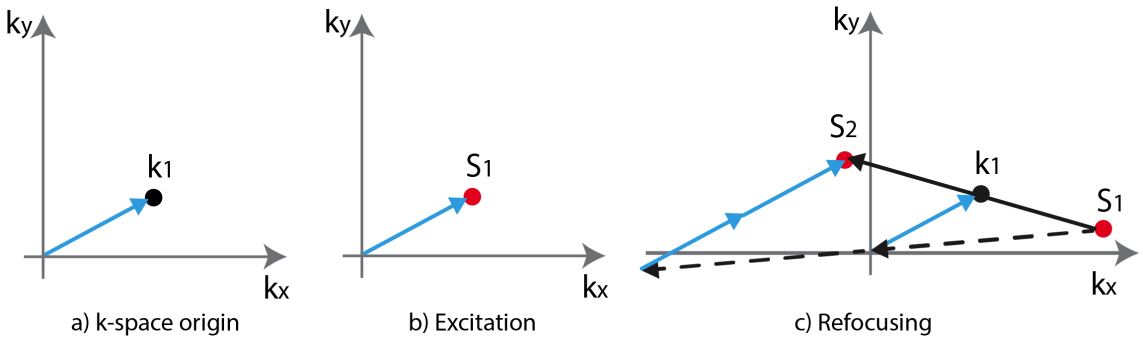

Figure 2.5: Basic k-space properties for RF phase gradient fields. a): The phase gradient is represented as a single point in k space, $\mathbf{k}_1$, referred to as the field "k space origin"; b): Excitation using the phase gradient results in an immediate excitation to origin $\mathbf{k}_1$; c) Refocusing an arbitrary spin state S_1 using the phase gradient is equivalent to a jump about the origin $\mathbf{k}_1$. The materials are reproduced from the article [20] with permission from the rights owner (John Wiley and Sons) under license number 4841130683566.

2.2.3 Same k-space, Two Definitions

In MRI $\mathbf{k}$ is used to describe the spin state. Here, we use $\mathbf{k}_1$ to describe the coil, however, these two are the same concepts. To illustrate this, one may consider a 1D imaging experiment consisting of a 90° excitation pulse followed by a constant magnitude gradient G applied for a time interval T, the detectable transverse magnetization is given by

$$M_{xy} = M_0 e^{i\phi(\mathbf{r})} = M_0 e^{i\gamma T \mathbf{G}\cdot\mathbf{r}} = M_0 e^{i2\pi \mathbf{k}\cdot\mathbf{r}} \tag{2.10}$$

Now let us consider a 90^{-Y} RF excitation pulse applied with an RF phase gradient. Similarly, given an initial longitudinal magnetization of M_0, the excitation pulse results in transverse magnetization of

$$M_{xy} = M_0 e^{i\phi(\mathbf{r})} = M_0 e^{i2\pi \mathbf{k}_1\cdot\mathbf{r}} \tag{2.11}$$

The above two equations are mathematically equivalent. Hence, $\mathbf{k}$ and $\mathbf{k}_1$ are representing identical concepts, but are simply derived from different point-of-view.

2.2.4 k-space Actions for RF Pulse Transmission using a Phase Gradient

Excitation pulse: In MRI experiments, the sequence typically starts with an excitation pulse, which tips a certain portion of longitudinal M_z down to the $x-y$ plane so that the spatial information from the imaging object can be extracted later. Here, the discussion is restricted to 90° excitation pulse only, as this is what will be used in a standard TRASE pulse sequence that will be introduced in the coming sections.

In the previous section the equivalence of Eq.2.10 and Eq.2.11 has already identified that the spatial encoding is immediately contained in the phase of the NMR signal using a single 90° excitation pulse, *i.e.*, the spin system is excited directly to the k-space origin $\mathbf{k}_1$, as illustrated in Figure 2.5(b). To help explain this, a different perspective based on spin rotation is provided.

In Figure 2.6(a), consider a 1D object that has three spins located at different y positions. The conventional 90° excitation first tips all the spins down to $+y$ axis. These spins then precess at slight different frequencies due to the presence of B_0 magnitude gradient along y axis, resulting in a phase evolution after time interval T.

In Figure 2.6(b) a B_1 phase gradient G_{1y} is plotted. For the same 1D object 90° excitation pulse tips down spins at different locations within x-y plane, with phase modulation immediately imparted. The ultimate spin states are identical using two different excitation methods, corresponding to the same location in k-space, as seen by Figure 2.5(b).

Refocusing pulse: Similarly, the investigation of refocusing pulse transmit starts with the simplest case in spin state. Imagine a single refocusing pulse with phase ϕ_1 that is applied to reverse an initial transverse (M_{xy}) magnetization from phase θ_1 to θ_2 symmetrically about ϕ_1.

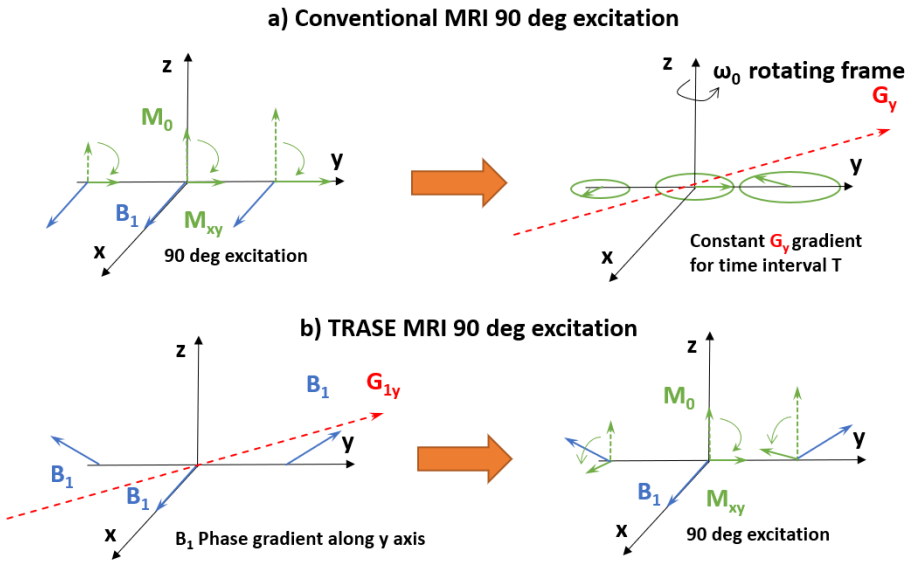

Figure 2.6: The same spin state produced by two different excitation methods: a) Conventional 90 degree excitation using uniform RF field plus constant B_0 gradient G_y turned on for a time interval T; b) Direct 90 degree excitation using phase gradient G_{1y}.

This procedure is depicted in Figure 2.7(A),(B). Due to the symmetry, it is straightforward to write down the phase change from the figure:

$$\theta_1 - \phi_1 = 2\pi - \theta_2 + \phi_1 \longleftrightarrow \theta_2 - \theta_1 = -2\theta_1 + 2\phi_1 \tag{2.12}$$

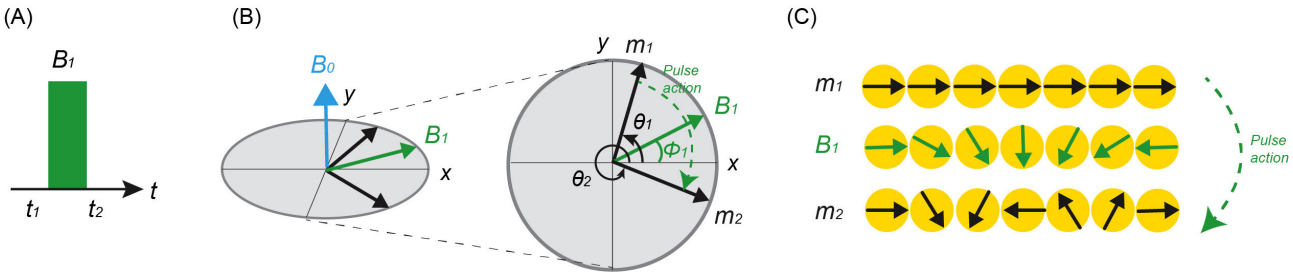

Figure 2.7: The encoding action of a 180° RF pulse. (A) A single 180° RF pulse in time domain. (B) Transverse magnetization m_1 is transformed into m_2 by reflecting about a direction defined by the phase of the refocusing pulse. (C) Refocusing by a B_1 phase gradient produces spin dephasing, *i.e.*, shift in k-space. The materials are reproduced from the article [19] with permission from the rights owner (John Wiley and Sons) under license number 4841131295111.

The above equation demonstrates the phase after refocusing RF pulse is determined by the initial spin phase θ_1 and local RF pulse phase ϕ_1. However, this only applies to conventional

MRI where no spatial-dependent phase variation exists, *i.e.*, ϕ_1 is a constant value for all spins seeing the refocusing B_1 pulse. Recall Eq.2.8 that $\phi_1(\mathbf{r}) = \mathbf{G}_1 \cdot \mathbf{r} = 2\pi \mathbf{k}_1 \cdot \mathbf{r}$, the above equation (after subtraction of 2π) is updated to the following expression when phase gradient $\phi_1(\mathbf{r})$ applies:

$$\theta_2 - \theta_1 = -2\theta_1 + 2\phi_1(\mathbf{r}) = -2\theta_1 + 2\pi[2\mathbf{k}_1 \cdot \mathbf{r}] \tag{2.13}$$

which proves that refocusing by a B_1 phase gradient field produces spin dephasing, as illustrated in Figure 2.7(C). Specifically, when applied with an RF phase gradient, a single 180° pulse rotates initial transverse magnetization M_{xy}^- about the B_1 field direction $\phi_1(\mathbf{r})$ to M_{xy}^+:

$$M_{xy}^+ = M_{xy}^- e^{i[-2\theta_1 + 2\phi_1(\mathbf{r})]} = M_{xy}^{-*} e^{i2\pi(2\mathbf{k}_1 \cdot \mathbf{r})} \tag{2.14}$$

Note that $M_{xy}^{-*} = M_{xy}^- e^{-i2\theta_1}$, denoting the complex conjugate of initial transverse magnetization M_{xy}^-.

Again, it is more convenient to understand the refocusing effect in k-space. For the imaging phantom as a whole, the final k-space location $\mathbf{k}^+$ corresponding to M_{xy}^+ is obtained through two steps, assuming the initial k location for M_{xy}^- is $\mathbf{k}^-$.

- **Step 1** M_{xy}^{-*} - Refocusing with phase gradient first results in a reversal **(1^{st} jump)** in sign ($\mathbf{k}^- \longleftrightarrow -\mathbf{k}^-$) due to the complex conjugate of M_{xy}^-, which is a familiar action of an ordinary refocusing pulse.
- **Step 2** $e^{i2\pi(2\mathbf{k}_1 \cdot \mathbf{r})}$ - The exponential phase term represents a spatially dependent phase increment, *i.e.*, a shift in k space. This corresponds to a 2^{nd} **jump** along the encoding direction of $+2\mathbf{k}_1$.

By using a phase gradient to transmit single refocusing pulse, the corresponding two jumps in k-space can be written as (these two jumps are visible in Figure 2.5(c))

$$\mathbf{k}^{+} = -\mathbf{k}^{-} + 2\mathbf{k}_1 \tag{2.15}$$

Examine above equation, rewrite it as

$$(\mathbf{k}^{+} - \mathbf{k}_1) = -(\mathbf{k}^{-} - \mathbf{k}_1) \tag{2.16}$$

Therefore, the refocusing action is simply equivalent to a reflection about the coil k-space origin $\mathbf{k}_1$, which is consistent with the behavior of a uniform phase coil, for which $\mathbf{k}_1 = 0$.

So far single excitation and refocusing RF transmit pulses are explicitly demonstrated for TRASE, and the recommended way to digest these concepts would be the understanding of their corresponding k-space actions. Unfortunately, from Eq.2.16 if the same phase gradient is used for both excitation and refocusing, *i.e.*, starting with $\mathbf{k}^{-} = \mathbf{k}_1$, acquisition of data is limited to one single k-space point only, since the k-space location is unchanged: $\mathbf{k}^{+} = \mathbf{k}^{-}$. No further k-space traversal is achieved. Since the first excitation pulse initializes a direct jump to the coil origin in k-space, so in principle the idea of using a single excitation to achieve high-resolution MR imaging is possible, but very difficult as it requires the generation of B_1 fields with impractically large phase gradients, which are unachievable for a volume coil configuration. However, in the next section it will be shown that high-resolution is achievable by exploiting the properties of the NMR spin-echo to amplify the effect of the RF phase gradient strength by orders of magnitude. [20]

2.3 TRASE MRI Encoding Principles and Properties

2.3.1 Comparison of Three MRI Encoding Methods

The essence of MRI relies on the introduction of spatial dependence into the NMR experiment using a *gradient* system. The conventional encoding principle uses modulated magnetic field

Encoding Method	Gradient Type	Static field	RF field
Frequency encoding (conventional)	Main field	$B_0 + x \cdot G_x$	B_1
Rotating frame imaging	RF amplitude	B_0	$B_1 + x \cdot G_{1x}$
TRASE	RF phase	B_0	$B_1 e^{(ix \cdot G_{1x})}$

Table 2.1: Comparison of three MRI encoding methods. Table data is adapted from the article [20], with permission granted from the rights owner (John Wiley and Sons) under license number 4841130683566.

gradient G in the main static magnetic field B_0. However, this idea can be realized also in other approaches. For example, a gradient in the amplitude of the RF field B_1 (a.k.a. rotating frame imaging) was used to encode spatial information as an alternative imaging strategy in the early days. This technique is underused due to artifacts arising from uncompensated-for off-resonance effects [22]. In analogy to this idea, another gradient embedded in the phase of the B_1 field is also expected to allow MRI encoding, acting as a third type of magnetic field gradient for MRI imaging - Transmit Array Spatial Encoding (TRASE). Table 2.1 summarizes the three types of gradient definition [20].

2.3.2 1D TRASE Imaging

From the previous section, three concepts involved with the phase gradient were explained in MRI k-space. Since these rules will be applied in the entire thesis, these concepts are listed here as a reminder before the introduction of TRASE encoding principles:

- **k-space origin**: Each phase gradient is represented as a single point in k-space, known as a k-space origin
- **Excitation with phase gradient**: The RF excitation pulse results in a direct jump to the corresponding k-space origin
- **Refocusing with phase gradient**: The RF refocusing pulse results in an immediate jump (point reflection) about the corresponding k-space origin

Spatial encoding with two refocusing pulses

The above three rules do not show progressive phase evolution. However, with one more step it can be shown that the properties of phase gradient refocusing pulses allow an echo train to be constructed, where all echoes (each corresponds to a different k-space point) are sampled.

Recall that for a conventional MRI readout encoding, a B_0 gradient $\mathbf{G}_0$ is applied over a time interval Δt, during which spin phase evolves steadily even though only discrete sampling is made to record data. This spin phase accumulation $\Delta\phi$ is proportional to both the gradient strength and duration:

$$\Delta\phi = \gamma \mathbf{G}_0 \cdot \mathbf{r} \Delta t \tag{2.17}$$

This proportionality between phase increment and spatial position is sufficient for Fourier-based MRI encoding [32].

Referring to Eq.2.13 and Eq.2.8, a clear expression of phase change after a single refocusing pulse transmitted with a phase gradient $\mathbf{G}_1^A$ can be obtained:

$$\theta_2 - \theta_1 = -2\theta_1 + 2\mathbf{G}_1^A \cdot \mathbf{r} \tag{2.18}$$

This equation also contain the proportionality (see Eq.2.17), but with an extra unwanted initial phase θ_1. To get rid of it, imagine a second refocusing that is applied with a different phase gradient $\mathbf{G}_1^B$, the cumulative phase change as a result of both refocusing pulses can be summarized as

$$\theta_3 - \theta_1 = 2(\mathbf{G}_1^B - \mathbf{G}_1^A) \cdot \mathbf{r} \tag{2.19}$$

Provided that the two RF phase gradient are different, this equation relates phase increment

and spatial position, creating another form for Fourier imaging.

As usual, it is more intuitive to investigate the corresponding action of these two consecutive refocusing pulses in k-space, where $\mathbf{G}_1^A$ and $\mathbf{G}_1^B$ are substituted by $\mathbf{G}_1^A = 2\pi\mathbf{k}_A$ and $\mathbf{G}_1^B = 2\pi\mathbf{k}_B$. In Figure 2.8(A), as each refocusing RF pulse introduces a jump about its own origin, an arbitrary spin state S_1 undergoes the first jump about k-space origin k_A and locates at spin state S_2. A second jump about k_B is initialized due to the second RF refocusing pulse, which reflects the spin state from S_2 to S_3. The overall effect of two successive RF refocusing pulses with different phase fields $(\mathbf{k}_A, \mathbf{k}_B)$ is to translate any arbitrary k-space point by $\Delta\mathbf{k}_{BA}$.

To determine the value of $\Delta\mathbf{k}_{BA}$, recall Eq.2.14, then it can be written as:

$$M_{xy}^2 = M_{xy}^{1*} e^{i2\pi(2\mathbf{k}_A\cdot\mathbf{r})} \quad ; \quad M_{xy}^3 = M_{xy}^{2*} e^{i2\pi(2\mathbf{k}_B\cdot\mathbf{r})} \tag{2.20}$$

Combining the above two equations, a derivation is obtained:

$$M_{xy}^3 = M_{xy}^1 e^{i2\pi\Delta\mathbf{k}_{BA}\cdot\mathbf{r}} = M_{xy}^1 e^{i2\pi[2(\mathbf{k}_B-\mathbf{k}_A)\cdot\mathbf{r}]} \tag{2.21}$$

Thus, the combined effect of the two refocusing pulses is equivalent to a translation in k-space (see Figure 2.8(A)):

$$\Delta\mathbf{k}_{BA} = 2(\mathbf{k}_B - \mathbf{k}_A) \tag{2.22}$$

By equating two phase increments in Eq.2.17 and Eq.2.19, an equal encoding is to be made from two approaches:

$$\Delta\phi = (\gamma\Delta t)\mathbf{G}_0 \cdot \mathbf{r} = 2(\mathbf{G}_1^B - \mathbf{G}_1^A) \cdot \mathbf{r} \tag{2.23}$$

Therefore, as least in principle, any conventional B_0 encoded Fourier MRI experiment can be re-implemented as an B_1 encoded experiment which transmits two consecutive RF refocusing pulses with a spatial phase gradient of $\mathbf{G}_1^A$, followed by another one with $\mathbf{G}_1^B$, provided Eq.2.23 is satisfied. The two encoding paradigms are illustrated in Figure 2.8(B),(C), together with respective k-space representations.

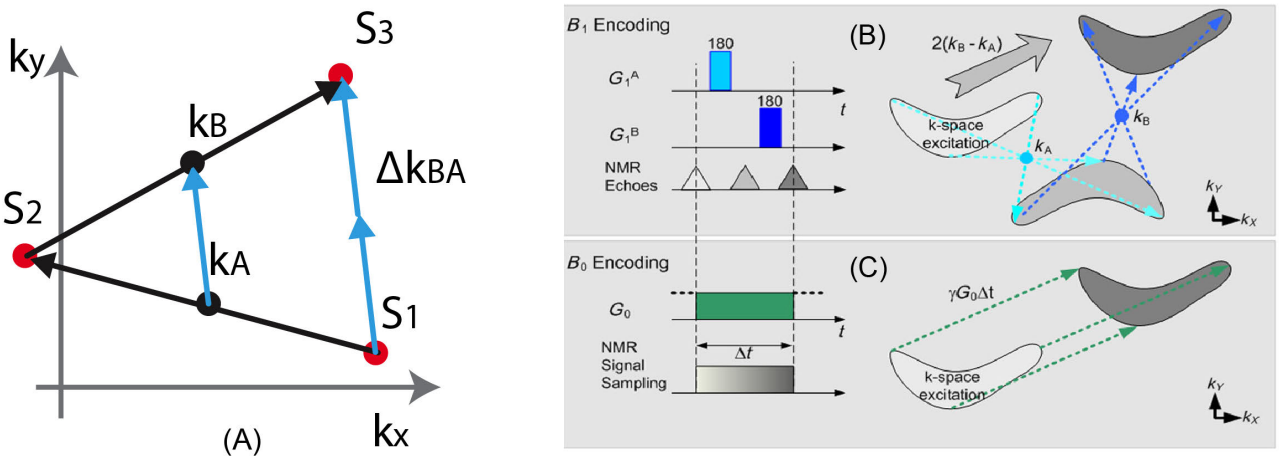

Figure 2.8: k-space properties for two refocusing pulses. A) The effect of two successive refocusing pulses with different fields ($\mathbf{k}_A$, $\mathbf{k}_B$) is to translate an arbitrary k-space point by $\Delta\mathbf{k}_{BA} = 2(\mathbf{k}_B - \mathbf{k}_A)$. B) Two point reflections resulting in a translation of signal in the k-space. C) Continuous k-space translation cause by B_0 encoding. The materials are reproduced with permissions from the rights owner (John Wiley and Sons) under license number 4841131295111 for the article [19], and 4841130683566 for the article [20].

1D TRASE Spin Echo Train

The Figure 2.8 has proved that the $(180_A - 180_B)$ RF refocusing pulse pair can be used as the basis for k-space imaging. For an echo train (echo train length of N) consisting of a series of refocusing pulse pair $(180_A - 180_B)_N$, the situation is very similar.

To see how it works, let's consider a transmit coil array (the exact generation of such coil array will be introduced later in the next chapter) which is capable of producing two different phase gradients: $\mathbf{G}_1^A$ and $\mathbf{G}_1^B$. After the first 90° excitation, the refocusing pulses are transmitted alternatively by two fields $\mathbf{k}_A$ and $\mathbf{k}_B$, which can be specifically expressed as: $90_A - 180_A - Obs_1 - 180_B - Obs_2 - 180_A - Obs_3 - 180_B - Obs_4, ...$, where Obs_i represents the

observed magnetization for the i^{th} echo. This echo train is visually depicted in Figure 2.9(a), being considered as the standard 1D TRASE imaging sequence.

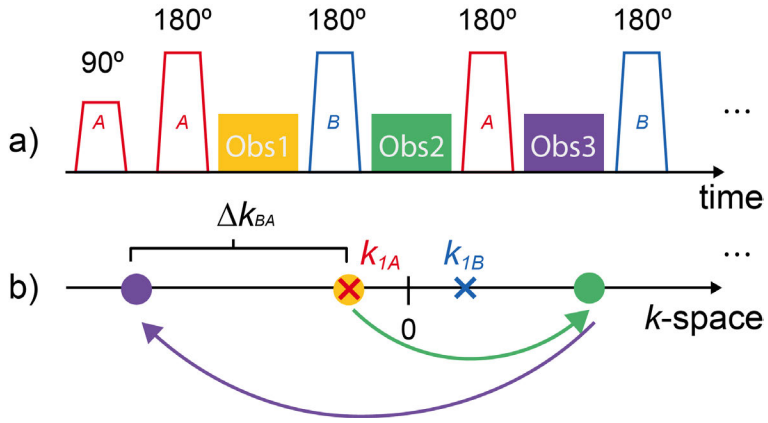

Figure 2.9: A standard 1D TRASE phase gradient imaging sequence. a) The basic 1D TRASE pulse sequence including a excitation pulse followed by a train of refocusing pulses applied alternately between field $\mathbf{k}_{1A}$ and $\mathbf{k}_{1B}$. NMR signal is measured at $Obs_{1..3}$ after each refocusing pulse. b) The corresponding k-space sampling pattern with k-space origins represented by crosses: $\mathbf{k}_{1A}$, $\mathbf{k}_{1B}$, and sampling locations depicted as color dots.

The MRI users are familiar with the resulting k-space trajectory by a specific pulse sequence, so it is better to re-describe the echo train behavior in k-space. The first 90_A excitation pulse excites the spins to coil A k-space origin $\mathbf{k}_{1A}$, followed by the first 180_A which essentially does not move the k point (reflect about itself). Therefore, the first observation Obs_1 is obtained at $\mathbf{k}_{1A}$, as represented in Figure 2.9(b) by the "orange circle". The second refocusing pulse 180_B causes a reflection about origin $\mathbf{k}_{1B}$, resulting in an instant jump to the "green circle", at a step size of $\Delta|\mathbf{k}_{BA}| = |2(\mathbf{k}_{1B} - \mathbf{k}_{1A})|$, see Eq.2.22. The subsequent refocusing pulses take turns triggering a series of jumps about either $\mathbf{k}_{1A}$ or $\mathbf{k}_{1B}$, during which the measurements (Obs_N) are taken to record the discrete phase evolution.

The k coordinates of observations are different depending on the observer due to the fact that the observed k-space coordinates k_{obs} is equal to the conventional k-space coordinate k_{conv} minus the k-space origin of the RF phase gradient receiver k_{1RF-RX}:

$$k_{obs} = k_{conv} - k_{1RF-RX} \tag{2.24}$$

For conventional MRI which typically uses uniform receive coil $k_{obs} = k_{conv}$. Here we assume all observations Obs_N are made through receive field $\mathbf{k}_{1A}$, so the k-space coordinates k_{obs}, listed in the order observed, are: $(0, \Delta|\mathbf{k}_{BA}|, -\Delta|\mathbf{k}_{BA}|, 2\Delta|\mathbf{k}_{BA}|, -2\Delta|\mathbf{k}_{BA}|, 3\Delta|\mathbf{k}_{BA}|, ...)$. In this case data reordering is required prior to image reconstruction using F.T. transformation, as demonstrated in Figure 2.9(b). For this sequence composed of N (odd) refocusing pulses, the recorded k-space data is centrically from $-(N-1)/2\Delta|\mathbf{k}_{BA}|$ to $(N-1)/2\Delta|\mathbf{k}_{BA}|$, making 1D TRASE encoding feasible.

2.3.3 TRASE Image Field-of-view (FOV)

In conventional MRI, the conversion between k-space and image domain is based on F.T., so there is a relationship between the axes in k-space and the image domain [2]:

$$\Delta w \cdot \Delta k = 1/N \tag{2.25}$$

in which Δw, Δk and N represent pixel size, k-space spacing, and number of digitized samples, respectively. Starting from this equation, two commonly-used expressions can be derived, which also applies to TRASE MRI.

With Eq.2.25, FOV is inversely proportional to the spacing Δk between samples in k-space, as seen by Figure 2.10. This can be expressed as:

$$FOV = N \cdot \Delta w = 1/\Delta k \tag{2.26}$$

Therefore, the FOV for $(180_A - 180_B)$ 1D TRASE standard sequence takes the form of:

$$FOV = 1/|\Delta\mathbf{k}_{BA}| = 1/|2(\mathbf{k}_B - \mathbf{k}_A)| \tag{2.27}$$

Recall Eq.2.8 this relationship is also equivalent to:

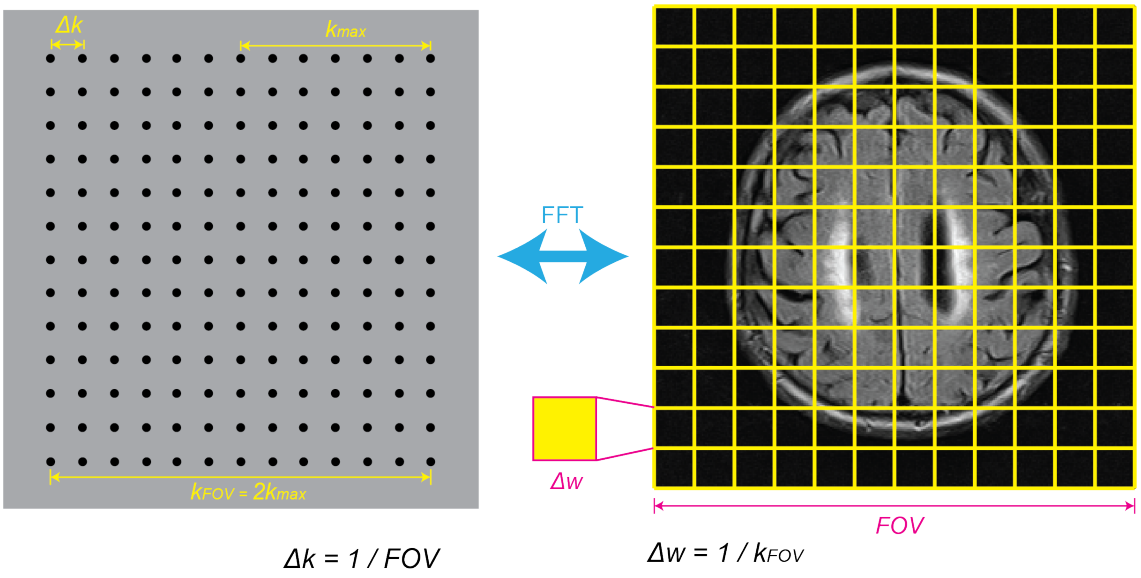

Figure 2.10: The determination of image field-of-view and pixel size. The brain figure is from the source: `https://commons.wikimedia.org/wiki/File:NPH_MRI_105.png` (permission granted)

$$FOV = 1/|2(\mathbf{k}_B - \mathbf{k}_A)| = \pi/|\mathbf{G}_1^B - \mathbf{G}_1^A| \tag{2.28}$$

which means the FOV without aliasing is the distance over which $|\mathbf{G}_1^B - \mathbf{G}_1^A|$ is equal to π. For example, if 1D TRASE encoding along x axis is performed with $\mathbf{G}_1^B = 4.0$ deg/cm, $\mathbf{G}_1^A = -4.0$ deg/cm, the FOV along x axis $FOV_x = \pi$ / |4.0 - (-4.0) deg/cm|= 22.5 cm.

One possible approach to increase TRASE FOV is to use multiple fields as the receiver simultaneously, provided the coupling among coils are adequately minimized. For instance, for the same 1D TRASE sequence (see Figure 2.9) if field $\mathbf{k}_{1B}$, instead of $\mathbf{k}_{1A}$ as we described previously, is used for receiving, all previous k-space coordinates observed by field $\mathbf{k}_{1A}$: $(0, \Delta|\mathbf{k}_{BA}|, -\Delta|\mathbf{k}_{BA}|, 2\Delta|\mathbf{k}_{BA}|, -2\Delta|\mathbf{k}_{BA}|, 3\Delta|\mathbf{k}_{BA}|, ...)$ are shifted by $\mathbf{k}_{1A} - \mathbf{k}_{1B} = -1/2|\Delta\mathbf{k}_{BA}|$, resulting in a new set of points $(-1/2|\Delta\mathbf{k}_{BA}|, 1/2|\Delta\mathbf{k}_{BA}|, -3/2|\Delta\mathbf{k}_{BA}|...)$. Reorder and compose two sets of k points together can generate a denser set of data in k-space, resulting in a double image FOV.

2.3.4 TRASE Image Pixel Size

From the same Eq.2.25, an inverse relation also holds (see Figure 2.10) between Δw and the range between the highest positive ($+k_{max}$) and negative ($-k_{max}$) spatial frequencies in k-space. Defining $k_{FOV} = (+k_{max}) - (-k_{max}) = 2k_{max}$, the image pixel size Δw is given by:

$$\Delta w = 1/(\Delta k \cdot N) = 1/2k_{max} = 1/k_{FOV} \tag{2.29}$$

For a 1D TRASE sequence with an echo train length of ETL, i.e. the number of jumps in k-space = ETL, the resulting pixel size is given by:

$$\Delta w = 1/(|\Delta k_{BA}| \cdot ETL) = 1/|2 \cdot ETL \cdot (\mathbf{k}_B - \mathbf{k}_A)| \tag{2.30}$$

Ideally, Δw determines MR image spatial resolution. However, it should be mentioned that any mechanism leading to loss of signal down the echo train such as T_2 losses and diffusion, will degrade MR image spatial resolution [33].

2.3.5 TRASE Single k-space Line Duration

Due to the nature of TRASE encoding principle, the later echoes always correspond to the high spatial frequency information in k-space. Therefore, the effects of T_2 decay causes blurring which is typically referred to as peak broadening of point spread function (PSF). A rule-of-thumb is that the total duration per echo train should be no longer than 1.2 times the shortest T_2 to be imaged [33]. This T_2 constraint requires the duration of RF pulse to be shortened, thus, hard pulses are commonly used in TRASE. Assuming the echo spacing between two adjacent refocusing pulses is T_{sp} (see Figure 2.11), and ignoring the timing cost for the first excitation, the duration of a single spin echo train T_{scan} can be characterized as:

$$T_{scan} \approx ETL \times T_{sp} \leq 1.2T_2 \tag{2.31}$$

where $T_{sp} = T_p + T_{acq}$, T_p is pulse duration, and T_{acq} is acquisition window. Based the above equation, it can be concluded that for tissues with short T_2 values, a highly efficient TRASE sequence with short pulse duration and small echo spacing (*i.e.*, high duty cycle) is needed.

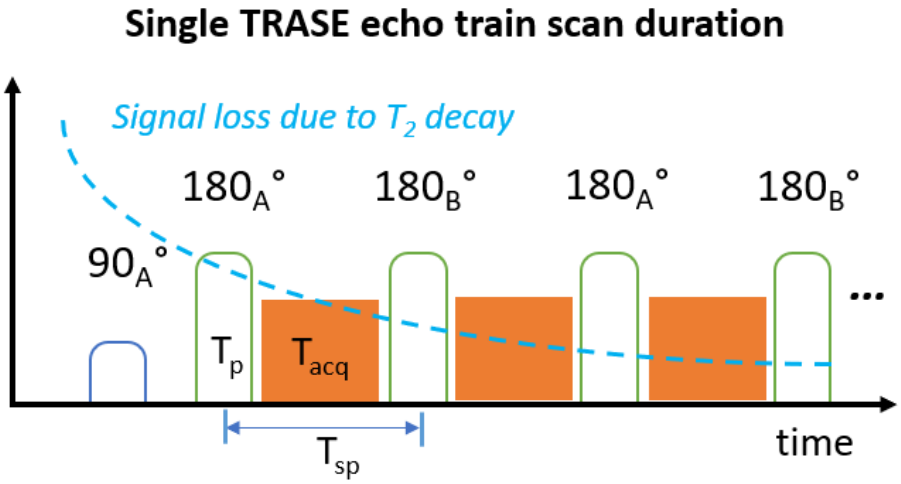

Figure 2.11: Schematic of different timing definition listed in 1D TRASE sequence. Hard pulse duration: T_p; Data sampling window: T_{acq}; Echo spacing: $T_{sp} = T_p + T_{acq}$.

2.3.6 2D TRASE MRI Encoding

In this section, the encoding principle of 2D TRASE will be introduced. It is essentially an extension of 1D TRASE encoding principle as introduced earlier, however, depending on the number of applied RF phase gradients, different k-space jump trajectories are presented.

2D encoding with three phase gradients

The 1D TRASE encoding principle can be extended to 2D imaging. To achieve this, at least a third non-collinear RF phase gradient ($\mathbf{k}_C$) is needed, since with this added phase gradient three non-parallel encoding axes can be made, with each corresponding to a pair of fields, *i.e.*, $\Delta\mathbf{k}_{BA}$, $\Delta\mathbf{k}_{CA}$, $\Delta\mathbf{k}_{CB}$. These three encoding axes define a plane and so make

2D traversal possible, see Figure 2.12(a). Using merely $\Delta\mathbf{k}_{BA}$ pair produces a single line of k-space acquisition, as illustrated in Figure 2.12(b). For 2D encoding an example of such process is introduced to acquire $M \times N$ data matrix, where $M/2$ trains use refocusing pulses: $C-(AC)_i-(AB)_{N/2}$, while the other $M/2$ trains use refocusing pulses: $C-(AC)_i-(BA)_{N/2}$, in which $i = 0..M/2-1$. Note that for all sequence 90° excitation is transmitted through field $\mathbf{k}_A$, and the notation $(AC)_i$ indicates 180_A-180_C repeated i times. These set of k-space trajectories are shown in Figure 2.12(c)-(e).

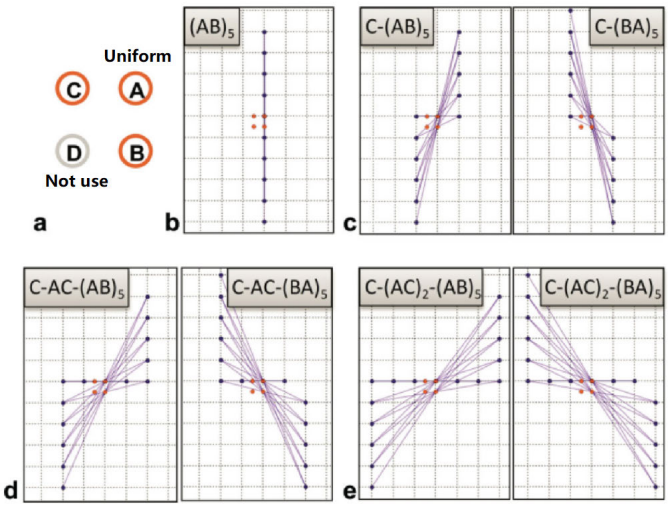

Figure 2.12: Examples of a set of 2D TRASE k-space trajectories using three phase gradients. **(a)**: Four non-collinear k-space origins, where A represents an uniform RF field, D is not used for encoding. **(b)**: Sequence $(AB)_5$ yields a central vertical k-space line. **(c)** $C-(AB)_5$ and $C-(BA)_5$ sequence pair together provides the first pair of off-center vertical lines. Similarly, sequence pairs in **(d)** and **(e)** generate the second and third pair of off-center vertical lines in k-space. The figure is obtained from the article [20] with permission from the rights owner (John Wiley and Sons) under license number 4841130683566.

2D encoding with four phase gradients

To achieve high resolution 2D TRASE encoding, it is preferred to use four non-zero phase gradients, *i.e.*, no uniform B_1 field, since for each jump, the step size Δk is enlarged, resulting in wider k-space coverage for a given ETL.

For clarification now let's consider another example of 2D TRASE encoding with four non-

zero phase gradients, each corresponding to an off-center k-space origin: ($+X$, $-X$, $+Y$, $-Y$). In this example only 16 trains with each consisting of 8 refocusing pulses are shown, although much longer trains may be used in practice. The Figure 2.13(A) contains an table that lists the applied phase gradients in each train; The Figure 2.13(B) shows a specific echo train sequence No.9 including transmission of refocusing pulses using different phase gradients and respective data sampling. In Figure 2.13(C) the corresponding k-space locations of the sampled data are labeled. For all four phase gradients of equal magnitude, a uniform sampling density of a two-dimensional k-space is delivered, creating a rotated square k-space coverage. Since data density are evenly spaced on a two-dimensional Cartesian grid in k-space, simply a standard two-dimensional F.T. is needed for image reconstruction. Additionally it should be noted that in this scheme there is some redundancy between trains in the early part, but the repeated samples points may be averaged to contribute the signal-to-noise ratio.

Moreover, following the same logic it can be found that four non-collinear and non-coplanar fields are sufficient for 3D imaging. This is beyond the scope of this thesis, however, for interest the details regarding this topic can be found in the literature [24].

2.3.7 Specific Absorption Rate (SAR) for TRASE MRI

MRI is a non-invasive imaging technology that produces highly-detailed anatomical images without the use of damaging radiation. However, certain considerations of safety issues are required due to the fact that MRI uses strong external magnetic field and RF pulses. Specific absorption rate (SAR), defined as the power absorbed per mass of tissue with an unit of watts per kilogram (W/kg), is a measurement of the rate at which energy is absorbed by the human body when exposed to RF field. Since TRASE MRI features the use of many refocusing RF pulses, a good estimation of SAR is mandatory. For MRI, the SAR limits are described in International Electrotechnical Commission (see details in document IEC 60601-2-33:2002), which provides specific requirement for different regions of body, see Table 2.2.

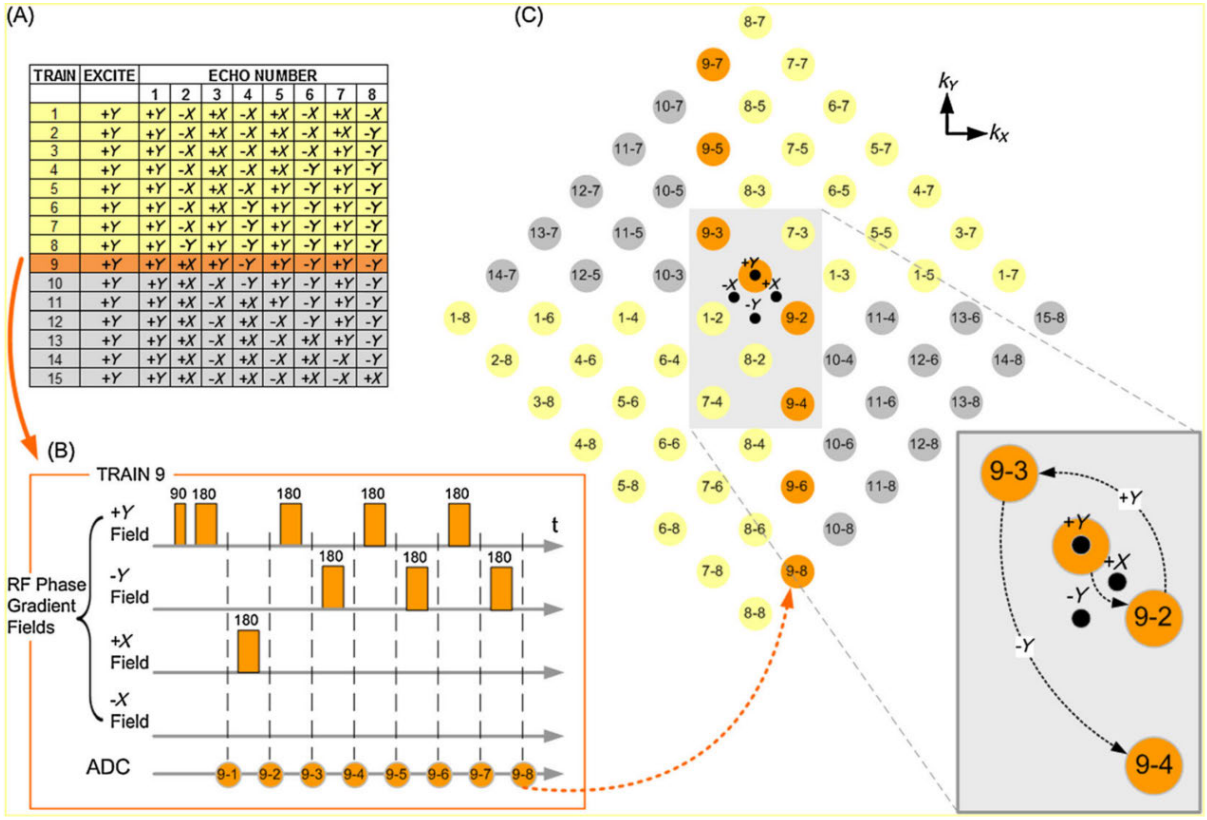

TRAIN	EXCITE	ECHO NUMBER							
		1	2	3	4	5	6	7	8
1	+Y	+Y	-X	+X	-X	+X	-X	+X	-X
2	+Y	+Y	-X	+X	-X	+X	-X	+X	-Y
3	+Y	+Y	-X	+X	-X	+X	-X	+Y	-Y
4	+Y	+Y	-X	+X	-X	+X	-Y	+Y	-Y
5	+Y	+Y	-X	+X	-X	+Y	-Y	+Y	-Y
6	+Y	+Y	-X	+X	-Y	+Y	-Y	+Y	-Y
7	+Y	+Y	-X	+Y	-Y	+Y	-Y	+Y	-Y
8	+Y	+Y	-Y	+Y	-Y	+Y	-Y	+Y	-Y
9	+Y	+Y	+X	+Y	-Y	+Y	-Y	+Y	-Y
10	+Y	+Y	+X	-X	-Y	+Y	-Y	+Y	-Y
11	+Y	+Y	+X	-X	+X	+Y	-Y	+Y	-Y
12	+Y	+Y	+X	-X	+X	-X	-Y	+Y	-Y
13	+Y	+Y	+X	-X	+X	-X	+X	+Y	-Y
14	+Y	+Y	+X	-X	+X	-X	+X	-X	-Y
15	+Y	+Y	+X	-X	+X	-X	+X	-X	+X

Figure 2.13: Examples of data acquisition for 2D TRASE using four phase gradients. A) Sequence Table showing a set of 15 echo trains for a sampling of 8 × 8 k-space matrix. B) The NO.9 echo train details including use of four (+X, -X, +Y, -Y) gradients and the k-space data measurement. C) The corresponding k-space locations of the sampled points, as well as the location of four phase gradients. The figure is obtained from the article [19] with permission from the rights owner (John Wiley and Sons) under license number 4841131295111.

	Whole Body SAR	Partial Body SAR	Head SAR	Local SAR (a)		
Body Region	Whole Body	Exposed Body Part	Head	Head	Trunk	Extremities
Operating Mode	(W/kg)	(W/kg)	(W/kg)	(W/kg)	(W/kg)	(W/kg)
Normal	2	2-10 (b)	3.2	10 (c)	10	2
1st Level Controlled	4	4-10 (b)	3.2	20 (c)	20	40
2nd Level Controlled	>4	>(4-10) (b)	>3.2	>20 (c)	>20	>40
Short Duration SAR	The SAR limit Over any 10 second period shall not exceed two times the stated values					

Note: Averaging time of 6 minutes.
(a) Local SAR is determined over the mass of 10 g;
(b) The limit scales dynamically with the ratio - exposed patient mass/ patient mass:
Normal operating mode: Partial body SAR = 10 W/kg - (8 W/kg * exposed patient mass/ patient mass)
1st Level Controlled": Partial body SAR = 10 W/kg - (6 W/kg * exposed patient mass/ patient mass)
(c) In cases where the orbit is in the field of a small local RF transmit coil, care should be taken to ensure that the temperature rise is limited to 1 °C.

Table 2.2: The SAR limits for MRI described in IEC 60601-2-33. Data source: `https://en.wikipedia.org/wiki/Specific_absorption_rate`

The accurate calculation of SAR is challenging because the electric field created by the transit coil is not measurable *in vivo* (an RF coil generates both magnetic and electric field components which will be discussed in the next Chapter). However SAR is related to field strength, radio frequency power, duty cycle, transmit coil and body size, where a convenient proportionality exists [34]:

$$SAR \propto W \cdot R \tag{2.32}$$

in which W and R represent deposited energy per pulse and pulse rate, and hold the relationships:

$$W \propto \frac{B_0^2 \theta^2}{\eta^2 T_p} \tag{2.33}$$

$$R = \frac{DutyCycle}{T_p} \tag{2.34}$$

Field B0 (T)	180° Pulse Duration t (μs)	Rate R (Hz)	Mass m (kg)	Scaled Pulse Energy $E_p = (\frac{B_0}{0.2})^2 * \frac{500}{t} * 0.00198$ (J)	Power W = E_P * R (W)	SAR W/m (W/kg)	Duty Cycle (%)	Train duration ($ETL = 128$) $T_{train} = \frac{128}{R} * 1000$ (ms)	Comments
0.2	500	1000	4.6	$1.98 * 10^{-3}$	1.98	0.43	50.0	128.0	Measured by Deng
0.2	200	2900	4.6	$4.95 * 10^{-3}$	14.36	3.12	58.0	44.1	
0.2	250	3600	4.6	$3.96 * 10^{-3}$	14.26	3.10	90.0	35.6	run almost continuously
0.3	250	1600	4.6	$8.91 * 10^{-3}$	14.26	3.10	40.0	80.0	
0.3	280	1786	4.6	$7.96 * 10^{-3}$	14.21	3.09	50.0	71.7	
0.35	250	1200	4.6	$1.21 * 10^{-3}$	14.55	3.16	30.0	106.7	0.35T is reasonable
0.4	280	893	4.6	$1.41 * 10^{-3}$	12.63	2.75	25.0	143.4	
0.5	300	667	4.6	$2.06 * 10^{-3}$	13.75	2.99	20.0	192.0	
1	500	500	4.6	$4.95 * 10^{-3}$	24.75	5.38	25.0	256.0	Too High

Table 2.3: The scaled SAR calculation based on actual SAR measurement (first row) at 0.2 T using 500 μs hard refocusing pulses with 50% duty cycle. The maximum SAR limit allowed for head is set to 3.2 W/kg.

where θ and η are flip angle and RF waveform factor, respectively. $Dutycyle$ =100% means RF pulse is always on.

For TRASE which uses rectangular shape refocusing pulses, the SAR formula can be rewritten as:

$$SAR_{TRASE} \propto \frac{B_0^2}{T_p^2} \cdot DutyCycle \tag{2.35}$$

With the above equation, it is possible to empirically calibrate the expected SAR between different cases. Deng [25] made NEMA RF power calibration measurements for a head phantom on 0.2 T MR system using 180° 500 μs hard pulses at a duty cycle of 50% with no breaks for TR, measuring a SAR of 0.46 W/kg. Based on this reported data, Table 2.3 is made here to compare the scaled SAR under different circumstances.

At an external magnetic field of 0.2 T calculations for head show that approximately 2900 200 μs pulses per second would remain within SAR limits, *i.e.*, SAR$\leq$3.2 W/kg. At this rate 128 $\times$ 128 k-space points could be acquired in less than 6 seconds, with each echo train shorter than 45 ms. This is efficient enough to encode very short T_2 tissues such as T_2 of 42 ms for white matter at 0.2 T [11]. Although this is an approximate and raw calculation ignoring sequence design details, the data rate provided by TRASE is clearly practical for anatomical imaging at 0.2 T. However since SAR increases with the square of the B_0 field strength, the permissible pulse rate falls rapidly for higher fields, and the use of many long TRASE echo

trains becomes progressively more restrictive. For instance, since $(1.0/0.2)^2 = 25$, the SAR at 1.0 T is 25 times higher than at 0.2 T, illustrating that the high field MRI regime is not hospitable to TRASE encoding. For full TRASE encoding, fields in the range of 0.3 T to 0.4 T or lower are more feasible [13]. In this thesis, all MRI data were acquired using a 0.22 T permanent magnet with a shortest pulse duration of 200 μs, and a maximum duty cycle lower than 40%. With a relatively long TR (2 to 3 seconds), these TRASE sequences clearly would not reach SAR limits, therefore, SAR calculations were not performed and/or reported in the following chapters.

2.3.8 Comparison Between Conventional and TRASE MRI

So far the theories, encoding principles, and a variety of TRASE imaging properties have been explicitly discussed. A brief comparison between TRASE and conventional MRI is provided.

Hardware

Due to the difference of encoding principle, the requirements for the implementation of TRASE deviate significantly from conventional MRI. In this section, I will summarize their differences in hardware.

- **Magnet**: Due to the SAR limit, TRASE MRI is suitable for low-field, preferably lower than 0.4 T MRI systems which can use permanent magnet designs. Therefore, the cost of magnet for TRASE is much lower than high field magnets typically manufactured with superconducting techniques. However, at low-fields the image SNR is expected to be lower.

- **Gradient System**: The key feature of TRASE MRI is that the ordinary B_0 gradient and the associated hardware are not needed, hence, can be removed entirely. This not only makes TRASE MRI lighter, but also allows MRI to be accessible for areas where

stable power supply is not present, as gradient amplifier is rather power-consuming. The associated side effects such as eddy current and acoustic noise are also eliminated.

- **RF transmission/receive System**: TRASE is based on the innovation of encoding MRI data using RF phase gradients. To implement this technology, it requires new design of MRI RF systems including novel RF coil geometry, high duty cycle RF power amplifier, and even new RF transmit/receive console. In general, TRASE MRI uses multiple phase gradients alternately, each of which needs to be uniquely created and not to interact with other phase gradients while one is on. In next chapter the main focus will be on these topics regarding how phase gradients can be generated with novel RF coil designs, and the corresponding driving methods.

- **Computer**: Although no specific image processing technique is required for TRASE (i.e. TRASE is still a Fourier-based imaging technique), the console needs to be capable of generating multiple control signals including gating, RF input, and optical pulses (if needed), etc., to manipulate the transmission for different phase gradient fields.

Scan speed

Unlike conventional MRI which causes continuous phase accumulation using B_0 gradient, TRASE phase evolution occurs discretely at each refocusing pulse, with each echo represented a single point in k-space. This means the speed of TRASE is inherently slower than conventional MRI, and this may be more inefficient when TRASE technique is applied to multi-dimensional encoding. For real-time MRI imaging, TRASE is not ideal. One potential solution for this would be applying TRASE in parallel with conventional encoding principles, as TRASE is just an alternative method of encoding k-space data. An idea of hybrid B_0 and B_1 encoding has been described in previous study for wrist imaging, where only in-plane 2D data were acquired with TRASE while the third dimension was encoded with ordinary B_0 phase encoding with the use of switched B_0 gradients [19]. Cooley et al. [12] proposed a portable MRI scanner prototype capable of utilizing TRASE for the third dimen-

sion encoding while achieving 2D MRI encoding based on generalized projections created by a "built-in" gradient field [11], *i.e.*, rotating spatial encoding magnetic field.

Although the technology is quite different, the k-space spatial encoding produced by TRASE is equivalent to that of conventional MRI in terms of data acquisition. This commonality implies that in principle at least, any of the many existing MRI acquisition and data processing techniques can be directly employed for TRASE. One preliminary work has indicated that the partial Fourier techniques can accelerate 1D TRASE encoding [35]. Therefore, there is a feasibility of applying other acceleration techniques (parallel imaging and sparse encoding) for TRASE MRI.

Geometric errors

TRASE MRI encoding, similar to conventional MRI techniques, suffer from image geometric distortions/errors. Since TRASE uses B_1 phase gradient to encode MRI data, the non-linearity of such phase gradient causes image distortions, which is somewhat analogous to the non-linearity of conventional B_0 magnitude gradient. In Eq. 2.8, the B_1 field is defined with a constant magnitude. However, in actual coil constructions, $|B_1|$ inhomogeneity exists so refocusing pulses will not always be 180°. This not only causes signal loss down an echo train, it also introduces phase errors, which may cause geometric errors. In Chapter 4 and 5, I will discuss these two B_1 field imperfections (non-linearity and magnitude variation), and show their impacts on resulting MR images. Additionally, TRASE uses an array of RF transmit coils, therefore, coil couplings will also introduce B_1 field errors (magnitude and phase), hence, leading to image geometric errors if not carefully mitigated. Such image distortions are investigated in Chapter 6, with a potential solution proposed in Chapter 7.

B_0 inhomogeneity is another potential source of geometric errors. TRASE uses spin echo sequence to encode MRI data so a limited level of static B_0 inhomogeneity is often not an issue. However, in highly inhomogeneous B_0 fields, the use of hard pulses complicates the excited region and may introduce additional geometric distortions. Overall, the impact of

B_0 inhomogeneity on TRASE encoding is quite complex and to my knowledge, has not been explicitly studied yet.

Chapter 3

RF Transmit Coils for TRASE MRI

3.1 Basics of RF Transmit Coils

Now, let's shift attention to the discussion of RF coils. Although RF coils offer both transmit and receive functions, the modern scanners often use separate transmit and receive coils, meeting different needs. I will limit the scope to transmit coils only, as this is more relevant to TRASE encoding technique. It should be mentioned that in all MR experiments reported in this thesis, no receive-only coil was constructed, *i.e.*, one of the TRASE transmit array coils was connected to a transmit/receive (T/R) switch, serving as a receiver as well. However, further work to build receive only coils for TRASE is necessary to improve image quality.

3.1.1 Resonating RF coils

Using resonating coils to transmit RF pulses, the net magnetization M_0 can be rotated away from its alignment with the main magnetic field B_0. The transmit RF coils generate the B_1 field, which is perpendicular to the main magnetic field B_0, and oscillates at the resonance frequency ω_0, also known as the Larmor Frequency. To build such RF coil, an electrical circuit composed of discrete components that can act as a resonator are needed. In this thesis, the resonating RF coils were built upon inductors (coil wire) and capacitors.

Inductors have a resistance R_L and a reactive impedance X_L which increases linearly with

the frequency ω_0:

$$X_L = \omega_0 L \tag{3.1}$$

where L is the inductance. On the other hand, the capacitor has reactive impedance X_C which decreases with the frequency ω_0:

$$X_C = 1/(\omega_0 C) \tag{3.2}$$

where C is the capacitance. The contribution of the conductor losses is represented by a resistance R_C. The resonance can occur under series (low impedance) and parallel (high impedance) configurations, as shown in Figure 3.1. The resonance condition is described as:

$$\omega_0 = 1/\sqrt{LC} \tag{3.3}$$

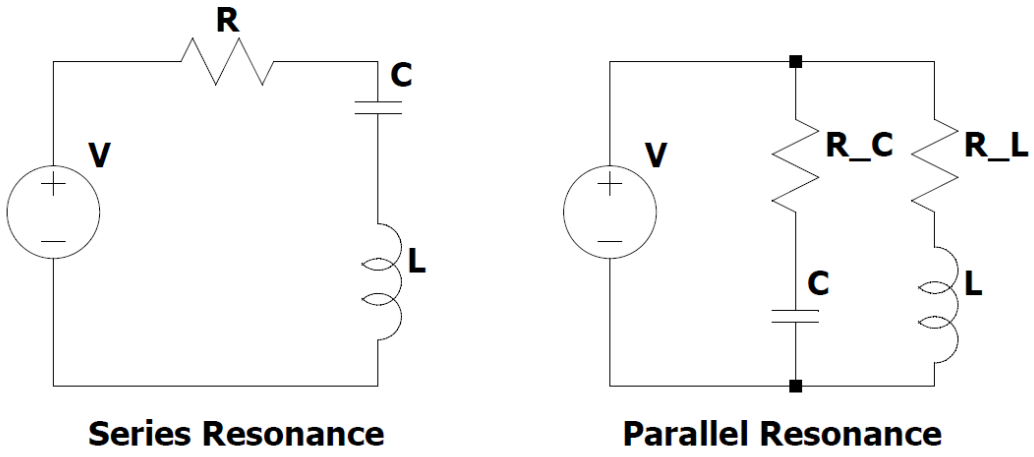

Figure 3.1: Two different LC resonating circuits.

It should be noted that the circuits depicted in Figure 3.1 such as the L and C are not necessarily actual components present on the RF coil, but the values can be determined based on the specific layouts of interest. When the resonance condition is met, the energy exchanges back and forth between the capacitor and the inductor, at each cycle, and dissipates slowly in

the resistive components. Thus, the current amplitude is a maximum on resonance because the system stores energy, resulting in most efficient power use for the generation of B_1 field.

3.1.2 Tuning/Matching

Tuning and matching the RF coil to the desired Larmor frequency and characteristic impedance of the MR scanner's RF system is necessary for optimal performance. These two steps often cannot be neglected as they are generally patient/load - specific, in this thesis work, both steps were manually adjusted.

RF Coil Tuning

When a sample is positioned in the coil, depending on the sample's properties, the RF magnetic and/or electric fields are distorted which produce small but significant changes, resulting in a drift of the coil's resonance frequency. Tuning the coil to the right frequency is analogous to the tuning of a radio receiver to the desired radio station. Failure to do this will lead to a severe degradation in sensitivity and image quality. Recall Eq.3.3 it is straightforward to see the coil's resonating frequency can be corrected accordingly by adjusting either capacitance or inductance. In reality the adjustments are usually made via variable capacitors that include a static and a movable electrode separated by a high quality dielectric. These variable capacitors are placed in the probe head at a short distance from the coil and comprise the tuning circuitry.

RF Coil Impedance Matching

Patients or loading samples vary widely in size and shape, which can change the impedance (electronic loading) of the RF transmit coils in different ways. For optimal energy transfer between the coil and the patient, the impedance of the RF coil shall be matched to the impedance of the transmission lines (*i.e.*, the wires connecting the RF amplifier and the

coil). If an impedance mismatch is present, RF power generated by the amplifier will not be fully transmitted into the patient, but part of it will be reflected back at the RF transmission line interface. As a result, this requires high power rating from the RF amplifiers and more importantly, can damage the RF systems. To quantify this effect, we introduce the voltage reflection coefficient Γ_0 as the ratio of reflected to incident voltage wave [36]:

$$\Gamma_0 = \frac{Z_L - Z_0}{Z_L + Z_0} \tag{3.4}$$

where Z_L is the load impedance, Z_0 is the characteristic line impedance, and is usually considered as 50 ohm in RF transmission line. When an impedance match is obtained, *i.e.*, $Z_L = Z_0$, the reflected RF power is minimized. However the coil input impedance itself Z_{coil} rarely satisfies this condition, so a matching circuit is often built and connected to transform it to Z_0. The design of matching circuits can be widely found in the RF literature using different methods (see details in [37]), but they can all be translated into an ideal transformer which allows an impedance conversion $Z_L = N^2 Z_{coil}$, where $N = N_s/N_p$ denotes the turns ratio of the transformer, as shown in Figure 3.2.

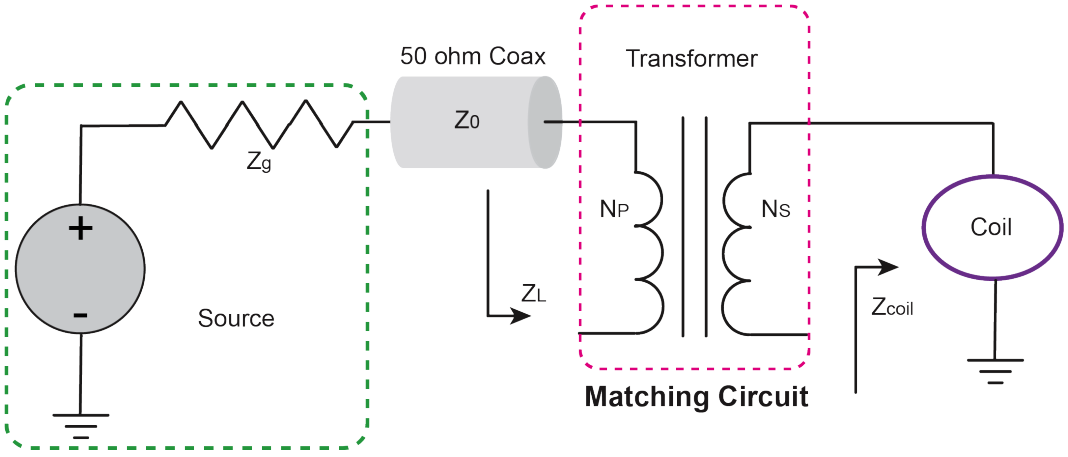

Figure 3.2: An illustration diagram of connection using impedance matching for transmit RF coil.

3.1.3 Coil Evaluation

Quality Factor and Sensitivity

The quality factor Q of an RF coil is defined as the ratio of the stored energy to the energy loss per cycle. Since the power dissipated is the real part of the total power while the imaginary part of the power gets stored, the Q is defined as the ratio of reactance X to resistance r:

$$Q = \frac{|X|}{r} \tag{3.5}$$

The transmit sensitivity Ψ is defined as the B_1 field produced per unit input power: $\Psi = |B_1|/\sqrt{P}$. The sensitivity has a maximum value of Ψ_0, *i.e.*, intrinsic sensitivity, provided the coil had no losses. Ψ and Ψ_0 are linked by efficiency η:

$$\Psi = \Psi_0 \cdot \sqrt{\eta} \tag{3.6}$$

in which η can be evaluated as $\eta = 1 - Q_l/Q_u$. In this case, the Q factor is distinguished by Q_l (Coil loaded with the sample) and Q_u (probe unloaded or empty), respectively [37].

Scattering Parameters

In books and technical literature regarding RF systems, the scattering or S parameters play a major role, as they can be easily measured and related to familiar measurements like gain, loss, reflection coefficient, etc,. The S parameters can be defined for networks having any number of ports, but to better explain it, a two-port network is considered here only. All possible S-parameters of a two-port network can be described as S_{11}, S_{12}, S_{21}, and S_{22}, as indicated in Figure 3.3. Let a_1 be the voltage amplitude of the forward wave and b_1 the voltage amplitude of the reflected wave on port 1 (same to a_2 and b_2 on port 2), the meaning

of the S parameters are as follows:

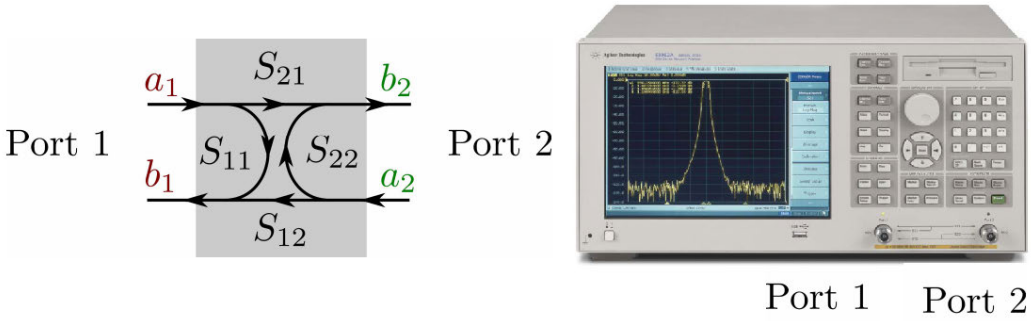

Figure 3.3: Four S parameters for a two-port network, together with the picture of a two-port network analyzer. Figure source: [38]

- $S_{11} = [\frac{b_1}{a_1}]_{a_2=0}$
- $S_{12} = [\frac{b_1}{a_2}]_{a_1=0}$
- $S_{21} = [\frac{b_2}{a_1}]_{a_2=0}$
- $S_{22} = [\frac{b_2}{a_2}]_{a_1=0}$

For passive components such as two RF probes, one can find $S_{21} = S_{12}$, representing the isolation between the two probes. However, for an active device such as a preamplifier, S_{21} and S_{12} are not equal. Now, the network behavior can be described in a matrix form as:

$$\begin{pmatrix} b_1 \\ b_2 \end{pmatrix} = \begin{bmatrix} S_{11} & S_{12} \\ S_{21} & S_{22} \end{bmatrix} \begin{pmatrix} a_1 \\ a_2 \end{pmatrix} \tag{3.7}$$

The S parameters are complex dimensionless values. The magnitudes are often expressed on a logarithmic scale as a power ratio in dB [37]:

$$|S_{ij}|(dB) = 20 * log_{10}(|S_{ij}|) \tag{3.8}$$

Note that in general S parameters are functions of frequency (*i.e.*, vary with frequency). With S parameter measurements we can evaluate RF coil, in many cases depicted in Figure 3.4.

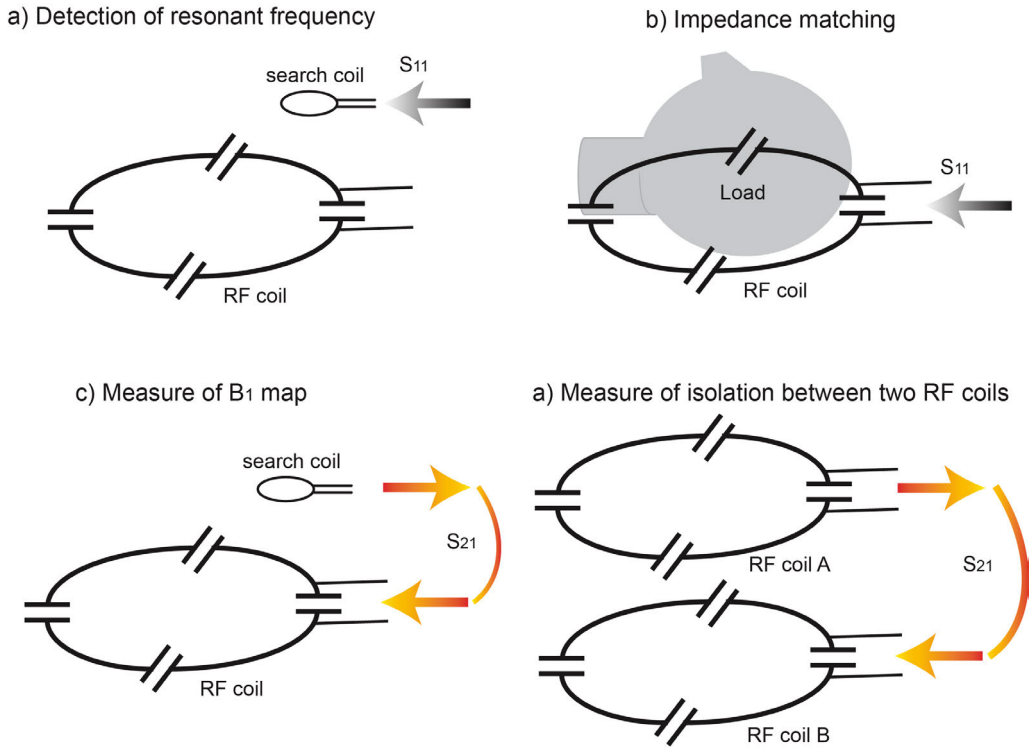

Figure 3.4: Examples of coil evaluations using S parameter measurements. Figure is adapted from [38].

For a single RF coil, which is a one-port network, the tuning and matching can be readily estimated. In Figure 3.4(a) S_{11} measured with a search coil has a dip at the resonant frequency of the RF coil, because the coil absorbs the most power radiated from the search coil at its resonant frequency. The panel (b) can evaluate the reflection coefficient when the coil is loaded. Once the coil is tuned, under proper impedance matching condition S_{11} measurement is expected to be small enough, *e.g.*, -20 dB or less. Using experimental setup of (c), the B_1 field can be picked up along the direction perpendicular to the search coil plane, through S_{12} measurement. After adequate normalization the B_1 map can be generated.

The TRASE technology requires the manipulation of several RF phase gradient coils in a sequence. For any one pair of RF coils, S_{12} is equal to S_{21} and represent the isolation

between two coils. In Figure 3.4(d) the matching and tuning can be verified for both coils with methods illustrated in (a) and (b) first. Then, the S_{12} measurement is a good indicator of how much this pair of coils is coupled, *i.e.*, transmitting with coil A results in current flowing through coil B. An good isolation is often at the level of $S_{12} \leq -20$ dB, which can be achieved with either active or passive decoupling techniques that will be discussed later.

3.2 Estimation of Magnetic Field Produced by RF Coils

3.2.1 Analytical Biot-Savart Approximation at Low-field MRI

When designing an RF coil, an important step is to study the resulting magnetic field direction and amplitude. At high-field MRI systems (*e.g.*, $\geq$ 3T), accurate calculation of the magnetic field generated by an individual RF coil can be quite challenging, and often is done by sophisticated and expensive full wavelength simulation programs which can provide numerical solutions for the complete Maxwell equations, because the wavelength of the driving RF is comparable with the linear dimension of the probe coil, so the effect of the induced far field (retardation effects) is not negligible, *i.e.*, currents following in the wire path are not in-phase. However, at low-field MRI system (*e.g.*, for 0.2T main magnetic field, the resonating frequency of proton is below 10 MHz), all conductive parts of the coil can be decomposed into elementary geometrical segments (typically straight line) carrying currents. For all segments the resulting magnetic field vectors can be calculated and summed using the Biot-Savart law, assuming the currents are in phase along the wire path. The Biot-Savart formula gives magnetic field $d\vec{B}$ produced at a point P, from the current I flowing in an arbitary wire configuration, and is expressed as [37]:

$$d\vec{B} = \frac{\mu_0}{4\pi} I \frac{d\vec{s} \times \vec{r}}{|r^3|} \tag{3.9}$$

in which $d\vec{s}$ and $\vec{r}$ are the positional vectors to the point P (see Figure 3.5), and μ_0 =

$4\pi \times 10^{-7}$ H/m is the permeability of free space.

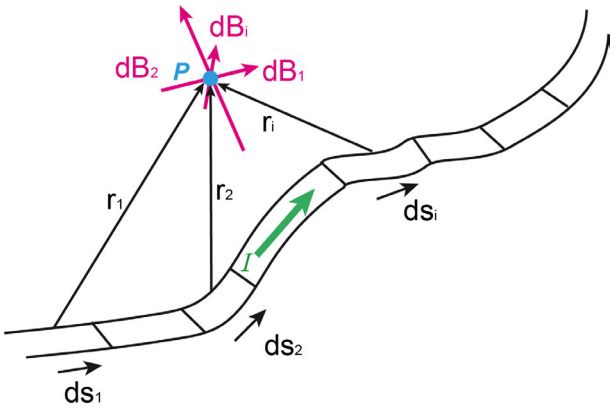

Figure 3.5: The $d\vec{B}$ contributions from different segments to point P. Each segment ds_i carries a current of I and gives rise to a contribution of $d\vec{B}_i$ at the point of P. The distance between P and the middle point of each element is characterized as r_i

One example is shown in Fig. 3.5, where the principle of superposition allows the magnetic field generated by all segments of the wire to be calculated. Therefore, the magnetic field $\vec{B}$ generated by the entire arbitrary wire is given by:

$$\vec{B} = \sum_i d\vec{B}_i = \frac{\mu_0}{4\pi} I \sum_i \frac{d\vec{s_i} \times \vec{r_i}}{|r_i^3|} \tag{3.10}$$

Although the Biot-Savart calculation is based on direct current assumption, it has been demonstrated as a fairly accurate indicator to approximate the resulting magnetic field caused by alternating current at low frequency. For TRASE running at 0.2T main magnetic field, Biot-Savart's law has been proved to be a reliable model [13].

3.2.2 Examples of B_1 Field Generated by Different Uniform RF Coils

Ideally, the produced magnetic field of all types of RF coils can be analytically calculated by Biot-Savart's law, provided the exact geometry is known. Each coil produces an RF magnetic vector field with three components, but only the two components orthogonal to the main magnetic field B_0 contribute to the NMR B_1 field. By assuming the static field

B_0 is applied in the z direction, the contributing transverse B_1 components are B_y and B_x, while any B_z component becomes a concomitant RF field, *i.e.*, does not contribute to B_1.

Without integration, several examples [37] of typical RF coils and the corresponding B_1 fields are shown in Figure 3.6.

- **Solenoid**: The solenoid allows very high sensitivity for MRI. However, as the generated B_1 field is parallel to the cylinder axis, this type of coil is not usable at modern superconductive axial magnets. Additionally, the inductance of such coil increases rapidly with the dimensions and can easily self-resonant at frequencies well below the Larmor frequencies used nowadays clinically. Therefore, the solenoid is more favorable for vertical and low external field, *e.g.*, 0.2 T and 0.5 T MR system at the Cross Cancer Institute, Edmonton.

- **Saddle**: Saddle coil features two identical current wires located on each half shell. The longitudinal wires are connected in series and driven by the same current source. Although saddle coils is cylindrically shaped, it produces B_1 field perpendicular to the main axis, hence, can be used for both vertical and longitudinal external B_0.

- **Birdcage**: The birdcage coil is more complicated, but it provides an improvement toward higher frequencies. Basically, in transmit operation sinusoidal currents are applied to each leg that are sequentially phase shifted around the coil's periphery, creating a homogeneous magnetic field inside the conductor. The details of birdcage coil design is out of the scope for this thesis, but details can be found in [37].

- **Helmholtz**: The Helmholtz pair is formed by two parallel circular coils driven by in-phase current. It has open configuration which give very good accessibility for the sample.

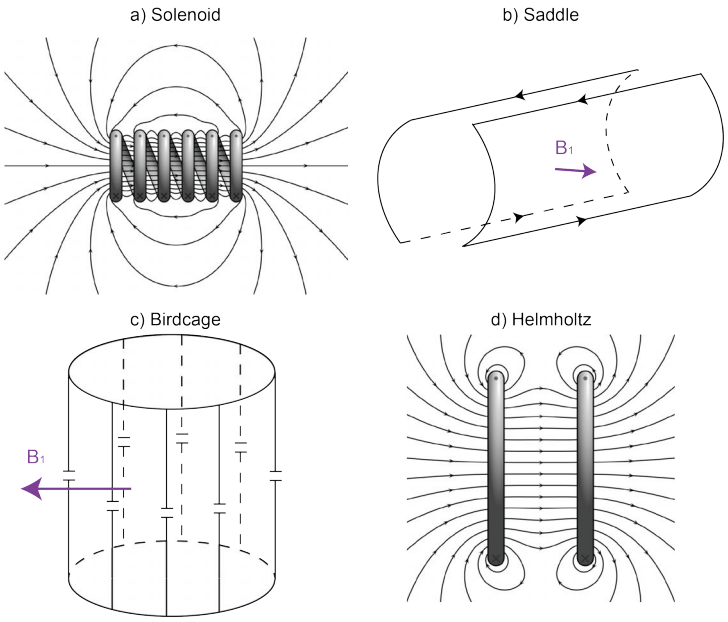

Figure 3.6: Examples of B_1 field generated by four uniform RF coils. The pictures of the solenoid (`https://commons.wikimedia.org/wiki/File:VFPt_cylindrical_loosely-wound_coil_2.svg`) and the Helmholtz coil (`https://commons.wikimedia.org/wiki/File:VFPt_helmholtz_coil2-rings.svg`) are from the Wikimedia Commons (permissions granted).

3.3 Transmit RF Coils Decoupling

One crucial component of TRASE transmitting is the effective enable/disable function of each coil in the coil set, otherwise the strong coupling between coils may, while transmitting with one coil, lead to "cross-talk" among other coils. Although coils can be coupled through different aspects: inductive/capacitive/resistive coupling, the main coupling mechanism for TRASE coil set is inductive coupling which is characterized by the mutual inductance. The mutual inductance M can be defined as the proportionality between the emf generated in coil 2 to the change in current in coil 1 which produced it, as shown in Figure 3.7:

$$emf_2 = -N_2 A \frac{\Delta B}{\Delta t} = -M \frac{\Delta I_1}{\Delta t} \tag{3.11}$$

During transmission the current induced in the other RF coils create magnetic fields that

add or subtract from the primary RF field, which ultimately results in inappropriate echo refocusing. The inductive coupling between TRASE coil set needs to be avoided.

The mutual inductance between two simple geometries such as straight wires, coaxial loops can be analytically calculated using accurate formula that can be found in the Grover book [39]. In situations involving complex geometries, the mutual inductance can still be obtained from a decomposition of the conductive structure into elementary components such as flat strips or straight elements of round wires, so the mutual inductance can be estimated by the thin wire approximation. A more accurate estimation can be made while considering the proximity effect using the Geometric Mean Distance method in which the distance between the current filaments differs from the centered geometric space between the conductors [39]. However, if the structure becomes more complicated, a numerical method is more efficient. In this project, the program *FastHenry* [40] is used to calculate both self- and mutual-inductances (the complex impedance matrix) of our coils. In FastHenry, the coil structure to be calculated is first decomposed in conducting planar sheets connected together based on the 3-D geometry by nodes. The flat conductor strips are then decomposed into a number of filaments forming a complex network circuit. The impedance matrix of the network is calculated using Grover formulae [39], and solved by an original and efficient numerical method described in the literature [40]. This convenient and free-to-use program has been proved to be well adapted for a large number of problems related to NMR probe design [37]. In chapter 5 and 6, I will show the use of this program to calculate coils' inductances.

3.3.1 Geometric Decoupling

In principle, decoupling of coils can be achieved geometrically. One simple way to achieve this is by rotating one coil with respect to the other to reduce the RF signal coupled. As shown in Figure 3.8(a), by setting the coil planes orthogonal, the magnetic flux seen by the other coil would be zero, therefore, producing no induced current. Another geometric decoupling technology uses the overlap placement between coils to eliminate the mutual inductance, as

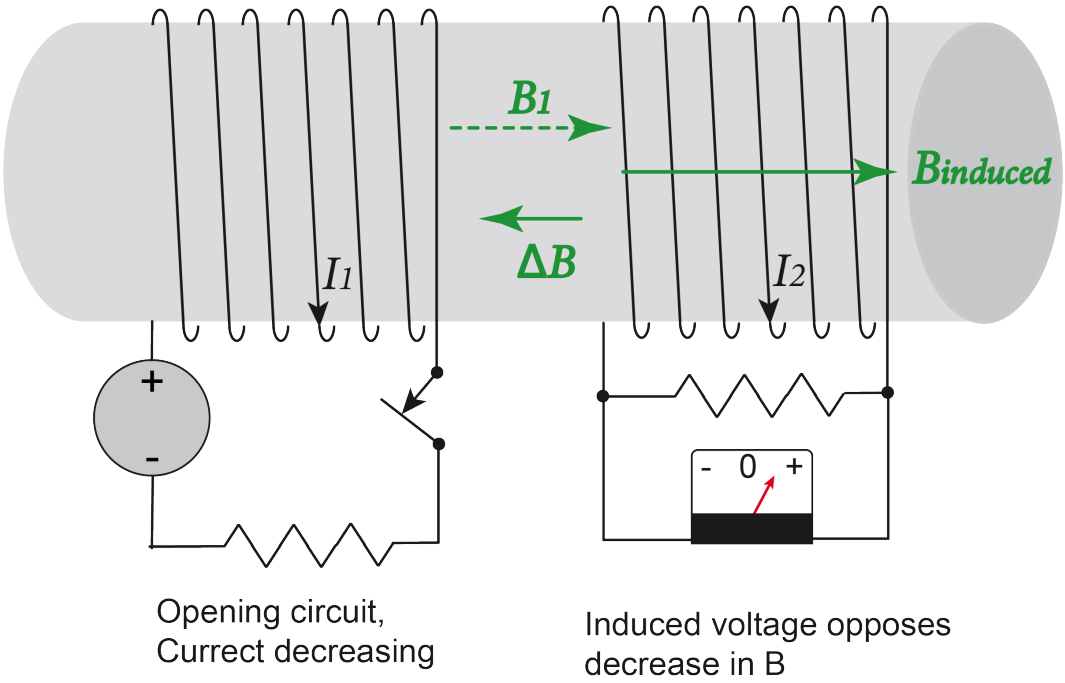

Figure 3.7: A simple example for coil coupling due to mutual inductance. The decreasing magnetic field ΔB on coil 1 (left) is seen by coil 2 (right), so the induced magnetic field on coil 2 $B_{induced}$ is generated and aligns in parallel with the original B_1 due to Lenz's law.

depicted in Figure 3.8(b). As expected, the mutual inductance depends on the coil geometry so an optimum overlapping placement can be found to force M to be zero. However, in reality it is difficult to perfectly decouple coils simply by adjusting the position, so there is a limitation on the maximum achievable decoupling by geometrical methodologies. Provided further decoupling capacity is needed, geometric decoupling should be accompanied by other effective approaches that cancel out or, minimize the induced currents in each coil.

3.3.2 Other Decoupling Techniques

Other than geometric decoupling, another commonly-used passive decoupling technique, especially in the design of a Tx/Rx switch, uses a crossed-diode circuit [41]. In a passive decoupling scheme, no external source is added to bias the diodes. During the transmitting period, the diode is biased to a high RF voltage and presents a low impedance. During the receiving period, it presents a high impedance because the very small nuclear magnetization

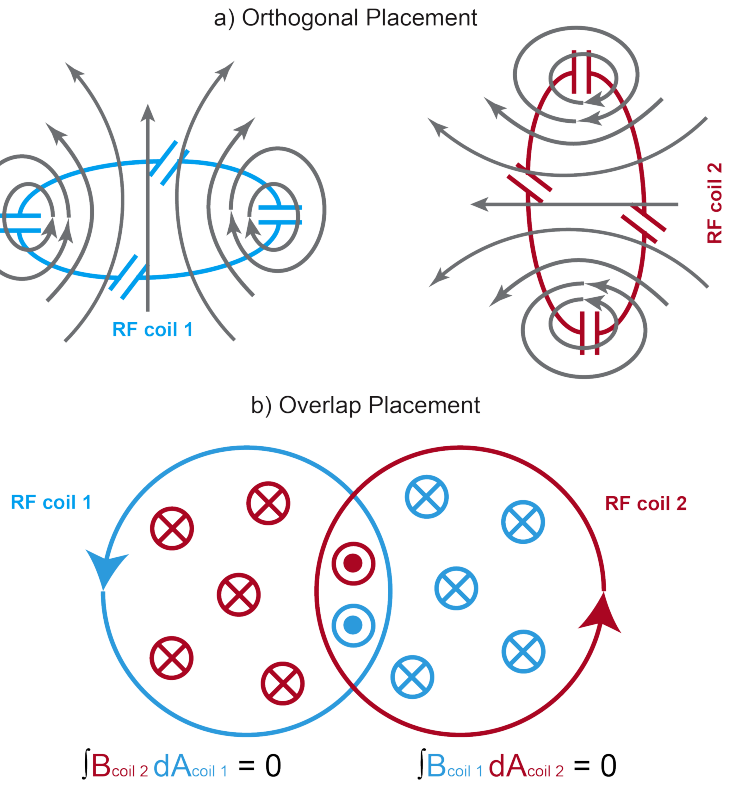

Figure 3.8: Two displacements of geometrical decoupling for two circular loops.

induction voltage is much lower than the cut-off voltage of the diode (*e.g.*, 0.6 V for silicon diodes).

Active decoupling often makes use of PIN diode which is a small semiconductor two terminal component particularly efficient for RF signal control. Although various circuit design were proposed in the literature [37], the concept remains same. In this case, the PIN diodes are biased by an external circuit that delivers current pulses, synchronized with the pulse sequence. This will allow the diode to switch between low resistance forward bias ("On") and high impedance reverse bias ("off") state which can switch on or off the RF coils. Here, a very basic circuit design for this purpose is introduced in Figure 3.9(a). A PIN diode is directly placed in series with the transmit coil's conducting path, with two RF chokes attached on both sides of DC source. When the diode is forward biased by a DC current, RF transmit coil will be turned on. When reversed biased, no RF current can flow through the diode. However, the series diode suffers from the potential thermal failure which can

melt solder. To address this issue, a co-author work specifically made for TRASE PIN diode driver system was proposed recently [17], as shown in Figure 3.9(b). With this design the RF current circulating inside the resonant trap is much lower than the current that direct design must handle. In detail, when the diode is reverse biased, the 4.79 μH inductor and 91 pF capacitor, together with the 560 pF tuning capacitor form a trap at the frequency of interest (8.2 MHz), not allowing any RF current to flow through the coil, *i.e.*, transmit coil is detuned. When the PIN diode is forward biased with a DC current, the 3.9 μH forms a resonant RF trap with the 91 pF capacitor in the branch below it. In this case, the 91 pF capacitor cannot resonate with the tuning capacitor, hence, the transmit coil is resonating and being turned on. Again two LC RF chokes are attached to prevent RF currents flowing on the DC power supply.

The PIN diodes are effective switches for RF frequencies in the MHz range, but at much lower frequency MRI systems (*i.e.*, kHz range), such use can be quite challenging. To overcome this, a fast RF switch for low- and ultra-low field NMR and MRI was proposed recently in 2020 [42]. Instead of using PIN diode in their design, a MOSFET-based switch was introduced in this article, achieving sub-μs switching of RF currents, and being proved to be compatible with TRASE technologies.

In a more efficient design, the current in the resonator is canceled out at the working frequency, improving the isolation to a high level. This concept can be implemented using a parallel RF transmit system which will be introduced in Chapter 7.

3.4 Practical RF Coil Construction and Evaluation

The purpose of this section is to share the hands-on experiences that I obtained in the construction, optimization, adjustments, and tests of RF coils in the lab. Here, I will use simple RF coils (saddle and solenoid) as the example to demonstrate these procedures which can be divided into five main steps:

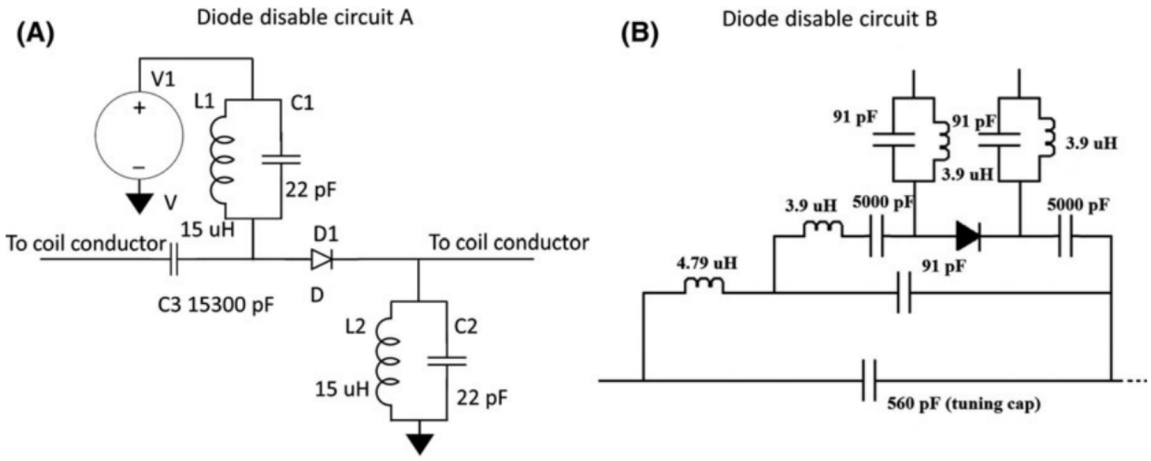

Figure 3.9: Two different disable circuits for active decoupling of RF transmit coils. A), Disable Circuit A), with diode directly in the RF current path; B), Disable Circuit B, with diode protected from the full RF current. Figures are reproduced from my co-author article [17], with permission granted from the publisher (John Wiley and Sons), under the license number 4841561163203.

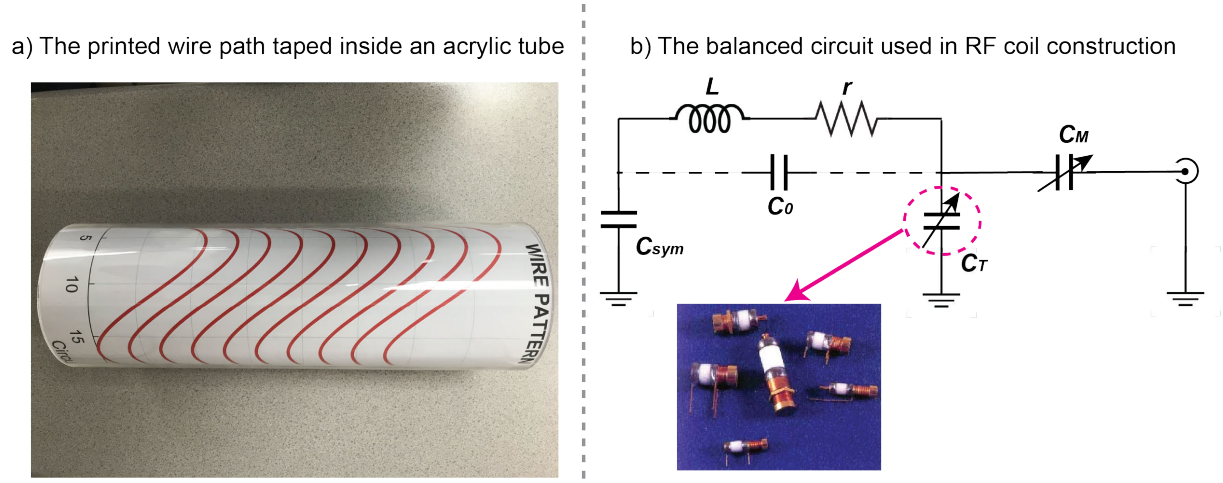

Figure 3.10: Coil construction using a printed wire path map and a balanced circuit. **a)** The coil wire path is printed in a piece of paper and taped inside an acrylic tube to guide the coil construction. **b)** A balanced circuit used in the RF coil construction. Here, L and r represent the coil inductance and in series resistance, respectively. C_{sym} is the symmetrization capacitor, C_T the variable tuning capacitor, and C_M the variable matching one. C_0 is the optional pre-tuning capacitor. A photo of variable capacitors is also attached.

Determination of coil geometry: In this project, the exact wire pattern for each coil is known and determined by analytical equations. The wire pattern is segmented into straight-line current segments which are further sent to a Biot-Savart MATLAB package [43] to calculate the resulting magnetic fields. Once the target B_1 field is achieved, The coil geometry containing wire path coordinates (X, Y, Z) are saved to guide the coil construction. The wire path is printed on a piece of paper which is taped inside a transparent cylindrical acrylic former, so following the printed traces, I can glue shielded copper wire (12 AWG solid hookup wire) on the surface of the coil former, as illustrated in Figure 3.10a). Since the generation of phase gradient is sensitive to the coil geometry, 3D printing technique is also implemented in this work to further increase the accuracy of coil construction by winding the wire upon a grooved 3D printed polylactic acid (PLA) former. The details of 3D printing setup is illustrated in Chapter 5.

Coil construction: Other components such as fixed-value/variable capacitors and inductors are then soldered on a custom-made PCB which is connected to the two ends of the coil wire to make it a resonating circuit. For MRI applications, the coil is sensitive to the magnetic part of the electromagnetic field, while the electric field component which causes dielectric loss due to capacitive coupling with the sample, and sample heating should be kept as low as possible. Additionally, the time varying currents in the coil radiate energy ("antenna effect"), resulting in coil's sensitivity degradation, and undesired strong couplings between the coil and surroundings. Therefore, the dielectric losses and the radiated energy should be minimized in coil design, which can be fulfilled in part by implementing a balanced circuit design. [37].

A rule-of-thumb for balancing the coil is to use symmetric configuration, *i.e.*, split the matching/tuning capacitors. Here, a balanced circuit is shown in Figure 3.10b), which not only allows the RF coil to be precisely balanced, it also permits to equilibrate the coil potentials respective to the ground. Compared with unbalanced configuration, this design is proved to increase Q factor and decrease the frequency shift when coil is loaded [37],

and only cannot compensate for the phase shift caused by coil resistance r. Therefore, this balanced configuration is used for all coils reported in this work. The inductance of coil L is first measured by connecting it to a capacitor (known capacitance) and detect the resonance frequency using the S_{11} measurement described in Figure 3.4a). With such inductance value, the calculation of the rest components is straightforward and can be chosen based on the inventory. Additionally, a segmentation of the coil wire by soldering capacitors in the long wire path thus allowing a maximum conductive length of up to 1/20 wavelength is desirable, because it can help distribute the electric field all around the coil and diminish the contribution of the coil antenna mode.

Since the balanced coil is connected to a coaxial asymmetric transmission line in MR experiments, in principle, a "balanced to unbalanced" transformer (sometimes also known as balun) is required. The role of such device is to avoid currents flowing on the external conductor of the coaxial cable, leading to the deleterious common modes which can induce additional losses, modify the tuning/matching condition, pick up extra surrounding noise, and are also responsible for cross-talk between the ports of a coil array [44]. The common mode is sensitive to the position of the cables with respect to the surrounding metal conductors, and is frequently evidenced as the "hand effect" that affect coil tuning when one touches the insulating jacket of the cable. In this project, when such hand effect is observed, I connect a shielded and balanced narrow balun (cable trap) to each coil to mitigate it. Such balun design and various alternatives can be found in the literature [37].

Tune and match an RF coil: Once a coil is built, the tuning and matching procedure is relatively simple using the test configurations described in Figure 3.4a) and Figure 3.4b). On the network analyzer, the measured reflection coefficient (S_{11} or S_{22}) is frequency swept. The tuning means a dip appears at the Larmor frequency, and a good matching condition is often met while such measurement is less than -20 dB. In Figure 3.11, two coils are connected to a two-port network analyzer, and by examining S_{11} and S_{22} measurements, it can be seen that both coils are tuned to 9.28 MHz and show acceptable matching results (*i.e.*, S_{11} and

$S_{22} = \sim$ -30 dB.) This was done by adjusting the variable capacitors C_T and C_M manually using a tuning stick tool, and in a situation where the range of variable capacitor is limited, one may find the use of a pre-tuning capacitor C_0 is needed. Firstly a small dip is quickly obtained by adjusting C_M. Secondly, the C_T, sometimes together with C_0, are varied in order to move the resonance across the operating frequency, slightly above or below, depending on the previous situation. This adjusting cycle is repeated multiple times until a good match is achieved at the desired frequency. Since variable capacitors have different adjustment types (*i.e.*, top, bottom, side), prior to purchase, the designer should make a clear plan regarding the position and orientation of each variable capacitor on the PCB, ensuing that manual adjustment is still available while the coil is loaded inside the magnet (frequency shift can occur while changing the load). A photo of different variable capacitors is also attached in Figure 3.10b).

Coil quality evaluation: A good understanding of the coil quality can help to evaluate the actual functioning of the coil in its final experimental environment. The Q factor measurement for the empty or loaded coil allows a preliminary evaluation of the probe sensitivity as explained in section 3.1.3. In my measurement, a cylindrical bottle filled with NaCl aqueous solution is used to mimic the effect of a moderately lossy sample. The Q factor is evaluated by loosely coupling the probe resonator to two small pick-up coils [4] (a picture of a constructed pick-up coil is shown in Figure 4.7 using a shielded and balance design introduced in the literature [45]). Two pick-up coil are connected to the two ports of the function generator, and by observing the S_{12} measurement, the Q factor is obtained from the frequency difference that exists between the -3 dB points of the circuit response, which gives Q the expression of $Q = \omega/\Delta\omega$, with $\Delta\omega$ representing the width at -3 dB of the frequency response curve. Note that this expression is different than the definition of Q as described in the section 3.1.3, however, it is a more practical method.

The above mentioned is the most precise method to evaluate Q, but is more delicate to set up. A easier method to measure Q value is to evaluate directly on the function generator

from the reflection coefficient (*i.e.*, S_{11}) at the -3 dB level, when the coil has been matched to 50 Ω. In this case, the measured Q factor is often named as: Q_{match}, and is equal to half the above intrinsic Q value: $Q_{matched} = Q/2$. The -3 dB points of the S_{11} parameter are well-defined in a network analyzer, so the Q value is conveniently obtained (most network analyzers can do this automatically). Moreover, Although the B_1 field map can be obtained by imaging a phantom in a MR experiment using the so-called double-angle method [46], it is also possible to measure a B_1 map with a pick-up coil. Using the S_{12} parameter, the tuned/matched coil is connected to one port, while one can observe the induced voltage in the pick-up coil connected to the second port. This procedure is explained in details in the methods section in Chapter 4.

Coil geometric decoupling: Now, we can make individual RF coil that is usable for MRI experiments. However, for TRASE MRI application, multiple RF coils need to combined together to form a coil array in which the inductive coupling may arise if they are not decoupled properly. The mutual inductance causes resonant frequency splitting (a bench S_{12} measurement can be found in Figure 5.4c)), which not only indicates a loss of sensitivity at the resonance frequency, and also shows that signal and noise are transferred from one coil to another [37]. An effective way to minimize the inductive coupling is to use the geometric decoupling methods introduced previously by adjusting their relative position. Here, I am using an example of saddle coil and solenoid coil to explain this concept. Despite that they are both cylindrical coils, the magnetic field generated by saddle and solenoid are inherently perpendicular to each other, as demonstrated in Figure 3.6. Therefore, when placing two coils coaxially, an optimum relative position exists to minimize their mutual inductance, which makes the independent RF transmission from each coil possible. In the bench measurement, both saddle and solenoid coils are first idependetly tuned to Larmor frequency (f = 9.28 MHz) and matched to 50 Ω, then connected to a two-port network analyzer. While starting inserting one coil into the other, one can see two dips (off 9.28 MHz) on S_{11} and S_{22} measurements, and a large S_{12} value (-5 to -10 dB) at f = 9.28 MHz. When

the inner coil is further placed inside, one can see the two dips on S_{11} and S_{22} get closer and in one particular position merge to a single resonance. By carefully adjusting the relative position (shift and rotation), one can achieve single resonance at $f = 9.28$ MHz for both S_{11} and S_{22}, together with a low S_{12} value (*i.e.*, - 20 dB). Sometimes, one may find both coils need to be slightly tuned and matched to achieve the optimal functioning condition. For example, in Figure 3.11, two coils are geometrically decoupled where S_{11}, S_{22}, and S_{12} are all around -30 dB at $f = 9.28$ MHz, indicating great coil tuning, matching and isolation.

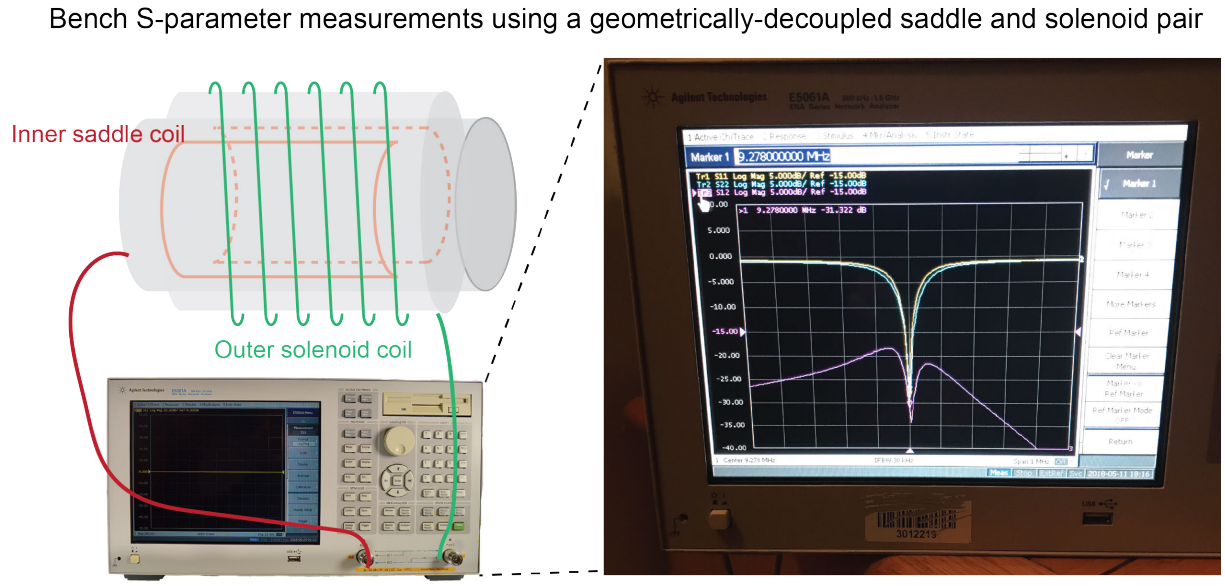

Figure 3.11: An example of S-parameter bench measurements using a geometrically-decoupled RF coil pair - saddle and solenoid. The inner saddle coil and outer solenoid are connected to the port 1 and 2 of a network analyzer. Two coil are coaxially placed to achieve a geometric decoupling condition, where the S parameters are measured as S_{11} = 30.5 dB, S_{22} = -30.7 dB, S_{12} = -33.6 dB at the frequency $f = 9.28$ MHz. These measurements indicate that both coils are well tuned and matched, and efficiently decoupled.

3.5 Review of TRASE RF Phase Gradient Systems

3.5.1 Specific Requirements for TRASE RF Coils

In the previous sections the importance of coil efficiency and stronger phase gradients has been explicitly discussed in the determination of higher resolution. For example, a clinically

useful imaging becomes increasingly feasible for a combination of parameters such as: gradients $\geq$ 5.0 deg/cm; pulses $\leq$ 200 μs; over imaging volumes FOV of $\geq$ 20 cm. However, there are $|B_1|$ homogeneity requirements for TRASE as well. Since TRASE relies on the phase reversal behavior of refocusing pulses for successful spatial encoding and minimization of image artifacts, the TRASE sequence requires effective refocusing behavior over the imaging volume for each pulse in the pulse train. From previous work [19], this constrains the maximum $|B_1|$ coil inhomogeneity to be less than approximately $\pm$10%, which corresponds to a usable refocusing flip angle range of approximately: 160° to 200°. I should mention that we only consider rectangular (hard) refocusing pulses and image reconstruction by Fourier Transform, however, other pulse designs [18] and other reconstruction techniques [47] may allow the $|B_1|$ homogeneity requirements to be relaxed.

3.5.2 Reported TRASE RF Phase Gradient Systems

Here, an overview is given to show different TRASE RF phase gradient coil(s)/system that are reported in the literature.

Spiral birdcage coil

Spiral birdcage coils were used to generate a transverse RF field with phase varying along longitudinal B_0 or superior-inferior (SI) axis [48]. As demonstrated in the literature[49], the B_1 field produced from a spiral birdcage demonstrates a phase variation consistent with the amount of twist, *i.e.*, one and half π twist over a 20 cm long spiral birdcage coil corresponds to a phase gradient of $G_1 = 1.5\pi/20$ cm = 13.5 deg/cm. In the year 2010, a pair of cylindrical spiral birdcage coils (with twist of +1.5/-1.5 π) were wound with copper tape on a single 20.0 cm long, 9.0 cm diameter former, both of which were used to encode 1D TRASE data [20]. With the PIN diode decoupling techniques, each spiral birdcage coil independently produced a unique linear RF phase gradient (measured at +/- 12.5 deg/cm) along SI axis.

Helmholtz-Maxwell (H-M) coil pair

The spiral birdcage coils is able to provide strong phase gradient. However, for geometries in which the patient axis does not coincide with the B_0 axis (such as permanent magnets with vertical B_0 field, like 0.2 T/0.5 T MR system at CCI and some Halbach array permanent magnets), the spiral birdcage is not practical for *in vivo* imaging as patient access is impossible. For this reason an optimized Helmholtz-Maxwell coil pair was demonstrated in 2013 [25], which allows one-dimensional encoding in a horizontal direction for a vertical B_0 field magnet geometry. Refer to Eq.2.8, an RF phase gradient coils can be composed of a superposition of two orthogonal field components, having respectively cosine and sine amplitude distributions along the phase gradient direction. This can be written as:

$$\mathbf{B}_1(\mathbf{r}) = |\mathbf{B}_{1xy}|e^{i\mathbf{G}_1\cdot\mathbf{r}} = \mathbf{i}B_{1x}(\mathbf{r}) + \mathbf{j}B_{1y}(\mathbf{r}) = \mathbf{i}|\mathbf{B}_{1xy}|\cos(\mathbf{G}_1\cdot\mathbf{r}) + \mathbf{j}|\mathbf{B}_{1xy}|\sin(\mathbf{G}_1\cdot\mathbf{r}) \quad (3.12)$$

This configuration can be achieved using a double Maxwell pairs in a crossed arrangement (the sine field component) and a curved Helmholtz (the cosine field component). With this H-M coil pair two opposite phase gradient with the same amplitude can be created simply by changing the polarity of the double Maxwell pairs controlled by the state of one 180° phase-shifter, resulting in the transition from a sine field to a -sine field. The practical design, mathematical descriptions, and driving requirements for this design are documented in the literature [25]. Two-dimensional *in vivo* human wrist images were acquired using two H-M coil pairs, demonstrating the potential of TRASE for clinical use [19]. Additionally, the decoupling between H-M pair was improved by the disable circuit described in Figure 3.9(b), achieving a faster TRASE encoding as reported in [17].

Birdcage-Maxwell coil pair

A coil pair using the combination of birdcage and Maxwell was demonstrated in the literature [11]. This coil pair is a cylindrical Helmholtz - Maxwell concept, in which the cosine field is produced by a short multi-turn birdcage, not Helmholtz coil type. This Birdcage-Maxwell coil pair produces a gradient along the patient axis (SI). The coil pair are decoupled to S_{12} = -15 dB using a toroidal transformer to cancel the mutual inductance. TRASE experiments were performed upon a 3.29 MHz Halbach cylinder permanent magnet.

Other TRASE RF phase gradient coils

Other than the above three coil(s), I will give a brief introduction to more RF phase gradient coils introduced in the literature, without explaining the design details. In a recent article [42], a "twisted saddle" coil was demonstrated. Such coil is the wire-wound analog of a spiral birdcage design, which comprises four saddle-coil elements that are twisted by a 180 degree angle over the length. The target field method was originally introduced for the design of cylindrical B_0 gradient coils, however, people also attempted to design TRASE RF phase gradient coils using this technique. For example, Bellec [50], with such tool, introduced two different phase gradient coil designs for a horizontal and a vertical B_0 magnet, respectively. A 8-leg phase gradient birdcage coil was shown in a thesis [51], where the input current of each leg was computed using a target field method as well.

A key performance parameter for a practical imaging system is the rate at which k-space encoding may be achieved. This 'k-space trajectory speed' is analogous to the maximum gradient strength in a conventional B_0 gradient system. Consider a sub-section of a TRASE echo train consisting of two refocusing pulses of $(-\tau_A-\tau_B-)$, where τ denotes pulse duration. To quantify encoding performance we will define a 1-dimensional TRASE image encoding efficiency metric as follows: Encoding Efficiency = $\Delta G_{AB}/(\tau_A + \tau_B)$. The inter-pulse delay (for signal acquisition) has been omitted from this metric, as the selected value is not in-

Geometry	Coil I.D. (cm)	Coil O.D. (cm)	Imaging Volume FOV x L (cm)	Phase Gradient G (deg/cm)	Gradient Direction(s)	Reported Pulse Len (t_p) (μs)	Encoding Efficiency ($2G/2t_p$) (deg/cm) / ms
Twisted Birdcage (Sharp, 2010)	9	9	$2.5 \times 2.5 \times 14$	12.5	$\parallel B_0$ and SI	800	15.6
Helmholtz - Maxwell (Deng, 2013)	22	42	$16 \times 16 \times 14$	5	$\perp B_0$ and SI$\perp B_0$ and LR	300	16.6
Helmholtz - Maxwell (Der, 2018)	22	42	$16 \times 16 \times 14$	5	$\perp B_0$ and SI$\perp B_0$ and LR	130	38.5
Birdcage - Maxwell (Stockmann, 2016)	18	22	$4 \times 4 \times 13$	2.25	$\perp B_0$ and SI	192	11.7
Twisted Saddle (Nacher 2020)	13.3	13.3	$1 \times 7 \times 7$	7.0	$\parallel B_0$ and SI	78	89.7

Table 3.1: Comparative data for TRASE phase gradient systems. Twisted birdcage and twisted saddle coil can encode along the patient axis (superior-inferior, SI), and are usable for the longitudinal B_0 geometry ($\parallel B_0$). The hybrid coil pairs Helmholtz - Maxwell and Birdcage - Maxwell are only usable for the transverse B_0 geometry ($\perp B_0$), where Helmholtz - Maxwell can encode along two axes - patient axis (SI) and lateral axis (Left-Right, LR), while Birdcage - Maxwell only encodes along the patient axis (SI). Note that RF phase gradient coils designed using the target field approach are not included.

dicative of the transmit hardware encoding performance. In analogy with conventional B_0 gradient coils, gradient coil size is a major determinant of encoding efficiency. A larger phase gradient coil will have a lower encoding efficiency for two reasons. Firstly, the phase gradient strength scales inversely with coil linear dimensions, and secondly for a given available RF power, the pulse length will be longer (with details depending upon coil geometry). Higher available RF power will increase the encoding efficiency of the overall phase gradient system. Table 3.1 provides information collated from the literature on TRASE encoding systems.

A variety of TRASE coils are introduced in this section. Some coils have favorable geometric and field performance, but unfortunately are unusable with a transverse B_0 field (*e.g.*, spiral birdcage). For coil pair such as the Helmholtz - Maxwell and Birdcage - Maxwell, they have the disadvantage of a large difference between the inner and outer diameters, resulting in a

significant loss in imaging volume. In the following chapters, I will introduce a new type of compact and efficient phase gradient coil design for TRASE imaging. It has a large number of attractive characteristics and allows MR encoding along the B_0 direction for a transverse B_0 geometry, offering more options for TRASE users while designing a multi-dimensional encoding RF coil array.

Chapter 4

One Coil - The Twisted Solenoid RF Phase Gradient Transmit Coil [1]

4.1 Introduction

4.1.1 The Developments of TRASE RF Coils

Here, a short review of TRASE is given for those key concepts that are described in previous chapters. TRASE is an MRI method that achieves k-space encoding by the use of gradients in the phase of the RF transmit fields, instead of gradients in the static (B_0) field. Clinical-level millimeter spatial resolution has been demonstrated in phantom studies [20] [25] [19]. Since TRASE allows the B_0 gradient encoding system to be replaced by simpler RF technology, TRASE is a promising technique for low-field, low-cost MRI systems [11]. These systems often employ permanent magnets with a transverse or vertical B_0 magnetic field. The TRASE pulse sequence consists of an echo train using 180° refocusing pulses, in which the phase gradient transmit field is switched between each RF pulse, in an alternating pattern. Since image quality is critically dependent upon the ability to efficiently generate these B_1 fields with uniform magnitude and strong phase gradients, there is an ongoing need for improved coil designs and the associated RF technologies.

[1] The materials in this chapter have been published in the journal of *Journal of Magnetic Resonance* [13].

One limitation of current TRASE systems is that no practical transmit design for encoding along the B_0 direction for a transverse B_0 geometry has been proposed. Such a coil must generate a B_1^+ field vector whose direction varies along the transverse B_0 direction so as to create a linear phase slope along B_0 for spatial encoding. In a theoretical study Bellec et al. applied a target field design process for a G_y phase gradient for a transverse B_y directed B_0 field, resulting in a strong phase gradient, but limited $|B_1|$ homogeneity [50]. This work demonstrated that a phase gradient for this geometry is possible in principle, however, experimental results were not presented.

The first RF phase gradient coil used for TRASE was a twisted birdcage coil [20] [52] modified with a twist about the axis in the B_0 direction. For a conventional superconducting magnet design, this corresponds to a twist along the patient superior-inferior axis. The spark for this work was to ask the question: "Is there an analogous twisted geometry for low field magnets, for which the B_0 direction is transverse?"The standard coil for low field systems is the solenoid which cannot be directly applied in TRASE MRI, so this suggests a solenoid twisted about a transverse axis [53], which would retain all the desirable features that a solenoid coil possesses for a transverse B_0 field (high efficiency ($\mu T/A$), uniformity, large imaging field-of-view (FOV) relative to aperture, cylindrical geometry), while simultaneously generating a phase gradient along a transverse axis. In this chapter the use of the twisted solenoid transmit RF coil in spatial encoding for a cylindrical coil geometry will be introduced. In this work I designed, constructed and experimentally verified a twisted solenoid coil pattern, subject to the multiple constraints of maximizing efficiency, $|B_1|$ uniformity and phase gradient strength. Since the usable imaging volume is effectively defined by the $|B_1|$ uniformity, the FOV is not an independent design constraint. Similarly, phase gradient linearity was not enforced as a design constraint, since all designs provided acceptable linearity.

4.1.2 TRASE Array Configurations

There are a number of different possible transmit hardware configurations, as shown in Figure 4.1. In Figure 4.1A and Figure 4.1B, two different configurations are shown for driving a Helmholtz-Maxwell (HM) pair. Both HM coil elements must be driven simultaneously to produce a phase gradient field. To allow the phase of the Maxwell coil to be reversed, it is necessary that the two elements be driven independently and so the coupling parameter S_{12} becomes important. A value of at least $S_{12} < -15$ dB, or preferably $S_{12} < -20$ dB is desirable to ensure effective decoupling. This level of decoupling is achievable, but requires rather delicate adjustments [25] [11]. A significant advantage of twisted designs (shown in Figure 4.1C and Figure 4.1D) is that the resonant elements are driven sequentially, so it is not necessary to geometrically decouple elements which are simultaneously enabled and tuned to the same frequency. For this reason, twisted pair designs are more robust to experimental perturbations than HM coils. In all configurations, active enable / disable has been shown, because for 2D encoding applications (with a total of 4 coils) this function is expected to be required.

Configuration A shows a single RF power amplifier (RFPA) with a power splitter and actively-controlled phase shifter, both located after the single amplifier [25]. This configuration has the disadvantage that these additional RF components must operate under high power conditions. Deng et al. used configuration A including a high power RF splitter, a high power PIN diode phase shifter, and PIN diode coil element disable circuitry [25]. Configuration B alleviates the need for high power components (*e.g.*, phase shifter), at the expense of a second amplifier, although this is mitigated because each individual amplifier has a lower peak power requirement, than in A. Configuration B uniquely allows some limited flexibility to adjust the gradient strength by adjustment of the relative drive levels, whereas configuration A has a fixed power ratio determined by the design of the high power RF splitter. Both configurations A and B demand a high duty cycle from the RFPA because both coils are active for generation of both positive and negative phase gradients.

Configurations C and D show respectively single and dual RFPA configurations for a pair of twisted coils. Configuration C requires a higher duty cycle and a high power switch, whereas D requires one RFPA for each coil. Of all the configurations, Configuration D has the lowest duty cycle requirement (indicated graphically by shaded the RFPA in standby in white), hence, D is used in this thesis.

The various configurations have different characteristics when extended to 2-dimensional encoding. In A, if a single RFPA is maintained, then cascading of phase splitters and an additional switch is required. Configurations B and D require additional power amplifiers but are otherwise straightforward. Configuration C would require a 3- or 4-way high power RF switch.

4.1.3 Performance of Phase Gradient Systems

A "phase gradient system" comprises one or more RF power amplifiers (RFPAs) and an RF transmit array capable of producing phase gradient fields. For an RF coil A with k-space origin of k_A (1/m), the inherent B_1 phase gradient is $G_A = 2\pi k_A$ (rad/m). One may consider 1-dimensional encoding, which requires the production of two different RF transmit field patterns (A and B), both with (preferably) uniform B_1 field magnitude, but maximally different B_1 phase gradients. Denoting the phase gradient difference between the two fields as ΔG_{AB}.

The image FOV for a single-shot echo train using fields A and B is the reciprocal of the k-space sampling interval, *i.e.*, FOV $= 1/2|k_A - k_B| = 1/2\Delta k_{AB}$. The pixel separation ('pixel size') $\Delta x = \text{FOV}/ETL$, where ETL is an integer 'echo train length' equal to the number of echoes. For example, for two phase gradient coils of strengths +5.0 deg/cm and -5.0 deg/cm and $ETL = 128$; we have $\Delta k_{AB} = 10.0$ deg/cm $= (10/360)\ /0.01 = 2.78$ cycles/meter. The pixel size is therefore:

$$\Delta x = \text{FOV}/ETL = 1/(2 \times \Delta k_{AB} \times ETL) = 1/(2 \times 2.78 \times 128) = 1.41 \text{ mm}.$$

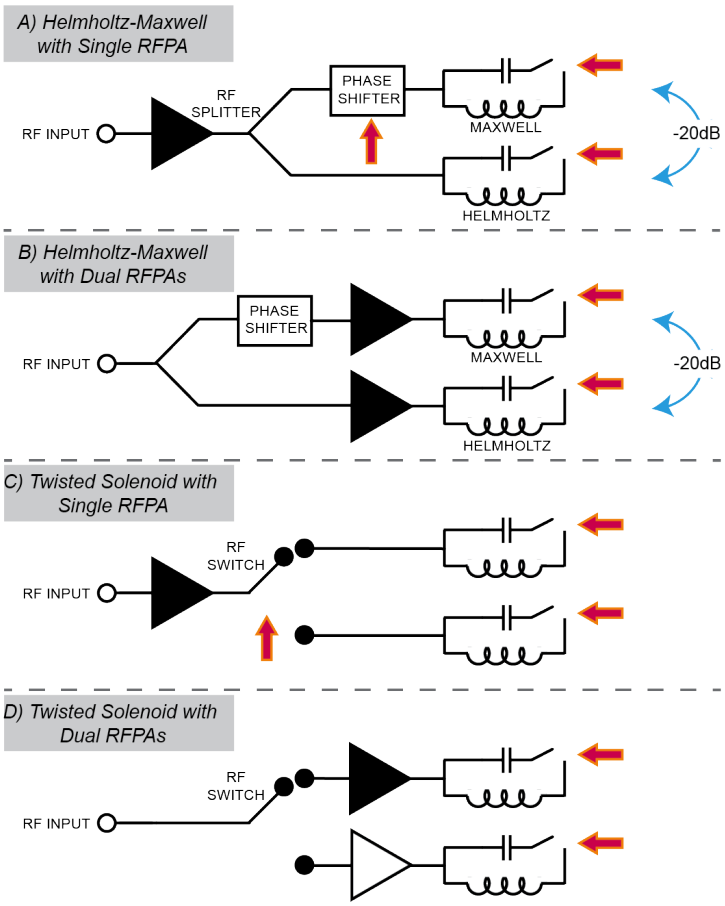

Figure 4.1: Four possible TRASE transmit configurations for a single encoding axis. **A)** Helmholtz-Maxwell pair using a single RF power amplifier (RFPA). **B)** Helmholtz-Maxwell pair using dual RFPAs. Both of these configurations require good geometric decoupling, *i.e.*, $S_{12} < -20$ dB. **C)** A pair of twisted coils using a single RFPA. **D)** A pair of twisted coils using dual RFPAs. Each configuration is shown with a single RF input, although configurations B and D could alternatively be driven by dual transmit channels. High power active elements (under PIN diode control) are shown with a red arrow.

This raw resolution calculation shows that rather modest and achievable phase gradients are sufficient to attain clinical level spatial resolution, provided that a long echo train may be used. This is the motivation behind this research program aimed at developing the technology to perform these experiments.

4.2 Theory

4.2.1 Tilted and Twisted Solenoids

Solenoids can be tilted and paired to produce a uniform transverse magnetic field. For a superconducting DC application, Goodzeit et al.[54] proposed a two-element double helix dipole constructed from two tilted solenoid coils. By use of opposing currents their design cancels the longitudinal solenoidal component, to obtain a resultant dipole field. The field is uniform within the bore. These solenoids are tilted, but not twisted, so do not produce the phase gradient required for TRASE. Alonso has applied the same tilted double helix dipole field as an NMR RF coil [55].

Fortuitously, analytical fields for twisted solenoids of exactly the type that is needed for TRASE are to be found in the literature on magnet design [56] [57] in the form of 'Modulated Double Helical Coils'. Just one of these coils is required to produce a field gradient for TRASE. In this chapter I will present the first use of the twisted field pattern in a NMR RF coil, as an imaging gradient. Since the application is low-field imaging, the quasi-static (DC) analysis of the coil field pattern is applicable.

4.2.2 Ideal Long Twisted Solenoid

In this section, I will show how phase gradient strength and $|B_1|$ uniformity vary as a function of twist parameter, coil diameter and diameter of imaging volume. This will be based on the analytical solution for the infinite, closely wound twisted solenoid of Queval [57].

Wire Path on Cylindrical Surface

Considering coil geometries for which a wire wound on the surface of a cylinder lies on the parametric curve $P(\theta)$:

$$\begin{aligned} P_x(\theta) &= a\cos(\theta) \\ P_y(\theta) &= a\sin(\theta) \\ P_z(\theta) &= A\sin(n\theta+\psi) + (h/2\pi)\theta \end{aligned} \tag{4.1}$$

where the parameters are as follows (see Figure 4.2):

- a (m) - coil turn radius (radius of cylindrical former)
- A (m) - twist or modulation amplitude, which controls the phase gradient strength. (For a uniform solenoid, $A = 0$.)
- n - coil multipole order. For TRASE purposes, this parameter is restricted to $n = 2$.
- ψ (radians) - winding shift (not shown in Figure 4.2). Note that a rotation of the TRASE coil former about the z axis by $\Delta\alpha$ is equivalent to a $2\Delta\alpha$ change of winding shift (This will be explained later in this chapter)
- h (m) - turn advance or pitch (Turns/meter = $1/h$)
- θ (rad) - cylindrical coordinate varying between $-N\pi$ and $+N\pi$ (shown in Figure 4.2), where N represents the number of coil turns

To illustrate, consider two examples. Firstly, a single circular planar loop of radius a is given by the curve $P(-\pi) \rightarrow P(\pi)$, for $A = 0, \psi = 0, h = 0$. Secondly, a 4-turn solenoid of turn radius a and length L, is given by the curve $P(-4\pi) \rightarrow P(4\pi)$, for parameters $A = 0, \psi = 0, h = L/4$.

For the twisted solenoid designs in this work I will fix $\psi = 0$ and $n = 2$. Other designs are obtained by simple rotation of the former or wire pattern. This condition of $\psi = 0$

corresponds to the wire axial offset $P_z(\theta)$ starting at zero for $\theta = 0$. If one refers to $\theta = 0$ as the 'top' of the coil, this geometry will produce a phase gradient in the x, up-down direction. The maximum z (axial) offset of the wire occurs $2n = 4$ times per turn, for values of θ satisfying $|\sin 2\theta| = 1$, *i.e.*, $\theta = -3\pi/4, -\pi/4, \pi/4, 3\pi/4$....

Magnetic Field

To calculate the field within the cylindrical aperture due to a steady current in the wire, the continuous current sheet approximation is used, which is equivalent to a coil wound tightly with thin wire. Although the fields outside the aperture are non-zero, I will ignore these, as the concern is the imaging volume within. So for a thin wire, tightly wound coil of radius a and infinite length with its axis along the z–axis, current I, the B field components in cylindrical coordinates (ρ, θ, z), within the aperture ($\rho < a$) are [57]:

$$\begin{aligned} B_\rho &= -\mu_0 \frac{I}{h} \frac{A\rho}{a^2} \sin(2\theta + \psi) \\ B_\theta &= -\mu_0 \frac{I}{h} \frac{A\rho}{a^2} \cos(2\theta + \psi) \\ B_z &= \mu_0 \frac{I}{h} \end{aligned} \tag{4.2}$$

B_ρ is the radial component, B_θ is the circumferential component, and B_z represents the axial component. Defining Cartesian coordinates $(x, y, z) = (\rho\cos\theta, \rho\sin\theta, z)$, and transforming these field components to Cartesian coordinates:

$$\begin{aligned} B_x &= -B_\theta \sin\theta + B_\rho \cos\theta \\ B_y &= +B_\theta \cos\theta + B_\rho \sin\theta \\ B_z &= \mu_0 \frac{I}{h} \end{aligned} \tag{4.3}$$

Notice that the B_z uniform solenoidal component is unaffected by the twist modulation.

NMR B_1 Field

For the NMR purposes, I wish to use the twisted solenoid as a B_1 RF transmit coil. In what follows it is always useful to bear in mind that the direction of the B_1 *field itself* is in

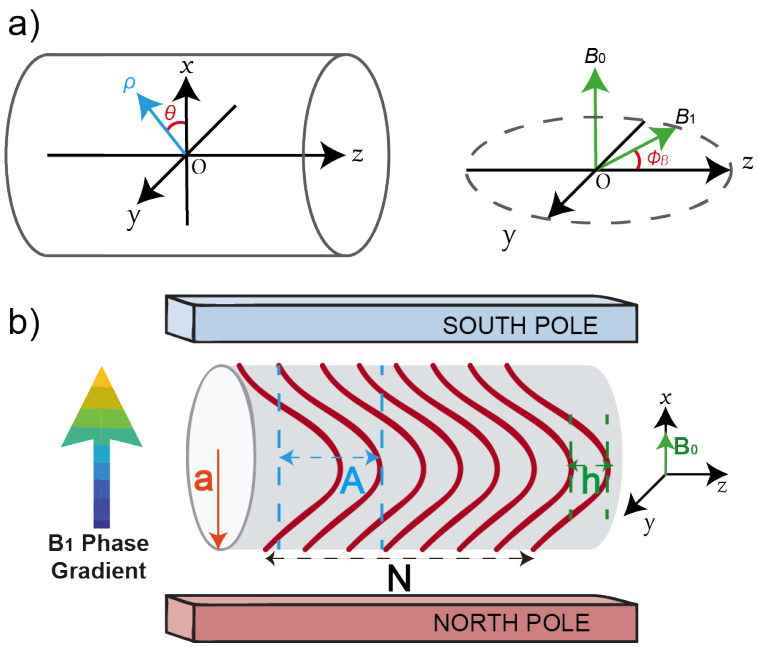

Figure 4.2: **a)** Cylindrical (ρ, θ, z) and Cartesian (x, y, z) coordinate systems, showing cylindrical coil former. The main magnetic field B_0 is applied vertically, that is along the x direction. The B_1 field is the RF field in the yz plane and has phase ϕ_B, which is x-dependent: $\phi_B(x)$; **b)** A cartoon of a twisted solenoid coil positioned inside a magnet. The parameters that determine coil wire pattern are depicted.

general distinct from the direction of the B_1 *phase gradient*. As for all RF coils, the coil itself produces an RF magnetic vector field with three components, but only the two components orthogonal to the main magnetic field B_0 contribute to the NMR B_1 field. In this section I will restrict the discussion to the case of the static field B_0 applied in the x direction, which is set as the vertical direction. For this B_0 field direction, the contributing transverse B_1 components are B_y and B_z, while any B_x component becomes a concomitant RF field, *i.e.*, does not contribute to B_1, hence, can be ignored in the discussion. The B_1 field components, magnitude $|B_1|$ and phase ϕ_B can be written as:

$$\begin{aligned} B_y &= +B_\theta \cos\theta + B_\rho \sin\theta \\ B_z &= \mu_0 \frac{I}{h} \\ |B_1| &= \sqrt{B_y^2 + B_z^2} \\ \phi_B &= \tan^{-1} \frac{-B_y}{B_z} \end{aligned} \tag{4.4}$$

For this definition of the phase, $\phi_B = 0$ over the central horizontal ($x = 0$) plane. Since for this infinite current sheet, none of the field components are a function of z, there is no possibility of an axial B_1 phase gradient, *i.e.*, $G_z = 0$. However, what's needed is to define gradients in B_1 phase ϕ_B in both lateral (i.e. non-axial) directions:

$$G_x = \frac{\partial \phi_B}{\partial x}, \quad G_y = \frac{\partial \phi_B}{\partial y} \tag{4.5}$$

For the chosen coil rotational orientation ($\psi = 0$), the B_1 phase gradient is in the vertical x-direction only (parallel to B_0) because B_z is uniform and B_y only varies as a function of x. This can be shown as follows:

$$\begin{aligned} B_y &= +B_\theta \cos\theta + B_\rho \sin\theta \\ B_y &= -\mu_0 \frac{I}{h} \frac{A\rho}{a^2} \Big[\cos(2\theta + \psi)\cos\theta + \sin(2\theta + \psi)\sin\theta \Big] \end{aligned} \tag{4.6}$$

which, using trig identities, $x = \rho\cos\theta$, and $\psi = 0$, simplifies to:

$$B_y = -\mu_0 \frac{I}{h} \frac{A\rho}{a^2} \cos(\theta + \psi) = -\mu_0 \frac{I}{h} \frac{Ax}{a^2} \tag{4.7}$$

The ratio of the B_1 components is:

$$\frac{B_y}{B_z} = \left(\frac{-A\rho}{a^2} \right) \cos\theta = \frac{-Ax}{a^2} \tag{4.8}$$

and the B_1 phase is:

$$\phi_B = \tan^{-1} \frac{-B_y}{B_z} = \tan^{-1} \left(\frac{Ax}{a^2} \right) \tag{4.9}$$

Since the phase is a function of x only, it can be concluded that $G_y = 0$, and for the phase gradient in the x-direction:

$$G_x = \frac{\partial \phi_B}{\partial x} = \frac{\partial}{\partial x} \left[\tan^{-1} \left(\frac{Ax}{a^2} \right) \right] = \frac{A/a^2}{1 + (Ax/a^2)^2} = \left(\frac{1}{a} \right) \frac{A/a}{1 + (A/a)^2 (x/a)^2} \tag{4.10}$$

where (A/a) is the normalized degree of twist, and (x/a) the normalized distance along the encoding axis. This (x/a) factor indicates a non-linearity in the gradient, *i.e.*, the gradient strength is a function of position along the encoding direction. The overall factor of $(1/a)$ indicates that for a given coil geometry, the phase gradient strength is inversely proportional

to coil size, which is indeed an expected behaviour for any design of a phase gradient coil. As a general rule, a smaller coil will have both a shorter pulse length and a stronger gradient.

From the above equations, the magnitude of the B_1 field is calculated from the orthogonal sum of uniform axial and quadratic lateral components:

$$|B_1| = \sqrt{B_y^2 + B_z^2} = \sqrt{\left(-\mu_0 \frac{I}{h}\frac{Ax}{a^2}\right)^2 + \left(\mu_0 \frac{I}{h}\right)^2} = \mu_0 \frac{I}{h}\sqrt{\left(\frac{Ax}{a^2}\right)^2 + 1} \tag{4.11}$$

These analytical solutions for phase gradient G_x and field strength B_1 (Eq.4.10 and 4.11) for the ideal infinite twisted coil are illustrated in Figure 4.3, for a range of turn modulations. The figure illustrates that as the turn modulation is increased, the phase gradient increases, but the $|B_1|$ uniformity decreases, and the phase gradient linearity decreases. The choice of a modulation amplitude therefore involves a design trade-off between these three performance measures.

In summary, the magnitude of the B_1 field varies in the x direction only, and so is uniform over any horizontal plane. Over the central horizontal $x = 0$ plane, the magnitude of the field is unaffected by the coil twist and is given by: $|B_1| = \mu_0 I/h$. The phase of the B_1 field similarly only varies in the vertical direction, so again the B_1 phase is constant over any horizontal plane. Over the central horizontal $x = 0$ plane the direction of the B_1 field is purely axial, as for a conventional solenoid. For a long twisted solenoid, since the field pattern varies as a function of x only, the field pattern over all transaxial planes are identical.

Generation of Different Phase Gradients by Coil Rotation

The generation of phase gradient G_x has been discussed, assuming a winding shift $\psi = 0$. However, with appropriate values of winding shift, other phase gradients such as -G_x, G_y and -G_y can also be created. Examining Eq.4.7, a reversed B_y field is generated when $\psi = \pi$ because $\cos(\theta + \pi) = -\cos(\theta)$, resulting in the generation of the opposite phase gradient -G_x using Eq.4.10.

Phase Gradient	Winding Shift (ψ)	Coil Rotation
$+G_x$	0°	0°
$-G_x$	180°	90°
$+G_y$	270°	135°
$-G_y$	90°	45°

Table 4.1: Winding shifts and coil rotation for 4 orthogonal phase gradient directions. Other transverse gradient directions are also possible (not shown.)

The creation of a phase gradient along y axis G_y is achieved as follows. For a winding shift of ($\psi = 3\pi/2$), using trig identities and $y = \rho \sin\theta$, Eq.4.7 simplifies to:

$$B_y = -\mu_0 \frac{I}{h} \frac{A\rho}{a^2} \cos(\theta + 3\pi/2) = -\mu_0 \frac{I}{h} \frac{Ay}{a^2} \tag{4.12}$$

and the B_1 phase is:

$$\phi_B = \tan^{-1} \frac{-B_y}{B_z} = \tan^{-1} \left(\frac{Ay}{a^2} \right) \tag{4.13}$$

Now the phase only depends upon the y coordinate, so there is no gradient along x axis, *i.e.*, $G_x = 0$. The phase gradient in the y-direction can be expressed as:

$$G_y = \frac{\partial \phi_B}{\partial y} = \frac{\partial}{\partial y} \left[\tan^{-1} \left(\frac{Ay}{a^2} \right) \right] = \frac{A/a^2}{1 + (Ay/a^2)^2} = \left(\frac{1}{a} \right) \frac{A/a}{1 + (A/a)^2 (y/a)^2} \tag{4.14}$$

This formula is identical to Eq.4.10, with only x substituted by y. Similarly, it can be proved that winding shift ($\psi = \pi/2$) is capable of producing -G_y phase gradient along y axis. These gradient directions and winding shifts are summarized in Table 4.1. In summary, to generate four different phase gradients G_x, -G_x, G_y and -G_y, the corresponding coil rotation should be half of the winding shift, which are $\psi = 0°$, 180°, 270° and 90°, respectively, meaning that rotation of coil former by 1° is equivalent to 2° rotation of phase gradient orientation.

One may find this is not intuitive and likely to cause confusion during practical construction, so a better way to understand the winding shift is needed. Here I link the winding shift ψ with another parameter ϕ which denotes the rotation angle of coil former along axis z. Relative to the desired coil proposed previously when $\psi = 0$, *i.e.*, the geometry that produces phase gradient G_x, rotate the coil former along z by ϕ only results in a change of parametric curve

on P_z:

$$P_z(\theta, \phi) = A \sin[(n(\theta + \phi)] + (h/2\pi)\theta \tag{4.15}$$

Expand $P_z(\theta, \phi)$ and compare with $P_z(\theta)$ gives:

$$\psi = n\phi \tag{4.16}$$

For case of the presented twisted solenoid coil ($n = 2$), this can be understood as the rotation of coil by 180° does not change coil pattern distribution, since within the full circle rotation range $\phi \in [0, 2\pi]$ the wire path follows two periods of sinusoid waveforms. However, Table 4.1 is recommended for quick and easy look-up in practical coil construction.

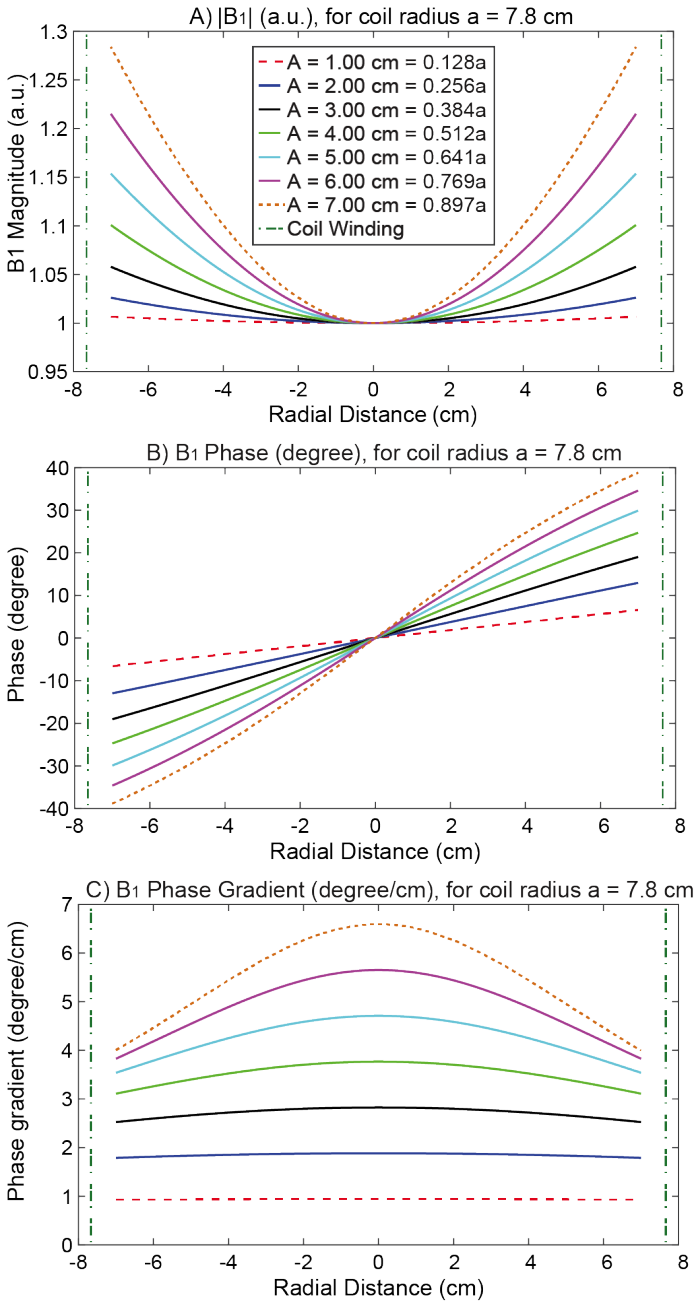

Figure 4.3: Field plots for analytical solution for ideal infinite twisted coil, for a range of turn modulations: ($A = 1$ cm, 2 cm,..., 7 cm) **A)** B_1 magnitude; **B)** B_1 phase, ϕ_B; **C)** Phase gradient, G_x. The radius of the coil winding is indicated by vertical green dotted lines. These plots show that as the modulation increases, the phase gradient strength increases, however the B_1 magnitude uniformity worsens, and the linearity of the phase gradient also deteriorates. Coil design therefore involves a trade-off between these parameters.

4.3 Methods

In this section I will describe the design of a practical RF transmit coil, based on the twisted solenoid geometry, for the purpose of TRASE imaging. The optimum design of conventional solenoidal transmit / receive coils at lower field has been studied by Blasiak et al. [58]. For the design of a 8.2 MHz solenoidal head coil (inter diameter (I.D.) 28 cm, length 28 cm), the authors reported an optimum balance between B_1 uniformity and SNR was achieved by a 9-turn coil using 1/4 inch outer diameter (O.D.) copper tubing.

For the design of TRASE transmit coils the priorities are different from those of Blasiak et al. since, although coil efficiency remains a design consideration, the coil field pattern produced has higher priority, because it determines the spatial encoding. Also, although, for convenience, the TRASE coil may often be used as receiver, in an optimized design a dedicated receive coil or array should be used, hence receiver performance of the twisted solenoid becomes a secondary consideration. In general, the tight specifications on the transmit field pattern of the coil tends to favour larger radius coils, whereas high sensitivity favours smaller radius coils.

4.3.1 Design Aims & Procedure

General Design Aims

The general design aim for the twisted solenoid is to maximize the phase gradient strength over a defined imaging volume, subject to constraints on B_1 homogeneity, coil efficiency and coil geometry. Also note that the geometry limits the maximum phase gradient strength, as the modulation A approaches radius a. The phase gradient linearity was not explicitly used as a criterion because while the other parameters affect the execution of the experiment, nonlinearity only affects the image geometry, which can be corrected for post acquisition. Also, given all geometric constraints, the phase gradient linearity is closely correlated with the other measures (see Figure 4.3). The maximization of coil efficiency is favoured by high

B_1 strength (*i.e.*, closer wound turns) and high coil Q. In this study decoupling between the two transmit coils (one twisted solenoid and one saddle) was achieved geometrically, which avoids the issue of potential Q degradation due to losses in PIN diode switches. Also, a fixed winding shift, $\psi = 0$ and a fixed coil radius (see below) are used, so the design task is reduced to finding optimum values for the following coil geometric parameters:

- A - modulation amplitude
- h - turn advance
- N - number of turns

Total coil length is not an independent parameter, but a maximum acceptable coil length is specified.

Specific Design Target and Constraints

To suit the magnet system used in this study, the coil design was based on a 6-inch O.D. acrylic cylindrical former, which corresponds to a coil turn radius of $a = 78$ mm. The maximum acceptable coil length along the z axis was specified as 450 mm. The conductor was wound with solid 12 AWG hookup wire (Digikey). Since the ultimate aim is to wind multiple such coils in a single cylindrical structure, this relatively narrow conductor diameter is beneficial, despite the potential for slightly increased ohmic losses. The design was also constrained to be an integer number of evenly-spaced turns, each of the modulated twisted geometry, as already described. No attempt was made to modify the coil design to compensate for the finite length of the coil, although there is scope to investigate this in future studies, as will be discussed in Chapter 8 addressing future work. The cylindrical target imaging volume was specified as follows:

1. A diameter of 110 mm, equal to 70% of the diameter of the cylindrical former (110 mm = 0.7 $\times$ 156 mm).

2. A length of 100 mm along the z-axis (axial direction)

It is worth commenting that this is a reasonable, yet arbitrary, choice of imaging volume, and that different target volumes would yield different coil designs. In particular, specifying a smaller target diameter (as percentage of coil diameter) would permit a larger modulation (*i.e.*, more twist) resulting in a stronger phase gradient.

Design Procedure

The design strategy adopted was to search through a large number of field simulations corresponding to candidate coil geometries, and to select an optimum design from ranking and scoring the field patterns.

In this work the B_1 field created by each coil winding pattern was calculated with Biot-Savart simulations using the BSMag MATLAB package, where the wire pattern was segmented into 720 straight-line current segments per turn [43]. An example MATLAB code is shown in Appendix I. For a relatively low frequency of interest (9.28 MHz), these quasi-static Biot-Savart simulations provide a good approximation of the magnetic field produced by coil currents, provided that the RF current phase does not vary significantly throughout the circuit. The rule-of-thumb is that current paths should be $L < \lambda/20$, which corresponds to around $L = 1.6$ m (free-space). In construction, capacitors were used to break up the long wire to mitigate wavelength effects [4].

Search Procedure: Parameters

The B_1 field was simulated using the following parameter search ranges:

- Depth of modulation, A(cm): 1.0 cm ... 10.0 cm, (in $\Delta A = 0.5$ cm increments)
- Turn spacing / pitch, h(cm) = 1.0 cm ... 10.0 cm, (in 0.5 cm increments)
- Number of turns, N = 2, 3, 4, 5, 6, 7, 8, 9, 10

#	Modulation A (cm)	Turn Advance h (cm)	Turns N (count)	Mean B_1 phase gradient G_x (deg/cm)	B_1 field strength per unit current at origin $B_1(0,0,0)$ (uT)	Median B_1 field strength per unit current within imaging volume B_{1med} (uT)	Wire length L (m)	Coil efficiency η_{coil} (uT· deg/cm)
1	5.5	3	10	5.27	36.61	37.05	6.81	195.39
2	6	3.5	10	5.51	32.44	32.88	7.10	181.14
3	5	3	9	4.98	35.67	36.03	5.88	179.48
4	5.5	3.5	10	5.14	32.51	32.88	6.81	168.93
5	5.5	3.5	9	5.23	31.78	32.16	6.13	168.14
6	5.5	4	9	5.12	28.61	28.92	6.13	148.02
7	5.5	4	8	5.22	27.92	28.24	5.45	147.33
8	6	4.5	8	5.49	25.39	25.71	5.69	141.14
9	5.5	4.5	8	5.12	25.44	25.70	5.45	131.56

Table 4.2: Simulation Results of Different Twisted Solenoid Coil Geometries

Select / Reject Criteria:

- The acceptance criterion for field uniformity was $|B_1|/|B_1 min| < 1.25$ over the imaging target volume, corresponding to a flip angle range of 160° to 200°.
- The acceptance criterion for mean phase gradient strength was $G_x \geq 5.0$ deg/cm.

Ranking Criteria: Coil winding patterns that passed the first test are shown in Table 4.2. These 9 designs were then ranked by defining a coil efficiency metric (η_{coil}) as the product of median B_1 field strength and mean phase gradient such that $\eta_{coil} = B_{1med} G_x$.

The Optimum Twisted Solenoid Coil For Construction

The top ranking design (labelled #1), a 10-turn coil with 3 cm turn advance and a 5.5 cm modulation, is shown in Figure 4.4 and Figure 4.5, and was selected for construction. As expected, the numerical results duplicated the general features of the analytical current sheet solution, but differ due to both the finite coil length and the finite turn spacing.

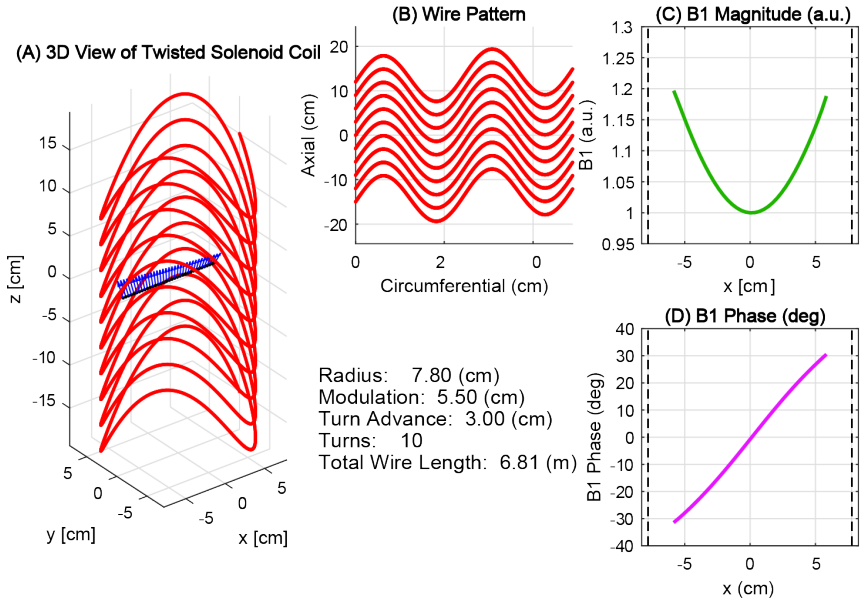

Figure 4.4: Field plots for optimum twisted solenoid coil using Biot-Savart's Law calculation **A)** 3D view of coil, showing field measurement points; **B)** Unrolled view of wire winding pattern; **C)** B_1 magnitude along x axis **D)** B_1 phase along x axis. Position of coil windings is indicated by vertical dotted lines. Geometric parameters are shown in the figure.

4.3.2 Coil Construction

Twisted Solenoid: A 10-turn 78 mm radius twisted solenoid was wound from 12 AWG solid hookup wire, upon a 6 inch (152 mm) O.D. cylindrical acrylic former. The twisted solenoid wire path is shown in Figure 4.4, where coil geometry parameter values are modulation $A =$ 55 mm, winding increment (turn advance) $h = 30$ mm. A schematic and photograph of the constructed coil are shown in Figure 4.6.

Saddle Coil: To demonstrate one-dimensional TRASE imaging encoding, a second coil is needed with a different phase gradient. One option is to use a conventional RF coil which provides zero phase gradient, here, an orthogonal saddle coil was constructed [4]. Using a 5 inch (127 mm) O.D. cylindrical acrylic former, the saddle coil was constructed with a length-to-diameter ratio of 2 and circular arcs of 120°. This particular geometry has been proved to be an optimal geometry for generating a uniform magnetic B_1 field, because no second order central field derivatives is generated in any direction [59]. The saddle coil

has an extra wire loop of diameter of 11 cm at one end, which allowed coil decoupling to be achieved purely geometrically, simplifying the experimental arrangement, and allowing twisted coil efficiency to be evaluated without potential losses from PIN diode circuitry. The saddle coil was configured with a T/R switch so that it can operate as either transmitter and receiver. The coil circuit schematics and photographs of the constructed coils are also shown in Figure 4.6.

4.3.3 MRI Equipment

MRI experiments were performed on a 9.28 MHz 4-poster permanent magnet with a vertical B_0 field (magnet picture shown in Figure 6.3), equipped with conventional B_0 imaging gradients with opening between planar gradient coils of 21.5 cm. The B_0 gradients were used for shimming only. The MRI system was controlled by an NRC TMX research console [60], equipped with a single transmit channel and two receive channels. The single transmit channel was configured to drive two RFPAs in alternation. Firstly, a 50:50 RF power splitter (Minicircuits) was used to divide the RF drive signal. Secondly, the RF gating signal was processed by an Arduino single board computer (Mega 2560) to generate two RFPA enable (gating) signals (A demonstration code is included in Appendix I). Following the detection of a trigger signal from the console, controlled by a user-defined program, the board generates two digital gating signals (+5 V) to alternately enable the RFPAs. The two independent RF power amplifiers used to drive the two coils were as follows: the twisted coil was driven by an AN8110 RF Amplifier (Analogic Corp MA, USA), and the saddle coil by a Tomco model BT00500 RF amplifier (Tomco Technologies, Australia). The T/R switch used was actively switched [37]. A low noise (noise figure=1.2 dB), 50 Ω, high gain (50 dB) pre-amplifier (AU 1448 - 8064) was used to amplify the received signal (Miteq, NY, USA).

4.3.4 Coil Q RF Power Measurement Procedures

For bench RF measurements, RF S-parameters and coil Q were measured using an Agilent Technologies E5061A network analyzer. RF voltages were measured using an oscilloscope (Model MDO4054B-3 Tektronix). Using two small search loops connected to the 50 Ω network analyzer, coil Q was measured under two conditions: 1) without load ($Q_{unloaded}$), and 2) with human forearm positioned in the center of the coil (Q_{loaded}). A cylindrical phantom, of diameter of 47 mm and length 80 mm, was used to mimic the forearm loading by adding NaCl to tap water until the same Q_{loaded} was reached.

RF power was measured in the magnet with the the solenoid coil being connected to the AN8110 RF amplifier, in series with an active T/R switch. Positioned in the magnet with loaded phantom, the twisted solenoid coil was tuned and matched, as indicated by reflection coefficient S_{11} measurement at the resonant frequency. The RF power required by the coil for a 180° flip angle (for a given pulse length) was determined from NMR measurements by first adjusting the power using a spin-echo sequence, maximizing the echo amplitude. The forward and reflected power in this condition was then determined from a calibrated directional coupler inserted into the RF output path. For verification, the RF output power was also calculated by measurement of the RF input signal to the RFPA and using the known gain of the amplifier at the Larmor frequency. This calculated output power is expected to match the sum of the forward and reflected power measurements.

4.3.5 Field Profile Measurement Procedures

To assess the amplitude and phase of the generated B_1 transmit fields, bench tests were performed with a pick-up/search coil to measure the two field components B_y and B_z within the specified imaging volume. The shielded and balanced pick-up coil was constructed from flexible co-axial cable [45], and formed an ellipse with major and minor axis 20 mm and 10 mm, respectively. Five different transaxial planes (z = -50 mm, -25 mm, 0 mm, 25 mm, 50

mm) were evaluated. In each z plane the field along three lines (y = -15 mm, 0 mm, +15 mm) were measured at 11 different x positions varying between -52 mm to +45 mm, with 5 repetitions. Throughout the entire procedure, the twisted solenoid coil was positioned on 10 cm thick foam blocks without loading, inside of which the pick-up coil was positioned perpendicular to the orientation of each evaluated field component. With a network analyzer, the S_{12} measurement mode was used to detect the B_y and B_z magnitude (linear scaling), and the corresponding phase information (to detect field sign reversal). The experimental setup is pictured in Figure 4.7

4.3.6 Calculations and Data Fitting Procedures

B_1 Magnitude and Phase: The B_1 magnitude and phase were calculated directly from the B_y and B_z measurements as $|B_1| = \sqrt{B_y^2 + B_z^2}$, and $\phi_B = \tan^{-1}(-B_y/B_z)$, both of which are plotted in Figure 4.8. The error associated with each point in the figure was calculated using error propagation, where the errors of B_y and B_z were represented by standard deviation of five raw measurements.

B_1 Phase Gradient Methods: The B_1 phase gradient was not directly estimated (by differentiating the measured phase points) as this is known to be a noise-sensitive procedure. Instead, to appropriately evaluate the phase gradient, I used second-order polynomials (as suggested by the simulation results) to directly fit the raw B_y and B_z measurements, because both magnetic field components are expected to be smooth functions. Next, using these two fitted field curves, the phase gradient was evaluated at 20 points evenly-spaced points on the x-axis:

$$G_x = \frac{\Delta \tan^{-1}(-B_y/B_z)}{\Delta x_i}$$

where Δx_i is defined as the chosen x interval. In the fitting process ΔB_y and ΔB_z (the estimates of the standard deviation of the error in predicting B_1 magnetic fields at x) were calculated using the MATLAB *polyval* function. These estimated errors were propagated to evaluate the accuracy of the evaluated phase gradient curves.

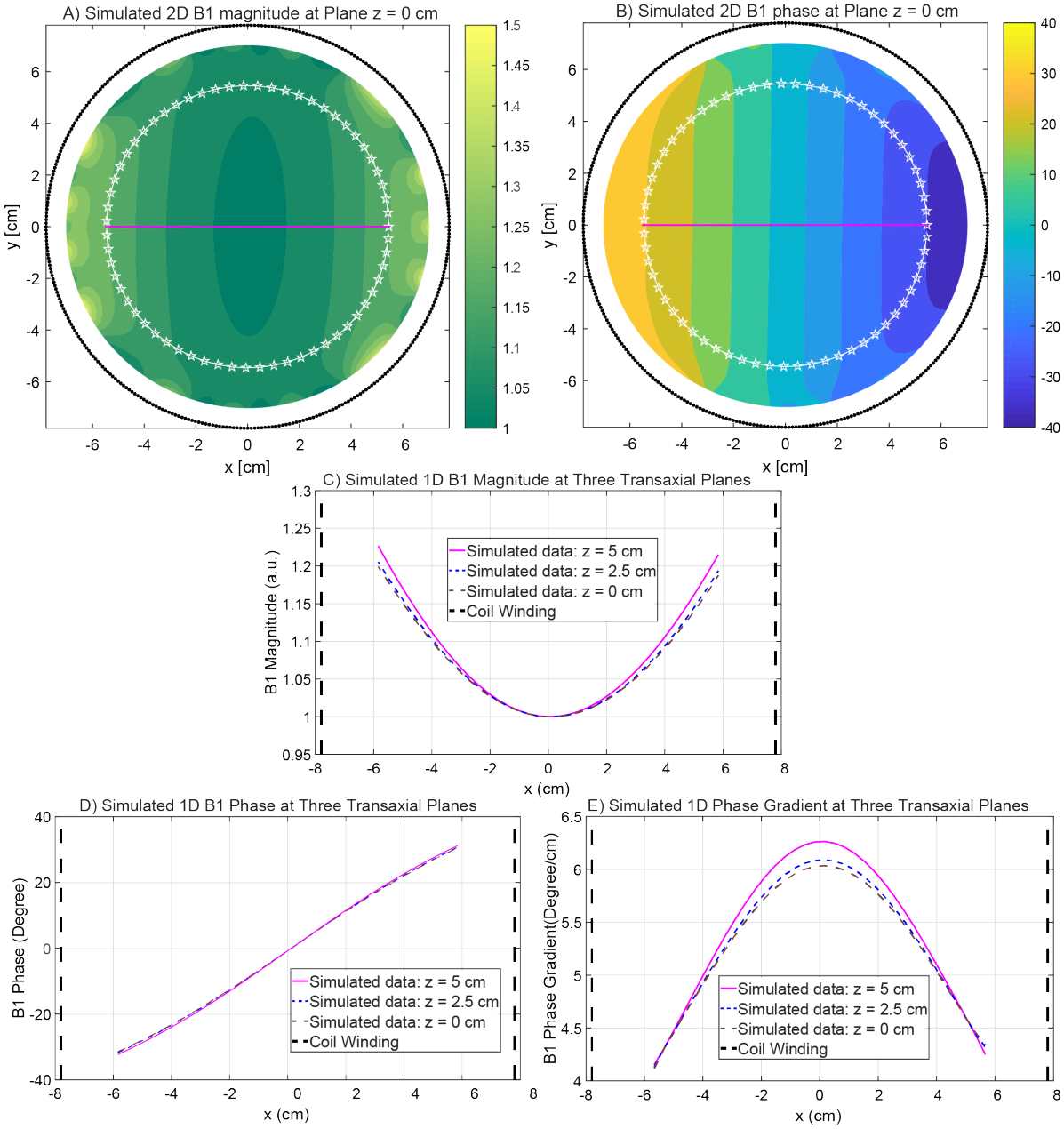

Figure 4.5: B_1 field plots using Biot-Savart simulations for the optimum coil design (a = 78mm, A = 55 mm, h = 30 mm, N = 10). 2D simulated B_1 field at plane $z = 0$ cm, showing: **A)** 2D B_1 magnitude map; **B)** 2D B_1 phase map. The coil winding and target imaging volume are depicted as black dotted line and white pentagram line, respectively. The horizontal magenta line indicates the position of the 1D profiles. For three different transaxial planes ($z = 0$ cm, 2.5 cm, and 5.0 cm) 1D profile lines are shown for: **C)** 1D B_1 magnitude; **D)** 1D B_1 phase; **E)** 1D B_1 phase gradient. $|B_1|$ lies in between 1.00 and 1.25 within the target imaging volume, corresponding to refocusing flip angle of 160° at the center of coil, and 200° approaching the coil windings. The phase gradient is strongest centrally, decreasing in strength radially. For larger z offsets, the phase gradient is slightly stronger, while the B_1 uniformity is slightly worse, which is a commonly seen trade-off [25].

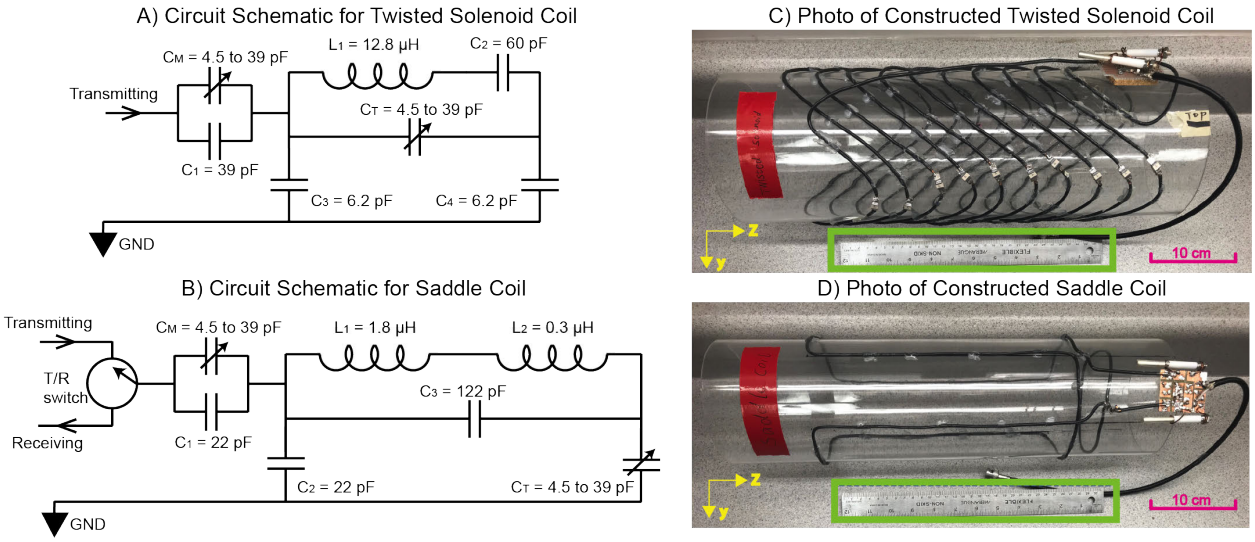

Figure 4.6: Photos of constructed coils and corresponding circuit schematics. **A)** Balanced circuit schematic for twisted solenoid coil. C_2 represents the value of ten capacitors in series with the long wire to mitigate wavelength effects; **B)** Balanced circuit schematic for saddle coil. L_2 denotes the extra circular wire loop on the coil right hand side, which can be adjusted for geometrical decoupling. Active T/R switch is also depicted in the schematic, showing that in TRASE experiment saddle coil is used as both transmitter and receiver; **C)** Photograph of constructed twisted solenoid coil; **D)** Photograph of constructed saddle coil. The saddle coil is at smaller size (O.D. of 5 inch), and nests inside the twisted solenoid coil (O.D. of 6 inch).

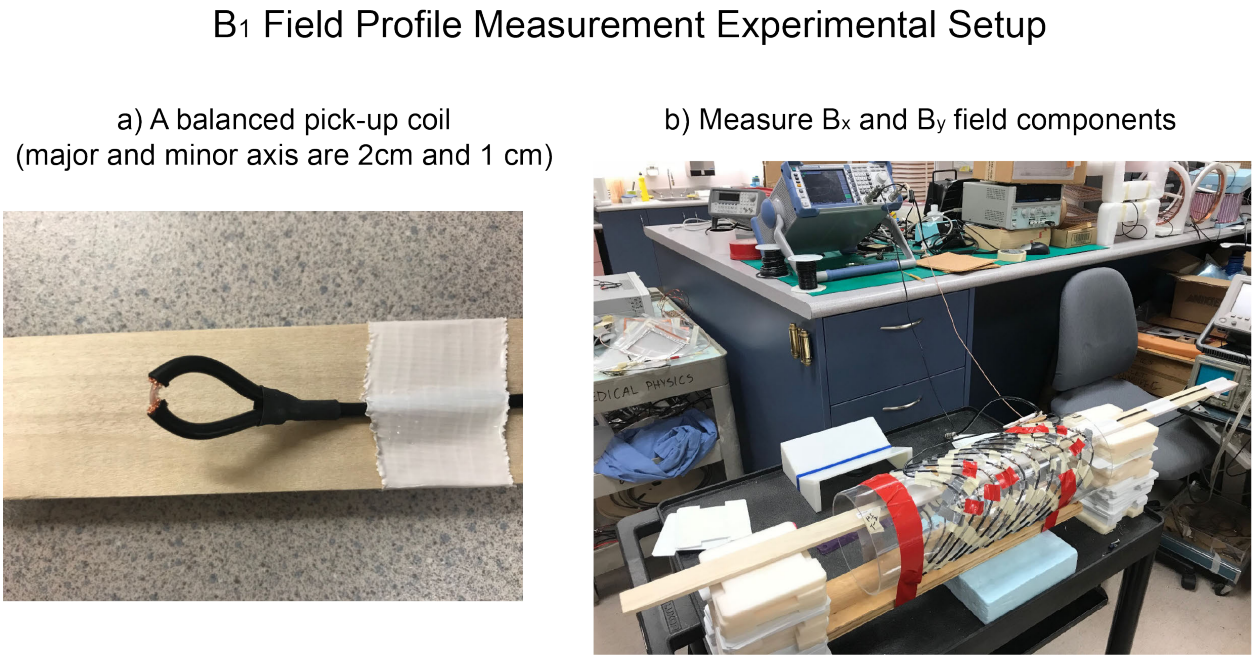

Figure 4.7: Photos of constructed small pick-up coil and the experimental setup for the measurements of B_1 field components B_x and B_y.

Signal	Power Gain From Measured Channel To Twisted Solenoid Coil	Peak-to-Peak Voltage Scope (50Ω)	Peak Power
Amplifier Forward Monitor	+40 dB	1.356 V	$P_{forward} = 45.97$ W
Amplifier Reflected Monitor	+40 dB	0.586 V	$P_{reflected} = 8.58$ W
Console input to RFPA	+64 dB	0.094 V	$P_{total} = 55.49$ W

Table 4.3: RF power measurements for twisted solenoid coil. The peak-to-peak voltage shown is for a 300 μs, 180° hard pulse.

4.4 Results

4.4.1 Coil Q and Power Results

Unloaded and loaded coil Qs was measured as $Q_{unloaded} = 390$ and $Q_{loaded} = 285$, respectively. The Q damping-ratio was $\zeta = Q_{unloaded}/Q_{loaded} = 1.37$. Within the magnet, with the NaCl doped phantom in position, the twisted solenoid coil was tuned to the resonant frequency f= 9.278 MHz, and matched to 50 Ω with $S_{11} = -22$ dB. For a single spin echo experiment, with a 300 μs, 180° hard pulse, the monitor peak-to-peak voltages were measured as $P_{forward}$ = 45.97 W, and $P_{reflected}$ = 8.58 W. For additional verification, the actual amplifier RF input power P_{input} was also measured using the scope. After amplification of +64 dB, the total output RF power generated from the amplifier was calculated as $P_{total} = 55.49$ W (see details in Table 4.3). The sum of $P_{forward}$ and $P_{reflected}$ 54.55 W agrees closely with this measurement. In conclusion, a power level at the coil of around 46 W is required to drive a 300 μs 180° hard pulse with a forearm-like phantom. Although the coil itself was well matched, the additional components between amplifier and coil (long (approx.) 5m cable, T/R switch) may have contributed to the reflected power.

4.4.2 Coil Field Plot Results

The measured coil field data including $|B_1|$, phase and phase gradient are shown in Figure 4.8 and Figure 4.9. The simulated data are also shown in each plot for comparison. Due to the relative large size of the pick-coil (major and minor axes of 2 cm and 1 cm, respectively),

it was impractical to measure the fields at the edges of the targeted imaging volume. Additionally, when measurements were made at $x \geq 3.0$ cm, a displacement of $y = 1.5$ cm was the furthest off-center point that could be evaluated due to the cylindrical geometry of the coil. Therefore for consistency between measurements, I restricted all manual bench measurements to $y \leq$1.5 cm. Data are shown for planes at $z = 0$ cm, 2.5 cm and 5 cm in the figure. Similar measured B_1 magnitude and phase results for planes z = -2.5 cm and -5.0 cm are not shown. The deviation between simulations and measurements were evaluated by comparing measured points with the corresponding value on the simulated curve. Maximum deviations for B_1 magnitude, phase and phase gradient were 3.2%, 3.4%, and 8.3%, respectively.

4.4.3 TRASE Imaging Results

The pairing of the twisted solenoid and the saddle coil enabled a one-dimensional TRASE encoding to be conducted. The twisted solenoid coil was designed for transmission only, whereas saddle coil was responsible for both transmission and receiving, controlled by an active T/R switch. A TRASE imaging experiment was performed using a bottle phantom of diameter of 4.7 cm, length of 8.0 cm, containing tap water. At the resonant frequency f = 9.278 MHz, with phantom and both coils in position in the magnet, the scattering matrix was measured as S_{11} (saddle coil) = -32 dB, S_{22} (twisted solenoid coil) = -33 dB, S_{12} (geometrical decoupling) = -31 dB. The one-dimensional TRASE sequence used 300 μs hard pulses for both excitation (90° pulse) and refocusing (180° pulses), with echo spacing time T_{sp} = 2000 μs, ETL = 128, and number of averages, NA = 1. For each spin echo 32 points were sampled at a receiver bandwidth of 100 kHz, using the mean of the middle 16 points to represent a single data point in k-space. The applied sequence, phantom and obtained 1-D TRASE profile are shown in Figure 4.10. The width of 1D phantom image profile was represented by 19 pixels, corresponding to a mean pixel size of 2.47 mm/pixel and a mean phase gradient of G_x = 5.69 deg/cm.

To investigate the clinical potentials of this new twisted solenoid coil, the 2D images for a single slice (10 mm thick) bovine tibia with a diameter of ∼45 mm was obtained by combining 1D TRASE and 1D conventional phase encoding (TR = 300 ms, TE = 20 ms, T_{sp} = 480 μs, ETL = 128, 64 PE, NA = 16, FOV = 10 cm, and receiver BW = 100 kHz). For comparison, a regular 2D B_0 gradient spin echo MR image was also acquired with nearly equivalent timing parameters: TR = 300 ms, TE = 23 ms, 64 PE, NA = 16, FOV = 10 cm, and receiver BW = 20 kHz. These results can be found in Figure 4.11. Clearly, both 2D images display similar internal structures of the object, while TRASE image is noisier due to the use of a five times larger receiver bandwidth.

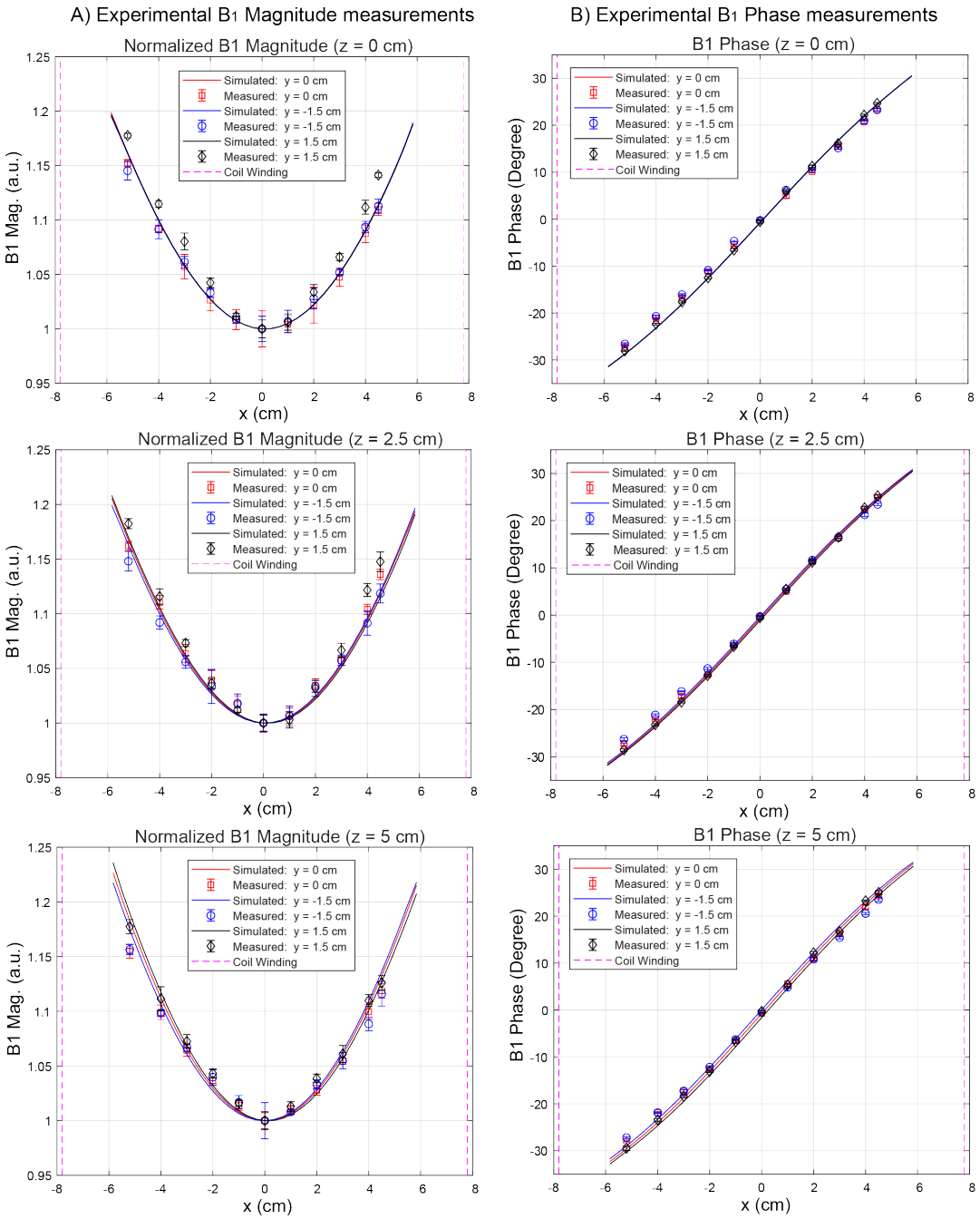

Figure 4.8: Experimental and simulated results for B_1 magnitude and phase. **A)** Comparison of simulated and measured B_1 magnitude along three different y lines on three transverse planes (z = 0 cm, 2.5 cm, 5.0 cm); **B)** Comparison of simulated and measured B_1 phase for the same locations as in A). The Biot-Savart simulated data are plotted in the figure as solid lines. The other two measured planes at z = -2.5 cm, -5.0 cm showed very similar results to these (not shown).

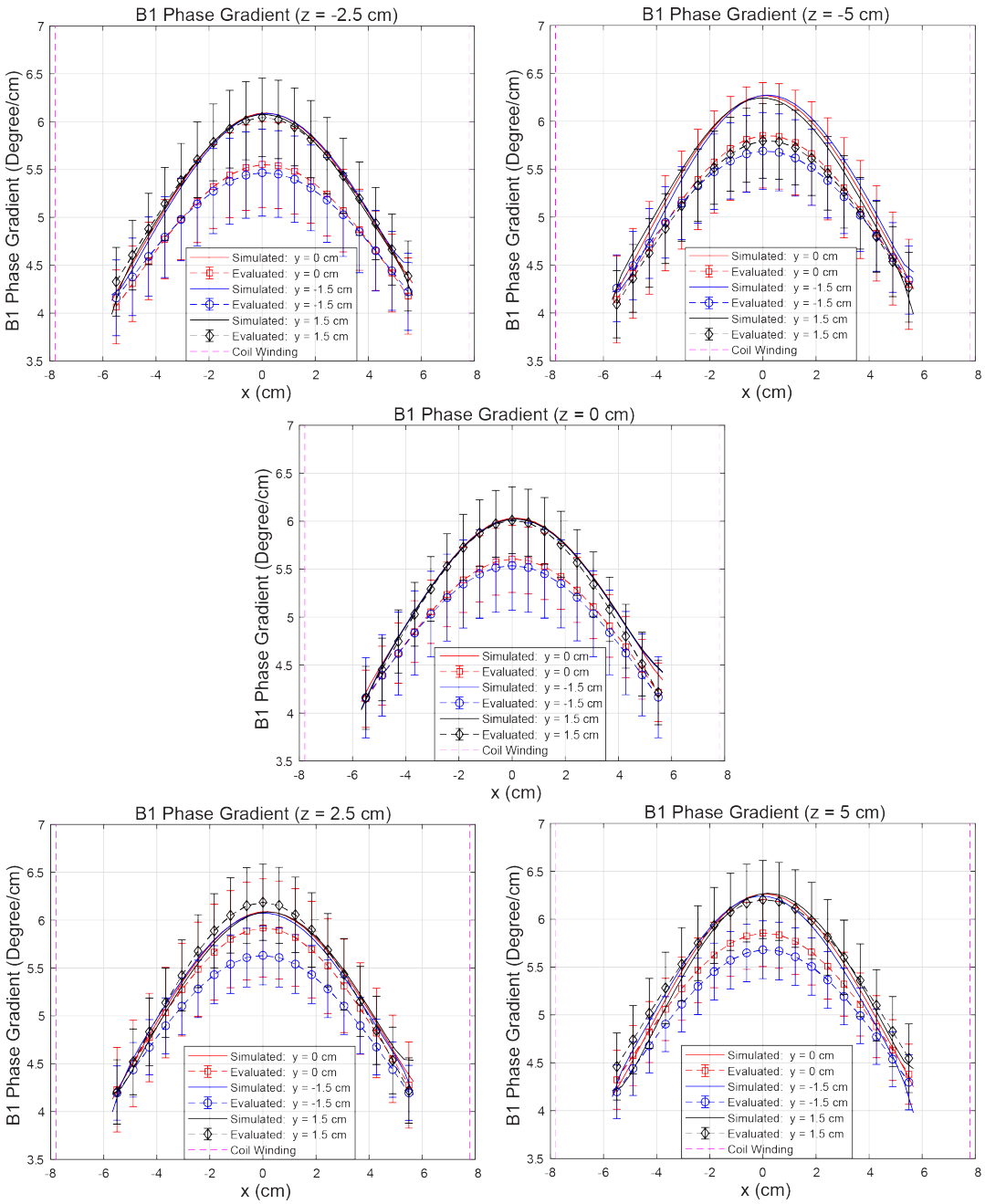

Figure 4.9: Bench measurement of B_1 phase gradient and simulation results. The Bio-Savart simulated and the measured B_1 phase gradients were both plotted for five z planes (z = -5.0 cm, -2.5 cm, 0 cm, +2.5 cm, +5.0 cm), and three y lines (y = -1.5 cm, 0 cm, 1.5 cm) on each plane. The measured phase gradient strength is equal to or lower than the simulation in all cases.

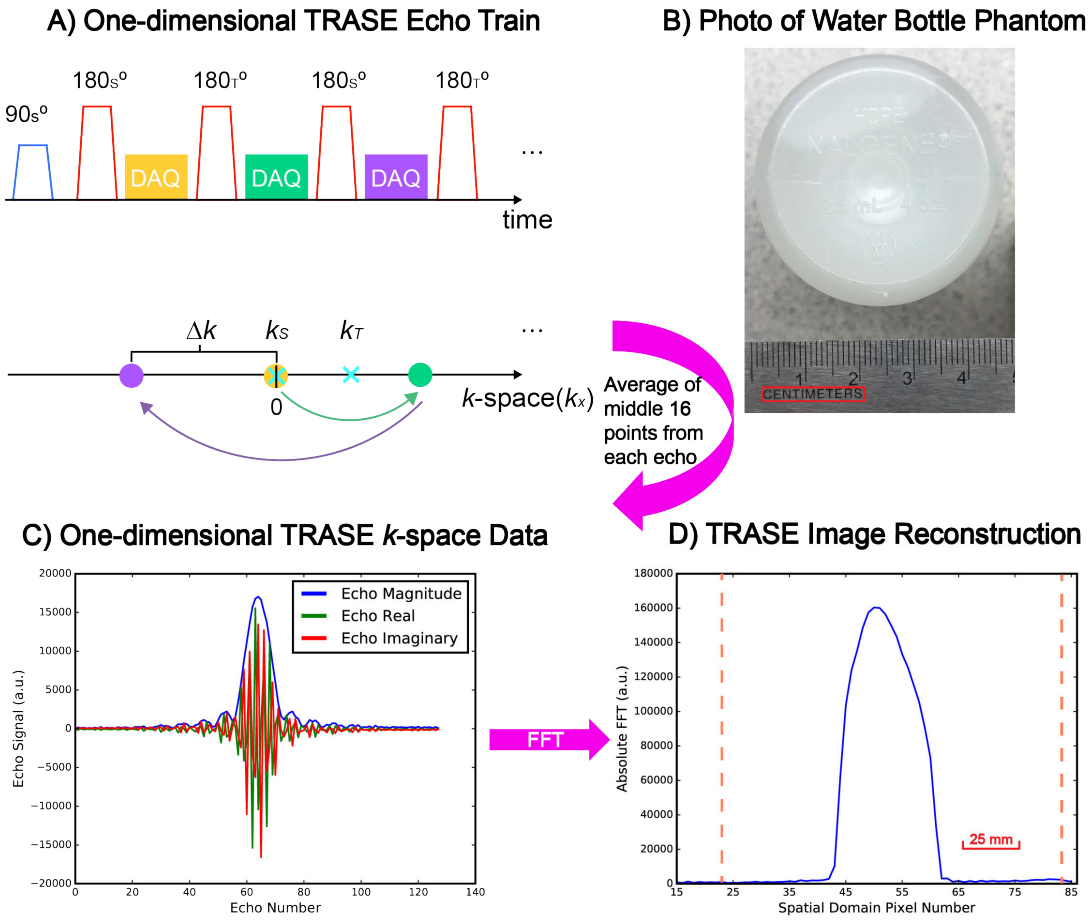

Figure 4.10: One-dimensional TRASE experiment **A)** 1D TRASE pulse sequence consisted of two groups of alternating refocusing pulses 180°_S and 180°_T, where S and T represent saddle and twisted solenoid coil, respectively. DAQ denotes the sampling of each echo between two adjacent 180° pulses. In k-space, each refocusing pulse activates a jump about the corresponding coil k-space origin (k_S and k_T). Note that the saddle coil produces a uniform B_1 field, i.e. zero phase gradient, hence the coil origin coincides with the origin of k-space. This pair of coils is sufficient to demonstrate the twisted solenoid coil's encoding capability. However, more efficient TRASE encoding could be achieved by using two twisted solenoid coils generating opposite phase gradients, which would double the k-space sampling interval Δk, providing higher resolution, for the same ETL. **B)** Imaged phantom filled with tap water. This cylindrical phantom has a diameter of 4.7 cm. The sequence parameters were NA = 1, T_{sp} = 2000 μs, pulse duration 300 μs for both excitation and refocusing pulses, readout 32 points at 100 kHz bandwidth, delays of 50 μs both before and after the refocusing pulses. **C)** Experimental acquired echoes along x axis. The echoes were re-ordered for display because the actual acquired echoes were in an order of $+k$, $-k$, $+k$,..., caused by the jump pattern in k-space. **D)** 1D TRASE image obtained from Fourier transform of acquired echoes in C). Based upon measurements, the pixel width was 2.47 mm while the FOV was 322 mm which covered the entire coil space. The coil position was also depicted here, indicated by dotted lines.

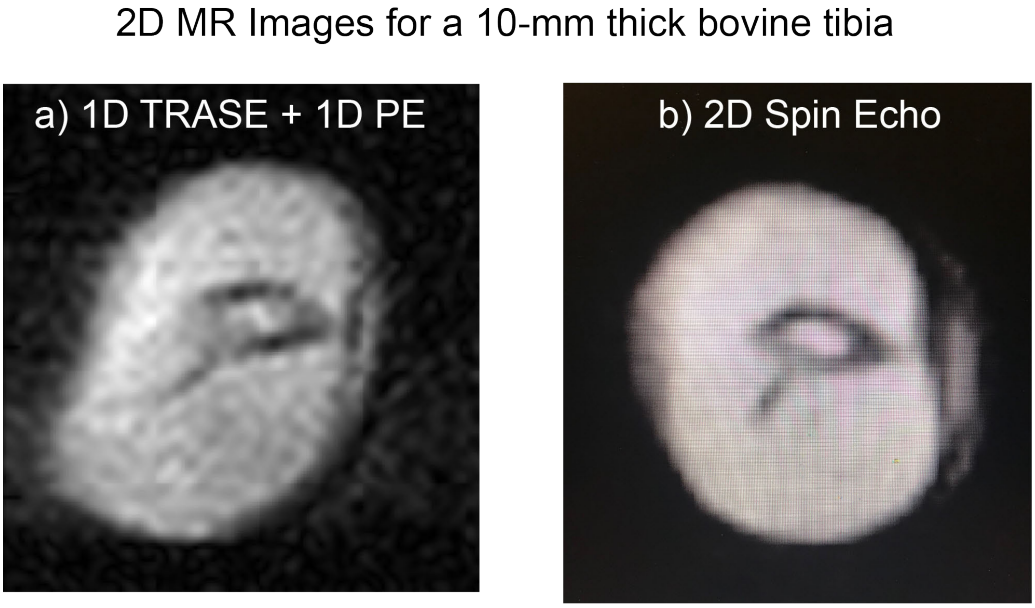

Figure 4.11: 2D MR experiments for a 10-mm thick bovine tibia slice, in a diameter of ∼45 mm **A)** 1D TRASE plus 1D conventional phase encoding, where the parameters are TR = 300 ms, TE = 20 ms, T_{sp} = 480 μs, ETL = 128, 64 PE, NA = 16, FOV = 10 cm, and receiver BW = 100kHz. **B)** 2D spin echo image acquired with parameters of TR = 300 ms, TE = 23 ms, 64 PE, NA = 16, FOV = 10 cm, and receiver BW = 20kHz. Although panel A is noisier due to larger receiver bandwidth, and is slightly distorted due to non-linear phase gradient strength, both images demonstrate very similar internal structures, demonstrating the use of TRASE for clinical *in vivo* applications.

4.5 Discussion

The B_1 magnitude measurements (Figure 4.8) agree closely with the Biot-Savart simulations, with no observable trend of deviation (largest deviation 3.2%). The phase plots also show close agreement (largest deviation of 3.4%), but with some discernible systematic deviation, as shown more clearly in the phase gradient plots, as discussed next. The measured phase gradient and the corresponding simulation results are shown in Figure 4.9. The simulated and measured data show good overall agreement with the strongest gradient strength appearing in the middle and decreasing radially. The largest point-to-point deviation is 8.3%. The B_1 phase plots in Figure 4.9 show that the measured B_1 phase gradients are either equal to or weaker than the simulations, but are generally within the error bars. For 4 out of 5 z planes (z = -5 cm being the exception), the y = 1.5 cm measured curve (black) showed the best match to the simulated curve. The measured data on these 4 z-planes presented similar trends for three y lines, with the phase gradient higher for y = 1.5 cm (black) than for y = -1.5 cm (blue). These discrepancies in the y-direction may have been caused by the straight return wire (see Figure 4.6) which could introduce an asymmetry in y-direction for the magnetic fields. The return wire path was not included in the simulations, because a long straight wire on the surface of a coil former generates a field $1/\pi$ smaller than that of a circular loop, at the location of the loop centre. However, it is preferable to include the return wire path by representing its location accurately in the future simulation. Other possible sources of discrepancy and measurement inaccuracy include imperfections in coil construction, the finite size of the pick-up coil, and the line of additional capacitors on one side of the coil.

An important aim of this work is to reduce the overall length of the echo train to reduce T_2 resolution loss. By the use of RF amplifiers allowing higher duty cycle, the 256 ms train duration used here could be significantly reduced (200 μs with two amplifiers, each operating at 25% duty cycle, yields 0.2 ms $\times$ 128 = 64 ms). To avoid resolution loss, as a rule-of-thumb,

the echo train should be no longer than 1.2 times the shortest T_2.

For a simple Fourier transform image reconstruction, the non-uniform magnitudes of the phase gradient will distort the resulting image due to variable spatial resolution, with the center of coil producing the highest resolution. However, since the variation of the phase gradient is known, based on the coil geometry, the image can be accurately reconstructed using other algorithms such as regularized least squares [47]. For future variants, it would be useful to study the design of the solenoid end turns to better control the coil length, while maintaining overall coil performance.

It can be concluded that Biot-Savart simulation is a good indicator for phase gradient generated by twisted solenoid coil, at relatively low operating frequency, although it cannot excluded regarding the possibility of deviation between the measured and simulated data based on the limits of the quasi-static approximation. Future full wave simulations and more precise control of coil construction may reduce this deviation.

The 1D TRASE imaging experiment resulted in a mean spatial resolution of 2.47 mm/pixel, corresponding to a measured mean phase gradient of $G_x = 5.69$ deg/cm, over the 4.7cm diameter of the bottle phantom. This is in close agreement with both the mean phase gradient from simulation of 5.79 deg/cm, (Figure 4.3), and also with bench measurements of 5.58 deg/cm (Figure 4.9) over the same region. These correspond to deviations of 1.8% and 2.0%, respectively.

In this work, the refocusing pulse applied in the measurement was 300 μs, which required a peak RF power at the coil of 46 W. Although it is difficult to make a direct comparison with previously reported results for other coil geometries because of variations in geometry, construction and RF power, the solenoid is an inherently power-efficient and space-efficient design, putting clinical resolution imaging with practical RF power levels and compact magnets within reach.

4.6 Conclusions

The main purpose of this project has been to introduce and evaluate the twisted solenoid coil relative to previously published designs of TRASE phase gradient encoding coil, most notably the rectangular Helmholtz-Maxwell coil array [25]. The twisted solenoid coil has a large number of attractive characteristics, inherited from the venerable solenoid coil, including the efficient generation of a large cylindrical volume of uniform B_1 field. Geometrically, the cylindrical twisted solenoid coil is compact, offering an open unobstructed aperture, a large fraction being usable as the imaging volume. The cylindrical outer shape is particularly advantageous for cylindrical Halbach-style permanent magnets, relative to the rectangular Helmholtz-Maxwell design.

For the twisted solenoid design, since the entire phase gradient field is produced by a single current path, the phase gradient strength and $|B_1|$ field homogeneity is reliably known and not subject to experimental perturbation. In contrast, the Helmholtz-Maxwell designs require current balancing between parallel elements, which must be simultaneously resonant, while remaining decoupled. However, by control of the current ratio the Helmholtz-Maxwell designs do offer the possibility of varying the gradient strength (albeit also the homogeneity), which might be useful in some applications.

The twisted solenoid phase gradient direction can be set to any transverse direction by rotating the coil about the cylindrical axis, remembering that a 1 degree rotation of the coil rotates the gradient direction by 2 degrees. Therefore the four phase gradient fields necessary for 2D encoding $(+G_x, -G_x, +G_y, -G_y)$ could be produced by a set of four concentric cylindrical twisted coils, each oriented at different rotation angles about the patient axis (z). This capability to rotate the gradient direction by simple coil rotation is not possessed by any other phase gradient coil design. Practical implementation of a multi-coil gradient set would require isolation between elements, which can be achieved by the use of PIN diode switches [17] to disable inactive elements.

4.7 Acknowledgements

This work is supported by the University of Alberta, Cross Cancer Institute, and Natural Sciences and Engineering Research Council (NSERC Grant/Award Number: RGPIN-2016-05183). I would like to thank Dr. Vyacheslav Volotovskyy, Dr. Nicola De Zanche, Mr. Aaron Purchase and Mr. Radim Barta for the valuable comments and advice.

Chapter 5

Two Coils - A Geometrically Decoupled Twisted Solenoid Coil Pair for High Resolution 1D Imaging [1]

5.1 Introduction

5.1.1 The Rationale for Combining a Pair of Twisted Solenoid Coil

The twisted solenoid, as introduced in Chapter 4 is a new category of TRASE RF coil which significantly expands the capabilities of TRASE MRI [13], [53], [61]. This type of coil has many advantages including high efficiency, reliable B_1 field, the generation of phase gradient along any transverse direction, and a large imaging volume within a compact cylindrical geometry. Since twisted solenoids are variants of regular solenoids, they inherit their advantages including high filling factor and optimal sensitivity [3]. The longitudinal B_1 field generated by solenoids is suitable for vertical or transverse B_0 field orientations [62], including Halbach array permanent magnet ring designs. In the low-field regime (commonly employed in TRASE MRI due to SAR limitations), the relatively low self-resonance frequency of twisted solenoid is not problematic.

[1] The materials in this chapter have been published in the journal of *Magnetic Resonance in Medicine* [16].

In the last chapter 1D TRASE MR phantom experiments were performed by transmitting refocusing pulses alternatively between a twisted solenoid, producing a non-zero phase gradient $\mathbf{G}_t = 2\pi\mathbf{k}_t$, and a saddle coil generating a uniform B_1 field, *i.e.*, a zero phase gradient $\mathbf{G}_s = 2\pi\mathbf{k}_s = 0$, see Figure 5.1. The achieved pixel size was reported as approximately 2.5 mm/pixel for a train of 128 echoes, with pulse duration 300 μs and echo spacing 2000 μs. High spatial frequency k-space points are always acquired toward the end of the echo train, so during a long echo train, T_2 decay can cause image blurring. Since 1D TRASE spatial resolution is inversely proportional to k-space traversal coverage, *i.e.*, the product of echo train length (ETL) and step size $\Delta x = 1/|2ETL \cdot (\mathbf{k}_t - \mathbf{k}_s)|$ [20], an obvious approach to double k-space coverage (and so reduce T_2 blurring) is the replacement of the saddle coil with a second twisted solenoid coil, generating the opposite phase gradient, *i.e.*, $\mathbf{G}_{t'} = -\mathbf{G}_t$. However, strong inductive coupling arises from this geometry in which the two concentric twisted solenoids almost act like a transformer. Without adequate decoupling the mutual inductance will cause a split in the resonance for each coil, and also during transmission one coil will induce current in the other, creating secondary magnetic fields that add or subtract from the primary B_1 field, impairing the experiment.

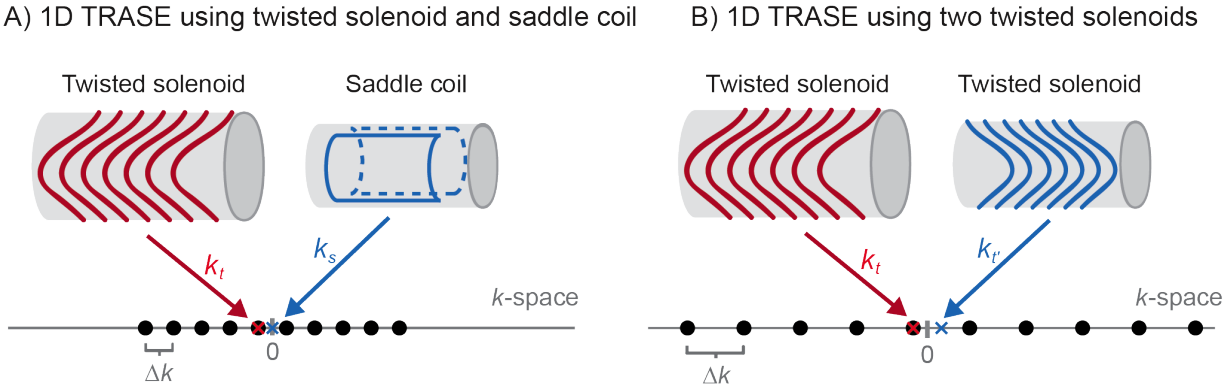

Figure 5.1: Illustration of 1D TRASE encoding using different coil pairs. **A)** one twisted solenoid and one saddle coil. The twisted solenoid generates a non-zero phase gradient corresponding to a non-zero coil origin $\mathbf{k}_t$ in k-space [13]. The saddle coil produces a uniform B_1 field, hence $\mathbf{k}_s = 0$. The line plot below shows k-space coverage for a train of 10 echoes (black dots). **B)** two twisted solenoids. The second twisted solenoid (blue) generates an opposite phase gradient and is represented as $\mathbf{k}'_t = -\mathbf{k}_t$ in k-space. For the same echo train of 10 echoes, a double k-space coverage is achieved, as the step size Δk is doubled.

5.1.2 Overview of TRASE Array Decoupling Techniques

For TRASE MRI, a high level of control of the RF transmit fields is central, imposing a requirement for coil isolation. Depending on the coil geometry and driving configurations, different approaches have been proposed. Active PIN diode controls have been commonly used in the TRASE literature, including spiral birdcage pair [20], Helmholtz-Maxwell pair [17], [19], [25], and the combination of these two types [20], [24]. Stockmann [11] applied a toroidal transformer to cancel the mutual inductance between Birdcage-Maxwell coil pair, while I myself [13] utilized the inherent orthogonal B_1 field between saddle and twisted solenoid for 1D TRASE encoding.

The strong coupling between concentric solenoids can place a significant demand on the design of active decoupling circuitry, due to high induced RF voltages [17]. Prior to embarking on the geometric decoupling technique which will be introduced in details within this chapter, I have spent several months testing some common decoupling techniques including toroidal transformers and active PIN diode switch, however, neither of them provides a reliable solution (see pictures of these "failure attempts" in Figure 5.2). For example, the strong coupling between a pair of twisted solenoid requires a very bulky toroidal transformer (like an actual donut) to achieve effective decoupling. This transformer is not only awkward to construct, it is also physically connected to the pair of twisted solenoid, preventing any flexible rotations and movements that may need for multi-dimensional TRASE encoding in the future development that will be introduced in the next chapter. The use of active PIN diode can complicate coil circuitry, and another technical challenge of active switching at low RF frequencies is avoidance of interactions, such as noise and switching transients, between the RF and switching circuits, which operate in close frequency ranges. Additionally, diode losses may cause quality factor (Q) loss and heating. Use of geometric decoupling would allow the elimination of PIN diode control and power subsystem, which would be advantageous for low-cost MRI applications. A sub-μs RF switch for low-field TRASE MR was proposed recently in 2020 [42], demonstrating a promising fast switch design based upon MOSFET.

Unfortunately, this article was not accessible and not demonstrated for the frequency in MHz range, when I was conducting the research project reported in this chapter.

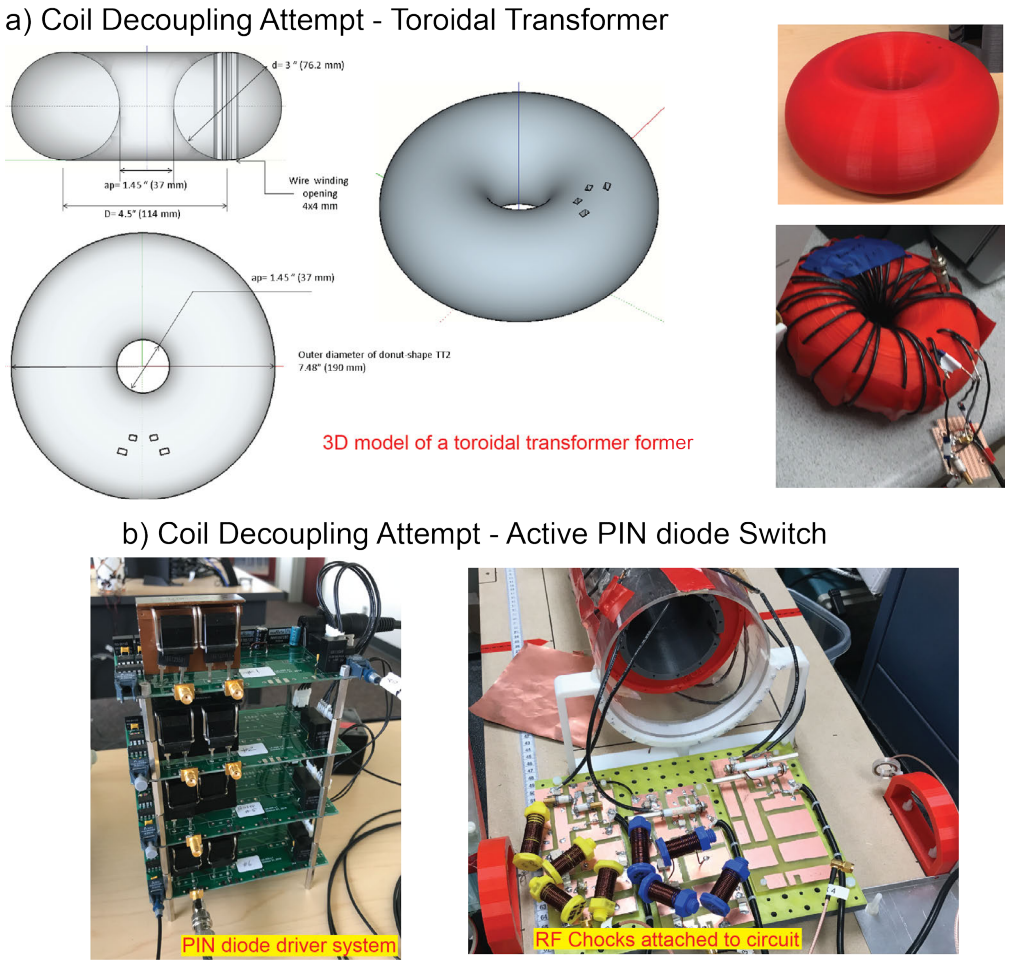

Figure 5.2: Pictures of two attempts to decouple a pair of twisted solenoids. **a)** A 3D printed toroidal transformer was made to decouple a pair of twisted solenoids. The dimensions of toroidal was determined based upon the mutual inductance between the twisted solenoid pair, and yielded a very bulky design like a donut. **b)** Another attempt was made to use a co-author work [17] - A PIN diode switch. This design complicates coil circuitry (*e.g.*, additional RF chocks) and system requirement (*e.g.*, need to use optical signals). In summary, neither of these two offered a reliable solution for twisted solenoid pair decoupling.

5.1.3 Decoupling Approaches for Concentric Solenoids

The strong mutual inductance between two coaxial solenoids have been analytically studied [63]–[67]. In 1946, in the famous nuclear induction experiment [26], Bloch achieved a good isolation between two solenoidal RF coils using orthogonal placement to reduce mu-

tual inductance, however, this configuration is not applicable for the requirement of coaxial placement. Also, the strategy to reduce mutual inductance between neighboring elements by adjusting the overlap region [68] is also not applicable. The low-impedance preamplifier decoupling approach [68] and digital post-processing techniques [69] can reduce mutual coupling in receiver arrays, but not applicable to transmit arrays [70], [71]. Shielded array designs [72] and capacitive or inductive networks [73]–[77] are also available, but typically require additional space or physical connections between coils, precluding independent functioning of each coil and for cylindrical array coils, critically decreasing the usable imaging volume [72]. Although some recent work has demonstrated effective decoupling techniques without physical connection between RF array elements, using induced current compensation or elimination [78]–[80], or even self-decoupled RF coils [81], these methodologies are more applicable to surface coils rather than volume coils.

In this chapter I will show that by adding extra regular (*i.e.*, untwisted) solenoidal extensions of the same diameter as each twisted solenoid (illustrated in Figure 5.3), it is practical to geometrically decouple a pair of twisted solenoid coils for high resolution 1D TRASE encoding. Since no electrical connection exists between the decoupled coils, the proposed configuration avoids obstructing the bore and importantly, also maintains independence of each coil. This is a more flexible arrangement than a toroidal transformer, allowing ready experimentation with different coil configurations and orientations.

5.2 Theory

5.2.1 Mutual Inductance

The mutual inductance M between two inductors is defined as the ratio of the electromotive force (EMF) induced in the second inductor to the rate of change of current $\Delta I/\Delta t$ in the first inductor:

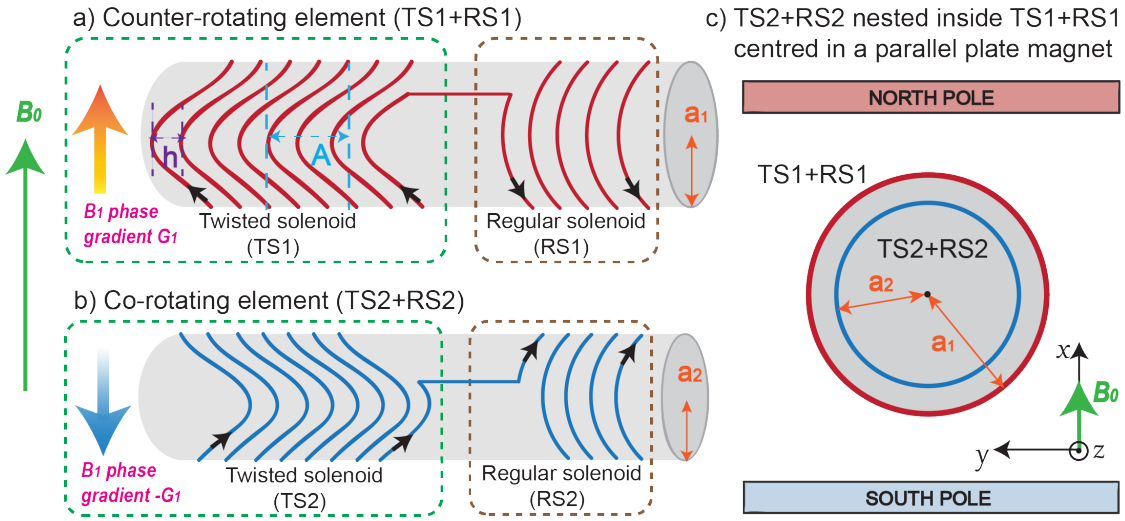

Figure 5.3: Schematic of a geometrically-decoupled twisted solenoid pair, containing two coil elements: **a)** counter-rotating element (TS1+RS1), consisting of a twisted solenoid (TS1) and a regular solenoid (RS1) with opposed currents, and **b)** co-rotating element composed of a smaller twisted solenoid (TS2) and a regular solenoid (RS2) with current in the same direction. **c)** coil pair geometry for an MRI experiment: the smaller (TS2+RS2) is nested inside (TS1+RS1) concentrically. The inner element is rotated by 90° relative to the outer to generate the opposite B_1 phase gradient.

$$EMF = -M\frac{dI}{dt} \tag{5.1}$$

The mutual inductance M may be either positive or negative depending on the polarity of the mutual voltage in reference to the direction of the inducing current [82], *i.e.*, change the winding orientation of one coil results in a sign change of mutual inductance.

The coupling coefficient k is a convenient measure of inductive coupling, where $k = 0$ indicates no inductive coupling, and $|k| = 1$ indicating full inductive coupling. k is related to mutual inductance, M, and self inductances, L_1, L_2, as follows:

$$k_{12} = \frac{M}{\sqrt{L_1 L_2}} \quad \text{where} \quad -1 \leq k \leq 1 \tag{5.2}$$

Although many formulae exist for the self and mutual inductance of two coaxial regular solenoids [63]–[67], none is available for the twisted geometry. The high k_{12} value expected for two coaxial twisted solenoids is illustrated in Figure 5.4a. For this example (radii 7.8

cm and 4.9 cm; lengths 40.25 cm and 21.75 cm), no relative shift along z axis, the coupling coefficient is $k_{12} = 0.221$, and both coils exhibit a split resonance peak (see Figure 5.4c).

5.2.2 Geometrically-decoupled Twisted Solenoid Pair

Su et al. [62] proposed a geometrically-decoupled two-element solenoidal array in which one element contains a counter-rotational solenoid section(s) to cancel the mutual inductance. Although designed for RF reception, the concept is applicable to the TRASE RF twisted solenoid array. The concept is illustrated in Figure 5.3 in which two twisted solenoids TS1 and TS2 with radii of a_1 and a_2 ($a_1 > a_2$) are oriented with a relative 90° rotation shift, generating two opposing phase gradients (a 1° rotation of the coil rotates the phase gradient direction by 2°) [13]. Two additional regular solenoid extensions RS1 and RS2 are connected in series with their corresponding twisted solenoids on the same coil former. The counter-rotating element (TS1+RS1) has solenoids connected in a reverse geometry such that the currents counter-rotate, while for the (TS2+RS2) element the currents co-rotate. The smaller element (TS2+RS2) is nested inside (TS1+RS1). In this configuration, the mutual inductance between the twisted solenoids is compensated by an opposite mutual inductance generated by the regular solenoids such that the pair of combined coils (TS1+RS1) and (TS2+RS2) present a low k value, signifying geometric decoupling.

5.3 Methods

In overview, the approach to demonstrate feasibility of geometric decoupling was as follows: 1) design two twisted solenoid coils using the previously described method in Chapter 4; 2) connect a regular solenoid in series with each twisted solenoid, with geometric parameters determined to minimize the mutual inductance between the pair; 3) verify that any deleterious effects on TRASE encoding performance due to the regular solenoids are at an acceptable level.

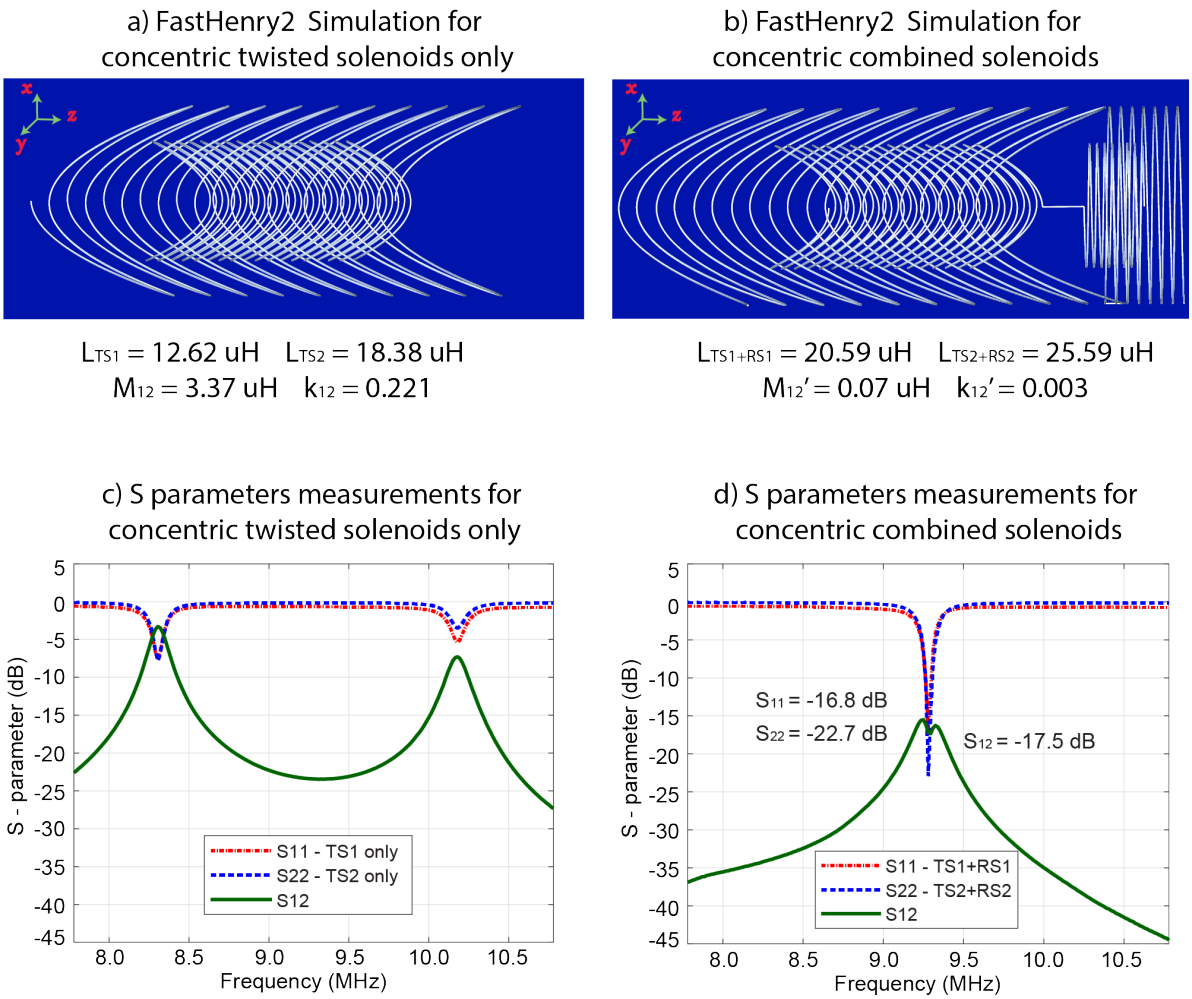

Figure 5.4: Coil coupling simulation and S parameters bench measurements. **a)** *FastHenry2* simulation of concentric solenoids TS1 and TS2, with no longitudinal z offset applied. The coupling coefficient $k_{12} = 0.221$ was calculated using simulated self- and mutual- inductances listed in the figure. **b)** The same *FastHenry2* simulation was performed when two regular solenoids RS1 and RS2 are attached. The nested TS2+RS2 coil was shifted along z axis by +2.0 cm to reduce the mutual inductance to its minimum, producing a coupling coefficient $k'_{12} = 0.003$. Panels **c)** and **d)** show bench S parameter measurements corresponding to coil configurations **a)** and **b)**, respectively. Resonant frequency split and strong interaction (high S_{12} value) observed in **c)** are remedied by the attached regular solenoids, resulting in no observable resonant frequency split and acceptable isolation S_{12} = -17.5 dB.

5.3.1 Coil Design Procedure

In previous study [13] the twisted solenoid geometry is characterized by the following coil geometric parameters (see Figure 5.3): a - coil turn radius, A - modulation amplitude, h - pitch, and N - number of turns. For a regular solenoid coil, the modulation $A = 0$. Therefore, the entire design starts with a search procedure for optimal geometric parameters for the two twisted solenoids, followed by the determination of geometries for the two attached regular solenoids aiming at minimizing mutual inductance.

B_1 field evaluation

To investigate potential B_1 field distortion introduced by the attached solenoids, numerical Biot-Savart simulations using the *BSMag* MATLAB package [57] were performed. The conductor was segmented into 720 straight-line current segments per turn, with assumptions: 1) that the coil wire is a single path; 2) that a quasi-static (DC) analysis is applicable at the low frequency of 9.28 MHz, *i.e.*, the current is in-phase. These assumptions were satisfied, with capacitors breaking up the long coil wire (see descriptions in Appendix II) such that each section is shorter than approximately a twentieth of an RF wavelength to reduce the current phase progression along the wire [4], [37]. I have previously verified the accuracy of Biot-Savart calculations for this regime [13].

Self- and Mutual- inductance simulation

To calculate self- and mutual- inductances, and resistances, the three-dimensional wire pattern coordinates generated from *BSMag* were input to the *FastHenry2* magnetoquasistatic approximation software [40], with each coil turn segmented into 720 rectilinear segments.

Since the operating frequency is relatively low (f = 9.28 MHz), in my simulation several assumptions were made that every segment carries a uniform current so the skin effect was not considered (see details regarding how to setup this simulation in Appendix II).

The conductivity of segment was specified to 5.8 $\times$ 10^4 [1/(mm*ohms)], corresponding to the conductivity of copper [40]. The (TS1+RS1) and (TS2+RS2) coils were simulated in a coaxial configuration, with a longitudinal shift (z axis) being the only free parameter available to minimize the mutual inductance, for a given group of four coils. An python code which makes *Fasthenry2* readable simulation file is appended for the curiosity of readers, as shown in Appendix II.

Specific design targets and constraints

Twisted solenoids: Two different twisted solenoid coils with radii a of 7.8 cm (TS1) and 4.9 cm (TS2) were designed with winding shifts ψ of 270° and 90° to generate $+G_y$ and $-G_y$ phase gradient, respectively [13]. The maximum coil length was specified as 45 cm and 30 cm for TS1 and TS2, respectively. The target imaging volume is dependent on coil radius and length, while the actual usable imaging volume is constrained by the smallest coil. The design task is to find optimal values for A, h and N as previously described [13], where I specified the cylindrical target imaging volume for each solenoid as follows: 1) radii of 4.7 cm (for TS1) and 2.9 cm (for TS2), equal to 60% of the diameter of the coil cylindrical former; 2) length of 10.0 cm (for TS1) and 8.0 cm (for TS2) along the z-axis (axial direction).

In the search procedures for both coils the range of modulation A and pitch h were from 1.0 cm to 10.0 cm with 0.5 cm increments, and number of turns N varied from 2 to 20. The acceptance criterion were: 1) B_1 field uniformity after normalization $|B_1|/|B_1min| \leq 1.25$ over the imaging target volume, corresponding to an effective flip angle range of 160° to 200°; 2) mean phase gradient strength over the imaging target volume greater than 5.0 deg/cm. All acceptable designs were then ranked based on the coil efficiency metric $\eta_{coil} = B_{1med} \cdot G_y$, where B_{1med} is median field magnitude, and G_y mean phase gradient strength, over the target imaging volume. The entire search procedure follows the same logic as introduced in Chapter 4.

Regular solenoids: Once the geometries of TS1 and TS2 were determined, two regular

solenoid coils RS1 and RS2 were specifically designed to decouple this twisted pair. To simplify construction and maintain independence of each combined coil, the radii for RS1 and RS2 were constrained to match TS1 and TS2, *i.e.*, $a = 7.8$ cm for RS1 and $a = 4.9$ cm for RS2. Therefore, only the pitch h and the number of turns N were adjusted to minimize the mutual inductance. The maximum coil length for (TS1+RS1) and (TS2+RS2) was set to 50 cm and 40 cm, respectively.

5.3.2 Coil Construction

Instead of using transparent acrylic tube as the coil former, this time all new coils were wound with solid 12 AWG hookup wire (Digikey) upon grooved 3D printed polylactic acid (PLA) formers. Formers were designed using 3D parametric modeller SketchUp 2014 (Trimble Inc., Sunnyvale, CA) to create stereolithography (STL) fabrication files. From the STL, G-code (RS-274) was generated using open source slicer software (Ultimaker Cura, Netherlands) and transferred to fused deposition modelling (FDM) 3D printers at a resolution of 100 μm (JG Aurora A5, Shenzhen Aurora Technology Co., Ltd, China). The detailed description of printing parameters is provided in Appendix II. Due to a printer height constraint of 30 cm, the longer formers were printed in two parts then welded with a soldering iron. The coil former weights are about 0.92 kg for TS1, and 0.64 kg for TS2 coil alone, as estimated by the slicer software.

For both combined coils, a balanced tune and matching circuit as described in [13], [37] was used. To improve decoupling performance and to mitigate coil ringing, a 40 Ω Q-damping resistor was connected in series with (TS2+RS2) coil. Stands were printed for each coil to set correct height and rotation angle and to allow mm-level axial positional adjustments for fine tuning of decoupling. It was necessary to connect each coaxial coil cable to a common ground at the Faraday cage, however, cable traps were found not to be necessary.

5.3.3 Coil Performance Measurements

The self-inductance of each coil were measured by resonating with a known reference capacitor (tolerance 5%), and compared with the self-inductance simulations from *FastHenry2*. The bench S-parameters (S_{11}, S_{22} and S_{12}) between coil pair (TS1, TS2), and (TS1+RS1, TS2+RS2) were measured using a vector network analyzer (Agilent Technologies E5061A). To assess the impact of the added solenoids, for resonators TS1 alone, TS2 alone, and combined elements (TS1+RS1), (TS2+RS2), loaded and unloaded Q were measured using two small balanced search loops connected to a 50 Ω network analyzer, where the loading phantom was a cylindrical bottle doped with 61.6 mM NaCl and 7.8 mM $CuSO_4$, of a radius of 3.5 cm and length of 14 cm (see pictures in Figure 5.5).

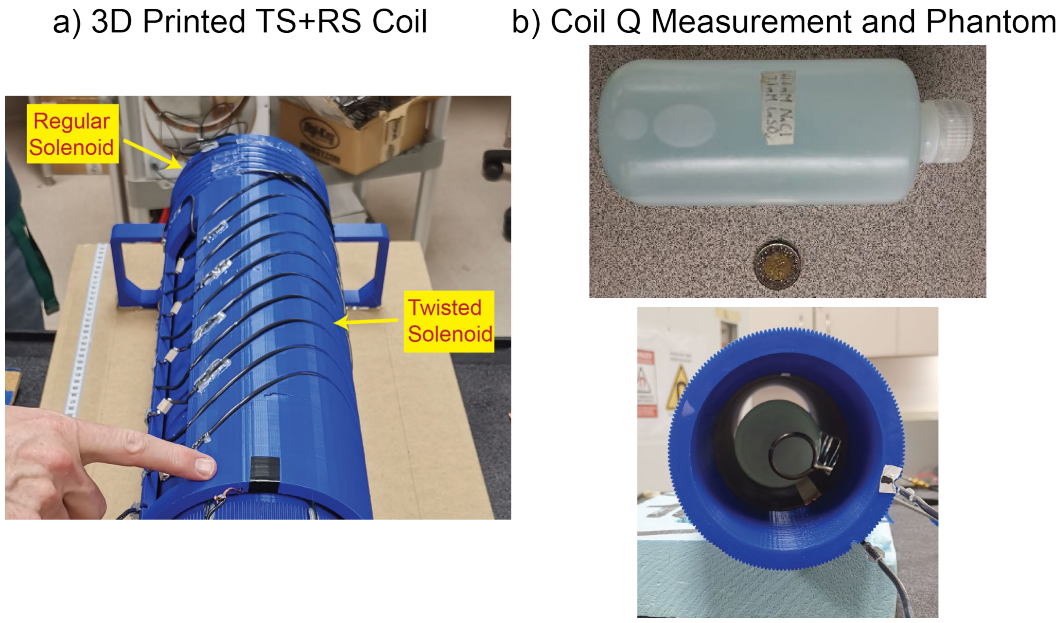

Figure 5.5: The 3D printed coil construction and quality factor Q measurement. **a)** The constructed TS1+RS1 is shown in the picture. **b)** The loading phantom and Q measurement using search pick-up coils.

5.3.4 TRASE MRI Experiments

A co-author work has demonstrated that 1D TRASE encoding performance can be improved if a XY-4 phase scheme is applied. The idea of XY-4 sequence introduces a 90° phase

difference between two successive refocusing pulses to compensate errors for both components of the transverse magnetization under conditions of $|B_1|$ inhomogeneity (details can be found in [83]). Here, single-axis TRASE encoding, using the XY-4 phase scheme, was performed using a 1D phantom with six 3 mm wide slots, 3 mm gap, 6 mm depth, 20 mm length, filled with tap water. Parameters were as follows: pulse duration $T_p = 200$ μs, echo spacing $T_{ep} = 800$ μs, echo train length (ETL) of 512, repetition time TR= 6 s, 32 averages. Each k-space point was the average of 8 points collected at 40 kHz bandwidth. Within the usable cylindrical imaging volume (radius 2.9 cm, length 8 cm), 1D TRASE profiles were measured for five z planes (z = -4 cm, -2 cm, 0 cm, +2 cm, +4 cm), and along three x lines (x = -2 cm, 0 cm, +2 cm) within each plane.

To evaluate the efficiency and imaging capability, a 2D T_2 phantom, total cross-section 6cm by 6cm, with multiple doped vials (various T_2 values listed in Table 5.1) was imaged by combining y axis 1D TRASE encoding with 1D B_0 phase encoding along either x or z axis (phase encoding duration 9 ms, FOV = 150 mm, steps = 128), without slice selection. TRASE parameters for 2D imaging were as for 1D, except: $ETL = 128$, $NA = 1$, repetition time $TR = 4$ s.

All MRI experiments were performed on a 9.28 MHz vertical B_0, shimmed 4-poster planar permanent magnet. The MRI system was controlled by an NRC TMX research console [60] configured to drive two independent transmit amplifiers and utilizing a single receive channel. In the single-axis TRASE encoding experiment, the (TS1+RS1) coil was driven by an AN8110 RF Amplifier (Analogic Corp MA, USA), and the (TS2+RS2) coil by a Tomco model BT00500 RF amplifier (Tomco Technologies, Australia). To drive both coils at a higher duty cycle, in the two-dimensional experiment a custom-made RF power amplifier system (see details in a co-author article [84]) which was capable of providing sequential operation of two RF output channels, up to 1 kW per channel, 50% RF duty cycle, +60 dB gain per channel, was implemented. In all experiments less than 200 W peak RF power was used.

Vial Letter	Diameter (cm)	Length (cm)	T_2 (ms)
A	2.8	6.0	Empty
B	2.8	6.0	35
C	1.1	4.5	600
D	2.8	6.0	280
E	2.8	6.0	17
F	3.2	6.8	600

Table 5.1: Multi-vial phantom size and the content T_2 value.

Coil Name	Radius a (cm)	Modulation A (cm)	Pitch h (cm)	Turns N	Mean B_1 phase gradient G_y (deg/cm)	Median B_1 field strength per unit current B_{1med} (μT)	Coil efficiency η_{coil} ($\mu T \cdot$ deg/cm)
TS1	7.8	5.5	3.0	10	5.26	37.07	194.99
RS1	7.8	0.0	0.9	7	N/A	N/A	N/A
TS2	4.9	2.5	1.0	17	6.16	106.68	657.28
RS2	4.9	0	0.6	8	N/A	N/A	N/A

Table 5.2: Optimal coil geometries for twisted and regular solenoid coils. TS1 and TS2 geometries were selected based on coil efficiency metric η_{coil} (based on Biot-Savart simulation of magnetic field only). RS1 and RS2 geometries were chosen to maximize geometric decoupling.

5.4 Results

5.4.1 Coil Geometric Parameters and Decoupling

The geometric parameters for the four coils are tabulated in Table 5.2. The TS1 and TS2 coil geometries shown passed all design targets and constraints, and yielded the highest coil efficiency (on the basis of Biot-Savart simulations). Since the purpose of the regular solenoids is to minimize the mutual inductance, coil efficiency parameters are not included. In the theory section it has been shown that the strong inductive coupling ($k_{12} = 0.221$) and resonant frequency splitting presented between two concentric twisted solenoids alone, as shown in Figure 5.4a and Figure 5.4c. When RS1 and RS2 were added to the simulation, with relative longitudinal shift $z = 2.0$ cm between two combined coils, the coupling coefficient reduced to minimum $k'_{12} = 0.003$, as illustrated in Figure 5.4b. This geometrically-decoupled coil configuration was verified using S-parameter bench measurements (see Figure 5.4d), where

Coil configuration	Measured self-inductance (μH)	Simulated self-inductance (μH)	$Q_{unloaded}$	Q_{loaded}	Damping ratio $\zeta = Q_{unloaded}/Q_{loaded}$
TS1	12.8	12.62	165	138	1.20
TS1+RS1	20.7	20.59	152	131	1.16
TS2	18.9	18.38	76	51	1.49
TS2+RS2	25.7	25.59	68	44	1.55

Table 5.3: Coil performance evaluations. Self-inductances of each coil were simulated using *FastHenry2*, and measured with known value capacitors. For loaded Q measurements a cylindrical bottle doped with 61.6 mM NaCl and 7.8 mM $CuSO_4$, at a radius of 3.5 cm and length of 14 cm was used.

both coils were functioning without resonant frequency split, with an acceptable isolation of S_{12} = -17.5 dB.

Coil self-inductance results and Q measurements are summarized in Table 5.3. The simulated *FastHenry2* and measured self-inductances for all configurations show close agreement, with a maximum deviation of 2.7%. Unloaded and loaded Q for each coil configuration were measured, followed by an estimation of coil damping ratio $\zeta = Q_{unloaded}/Q_{loaded}$. All reported results include a 40 Ω resistor added to TS2. The addition of regular solenoids resulted in an ζ reduction for TS1 solenoid by 0.04, and an ζ increment of 0.06 for TS2 solenoid, indicating only a minor impact on coil losses.

5.4.2 B_1 Field Calculation

B_1 magnitude and phase maps from analytical Biot-Savart calculations are shown for TS1 (Figure 5.6), and TS1+RS1 (Figure 5.7) over three transverse planes (z = -5 cm, 0 cm, +5 cm).

With the addition of RS1, B_1 phase gradients are still well generated over all evaluated planes, and B_1 magnitude inhomogeneity remains within the criteria $1.00 \leq |B_1| \leq 1.25$. Similar results are seen for the smaller twisted solenoid (see Figure 5.8), over planes z = -4.0 cm, 0.0 cm, +4.0 cm.

2D B_1 magnitude perturbation and B_1 phase distortion due to the attached regular solenoid

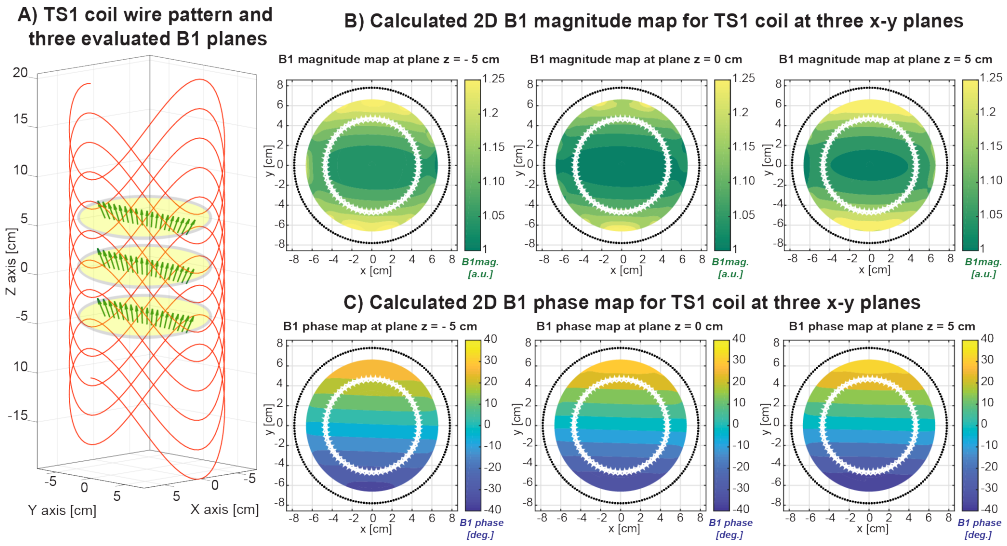

Figure 5.6: B_1 field plots using Biot-Savart calculations for TS1 coil. **A)** TS1 wire pattern (red), showing three evaluated B_1 planes located at z = -5.0 cm, 0 cm, 5.0 cm (yellow plane). To illustrate the phase gradient, B_1 field vectors (green arrows) are plotted along the y-axis for each plane. **B)** 2D B_1 magnitude map. **C)** 2D B_1 phase map at three evaluated planes, showing coil winding (black dotted line) and target imaging volume (white pentagram line). Within the target imaging volume (60%), B_1 phase gradients along y axis are created, where $1.00 \leq |B_1| \leq 1.25$.

coils are evaluated in Figure 5.9 for RS1, and in Figure 5.10 for RS2.

The main impact is on the planes closest to the attached solenoid. For TS1, plane z = 5.0 cm exhibits maximum 3.7% and 4.6° deviations for B_1 magnitude and phase; while for TS2, plane z = 4.0 cm shows smaller maximum deviations of 2.0% and 1.7° for B_1 magnitude and phase.

In Figure 5.11, simulated field data are shown along the central gradient axis (x = 0), for three transverse planes, with and without the attached solenoid. Due to the finite coil length, there are some B_1 field variations between the different transverse planes.

The effect of RS1 is to increase $|B_1|$ inhomogeneity but also the phase gradient strength of TS1, in the region close to RS1. Before attachment, the phase gradient strength ranged non-linearly between 4.3 to 6.8 deg/cm, however, following the addition of the counter-rotating RS1 coil, gradient strength increase to 4.4 to 8.3 deg/cm, see Figure 5.11(I). The phase

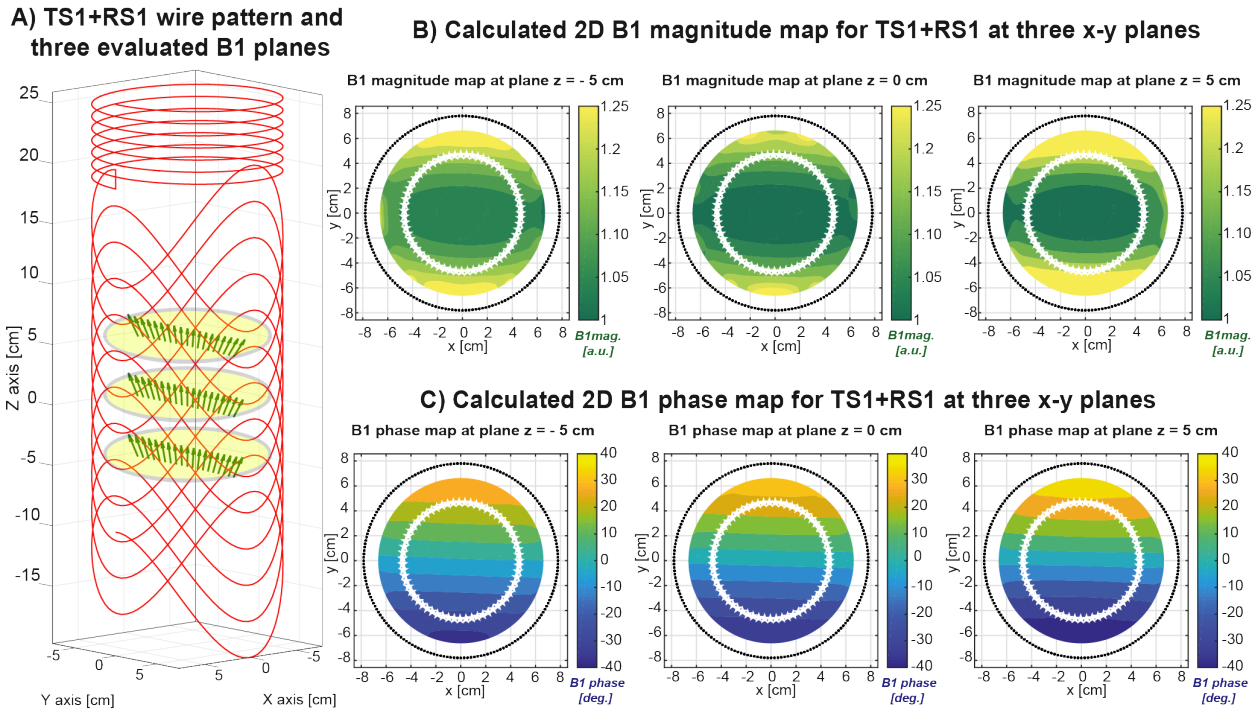

Figure 5.7: B_1 field plots using Biot-Savart calculations for TS1+RS1 coil. **A)** The wire pattern for TS1+RS1 counter-rotating coil (red), showing three evaluated B_1 planes located at z = -5.0 cm, 0 cm, 5.0 cm (yellow plane). B_1 field vectors (green arrows) are plotted, demonstrating a B_1 phase gradient along the y-axis for each plane. **B)** and **C)** depict the corresponding B_1 magnitude and phase maps on three planes. The coil winding and target imaging volume are shown as black dotted line and white pentagram line, respectively. Within the target imaging volume (60%), B_1 phase gradients along y axis are created, with $|B_1|$ varying between 1.00 and 1.25.

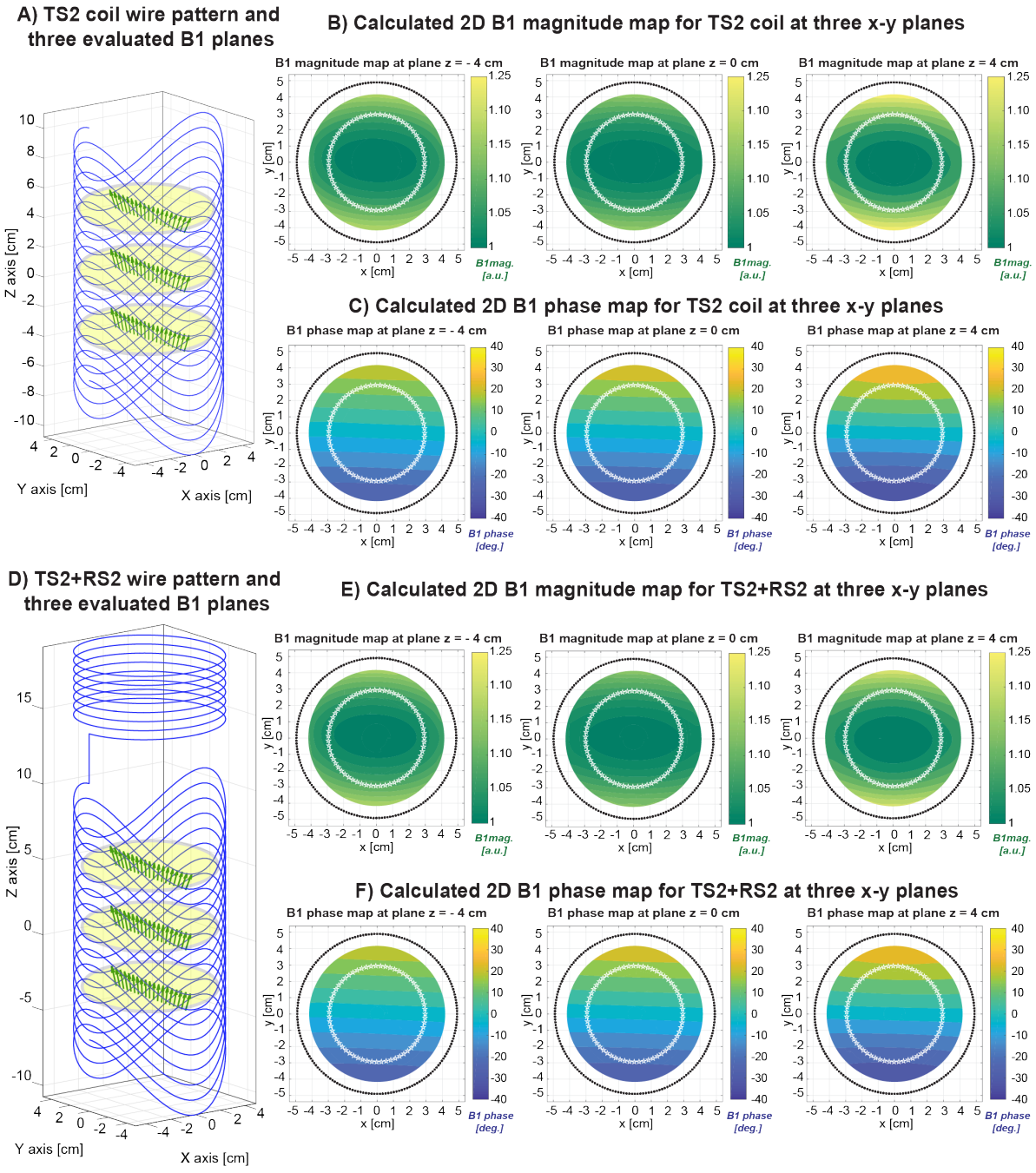

Figure 5.8: B_1 field plots using Biot-Savart calculations for TS2 and (TS2+RS2) coils. **A)** TS2 the wire pattern (blue) and three evaluated B_1 planes located at z = -4.0 cm, 0 cm, and 4.0 cm (yellow plane). To illustrate the phase gradient, B_1 field vectors (green arrows) are plotted along the y-axis for each plane. **B)** and **C)** demonstrate 2D B_1 magnitude and B_1 phase maps within three evaluated planes. The coil winding and target imaging volume are also depicted as black dotted line and white pentagram line. **D)** shows the wire pattern for (TS2+RS2) co-rotating element. **E)** and **F)** plot the corresponding B_1 magnitude and phase maps at planes z = -4.0 cm, 0 cm, 4.0 cm. For both coils within the target imaging volume (60%), B_1 phase gradients along y axis are generated, with $|B_1|$ lying in between 1.00 and 1.25.

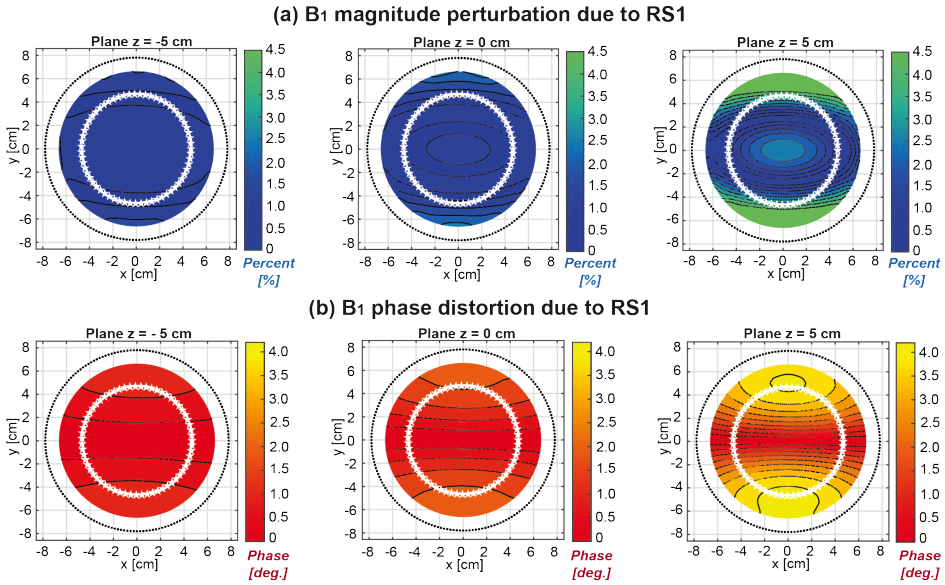

Figure 5.9: Simulated 2D B_1 field difference map with and without attached regular solenoid RS1. **(a)** and **(b)** show the difference of B_1 magnitude and phase between TS1 and TS1+RS1 coils at three evaluated z planes z = -5.0 cm, 0 cm and 5.0 cm. On all three planes within the target imaging volume (confined by white pentagram line) the largest B_1 magnitude perturbation (3.7%) and B_1 phase distortion (4.6°) were both observed at z = 5.0 cm plane which is the closest target imaging plane to the solenoid coil RS1.

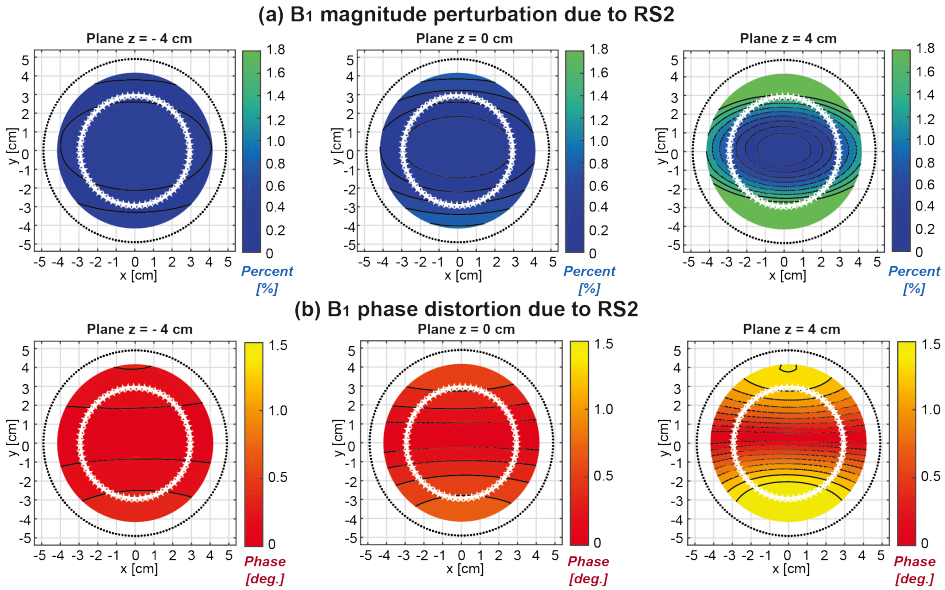

Figure 5.10: Simulated 2D B_1 field difference map with and without attached regular solenoid RS2. **(a)** and **(b)** display the difference of B_1 magnitude and phase between TS2 and TS2+RS2 coils at planes z = -4.0 cm, 0 cm and 4.0 cm. The nearest target imaging plane to the solenoid coil RS2 is z = 4.0 cm plane which is affected the most among three planes, where the largest B_1 magnitude perturbation and B_1 phase distortion in the target imaging volume are 2.0% and 1.7°, respectively.

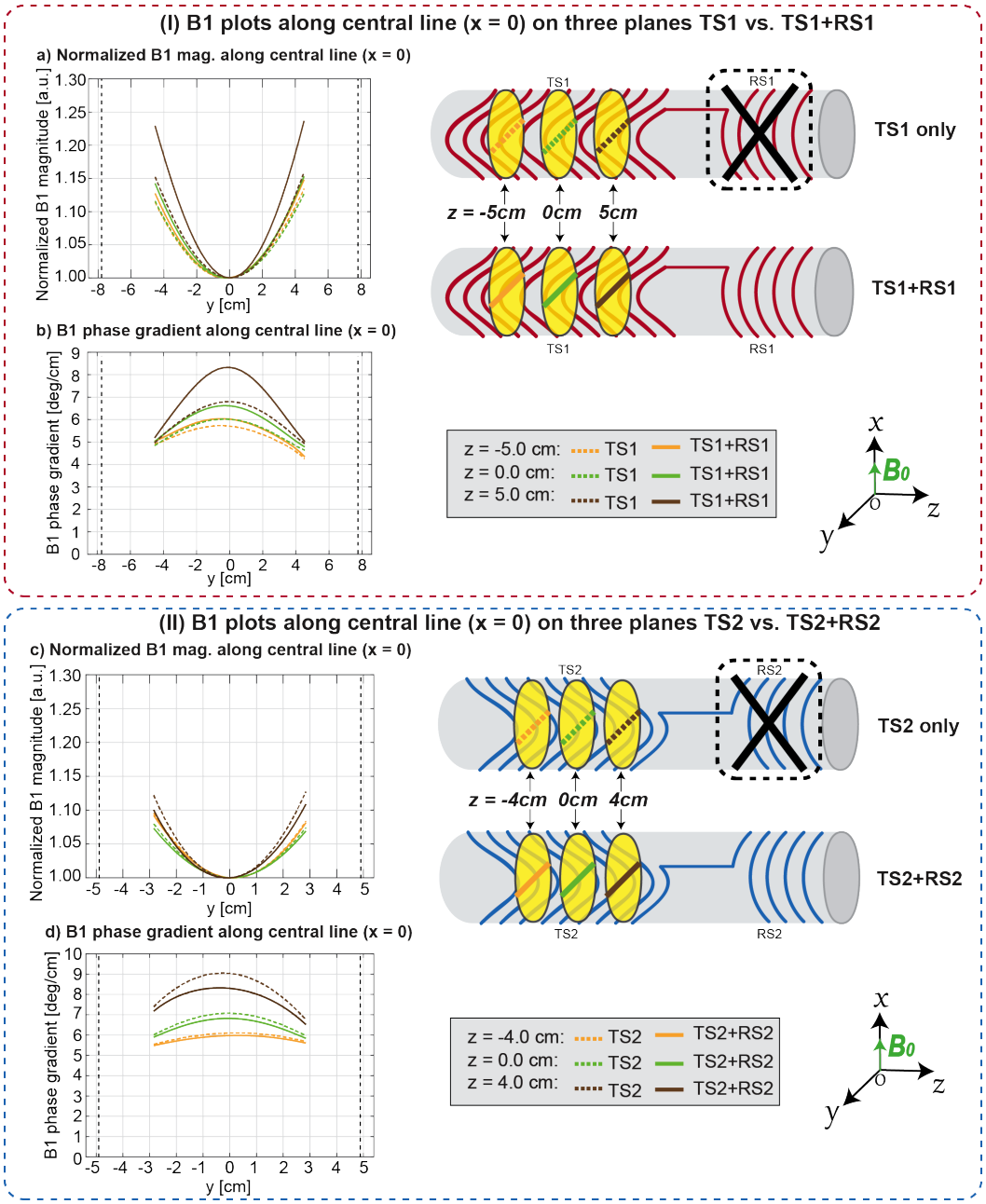

Figure 5.11: Simulated 1D B_1 field plots along central line ($x = 0$) on different evaluated planes. **(I)** plots B_1 field for six different central lines, where three dotted lines correspond to central lines located at three different planes (z = -5.0 cm (orange), 0 cm (green), 5.0 cm (brown) on TS1 coil only, while three solid lines represent central lines located in the same z location planes when RS1 coil is attached, i.e., TS1+RS1. The positions of each central line are also depicted in the coil schematics. The B_1 magnitude and B_1 phase gradient along these six central lines are shown in **a)** and **b)**, respectively. In figure **(II)** the same analysis for TS2 (dotted lines) and TS2+RS2 (solid lines) are provided in which the evaluated z planes changed to z = -4.0 cm (orange), 0 cm (green), 4.0 cm (brown). Panels **c)** and **d)** demonstrate B_1 magnitude and B_1 phase gradient data for six central lines with each represented in the right coil schematics as well.

gradient strength generated by TS2 coil alone ranges non-linearly from 5.5 to 9.1 deg/cm, see Figure 5.11 (II). However (unlike the TS1+RS1 case), the attached co-rotating RS2 coil leads a decreased gradient strength on all evaluated x lines, resulting in a phase gradient strength varying from 5.4 to 8.2 deg/cm.

5.4.3 TRASE Imaging Results

The coils were placed on stands at angles 135° and 45° (*i.e.*, a relative rotation of 90°) to generate two opposite phase gradients along the lateral y axis. To verify the existence of the expected phase gradients for this combined system, the B_y and B_z field components were probed with a small pick-up coil (elliptical, major and minor axes 20 mm and 10 mm) within the usable imaging volume for both combined coils (results not shown). The best geometric decoupling was achieved with (TS2+RS2) at z = + 1.5 cm offset, relative to (TS1+RS1), which is close to the z = 2.0 cm offset predicted from the simulation shown in Figure 5.4b. With phantom and both combined coils in position in the magnet (f = 9.28 MHz), the scattering matrix was measured as S_{11} (TS1+RS1) = -17.5 dB, S_{22} (TS2+RS2) = -22.6 dB, S_{12} (geometrical decoupling) = -16.8 dB (similar measurements as bench tests shown in Figure 5.4d). For NMR experiments, the smaller coil, (TS2+RS2), was connected to a passive T/R switch.

The 1D profiles using the 3 mm slot phantom are shown in Figure 5.12, reconstructed with a zero-fill factor of 8 [85], to enable smooth profile display and accurate counting of pixels. In each profile, the 3 mm slots were well-resolved, and by counting the pixels between the centers of the two outermost profile peaks (physical distance Δd = 30 mm), the average pixel separation (Δp) for each profile was evaluated to vary between 0.25 mm/pixel and 0.36 mm/pixel. The field-of-view was estimated from $FOV = ETL \times \Delta p$, resulting in FOV = 128 mm to 184 mm, corresponding to a range of mean phase gradient strength differences from 14.3 deg/cm to 10.0 deg/cm for the coil pair. In agreement with the B_1 field simulations of Figure 5.11, an increased gradient strength was observed for z planes closer to the attached

regular solenoids. However, the long and thin geometry of the slot phantom makes the 1D profiles sensitive to any misalignment between the direction of the slots and the phase gradient. A possible cause for the variation in profile quality (*e.g.*, broader and shorter right-most peaks in the $z = 2$ cm and $z = 4$ cm planes) is variation in the phase gradient direction, due to construction imperfections and inconsistencies, such as the return wire (not simulated).

The 2D images (1-D TRASE + 1D phase encoding) are shown in Figure 5.13. As can be seen by comparison with B_0 encoded image (see Figure 5.13B), in both transverse images of the multi-vial phantom (see Figure 5.13C and Figure 5.13D), the four non-empty vials can be identified with slight distortions observed due to non-uniform B_1 magnitude and non-linear B_1 phase gradients. The detailed description of multi-vial phantom is provided in Table 5.1. The echo spacing T_{es} was adjusted to achieve different duty cycles, given by T_p/T_{es}. As the duty cycle was increased from 20% to 32%, clearer images were obtained with shaper edges well defined for short T_2 vials B ($T_2 = 35$ ms) and E ($T_2 = 17$ ms), since the images suffered from less T_2 blurring. Additionally, since no slice-selection was applied, the vial cap is visible in the image, displayed as a smaller brighter circle in the central of each vial (see vial D).

A single vial, length 6.8 cm was imaged in the coronal plane (y-z), see Figure 5.13E. The entire vial phantom F was clearly shown in the coronal plane image, demonstrating that along the z direction the twisted solenoid pair still retains a good imaging capability. Vial F was oriented with its cap towards the attached regular solenoid, so an increased bottle size was observed due to stronger gradient strength, matching my simulation and 1D TRASE profile experiment in Figure 5.12.

5.5 Discussion

Both simulation and experimental results indicate that regular solenoids may be used to geometrically decouple two twisted solenoids, achieving a good isolation level of S_{12} = -

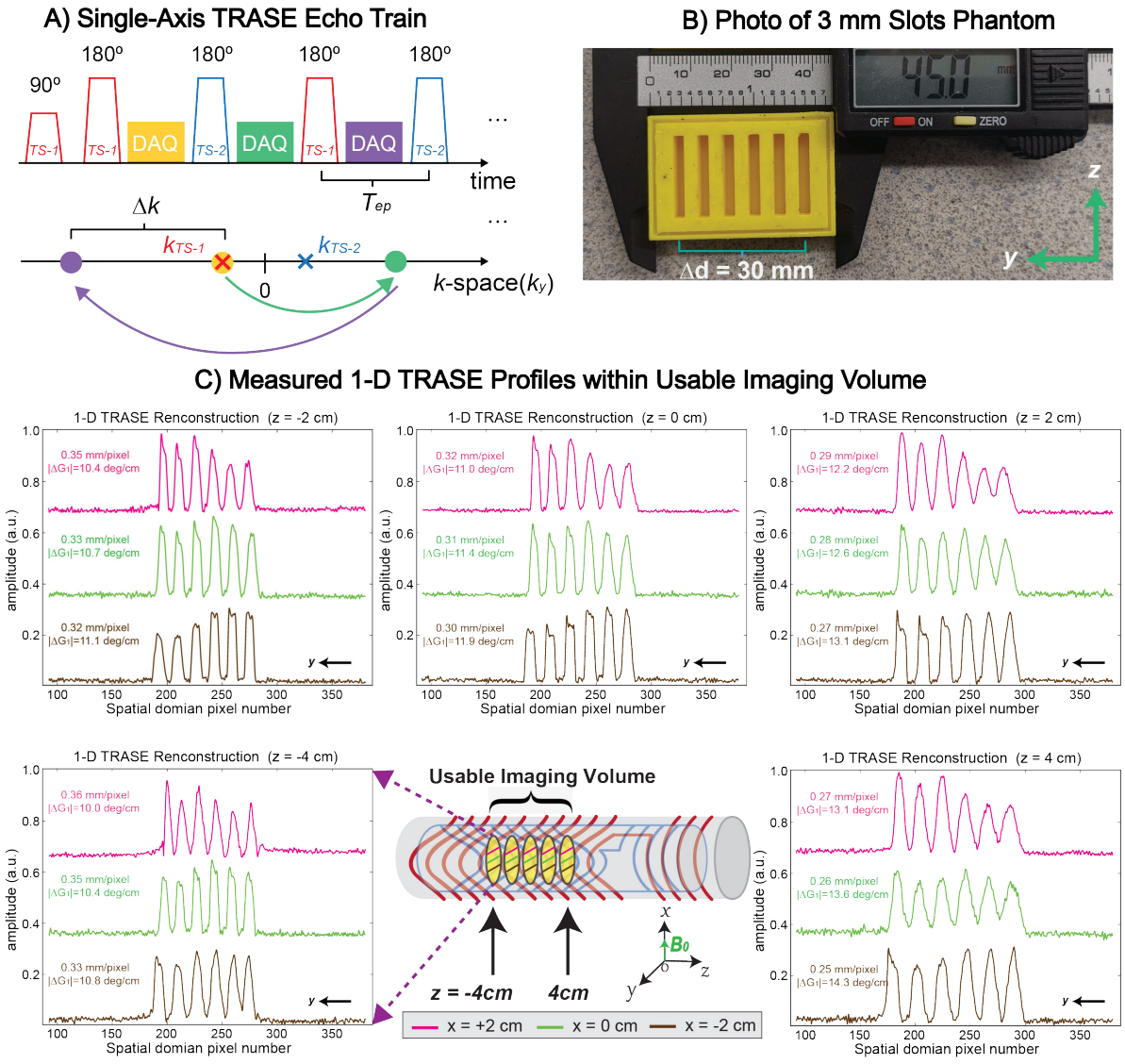

Figure 5.12: Single-axis TRASE experimental results. **A)** 1-D TRASE pulse sequence consisted of two sets of refocusing pulses transmitted by a pair of twisted coils alternatively. DAQ denotes spin echo sampling window. In k-space trajectory, each refocusing pulse triggers a jump about the corresponding coil k-space origin (k_{TS-1} and k_{TS-2}). The sequence parameters were $ETL = 512$, $NA = 32$, echo spacing $T_{es} = 800$ μs, pulse duration $T_p = 200$ μs for both excitation and refocusing pulses, readout 8 points at 40 kHz bandwidth. **B)** Photo of 3D printed slots phantom, size $W \times L \times H = 45 \times 30 \times 10mm^3$, with six 3 mm width slots, 3 mm gap, 20 mm length and 6 mm depth. **C)** Fifteen 1-D TRASE profiles measured along three different x lines (x = -2 cm, 0 cm, 2 cm) on five transverse planes (z = -4 cm, -2 cm, 0 cm, 2 cm, 4 cm), all within usable imaging volume. For display, the profiles were cropped and reconstructed with eight times zero-filling in k-space, but labelled with acquired pixel numbers. Based upon measurements, the average pixel separation ranged from 0.25 mm to 0.36 mm per pixel, corresponding to a range of mean phase gradient strength difference $|G_1|$ from 14.3 down to 10.0 deg/cm.

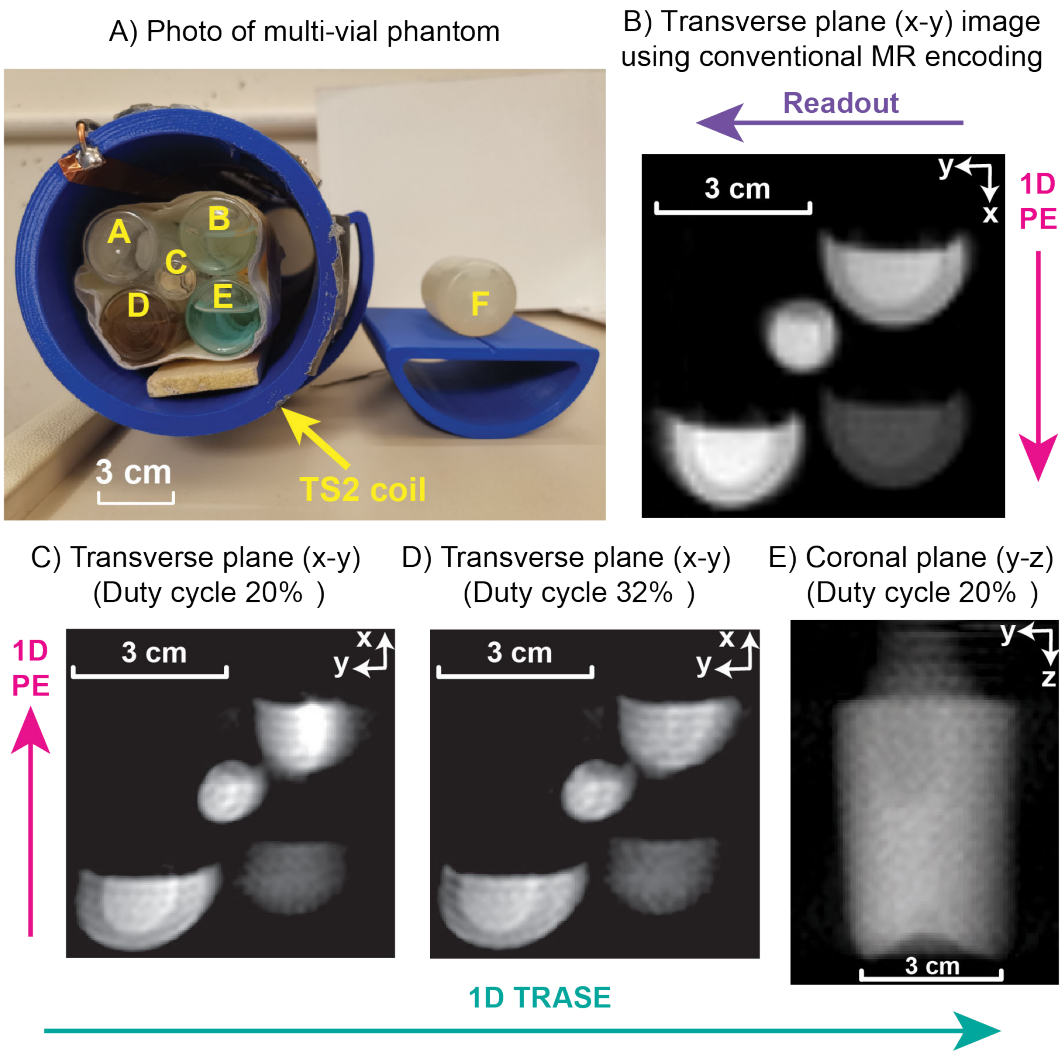

Figure 5.13: Combination of 1-D TRASE with 1-D B_0 phase encoding. **A)** Photo of multi-vial phantom each with different doped materials. The T_2 value for each vial is A (empty), B (35 ms), C (600 ms), D (280 ms), E (17 ms) and F (600 ms). The cross-section of five-vial phantom is 6.0 cm by 6.0 cm, slightly larger than our usable imaging volume (radius of 2.9 cm). Additionally, the length of vial F phantom is 6.8 cm which is covered by the maximum usable imaging length 8 cm along z axis (see details in Table 5.1). The 1D TRASE echo train has $ETL = 128$, $NA = 1$, nominal TRASE FOV of 150 mm, repetition time $TR = 4$ s, pulse duration $T_p = 200$ μs for both 90° and 180° hard pulses, phase encoding duration 9 ms, 128 steps, PE FOV of 150 mm. **B)** is a conventional SE B_0 gradient encoding image acquired in the same MR scanner using TS+RS2 coil only. Matrix size 128 × 128, FOV 150 mm on both x and y dimensions, readout bandwidth 10 kHz, $NA = 1$, echo time TE = 20 ms, repetition time $TR = 4$ s, pulse duration $T_p = 2000$ μs for both 90° and 180° sinc pulses, phase encoding duration 3 ms. **C)** and **D)** are measured transverse plane images using duty cycle of 20% and 32%, corresponding to an echo spacing T_{es} of 1000 μs, and 630 μs. **E)** Coronal plane image for vial phantom F. The entire phantom (at a length of 6.8 cm) is properly imaged with the geometrically-decoupled twisted solenoid pair.

17.5 dB, as demonstrated in Figure 5.4. From results in Table 5.3, it can be concluded that the *FastHenry2* simulator provides accurate inductance results for twisted solenoids at a low operating frequency $f = 9.28$ MHz. The attachment of a regular solenoid slightly decreases coil Q by a maximum of 10%. In any case, it may be necessary to restrict Q, so such Q losses are very manageable. In the experiments, I inserted a 40Ω resistor into TS2+RS2 to decrease coil Q, resulting in less coil ringing, mitigated effects of coupling, and better TRASE encoding results. To geometrically decouple the coil pair, the initial coil positions required delicate mechanical adjustments. However, once this condition is achieved, coil decoupling was insensitive to the load, and I did not observe failure of decoupling when different loads were used.

As shown in Figure 5.6, Figure 5.7, Figure 5.9, and Figure 5.8, Figure 5.10, only small B_1 magnitude perturbations and phase distortions were found within target imaging volumes after regular solenoids were attached. As would be expected, the effects are larger when the regular solenoid is closer to the twisted solenoid (for TW1+RS1 in this work). I observed that a counter-rotating geometry (TS1+RS1) increases the phase gradient strength, but at the cost of lower B_1 homogeneity, while the opposite effects were seen for the co-rotating geometry (TS2+RS2). The phase gradient strength depends upon the relative strengths of the axial B_z component and the lateral B_y component. The observed increase in gradient strength can be explained by the reduction in the magnitude of the B_z component, due to the influence of the counter-rotating solenoid, RS1, and vice versa for the co-rotating case. When encoding multi-dimensional k-space data using multiple coils, it is convenient to keep the phase gradients of similar amplitude [19], so the counter-rotating geometry is preferred for the larger twisted solenoids, which have a weaker inherent phase gradient.

The 1-D TRASE imaging experiment (Figure 5.12) resulted in an average pixel separation Δp of 0.25 mm to 0.36 mm, corresponding to a measured mean phase gradient strength difference $\Delta G_1 = 14.3$ to 10.0 deg/cm. To compare to a theoretically expected pixel separation, I also performed Bloch equation simulations (using 'MultiBloch' program) of the TRASE

sequence, based on the Biot-Savart predicted B_1 fields. I used third-order polynomials to fit the B_1 phase (corresponding to quadratic for B_1 phase gradient profile) along x lines, corresponding to the positions of experimental measurements. For a centrally-located small 30 mm object, the simulated images were very similar using either fitted quadratic phase gradient or a linear phase gradient (use peak phase gradient value) over this region. The result is that my experimentally measured Δp values are about 13% to 17% larger than simulated pixel separation $\Delta p'$, which varied between 0.22 mm to 0.32 mm. Possible causes for the discrepancy are: 1) relative rotational orientation error between coil pair actual encoding direction and the 1-D phantoms ($\pm 2^\circ$ to 3°); 2) exclusion of conductor return paths in B_1 field calculation and other mechanical inconsistencies; 3) residual coupling between the coils (The largest factor which will be demonstrated in the next chapter). Small residual coupling would be expected to cause some field cancellation, leading to reduced phase gradient strengths and resolution loss. In my previous work [13] a maximum 8.2% variation was observed between simulation and measurement for a single twisted solenoid coil. To investigate these possibilities further, tighter tolerances on all mechanical assemblies and wire layouts will be beneficial for the next iteration of coil design.

In support of this point, the mutual inductance simulation was not completely precise, since experiments showed that a 2 cm z-shift provided an improved null condition. So again, more accurate matching of simulated and physical geometry may help to resolve this inconsistency. Any other coupling mechanism (such as capacitive) not captured by the mutual inductance simulation will also require a compensating z-shift.

In MR experiments shown in Figure 5.12, the tap water in 1D phantom has long relaxation values, with T_1 of 4 to 5 seconds and T_2 of 2 to 3 seconds. Thus, no severe T_2 blurring was observed in this experiment where duration per echo train was $ETL \cdot T_{ep} = 512 \cdot 0.8$ ms = 410 ms. For practical TRASE encoding of biological tissues with short T_2 values, Figure 5.13 shows a 32% duty cycle was achieved, corresponding to a 80 ms TRASE echo train duration for 128 echoes. This short echo train would mitigate resolution loss caused

by T_2 decay for in vivo study of intermediate and long T_2 tissues (*i.e.*, $T_2 \geq 65$ ms [33]), with clinically-level image pixel separation ($\Delta p \leq 1.4$ mm), while still remaining within SAR limits [13]. To maintain spatial resolution for short T_2 tissues (*e.g.*, T_2 of 42 ms for white matter at 0.2 T [11], [86]), higher duty cycle and/or shorter RF pulse duration are required. To pursue this further, use of a separate receive coil would be helpful in reducing transmit pulse interference with the receive signal path. In addition, an independent receive coil or array could be optimized for maximum sensitivity, both geometrically and by the omission of the Q-damping resistor.

The inductance of a twisted solenoid coil increases rapidly with physical dimensions and in some cases may self-resonate below the Larmor frequency. Furthermore, when a regular solenoid is attached, the coil inductance increases further. This may be mitigated by reducing the number of coil turns. The relatively long coils would be suitable for in vivo imaging of extremities, however, for imaging larger FOVs or for more restrictive geometries, a coil designed with a length constraint would be preferable. With the proviso that shorter coil designs are desirable, this mutual inductive decoupling scheme is scalable and remains attractive for larger coils (*e.g.*, head coil). In contrast, active switches may require redesign to handle the higher RF currents and voltages present in larger coils.

Although twisted solenoids produce a non-uniform concomitant RF field directed along the B_0 direction, Bloch equation simulations show that this has no effect on spin trajectories. For a B_0 amplitude oscillation frequency (9 MHz) much greater than the nutation frequency (2.5 kHz), the spins respond only to the mean B_0 field.

Depending upon exact design parameters, the usable imaging volume of twisted solenoid coils is 60% to 75% of the coil diameter, which is considerable better than some previous phase gradient coils, but somewhat inferior to some other conventional RF coils, *e.g.*, over 80% for a quadrature birdcage with more than 8 legs [87].

As a final note, although the RS1 and RS2 regular solenoids were specifically designed to

decouple two solenoids with a relative rotation shift of 90°, I have also found by carefully adjusting the relative longitudinal shift (z axis), a good decoupling level (*e.g.*, S_{12} = -10 to -15 dB) could be achieved in any relative rotation, *i.e.*, 0 to π. This is relevant for extension to 2D TRASE encoding, which requires one more coil. This coil array geometry will be discussed in Chapter 6.

5.6 Conclusions

The twisted solenoid geometry has many advantages for TRASE encoding, including the compact cylindrical design, high efficiency, and large usable imaging volume. In this chapter it has been demonstrated that a pair of twisted solenoid TRASE coils can be geometrically decoupled, and in general that geometric decoupling is a viable alternative to active switched solutions, even for coil pairs with high inherent coupling. The avoidance of active diode switching for coil decoupling significantly simplifies coil circuitry, minimizes transmit switching speed constraints, and avoids reduction of coil efficiency imposed by diodes. Compared with my previously demonstrated coil set consisting of one twisted solenoid and one saddle coil [13], a doubled k-space traversal coverage was achieved using the same echo train length, enabling 1D high-resolution MR encoding for short T_2 samples, which is advantageous for practical clinical application. This gradient set is well suited to low B_0 field MRI magnets, such as Halbach arrays and bi-planar magnets.

5.7 Acknowledgements

I would like to thank Dr. Vyacheslav Volotovskyy and Mr. Radim Barta for the advice on coil construction. I would also acknowledge funding sources 1) Natural Sciences and Engineering Research Council of Canada, Grant/Award Number: RGPIN-2016-05183, and RGPIN-2015-03992; 2) 2018/2019 Alberta Cancer Foundation Antoine Noujaim Scholarship, Grant/Award Number: 27228; and 3) Canadian Space Agency FAST grant, for the support.

Chapter 6

Three Coils - A Geometrically Decoupled Three-Coil Set for 2D Imaging in the Axial Plane

6.1 Introduction

6.1.1 2D TRASE Encoding in the Axial Plane

In the last decade, in-depth efforts were made to improve TRASE imaging quality, particularly spatial resolution, under different categories including 1) new RF coil designs/combinations [11], [13], [16], [20], [24], [25], [50]; 2) optimization of RF system transmission efficiency [17], [84]; 3) investigations of techniques mitigating TRASE imaging artifacts [18], [47], [83]. To date, 2D TRASE encoding was performed using Helmholtz-Maxwell coil pairs [19] for a human wrist in coronal plane, demonstrating the potential of TRASE technologies for clinical use. However, achievable in vivo spatial resolution is restricted to poor coil efficiency and the need for active PIN diode switch [25]. Additionally, these coil pairs are bulky, require balanced drive, large gap, and cannot provide 2D encoding in the axial plane which is typically considered as the most favorable imaging plane (like a CT scan).

To address these issues, a new RF phase gradient coil based upon twisted solenoid geometry was proposed recently [13], [53]. This new type of coil generates highly effective longitudinal

B_1 field which is suitable for vertical or transverse B_0 field orientations. The original work [13] indicate that under different orientation twisted solenoid can encode along any direction within the axial plane [13]. Using this advantageous RF coil, it has been demonstrated one dimensional TRASE encoding can be achieved along vertical ($x-$) [13] and lateral ($y-$) axes separately, [16] without active PIN diodes, see Figure 5.1.

Since 2D TRASE encoding requires at least three non-collinear RF phase gradients [20], one simple way to approach this idea is the combination of one RF coil such as saddle coil generating a uniform B_1 field (*i.e.*, phase gradient $G_s = 0$), and two twisted solenoids producing two non-zero orthogonal phase gradients G_x and G_y. However, strong inductive coupling arises from this coil configuration where the mutual inductances (if not significantly reduced) among three coaxial coils will cause a split in the resonance for each coil, and more seriously, induce currents and create unwanted secondary B_1 fields.

6.1.2 Coil Set Decoupling

In the literature numerous studies were made to reduce mutual inductance between resonators. These work [68], [69], [72]–[77], [81] have been introduced in the last chapter, hence, will not be repeated here. The previous study I conducted [16] shows an effective geometric decoupling technique between two twisted solenoids with relative rotation of $\pi/2$, by adding extra regular (*i.e.*, untwisted) solenoidal extensions of the same diameter as each twisted solenoid. This configuration maintains independence of each coil and more importantly, can achieve a good level of isolation between two twisted solenoids in any relative rotation, that is, 0 to π, if relative longitudinal shift (z axis) is carefully adjusted. This is applicable for an extension to 2D TRASE encoding in the axial plane, since only one more saddle coil is required, which is known to be inherently geometrically-decoupled with solenoid variants. In this chapter, I will show this three-coil set and the experimental 2D MR images. Comparing with results obtained from "Multi-Bloch" simulators performed by a colleague Pallavi Bohidar, clearer requirements to drive this new coil set will be specified.

6.2 Theory

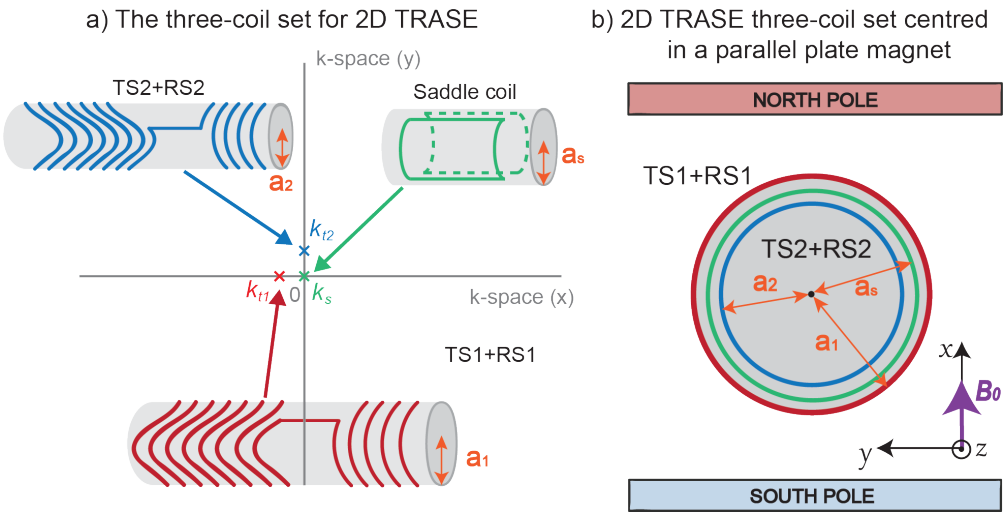

Figure 6.1: Schematic of a geometrically-decoupled three-coil set for 2D TRASE, containing previously demonstrated twisted solenoid pair TS1+RS1 and TS2+RS2, and a saddle coil. **a)** counter-rotating coil TS1+RS1 and co-rotating coil TS2+RS2 are positioned with a 45° relative rotation, generating phase gradients along x and y axis. The saddle coil produces a uniform B_1 field, so its corresponding coil origin is at the center of k-space. **b)** The three-coil set geometry for an MRI experiment: the smaller (TS2+RS2) is nested inside (TS1+RS1) concentrically, while the saddle coil is sandwiched between two twisted solenoids.

6.2.1 Mutual Inductance and Coupling Coefficient

In this work, the same equations as shown in Chapter 5 will be used, where mutual inductance M and coupling coefficient k between two inductors are:

$$EMF = -M\frac{dI}{dt}$$
$$k_{12} = \frac{M}{\sqrt{L_1 L_2}} \quad \text{where} \quad -1 \leq k \leq 1 \tag{6.1}$$

6.2.2 Geometrically-decoupled Three-coil Set

The same concept introduced previously is applicable to the 2D TRASE RF three-coil set consisting of the TS1+RS1 and TS2+RS2 (constructed in the last chapter) and a saddle

coil. The concept is illustrated in Figure 6.1 in which two twisted solenoids TS1+RS1 and TS2+RS2 with radii of a_1 and a_2 ($a_1 > a_2$) are oriented with a relative 45° rotation shift (instead of 90° as illustrated in Chapter 5), generating two B_1 phase gradients along x and y axis [13]. Although saddle coil can only generate zero phase gradient (*i.e.*, coil origin is the center of k-space), a third non-collinear RF phase gradient in k-space is mandatory for 2D TRASE experiment, therefore, a saddle coil nested between TS1+RS1 and TS2+RS2 was constructed, as shown in Figure 6.1b.

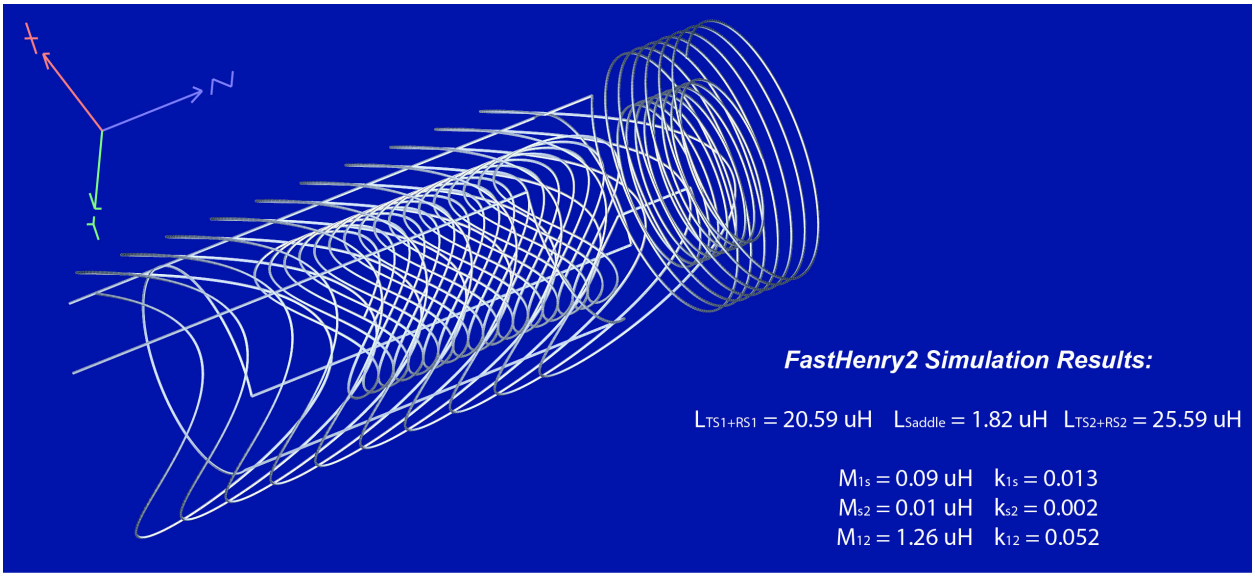

Figure 6.2: The three-coil coupling simulation using *FastHenry2*. The coil set contains concentric TS1+RS1, saddle coil and TS2+RS2. The nested TS2+RS2 coil was shifted along z axis by +4.5 cm, while no shift along z axis was needed for the saddle coil to reduce the mutual inductances to their minimum, producing coupling coefficients (TS1+RS1 and Saddle, $k_{1S} = 0.013$), (Saddle and TS2+RS2, $k_{S2} = 0.002$), and (TS1+RS1 and TS2+RS2 $k_{12} = 0.052$).

Note that the same TS1+RS1 and TS2+RS2 which were constructed in Chapter 5 are used in this configuration. The mutual inductance between TS1 and TS2 is compensated by an opposite mutual inductance generated by the RS1 and RS2, with different z longitudinal shift as the relative rotation shift is changed. Additionally, the B_1 field generated by the saddle coil is inherently orthogonal to the fields generated by twisted solenoids, which was verified by 1D TRASE experiment shown in Chapter 4. As a result, for this 2D TRASE coil

set, three pair of coils present low simulated k values: (TS1+RS1 and Saddle) $k_{1S} = 0.013$, (Saddle and TS2+RS2) $k_{S2} = 0.002$, and (TS1+RS1 and TS2+RS2) $k_{12} = 0.052$, signifying good levels of geometric decoupling, see Figure 6.2.

6.3 Methods

The feasibility of geometric decoupling, and B_1 field estimation has been explicitly demonstrated in the previous two chapters, hence, in this work I will mainly focus on the introduction of three-coil set and 2D TRASE experiments, and finally make a comparison between obtained 2D images and 'Multi-Bloch' simulations.

6.3.1 Coil Set Construction

The two combined twisted solenoids TS1+RS1 and TS2+RS2 constructed in Chapter 5 were reused in this work, with different relative rotation and shift along z axis. The saddle coil was wound with solid 12 AWG hookup wire (Digikey) upon grooved 3D printed polylactic acid (PLA) former in a radius of 6.4 cm that was designed using 3D parametric modeller SketchUp 2014. All 3D printing processes were identical to the methods described in the Appendix II of Chapter 5. The dimensions of each coil and position details are listed in Table 6.1. For each coil, a balanced tune and matching circuit as described in [13], [37] was used. The 3D printed stands were implemented for each coil to set correct height, rotation angle and to allow mm-level axial positional adjustments for fine tuning of decoupling. The *FastHenry2* simulation (see Figure 6.2) indicated that the coupling coefficient between TS1+RS1 and saddle coil is larger than that of saddle and TS2+RS2 (*i.e.*, $k_{1s} > k_{s2}$), to further improve the isolation a small transformer (*i.e.*, loops of wire) between TS1+RS1 and saddle was used, as can be seen in the picture overview of the array coil, Figure 6.3. Additionally, it was necessary to connect each coaxial coil cable to a common ground at the Faraday cage, while cable traps were found not to be necessary.

Coil Name	Radius a (cm)	Modulation A (cm)	Pitch h (cm)	Turns N	Coil Rotation (degree)	x Shift (cm)	y Shift (cm)	z Shift (cm)	Phase Gradient Direction
TS1	7.8	5.5	3.0	10	0	0	0	0	x
RS1	7.8	0.0	0.9	7	0	0	0	0	uniform
Saddle	6.4	n/a	n/a	n/a	0	0	0	0	uniform
TS2	4.9	2.5	1.0	17	45	0	0	4.5	y
RS2	4.9	0.0	0.6	8	45	0	0	4.5	uniform

Table 6.1: The coil geometries for all three coils composing of 2D TRASE coil set. The shift data along x, y and z axis are reported with respect to the position of TS1+RS1, of which center is assumed to be the origin of the coordinate system.

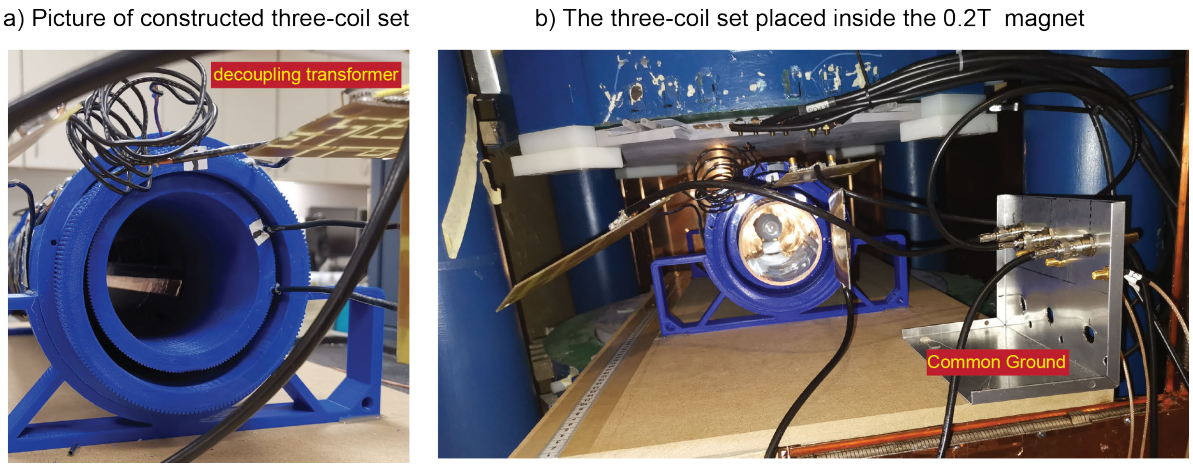

Figure 6.3: The picture of the constructed three-coil set. **a)** The coil set contains concentric TS1+RS1, saddle coil and TS2+RS2. A small transformer consisting of 3-5 loops of wire in a diameter of approximately 5 cm for both primary and secondary, is connected between TS1+RS1 and saddle coil. Manual adjustment of this transformer can further decrease the coupling between TS1+RS1 and saddle coil. The TS2+RS2 is rotated by 45° with respect to TS1+RS1 coil, as shown by the marker (white tape) attached to the 'top' of each coil. **b)** The picture of three-coil set placed inside the 0.2T shimmed 4-poster planar permanent magnet, loaded with a cylindrical imaging phantom with 3.8 cm diameter and 2 cm length, fully filled with tap water to eliminate air bubbles. 3D printed stands were used to accurately adjust the relative position of each coil. A common ground aluminum plate is implemented, and further attached to the Faraday cage that is not shown in the picture.

6.3.2 TRASE MRI Experiments

The loaded three-coil set was placed in the middle of a 9.28 MHz vertical B_0, shimmed 4-post planar permanent magnet, as shown in Figure 6.3b. To geometrically decouple the three-coil set, the initial coil positions required delicate mechanical adjustments. This condition is determined by bench measurements targeting at minimizing the S-parameter values of (S_{1s}, S_{s2} and S_{12}), using a vector network analyzer (Agilent Technologies E5061A).

Prior to conducting 2D TRASE experiments, the power input to each coil was adjusted to produce a 180 degree refocusing pulse. Once this calibration was completed, three individual 1D TRASE experiments (pulse duration $T_p = 300$ μs, echo spacing $T_{ep} = 1500$ μs, echo train length = 128, average number of 1) were first performed upon a cylindrical phantom (3.8 cm diameter and 2 cm length) which was fully filled with tap water to eliminate air bubbles, resulting in three 1D TRASE images using coil combinations of (TS1+RS1 and Saddle), (TS2+RS2 and Saddle), as well as two twisted solenoids (TS1+RS1 and TS2+RS2). This set of 1D TRASE experiments not only allows one to adjust the driving power on each coil, it also helps to confirm proper functioning of each coil before the 2D TRASE experiment.

The 2D TRASE sequence using three coils have been introduced in Chapter 2, see Figure 2.12. In this regime a $M \times N$ data matrix is acquired using $\frac{M}{2}$ of $C - (AC)_i - (AB)_{N/2}$ echo train and $\frac{M}{2}$ train of $C - (AC)_i - (BA)_{N/2}$ sequence. Coupled with the XY-4 phase scheme [83], this three-coil set 2D TRASE sequence was performed upon the same cylindrical phantom, and the MRI experiment parameters were as follows: pulse duration $T_p = 300$ μs, echo spacing $T_{ep} = 1500$ μs, imaging matrix $M \times N = 128 \times 128$, repetition time TR= $3s$, 1 average only. Each k-space point was the average of 8 points collected at 40 kHz bandwidth, while no slice-selection was applied during the acquisition. All three coils were placed on stands inside the magnet where TS1+RS1, saddle and TS2+RS2 were rotated at angles 0°, 0° and 45°, respectively, to generate three different phase gradients within the axial plane. The smallest coil, TS2+RS2, was connected to a passive T/R switch.

Similarly, the MRI system was controlled by an NRC TMX research console [60] configured to drive three independent transmit amplifiers and utilizing a single receive channel. In 2D TRASE experiment, the (TS1+RS1) and (TS2+RS2) coils were driven by a high duty cycle (maximum 50%) custom-made RF power amplifier system (see details in a co-author article [84]) which was capable of providing sequential operation of two RF output channels, up to 1 kW per channel. The saddle coil was driven by an AN8110 RF Amplifier (Analogic Corp MA, USA). In all experiments less than 300 W peak RF power was used.

6.3.3 Bloch Simulated 2D TRASE Images

To understand how the effects of B_1 field perturbations arising from residual inductive coupling among this three-coil set degrades 2D TRASE imaging quality, a collaborator Bohidar has performed Bloch simulations to match the experimental images that will be shown in the results section. While the details of this simulation study can be found in the literature [88], findings from that work will be used in this chapter for better understanding of coil interactions.

Specifically, Biot-Savart calculations (*BSmag* toolbox) were used to generate B_1 field maps for this three-coil set. Various weighting factors on the $|B_1|$, representing flip angle contributions from the secondary (un-driven) coils for each transmit pulse, were used to add the B_1 field components of primary and secondary coil geometries to simulate coil coupling. The weighting factors considered, in terms of the percentage field contribution, or equivalently in terms of total current in the coil array, from the primary coil were 97%, 95%, 89%, and 78%, which in terms of each individual secondary coil were 1.5%, 2.5%, 5.5%, and 11% respectively. Only cases where the current was assumed to be equally split between secondary coils was considered, to simplify the interpretation of the results. The coupled B_1 field maps were then used in a Bloch simulation program ("Multi-Bloch") to perform 2D TRASE MRI simulations. The reconstructed simulated 2D TRASE images demonstrate the impacts of varying levels of coil coupling, including an ideal case, *i.e.*, no coupling between three coils.

S parameters	TS1+RS1	Saddle	TS2+RS2
TS1+RS1	S_{11} = -14.2 dB	S_{1S} = -23.3 dB	S_{12} = -22.9 dB
Saddle	$S_{S1} = S_{1S}$	S_{SS} = -14.0 dB	S_{S2} = -34.9 dB
TS2+RS2	$S_{21} = S_{12}$	$S_{2S} = S_{S2}$	S_{22} = -26.7 dB

Table 6.2: The matrix of S parameters measured using a vector network analyzer, when geometrically-decoupled three-coil set was placed inside a magnet with a loading phantom, see configuration in Figure 6.3b.

6.4 Results

6.4.1 Coil Geometric Parameters and Decoupling

The geometric parameters for the three-coil set are tabulated in Table 6.1. In *Fasthenry2* simulation, the TS1 and TS2 coil geometries shown passed all requirements that are needed for TRASE imaging including uniform B_1 magnitude (maximum $|B_1|$ inhomogeneity is 10%) and phase gradient strength larger than 5.0 degree/cm, while keeping a large portion of volume for imaging purpose. When RS1 and RS2 were added to the simulation, with relative 45° rotation and longitudinal shift z = 4.5 cm between two combined coils, the coupling coefficient reduced to minimum k_{12} = 0.052, see Figure 6.2. The saddle coil was nested between TS1+RS1 and TS2+RS2 with no shift applied. Since it is naturally decoupled to solenoidal coil, it yields low coupling coefficients with both TS1+RS1 and TS2+RS2, being k_{1S} = 0.013 and k_{S2} = 0.002. This geometrically-decoupled three-coil set configuration (loaded and placed inside the magnet) was verified using S-parameter measurements (see data in Table 6.2), where all three coils were functioning without resonant frequency split, with acceptable isolation levels of S_{1S} = -23.3 dB, S_{S2} = -34.9 dB and S_{12} = -22.9 dB. The pictures of S measurements are shown in Figure 6.4.

6.4.2 TRASE Imaging Results

The best geometric decoupling was achieved with saddle coil at z = +1.5 cm offset and TS2+RS2 at z = + 3.5 cm offset, relative to coil TS1+RS1, which are both close to the

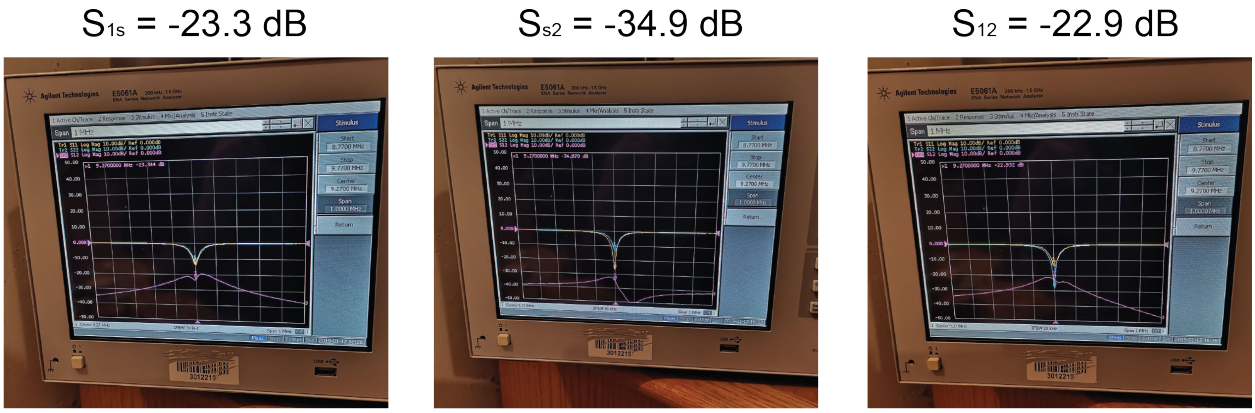

Figure 6.4: Pictures of S parameter measurements for the three-coil set. The network analyzer only has two ports, so each time only a pair of coil can be evaluated, while coil connections to the port needs to switched manually for other pairs. During the measurement, the third coil was terminated with a 50 Ω adapter. All measured S parameters are listed in Table 6.2.

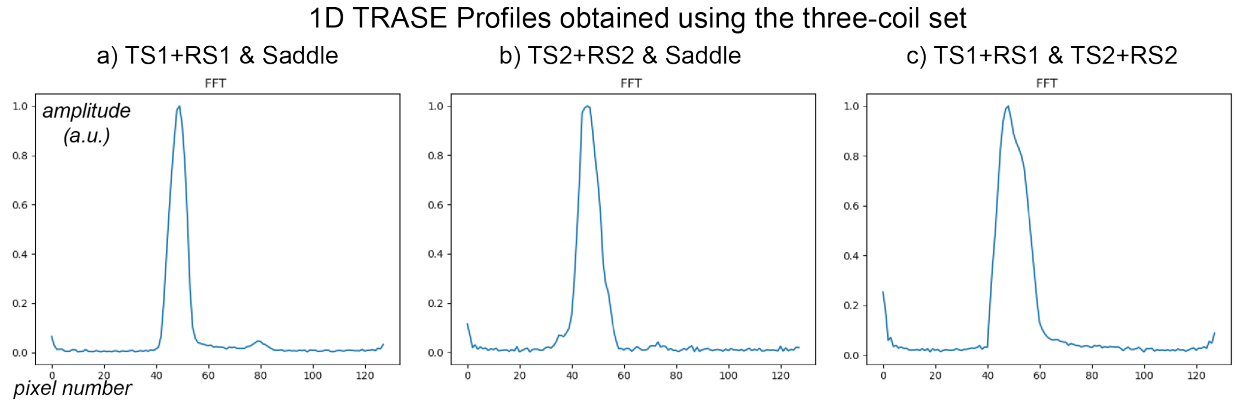

Figure 6.5: 1D TRASE profiles obtained using the three-coil set. Panel a), b) and c) were 1D TRASE images obtained using different coil pair combinations. The pixel number in each profile was reported as 15 (TS1+RS1 and Saddle), 18 (TS2+RS2 and Saddle) and 22 (TS1+RS2 and TS2+RS2), yielding a pixel width of 2.5, 2.1, and 1.3 mm (the phantom is in the diamter of 3.8 cm), hence, representing a phase gradient strength difference of 5.4, 6.6, and 8.1 deg/cm.

offsets predicted from the simulation shown in Figure 6.2.

Three individual 1D TRASE images are shown in Figure 6.5. The number of pixels was counted as 15 (TS1+RS1 and Saddle), 18 (TS2+RS2 and Saddle) and 22 (TS1+RS2 and TS2+RS2) from panel (a) to (c). The phantom has a diameter of 3.8 cm, so this yields a pixel width of 2.5, 2.1, and 1.7 mm, from (a) to (c), corresponding to a phase gradient strength difference of 5.4, 6.6, and 8.1 deg/cm. Since the saddle coil generates zero phase gradient, these results agree closely to the simulated gradient strength reported in Chapter 5 (see in Figure 5.11 green lines) in which $G_{TS1+RS1} = 4.7$ to 6.5 deg/cm and $G_{TS2+RS2} = 5.8$ to 6.8 deg/cm. With these values, a small amount of resolution loss was found in the panel c) profile (*i.e.*, 8.1 deg/cm $< \sqrt{5.4^2 + 6.6^2} = 8.5$ deg/cm). Despite small artifacts observed in these 1D images, and in particular, slight asymmetric shape and peak signal loss observed in panel c), these 1D TRASE images validated the proper functioning of each coil prior to 2D TRASE experiments. This set of 1D TRASE images is qualitatively comparable with the 1D TRASE images shown in Figure 5.12.

The 2D TRASE Fast Fourier transform (FFT) images without slice selection are shown in Figure 6.6. Since the imaging object is a cylindrical phantom, fully filled with tap water, the expected 2D image should be circular, as demonstrated in Figure 6.7A. However, as can be seen in Figure 6.6, the obtained 2D images show a semi-circular shape, with part of the phantom missing in the image, indicating that there was an encoding deficit (*i.e.*, loss of phase gradient strength) during this experiment. According to the images acquired previously in Chapter 4 and 5, it is known that the non-uniform B_1 magnitude and non-linear B_1 phase gradients generated by this three-coil should distort TRASE images slightly, however, such severe image distortions were unexpected. By examining the original k-space data, it was found that a small portion of k-space data yielded unreasonably out-of-range values during single echo train (results not shown), indicating an imperfect k-space data acquisition.

To narraow down the cause of this error, equipment malfunction was first excluded. This

included the confirmation of coil geometry and their relative positions inside the magnet. Other devices such as RF cables, network analyzer, RFPAs, various electronic components (*e.g.*, RF attenuators and splitters, etc.), as well as reconstruction codes were also tested with simple MR FID experiments, verifying their proper functionality, however, neither of those was responsible for the image artifact observed in 2D TRASE experiments. Although this was still a valid 2D TRASE experiment as the appearance of the object boundary was well defined, an in-depth investigation is required to understand the underlying cause of this artifact. Therefore, Bloch simulations were performed by my colleague Bohidar and I, in order to study the effects of the residual coupling among coils that were not fully eliminated by geometric decoupling techniques (*i.e.*, residual coupling).

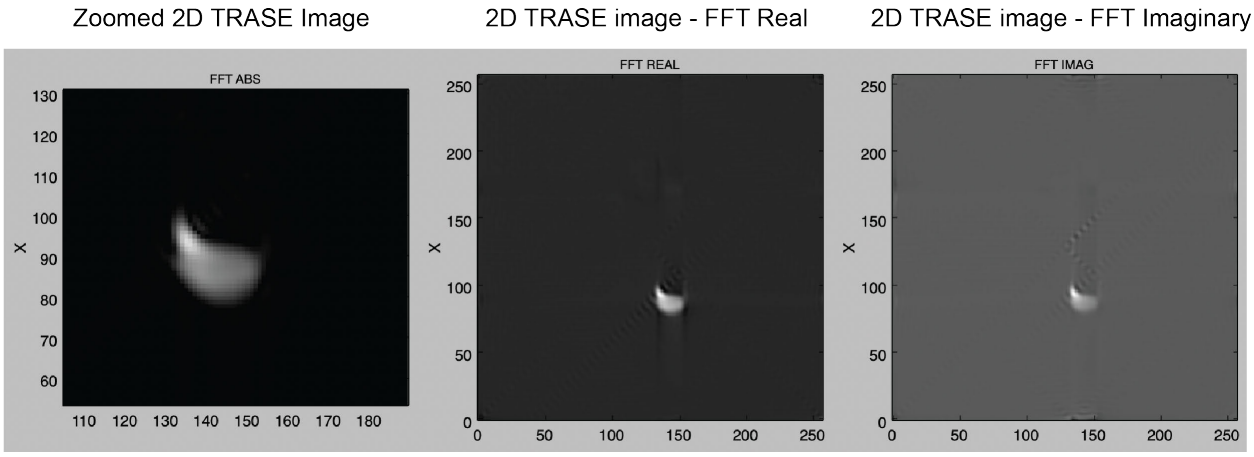

Figure 6.6: 2D TRASE images in the axial plane acquired using the three-coil set. The MR parameters are: pulse duration $T_p = 300$ μs, echo spacing $T_{ep} = 1500$ μs, imaging matrix $M \times N = 128 \times 128$, zero-filling of 2, FOV of 300 mm, repetition time TR= 3s, 1 average, receiver bandwidth 40 kHz. Each k-space point was the average of 8 points, and no slice-selection applied. The imaging phantom is a cylindrical object with 3.8 cm diameter and 2 cm length, fully filled with tap water. The obtained images show a semi-circular shape, with a partial of the object missing due to imperfect 2D TRASE encoding.

6.4.3 Bloch Simulations for Coil Interactions

From Biot-Savart simulation the B_1 field map of each coil is known. Various weighting factors, representing $|B_1|$ contributions from the secondary (un-driven) coils, were used to add the B_1 field components of primary and secondary coil geometries in an effort to simulate

coil coupling, producing the coupled B_1 field maps (an example of these coupled B_1 fields can be found in Appendix III). The effects of the B_1 errors caused by coupling include: a reduction of gradient strength, a shift in the B_1 phase location, and the loss of phase gradient linearity. The image artifacts arising from these errors will be discussed later. The coupled B_1 field maps were used in a Bloch simulation to perform 2D TRASE MRI simulations, where the ratio of $|B_1|$ contribution from primary coil versus secondary coils are manually adjusted in simulations. For example, 78% $|B_1|$ contribution from primary coil means 78% of 180° is from the conducting primary coil, while due to interactions the other two secondary coils also conduct and contribute 11% each for the $|B_1|$. The reconstructed images of a circular object from 2D TRASE simulations using varying levels of $|B_1|$ ratios are shown in the Figure 6.7. It showed that a $|B_1|$ contribution of 95% or higher is needed from the primary coil for image formation in 2D TRASE using the transmit three-coil set described in this work. While Bloch simulations were performed with assumptions (*e.g.*, the two secondary coils delivered the same amount of $|B_1|$ contributions) which might deviate from actual 2D TRASE experiments slightly, similar image quality degradations were found. As the levels of B_1 field coupling increase (from panel B to panel E in Figure 6.7), the uniformity of images were significantly affected by coil interactions, showing as certain bright regions. The circular object shape were also distorted and shrunken toward semi-circular shape. As an extreme case of coil interactions (22% $|B_1|$ contributions from secondary coils) shown in panel E, the boundary of a circular object was badly distorted. By comparison, it is believed that the performed 2D TRASE experiment lies in a situation between panel C) and D), where 89% to 95% $|B_1|$ contribution was originated from the primary coil. This is also consistent with the S_{12} measured in Table 6.2.

6.5 Discussion

Both *Fasthenry2* simulation (Figure 6.2) and experimental S measurements (Table 6.2) indicate that the three-coil set present high levels of isolation using geometric decoupling tech-

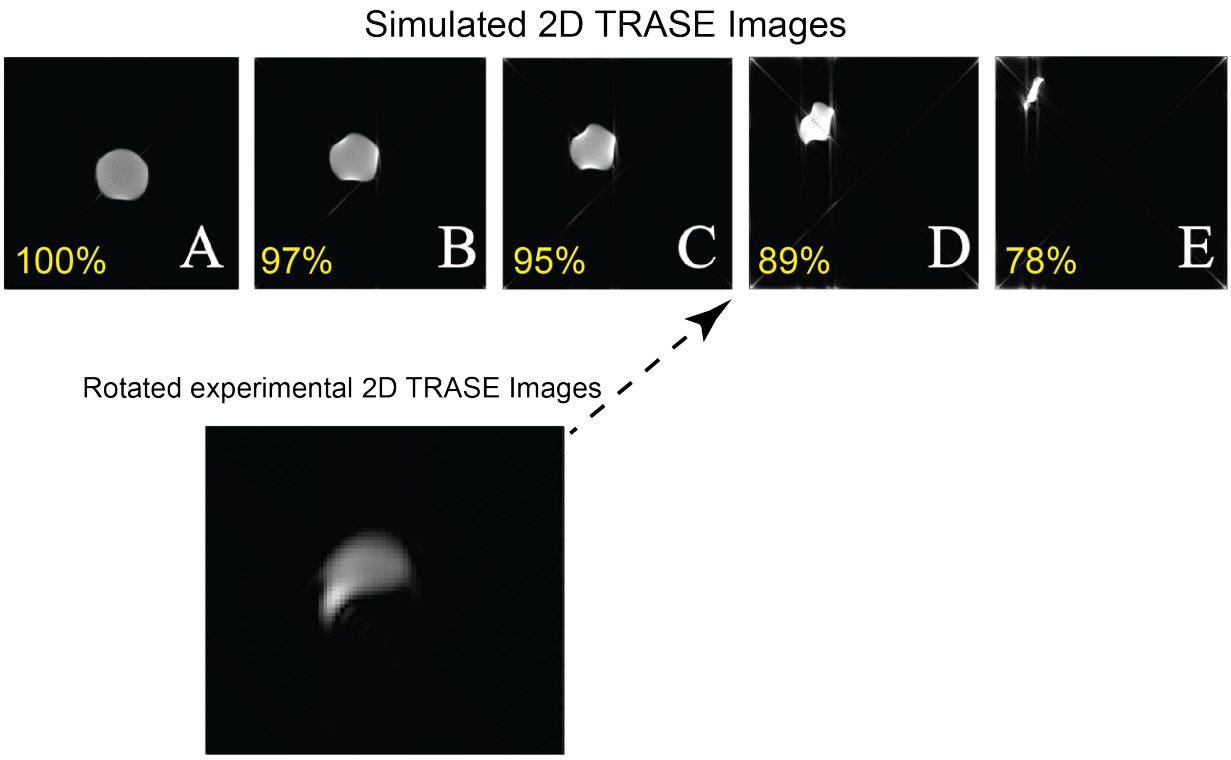

Figure 6.7: Reconstructed images of a circular object from 2D TRASE simulations using varying levels of $|B_1|$ contribution from the primary coil - (A) 100% (no coupling) (B) 97% (C) 95% (D) 89% and (E) 78%. As the levels of B_1 field coupling increase from panel (B) to (E), the object shape distortions significantly dominate the simulated 2D TRASE images. By comparison, the experimental 2D TRASE images displayed in Figure 6.6 show very similar image distortions, and can be categorized between panel C and D, demonstrating a value of 89% to 95% for the $|B_1|$ contribution from the primary. Images were adapted from [88].

niques including the addition of extra regular solenoids and a small transformer constructed with loops of wire. With this three-coil set geometry, 2D TRASE images were acquired, as shown in Figure 6.6. Due to imperfect 2D TRASE encoding, the FFT images show noticeable artifacts such as non-uniform signals (local signal enhancement) and distorted object boundaries. The Bloch simulations (see Figure 6.7) confirmed that the unwanted B_1 field contributions from secondary coils due to coil coupling, even at low levels of 10%, were sufficient to cause severe image artifacts that were similar to the experimental images. Therefore, a $|B_1|$ contribution of 95% or higher from the primary transmit coil is required for accurate 2D TRASE MRI.

As a support of this point, after the flip angle adjustments on each transmit primary coil I also performed three individual 1D TRASE experiments (see Figure 6.5) using any two of three coils pairs, producing three different 1D profiles for the cylindrical imaging object. It has been found that fairly good profiles were obtained in two coil pairs, while the 1D profile generated by the pair of two twisted solenoids TS1+RS1 and TS2+RS2 appeared to slightly distorted, *e.g.*, 1D profile in a slight asymmetric triangular shape. This was also in qualitative agreement with S parameter measurements where the lowest coil isolation was achieved between two twisted solenoids, *i.e.*, $S_{12} = -22.9$ dB.

The *Fasthenry2* mutual inductance simulation was not completely precise, since actual coil position showed that different z shifts provided an improved null condition, which could arise from other coupling mechanism (such as capacitive) not captured by the mutual inductance simulation. In simulations the turn number of regular solenoid was restricted to integer values (see Table 6.1), although the same simulation with larger search range may further decrease the coupling coefficients and guide a more efficient geometric decoupling. Undeniably, this also requires more accurate matching of simulated and physical geometry.

In the simulation studies [88] the coil interactions have resulted in noticeable B_1 field disturbances (see in Appendix III). These factors include reduced phase gradient strength and linearity, which caused distorted low spatial resolution images. A spatial shift in the phase

gradient was also observed, possibly caused by the superposition of out-of-phase induced currents (*i.e.*, the phase of the induced currents are likely different than the primary current), leading to a shifted image as can be seen in Figure 6.7 from panel A to E. The simulation results also suggest that the object shape distortions occur predominantly due to the B_1 phase errors (instead of B_1 magnitude errors). For this reason, the signal intensity from the sample gets mapped into incorrect spatial locations by a Fourier transform which leads to smearing in the image domain.

It cannot be denied that the acquired 2D TRASE images were badly distorted and not usable. Therefore, for clinical applications, artifacts caused by coil interactions should be carefully addressed with additional decoupling strategies. However, this three-coil set is inherently efficient for low-field vertical B_0 geometry. As the first TRASE 3-coil array, its capability of encoding x and y dimensions in the axial plane and making CT-like images, is a crucial step towards TRASE imaging for clinical purposes.

The results in this work indicates that, unlike traditional MR imaging, 2D TRASE is highly sensitive to coil coupling. While geometric decoupling techniques are simple and efficient to reduce coil interactions, for certain coil array(s) it may not be sufficient to produce artifact-free 2D TRASE images. Under this circumstance, other coil isolation methods may be used in conjunction with geometric decoupling to mitigate the remaining interactions in TRASE coil array. These include active RF switch (detuning), advanced coil circuitry design, and parallel RF transmit system (this will be discussed in the next chapter). However, it should be mentioned that geometric decoupling is an effective, reliable, and practical method to minimize coil interactions, and hence for TRASE coil array, should be implemented whenever is possibly achievable. It allows one to independently tune and match each coil since the splitting resonance is avoided. The understanding of the acceptable levels of coil interactions is considered as a significant step to a successful 2D TRASE imaging.

6.6 Conclusions

The twisted solenoid geometry is a promising candidate for TRASE encoding due to several advantages including the compact cylindrical design, high efficiency, and large usable imaging volume. In this chapter a three-coil set consisting of two twisted solenoids and one saddle coil is proposed. Each coil is isolated using geometric decoupling methods which are effective to decouple coil array even with high inherent coupling. Using this three-coil set, 2D TRASE MRI is sensitive to coil interactions such that an amount of merely 5% unwanted secondary B_1 fields could severely impair image quality. This result is a significant step in determining the acceptable levels of coil interactions. In case coil B_1 field isolation achieved by geometric decoupling could not fulfill this constraint, alternate or additional means need to be employed to increase the isolation up to the required level. These may include active RF switching, new coil circuitry design and advanced parallel transmit system. While the quality of acquired 2D images can be further improved, this work proposes an efficient three-coil set capable of generating 2D TRASE images in transvese plane for a vertical B_0 magnet for the first time. This gradient set is well suited to low B_0 field MRI magnets (*e.g.*, Halbach arrays and bi-planar magnets) which have clinical relevance as shown by others such as *Hyperfine Inc.*.

6.7 Acknowledgements

In this work I would like to thank my colleagues Pallavi Bohidar, Aaron Purchase and Abbas AlZubaidi for their advice on coil construction. I would also acknowledge funding sources 1) Natural Sciences and Engineering Research Council of Canada, Grant/Award Number: RGPIN-2016-05183, and RGPIN-2015-03992; 2) 2018/2019 Alberta Cancer Foundation Antoine Noujaim Scholarship, Grant/Award Number: 27228; and 3) Canadian Space Agency FAST grant, for the support of this work.

Chapter 7

Design of a Parallel RF Transmission System (PTx)

7.1 Introduction

Multi-transmit or parallel transmission (PTx) technology is an exciting development in MRI that was proposed in 2003 by Katscher et al ("transmit SENSE") [89]. In many ways it is the natural extension of widely used parallel receiver imaging in the 1980s, being considered as an important milestone in the history of MRI [68], [90]. The basic concept of PTx is relatively simple: the MRI signal is excited by transmitting the RF energy using several transmit coils as opposed to a single one. By dividing the coil into separate independently powered and controlled elements each produces their own B_1 subfields, the sum of these subfields constitutes the net B_1 field experienced by the tissue. This PTx idea is widely implemented at high fields (*i.e.*, 7 T in the brain and 3 T in the body), because the wavelength of the RF energy in the body becomes comparable to the size of the body, resulting in a strongly non-uniform transmit field profile [91]. Additionally, as already demonstrated in Chapter 2, SAR increases with the field strength thus introducing safety concerns at high B_0 fields. By applying PTx technologies it is possible to carefully control the homogeneity of RF excitation and the distribution of magnetic and electric fields produced in tissues, which can reduce standing wave (dielectric effect) shading artifacts as well as minimize RF-energy deposition

[92], [93].

In recent years the PTx techniques have found many applications in shortening RF pulse duration, enhancing spatial definition, reducing required RF power, B_1 shimming, and compensating patient-induced RF inhomogeneities [94]. In some 3 T systems, two channel transmitters are now installed as standard from the major vendors. A recent study in 2019 demonstrated a platform for 4-channel PTx MRI at 3 T [95]. Many new 7 T scanners are now equipped with multiple transmit channels. As an example, a 32-channel PTx add-on for 7 T MRI was proposed in 2019, showing very promising performance for ultrahigh field whole-body imaging [96]. With further developments of advanced RF engineering work such as optimal design of RF coils and amplifiers, The PTx technology matures and is hoped that will prove its efficacy for routine *in vivo* research and clinical use for high field MRI.

In addition to these benefits which promise a better imaging performance, the PTx has more capabilities. In recent studies it was shown that a parallel transmit array system can be used to cancel RF currents that are induced on a bare wire [97] and a loop receive coil [80], being implemented as an active decoupling approach. In the literature [80], it has been shown that during RF transmission the B_1-induced voltages can be minimized if a carefully-adjusted RF pulse (phase and amplitude) can be transmitted in the secondary coil simultaneously using a PTx system (practically, this induced current should be measured directly in the secondary coil in real time which will be discussed in the future work in Chapter 8). A total effective isolation of -70 dB was achieved between two coils by combining geometrical (-20 dB) and active PTx decoupling (-50 dB). For the three-coil set introduced in Chapter 6, the phase gradient B_1 field generated by each single coil is transmitted alternately during the spin echo train to impart a progressively increasing spatial phase modulation, with each k-space point collected by averaging the center points of each acquired echo. From previous work [88] and the results shown in Chapter 6, it is clear that in order to obtain a proper 2D TRASE image, pure geometrical decoupling among three RF coils are not sufficient to avoid coil cross-talks. To add further effective isolation, one solution is to combine this geometrically-decoupled

three-coil set, with an active-decoupling PTx system capable of generating three independent RF pulses.

However, the design of such a PTx system can be quite complex and expensive to purchase. In particularly, it requires rigorous control over timing, power, RF phase and amplitude at each channel. All RF transmitters need to be well synchronized with high temporal precision and each channel is driven by its own RF amplifier. If needed, each channel could be also equipped with its own T/R switch to allow bimodal operation. Alternatively, all RF coils can operate in transmit mode only while separate surface coil(s) can be used as receiver element(s), making a higher SNR acquisition in a shorter time, at the expense of additional coils that also need to be decoupled to the transmitters.

Since PTx technologies are mostly designed for high field MRI system, in this work I will propose the design of a low-field PTx system for TRASE MRI. Specifically, this PTx architecture features four channels, each of which can generate independent single-frequency RF pulses with full control over amplitude and phase modulation. I will only show examples of generating rectangular RF pulses, however, the PTx system is capable of generating arbitrary waveform shapes. This efficient new PTx system uses low-cost components and is hoped to find many applications in low-field, low-cost MRI regimes.

7.2 Theory

For an RF coil array such as TRASE RF system, multiple B_1 fields are generated by different RF coils. An example of a 2D TRASE coil array consisting of three RF coils (TS1+RS1, Saddle, TS2+RS2) equipped with a single transmission system is illustrated in Figure 7.1a). In this case the B_1 field generated by the primary transmit coil will induce currents in the other secondary RF coils, even if a good isolation of coils is achieved using pure geometric decoupling techniques (*i.e.*, 20 to 30 dB). In previous 2D TRASE study in Chapter 6, these small induced currents are found responsible for significant image degradations [88]. To add

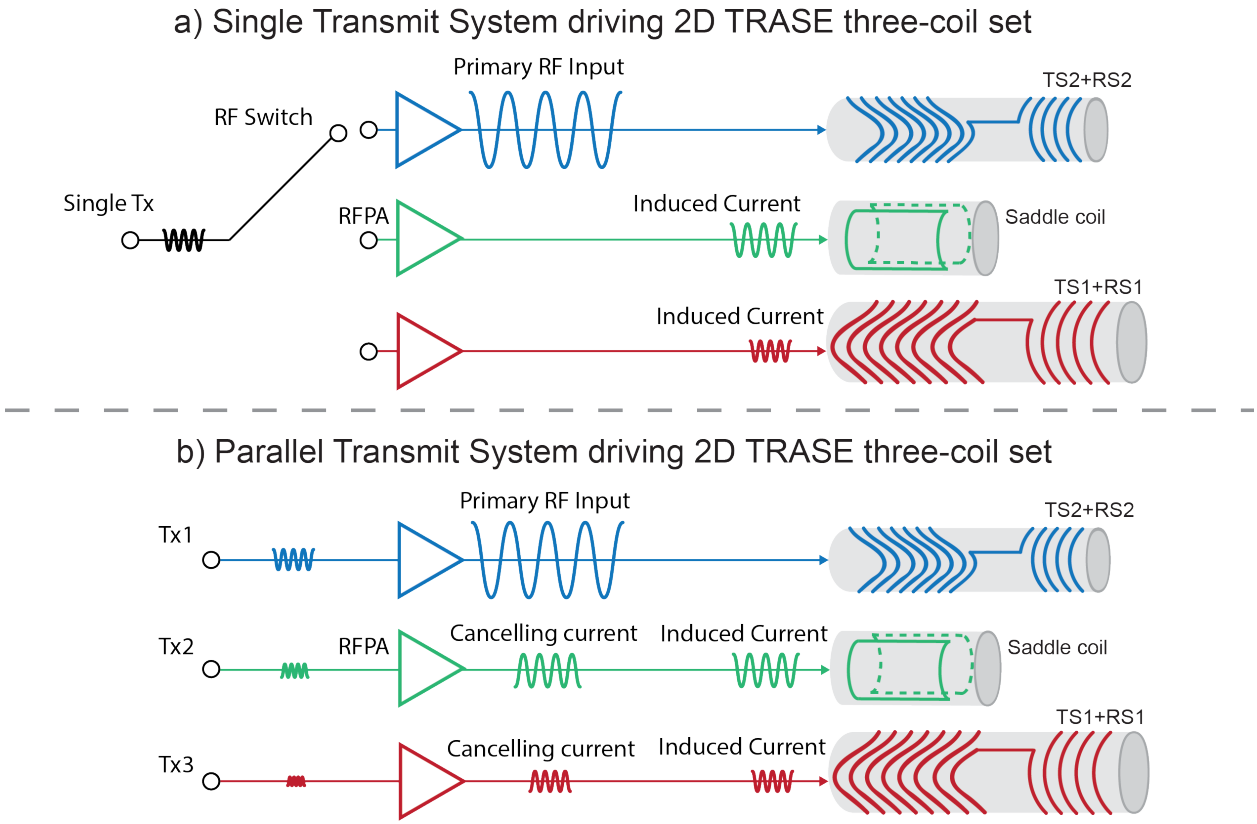

Figure 7.1: Schematic of different transmit system driving a geometrically-decoupled three-coil set for 2D TRASE, containing previously demonstrated twisted solenoid pair TS1+RS1 and TS2+RS2, and a saddle coil. **a)** The single transmit system generates only one RF input. All experiments performed in this thesis up to this point used such a system. Using an RF switch to select the line of signal transmission, while one primary coil is transmitting RF pulse, B_1 induced currents (due to residual coupling not captured by geometric decoupling techniques) in the other two secondary coils generate magnetic fields as well, resulting in a distorted B_1 field which affects TRASE encoding. **b)** The parallel transmit system (PTx) can generate three independent RF pulses simultaneously. To cancel the induced currents, two cancelling currents (same amplitude but opposite phase) can be generated on Tx2 and Tx3 individually. This effectively disables Tx2 and Tx3 transmission, allowing a clean TRASE encoding to be made.

further coil isolation, a PTx concept is adapted to cancel these induced RF currents shown in Figure 7.1b). While the primary coil is transmitting, using a PTx system it is possible to cancel the induced currents on secondary transmit RF coils, if the input parallel cancelling currents can be generated with precisely adjustable amplitudes and phases.

For a TRASE RF system with N coils equipped with PTx technologies, when the primary coil i is transmitting with current $I_{i,i}$, B_1 induced current in the secondary coil j can be described as $c_{i,j}I_{i,i}$ in which $c_{i,j}$ is a complex coefficient representing the geometric and electromagnetic factors that affect the amount of coupling between transmit coils i and j. By adjusting the parallel current input $I_{i,j}$ into the secondary coil j, one can theoretically achieve a cancellation of the total current in coil j while coil i acting as the primary transmit coil. This can be expressed as:

$$c_{i,j}I_{i,i} + I_{i,j} = 0 \tag{7.1}$$

For the example of a 2D TRASE coil array consisting of three RF coils, the above formula can be re-written as a vector form:

$$\begin{pmatrix} I_{11} & 0 & 0 \\ 0 & I_{22} & 0 \\ 0 & 0 & I_{33} \end{pmatrix} \begin{pmatrix} c_{11} & c_{12} & c_{13} \\ c_{21} & c_{22} & c_{23} \\ c_{31} & c_{32} & c_{33} \end{pmatrix} + \begin{pmatrix} I_{11} & I_{12} & I_{13} \\ I_{21} & I_{22} & I_{23} \\ I_{31} & I_{32} & I_{33} \end{pmatrix} = 0 \tag{7.2}$$

The I_{ii} is the current needed to drive a 180 degree refocusing pulse using coil i as the primary transmit coil, which depends on both coil efficiency and the loaded sample. To determine the value of $I_{i,j}$, it is sufficient to measure the induced current $c_{i,j}I_{i,i}$ and to solve $I_{i,j} = -c_{i,j}I_{i,i}$ (Note that c_{ij} = -1 in case of $i = j$). During a TRASE experiment, PTx is transmitting RF pulses into all coils while due to currents cancellation only the primary coil generates the desired B_1 field for TRASE encoding, achieving practical coil array isolations. This was verified in LTSpice simulation in Figure 7.2.

7.3 Preliminary Study using LTSpice Simulation

7.3.1 LTSpice Simulation Methods

To investigate the induced currents and their cancellations based upon PTx techniques, circuit simulations using *LTSpice IV* were performed. As shown in Figure 7.2a), the circuitry components were connected together to represent the actual circuits of two coils (TS1+RS1) and (TS2+RS2). The coupling coefficient of this pair of coils was set to $k_{12} = 0.052$, as suggested in the previous *FastHenry2* study in Chapter 6. In this circuit simulation two AC voltage source $V1$ and $V2$, each has a 50 Ω resistor in series, were connected to two coils separately. The primary transmit coil was TS1+RS1 so a 1 V amplitude AC supply was provided by $V1$ as a constant input. To evaluate the induced current in coil TS2+RS2 due to coil cross-talk (*i.e.*, single transmit system), in the first simulation the voltage source $V2$ supplied no current by setting the AC amplitude as 0V. In PTx simulation, various amplitudes and phases of $V2$ input were manually adjusted. In each simulation, the currents following through two coils $I(L1)$ and $I(L2)$ at frequency of $f = 9.28$ MHz were recorded.

The LTSpice simulation results are essential to guide the design of the PTx system, so in this section I will include all LTSpice simulation findings prior to the introduction of PTx system.

7.3.2 LTSpice Simulation Results

The LTSpice simulations results can be found in Figure 7.2b), Figure 7.2c) and Table 7.1. Table 7.1 lists the current $I(L2)$ values (flowing in the secondary coil TS2+RS2) under different $V2$ inputs (various combinations of amplitudes and phases), while the same $V1$ input was given into the primary coil TS1+RS1. Specifically, when no $V2$ supply was given, the induced current $I(L2)$ was 1.22 mA. This represents a signal transmission system as illustrated in Figure 7.1a), with the simulation plot shown in Figure 7.2b). The Figure 7.2c)

a) The schematic of LTSpice simulation for TS1+RS1 and TS2+RS2

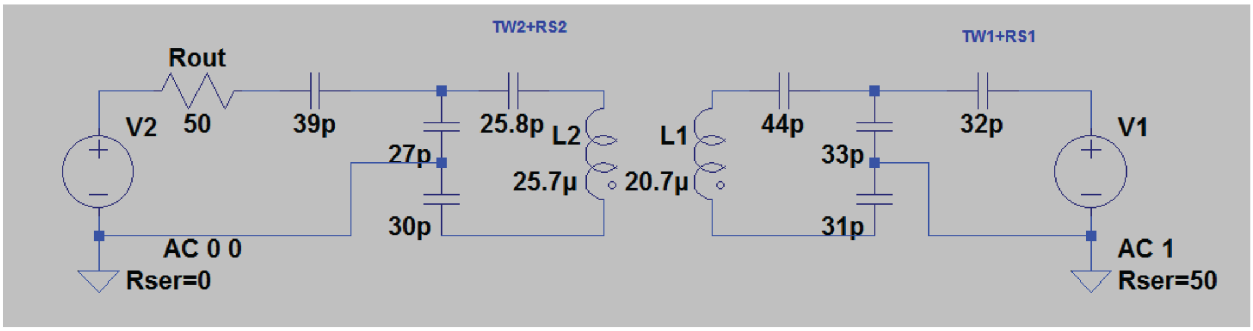

b) Simulated currents in coils using single Tx

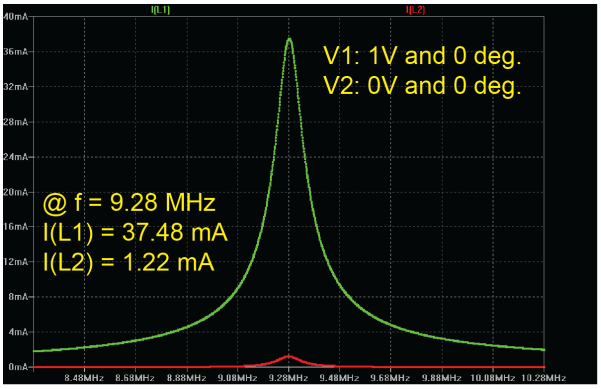

c) Simulated currents in coils using parallel Tx

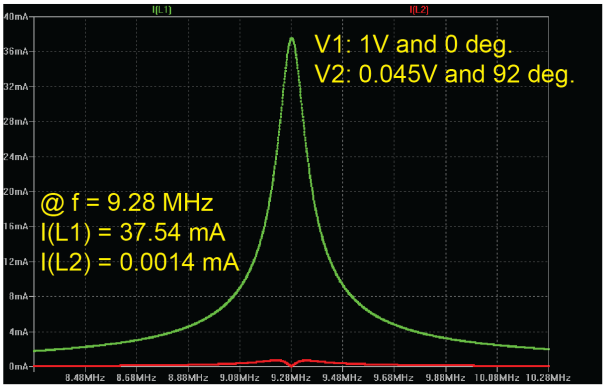

Figure 7.2: LTSpice circuit simulation for the geometrically-decoupled coil pair TS1+RS1 and TS2+RS2. **a)** Two coil circuits were simulated in LTSpice each was connected to a AC voltage source. In this simulation the primary transmit coil was TS1+RS1, so the voltage source $V2$ only generated a current input to cancel the induced current. **b)** Coil currents simulation results when $V2$ was not used. This represents the single transmission system which was used in the experiments reported from Chapter 4 to 6. For a 1 V amplitude AC supply on coil TS1+RS1, the induced current in the secondary coil was found to be 1.22 mA at the frequency of 9.28 MHz. **c)** Coil currents simulation results when $V2$ was enabled. This represents the concept of PTx and the best current cancellation was achieved ($I(L2)$ = 0.0014 mA at the frequency of 9.28 MHz) when the secondary coil was supplied by $V2$ using 0.045 V amplitude and 92 degree phase AC input. Between configuration b) and c) the current flowing through the primary coil $I(L1)$ increased by only 0.16%, indicating little impact on B_1 field generation for MR encoding.

Simulated $I(L2)$ (Milliampere)	$V2$ Input Amplitude (Volt)								
	$\|V2\|$ =	0 V	0.01 V	0.02 V	0.03 V	0.04 V	0.045 V	0.05 V	0.06 V
$V2$ Phase 0 deg.		1.22mA	1.26mA	1.36mA	1.50mA	1.67mA	1.77mA	1.87mA	2.08mA
$V2$ Phase 30 deg.		1.22mA	1.12mA	1.08mA	1.11mA	1.20mA	1.26mA	1.34mA	1.52mA
$V2$ Phase 60 deg.		1.22mA	0.999mA	0.809mA	0.680mA	0.650mA	0.677mA	0.729mA	0.890mA
$V2$ Phase 85 deg.		1.22mA	0.949mA	0.679mA	0.416mA	0.187mA	0.150mA	0.219mA	0.460mA
$V2$ Phase 90 deg.		1.22mA	0.946mA	0.672mA	0.399mA	0.129mA	0.045mA	0.158mA	0.429mA
$V2$ Phase 92 deg.		1.22mA	0.946mA	0.672mA	0.397mA	0.123mA	0.014mA	0.152mA	0.426mA
$V2$ Phase 95 deg.		1.22mA	0.947mA	0.673mA	0.401mA	0.137mA	0.066mA	0.166mA	0.433mA
$V2$ Phase 100 deg.		1.22mA	0.950mA	0.681mA	0.421mA	0.203mA	0.172mA	0.236mA	0.470mA
$V2$ Phase 120 deg.		1.22mA	0.987mA	0.780mA	0.627mA	0.574mA	0.595mA	0.645mA	0.808mA
$V2$ Phase 150 deg.		1.22mA	1.10mA	1.04mA	1.05mA	1.13mA	1.19mA	1.26mA	1.44mA
$V2$ Phase 180 deg.		1.22mA	1.24mA	1.32mA	1.45mA	1.61mA	1.71mA	1.80mA	2.02mA

Table 7.1: The LTSpice simulations for a geometrically decoupled coil pair TS1+RS1 and TS2+RS2 using different $V2$ inputs. The primary coil was TS1+RS1 and the input voltage source $V1$ in all simulations was kept as a constant (*i.e.*, 1 Volt amplitude and 0 degree phase). To cancel the induced currents on coil TS2+RS2, various combinations of phases and amplitudes were manually adjusted, where the best canceling was achieved when $V2$ input a signal of 0.045V amplitude and 92 degree phase, resulting in a 98.9% current reduction from 1.22 mA to 0.0014 mA at the frequency of 9.28 MHz. The simulation currents plot can be found in Figure 7.2b) and c).

demonstrates the optimal current cancellation scenario when a signal of 0.045 V amplitude and 92 degree phase was supplied at $V2$. In this case, a 98.9% current reduction was achieved by the transition of single transmission to a parallel transmission. In the meantime, the inclusion of $V2$ supply increased the current in primary coil $I(L1)$ by only 0.16% from 37.48 mA to 37.54 mA, indicating little change for MR encoding. Data in Table 7.1 also demonstrates that accurate adjustment in the amplitude and phase of $V2$ is needed to cancel the induced current. To verify such sensitivity, a bench measurement between TS1+RS1 and TS2+RS2 was also performed in the lab using a two-port function generator to mimic two transmission supplies, showing a close agreement (results not shown).

Despite the fact that in LTSpice circuit simulation coil characteristics such as efficiency and quality factor Q were not included, it is clear to see from these results that the PTx concept can be used to cancel the induced RF currents in secondary coil(s), thus, being implemented as an active decoupling approach. More importantly, in order to minimize the induced currents, accurate phase and amplitude adjustments in the input source are necessary. This is a key finding from this simulation, because the initial idea of using digital control components such as variable attenuator and phase shifter are unable to provide such

accuracy, *e.g.*, most purchasable phase shifters are working in the GHz range with a phase shift accuracy of 3 to 5 degree. In the following sections, I will introduce the design a PTx system using more advanced components.

7.4 Methods

7.4.1 Design of a New PTx System

The goal of this project is to design and implement a new, inexpensive parallel transmit system that is an improvement to the existing TRASE MRI transmit console which has receiver module and can generate single RF signals. By taking advantages of the current single transmission system (TMX console located in CCI) including stable synchronization clock (f = 10 MHz), Python-compatible MR sequence programming, and various outputs (*e.g.*, RFPA gatings and RF signals), the design of PTx was simplified to generate multiple RF signals with fully adjustable amplitudes and phases, controlled by a fast programmable controller. In practice, the target PTx design needs to have the following features:

- **A).** Have at least three channels that can generate RF waveforms simultaneously to drive a 2D TRASE RF system consisting of three coils;
- **B).** All transmit channels can generate sinusoidal waveforms with an identical frequency (*e.g.*, f = 9.28 MHz), and preferably within a range of 1 MHz to 10 MHz for potential use in other low-field MRI systems;
- **C).** The magnitude and phase of the RF waveform on each channel can be independently adjusted and updated promptly during an echo train, preferably within 100 μs;
- **D).** The generated RF pulses must maintain phase coherence with the MR system, *i.e.*, be synchronous with the reference clock.

To meet all design targets, Figure 7.3 shows an overview of an MR RF system, where the design of PTx is broken down into two main components - the waveform generator based upon AD9106-EBZ and a controller using Altera Terasic Cyclone V Analog-to-Digital (ADC) - System-on-Chip (SoC). The introduction for each board is given in the section 7.4.2. Additionally, it should be mentioned that the integration of current single transmit console and the newly-designed PTx, MR imaging receiving and reconstruction are beyond the scope of this project, hence, will not be reported in this chapter. Now, I will focus on the design and implementation of the PTx system only. Specifically, I will introduce the PTx system design and test using the following sections:

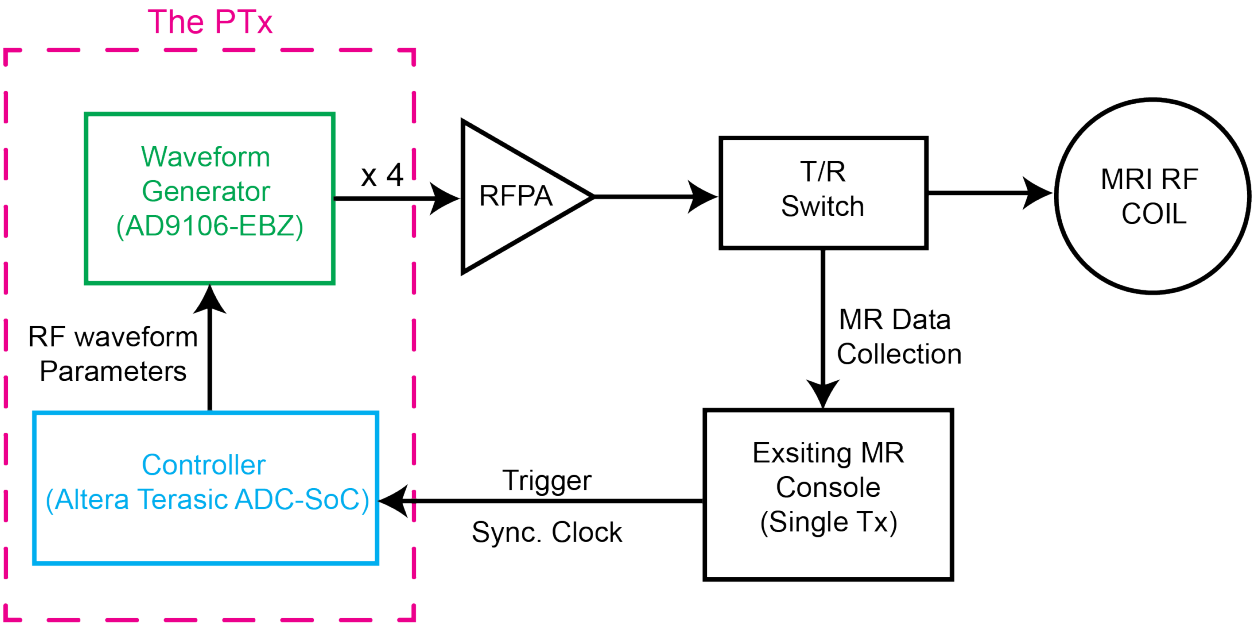

Figure 7.3: The layout of an updated MRI RF system equipped with the newly-designed PTx capability. The old existing single transmission MR console is replaced by the new PTx which contains two main components: 1) waveform generator based upon AD9106-EBZ; and 2) controller using Altera Terasic ADC-SoC. The existing MR console only provides trigger signals and a reference clock for system synchronization, while RF pulse generation is made by the PTx which has four output channels.

- **Introduction of Two Selected Boards** The design requirements have been listed in the above, based on these targets, I will list the reasons independently for why the two boards (AD9106-EBZ and Altera Terasic Cyclone V ADC-SoC) were selected, followed by a brief introduction for each.

- **Waveform Generation Control:** On both boards the exact controls which were divided into three main steps, are introduced. Technical details and board configurations including hardware and software are also discussed in this section.

- **Waveform Bench Measurements:** The bench measurements for RF pulse generations are introduced in this section. The "Phase I" measurement mainly focused on the evaluation of the SPI communication (*i.e.*, data transfer) between two boards, and the functionality of initializing waveform generation. The "Phase II" measurement tested the clock synchronization, and the generation of waveforms using an upgraded higher frequency clock and trigger signals from the controller.

7.4.2 Introduction of Two Selected Boards

Waveform generator: AD9106-EBZ

In this work the AD9106 chip was used as a waveform generator chip. It was chosen because it is a high performance, quad digital-to-analog converter (DAC) waveform source for generating waveforms using a 12-bit output direct digital synthesizer (DDS). This chip is capable of generating four single-frequency sine waveforms with a master clock up to 180 MHz, which satisfies the target low-field MRI applications. Alternatively, samples can be written to the SRAM and used for pattern generation, allowing users to generate any arbitrary waveform loaded in from a file. In addition, an internal pattern control allows one to program the profiles of four DACs including pattern period, offset, gain factor, and phase, etc., by writing values to the designated registers using the serial peripheral interface (SPI). Moreover, it should be mentioned that with AD9106 all four DACs share the same frequency. Therefore, for the need of generating waveforms with independent frequency in each channel, one may choose other chip such as AD9959. However, AD9959 has only 10-bit DAC, 2 bits lower than that of AD9106, and for the target TRASE MRI applications single frequency output is sufficient. Detailed description of this chip can be found in the literature [98].

The AD9106 chip is an ideal candidate meeting the needs, and it has an evaluation board (AD9106-EBZ) version available online from Digikey [99], see picture in Figure 7.4a). The original AD9106-EBZ is equipped with 1) AD9106 chip that is needed for RF pulse generation; 2) a peripheral interface controller (PIC) programmed to function as a PC USB interface to the SPI port; and 3) an AD9514 clock divider chip [100] that converts external clock source to a proper frequency clock input to the chip AD9106.

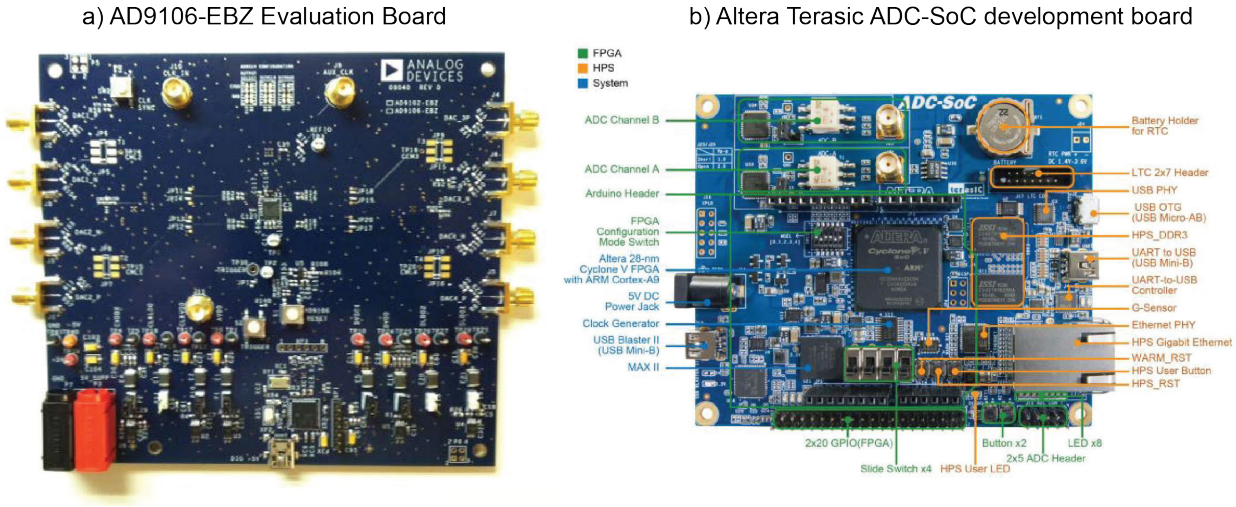

Figure 7.4: Picture of two boards used in the PTx. **a)** The original AD9106 Evaluation Board AD9106-EBZ [99]. **b)** Altera Terasic Cyclone V ADC-SoC development board. The FPGA and HPS parts are labeled with green and orange colors individually [101].

Controller: Altera Terasic Cyclone V ADC-SoC

In the literature some have attempted to use Raspberry Pi as a controller and combine it with AD9106-EBZ as a transmitter module for ultrasound applications [102], [103]. For TRASE MR applications, more elegant controls such as timing, speed and synchronization are required, so a Altera Terasic Cyclone V ADC-SoC board was selected as the controller in this project, see picture in Figure 7.4b). A system-on-chip (SoC) is an integrated circuit that integrates all or most components of a computer or other electronic system. These components almost always include a central processing unit (CPU), memory, input/output ports and secondary storage – all on a single substrate or microchip, the size of a coin, and

due to this reason SoCs consume much less power and take up much less area than multi-chip designs with equivalent functionality.

The selected controller features an Intel Cyclone V SoC device, which contains two main components: a Hard Processor System (HPS), and an field-programmable gate array (FPGA). The HPS contains an ARM Cortex* A9 dual-core processor, which is used to run Linux operating system and various peripheral devices such as timers, general-purpose input/output (GPIO), USB, and Ethernet [101]. Not only this SoC board has powerful hardware parts that are fully programmable to generate parameters needed to control AD9106-EBZ, it is also equipped with high-speed DDR3 memory and ADC capability, showing a great promise to be further developed as a receiver control module (not include in this project).

In this PTx design, the HPS and FPGA will be both used. Specifically, the HPS is responsible for updating register values inside the AD9106-EBZ through SPI communication. The FPGA is used to generate trigger and in-sync upgraded high-frequency clock signals (150 MHz) at the detection of dummy initialization signals including a 10 MHz clock and a trigger signal generated from the existing MR console. Additionally, the HPS and FPGA are on the same silicon chip and tightly coupled via a high-bandwidth interconnect system built from high-performance bus bridges, so they can easily access to each other [101]. However, for the goal of this project to demonstrate the design of PTx system and show its functionality, such communication is not mandatory.

7.4.3 Waveform Generation Control

The generation of waveforms using the PTx requires the coordination of two boards. In Figure 7.5, the connections between two boards are shown. In overview, the approach was as follows: (1) Configure two boards with required softwares and perform necessary modifications; (2) Establish a SPI communication between AD9106-EBZ and the HPS of Terasic ADC-SoC, so one can write proper register values to setup the AD9106 chip; (3)

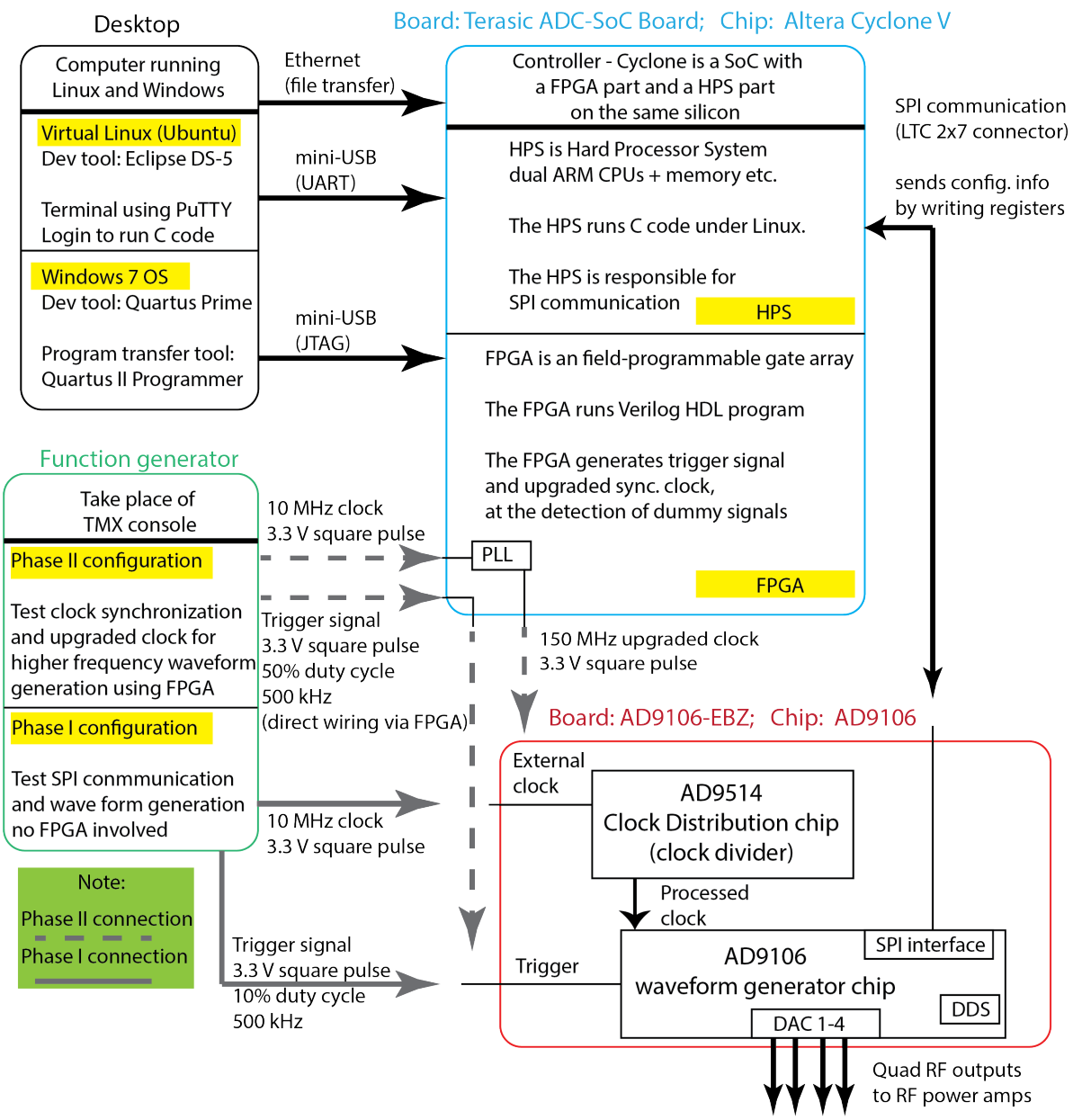

Figure 7.5: The schematic of wire connections in the PTx design. A desktop running host Windows 7 and virtual Linux (Ubuntu) operating systems was used to interact with the controller board (Terasic Cyclone V) to load C and Verilog HDL programs to HPS and FPGA, respectively. The waveform generator board AD9106-EBZ is equipped with a clock divider chip AD9514 and a main waveform generation chip AD9106 which contains DDS, SPI interface and DACs. The exact block diagram for AD9106 chip is demonstrated in Figure 7.6. The function generator is used to mimic the TMX console to provide necessary dummy signals (clock and trigger) to drive the PTx under two different configurations. In Phase I configuration (solid gray lines) no FPGA was needed, while in Phase II configuration (dotted gray lines) the FPGA was used to upgrade clock signal and provide the necessary trigger via direct wiring connection.

Program the FPGA of Terasic ADC-SoC and generate required clock and trigger signals to drive AD9106-EBZ for waveform generation.

Board modifications and configurations

AD9106-EBZ: In order to use the purchased AD9106-EBZ, several modifications are needed before it can be implemented as a waveform generator for the PTx, as described below.

- **Change clock divider setup** - In this work samples are clocked into the DAC using an external clock signal that is connected to the AD9514 [100], an on-board configurable clock divider. By default the AD9514 is set to divide by eight with external resistors, producing a processed clock signal. As a result, this will cause a significant aliasing problem if a high frequency signal output is needed. For example, if a 10 MHz clock is used as the external reference clock input, generation of sine waveforms with frequency larger 1.25 MHz is impossible with default divide number of eight. To avoid the aliasing issue, it is best to eliminate this divide effect, therefore, the first modification was to remove and solder 0 ohm external resistors on the AD9106-EBZ board to set up the divide number to be one, see details in Appendix IV.

- **Disable PIC USB interface** - Inside the AD9106 chip, the waveform output depends on the control register values which can be configured through SPI communication. Originally, the AD9106-EBZ is equipped with a PIC that allows one to update register values through a USB interface. However, for clock synchronization purpose, the PTx design uses a Altera Terasic ADC-SoC to control the waveform generator rather than a Windows PC, so the PIC has to be disabled and hand in full control to the Altera Terasic ADC-SoC controller. The modifications that was made for this change can be found in Appendix IV.

- **Board power and trigger** - The waveform generation is started by a negative edge on the trigger terminal. By default the trigger signal for default AD9106-EBZ board is

from "Trigger_PIC" which relies on the use of USB. Since the USB interface is removed and the plan is to send the trigger signal from the controller, modification on the board for trigger signal is needed. Additionally, the power connections to the AD9106-EBZ were also modified. These modifications are also detailed in Appendix IV.

Altera Terasic ADC-SoC: While no additional physical modifications are needed for the controller board, certain configurations are mandatory. Here, I will only list several main steps required to configure the board. For detailed setup procedures, the reader can refer to the literatures [101], [104]–[106].

- **Use HPS part** - In order to develop the controller Terasic ADC-SoC board, a Linux system was first stored onto a microSD memory and was inserted into the controller board and booted by the ARM processor. The HPS part was then connected to a computer running a virtual Linux system (Ubuntu 19.1), via a mini-USB cable that was connected to a UART-to-USB port. On the computer, a terminal program PuTTY (via the same mini-USB cable) was used to access the board with administrator-level privileges, allowing one to modify board settings and execute programs. The HPS can run C programs which were developed upon "Eclipse DS-5", an Integrated Development Environment (IDE) that combines the Eclipse IDE from the Eclipse Foundation with the compilation and debug technology of the ARM tools. It also combines the GNU tool chain for ARM Linux targets. One can use Eclipse for DS-5 as a project manager to create, build, debug, monitor, and manage projects for ARM targets [107]. Once an executable C program is made, it needs to be transfered to the controller using a network connection, which was established between the controller board and the computer using an Ethernet cable. In most cases, the IP address of the controller board needs to be adjusted so that it shares the same subnet with the computer's network.

- **Use FPGA part** - The connection to FPGA part was slightly different. In this case,

The FPGA part was configured through IEEE standards Joint Test Action Group (JTAG) interface, and connected to the same computer running a host Windows7 operating system, via the second mini-USB cable. The FPGA program was written by Verilog HDL using Quartus Prime 18.1 on Windows PC, and the program was downloaded directly into the Cyclone V SoC FPGA in Quartus II programmer. However, it should be mentioned that the configuration information will be lost when the power is off, so during the experiment the JTAG connection needs to be maintained.

Register setup on AD9106 via SPI interfaces

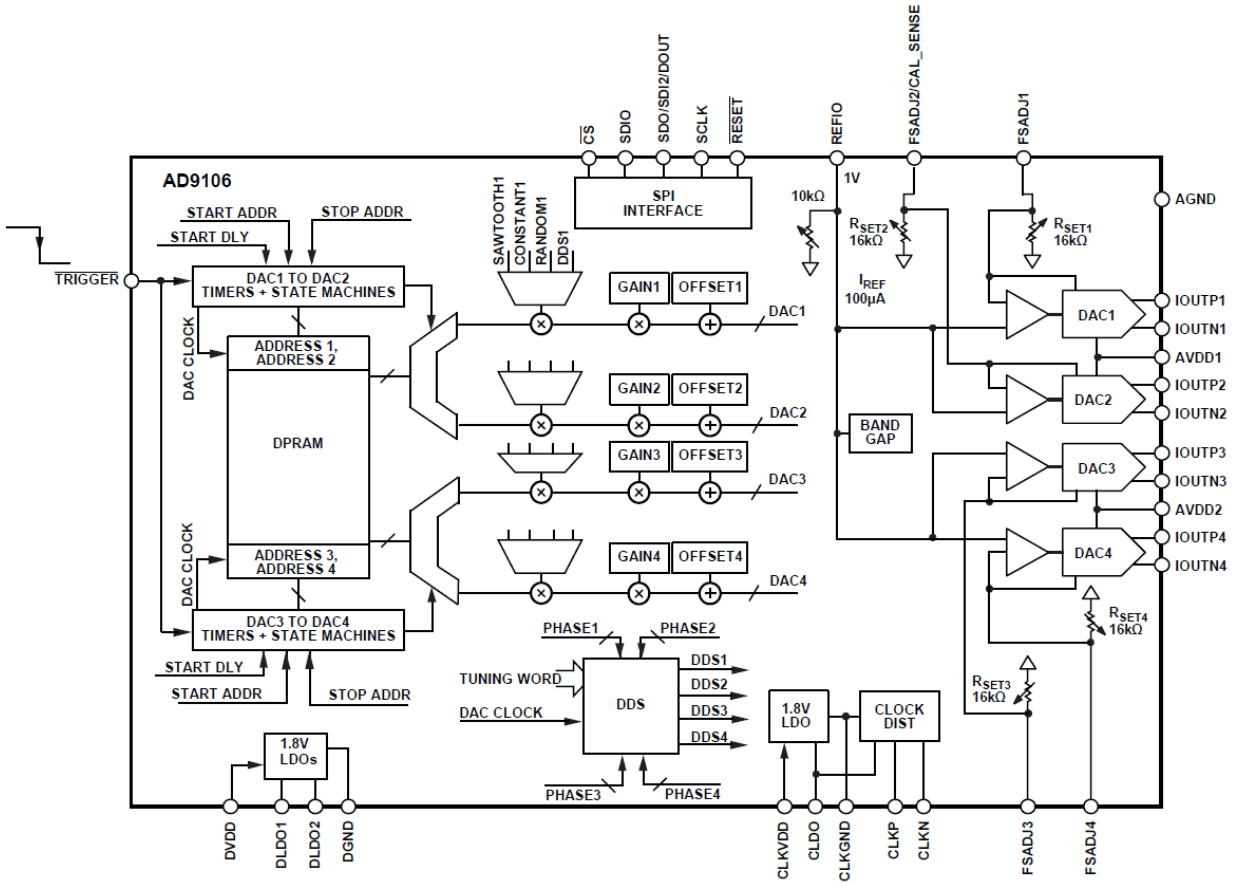

Figure 7.6: The block diagram of the waveform generation chip AD9106. It is equipped with a SPI interface, quad DACs, and DDS, which as a whole, are specifically designed for elegant RF waveform generation [98].

SPI controls between two boards: A detailed block diagram for the chip AD9106 is shown

in Figure 7.6. The SPI interface on AD9106 operates as a standard synchronous serial communication port, with MSB first and a 4-wire interface which allows read/write access to its registers. As shown in Figure 7.7a), [98] "$\overline{CS}$" is a chip select pin. When "$\overline{CS}$" is active low, it initializes data transfer at a rate up to the "SCLK" clock. To write register values, the user needs to first specify the read/write bit ($R/\overline{W}$) to be digital 0 on "SDIO" line, and then the 15-bit register address (A14 to A0), followed by the 16-bit data word (D15 to D0). It is also possible to read register values if ($R/\overline{W}$) is set to digital 1, which is useful in the development stage.

The HPS on Terasic SoC board was programmed and configured using National Semiconductor Microwire protocol [104]. As the master SPI it is equipped with a slave select signal "ss". When data transmission begins, a 16-bit control word is first sent out on the "txd" line. Immediately after the LSB of the control word is transmitted, the SPI master begins transmitting the data frame to the slave peripheral. Similarly, it is also a 4-wire SPI interface, so data receiving is available. However, there is one clock cycle delay in the "rxd" line under receiving mode, as depicted in Figure 7.7b). The physical SPI interface connections between two boards is shown in Figure 7.7c).

Register setup on AD9106: The AD9106 is highly configurable with 60 writable registers. For waveform generation, only a select number of registers need to be updated, while most registers can be left with their default values. Since this TRASE MRI application utilizes sinusoidal hard pulses, in Table 7.2 only the registers required to configure a sinusoid waveform generation on a single channel (*i.e.*, DAC1) are listed. The register setups can be replicated to generate three additional sinusoid waveforms on DAC2, DAC3, and DAC4 with adjustable phases and amplitudes. A "write-SPI.c" code is attached in Appendix IV showing this SPI configuration.

The setup of register values for sinusoidal waveform generation on DAC1 is as follows: SPICONFIG is first written to 0x0000 to reset all registers to the default values. WAV2_1CONFIG is configured to 0x3232 to select DDS1 as the output. At the default state, the waveform

a) SPI timing diagram for writing/reading registers on AD9106, MSB First, 4-wire

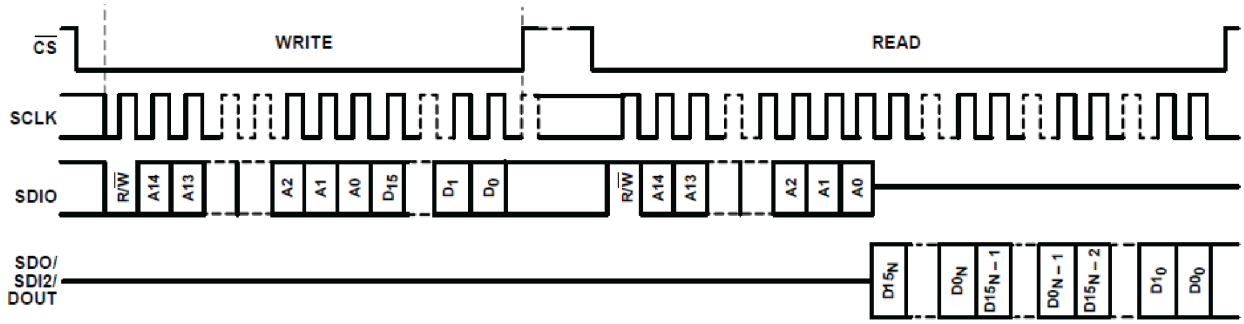

b) SPI master microwire transfer (receiving) on the HPS of Terasic, 4-wire

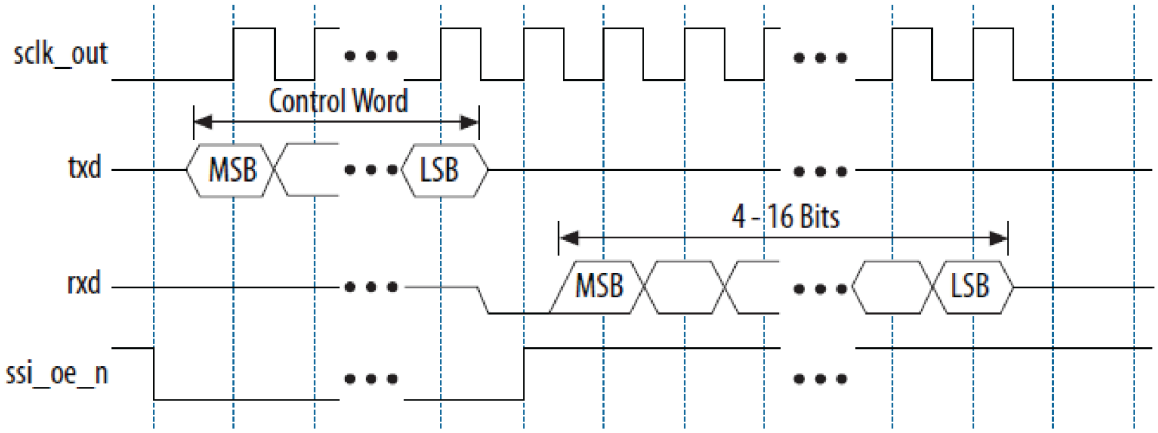

c) SPI Interface connections between Terasic (master) and AD9106 (slave) board

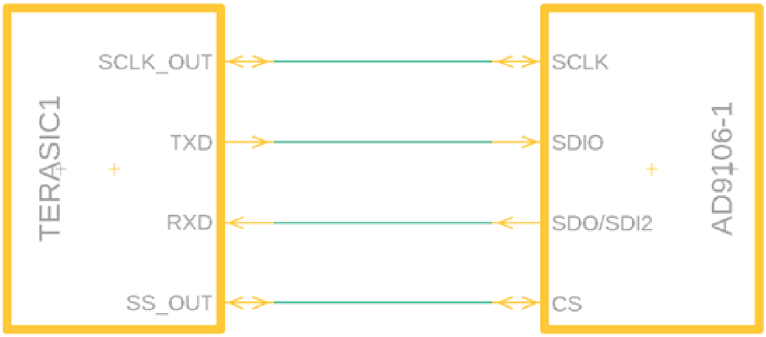

Figure 7.7: SPI controls on the PTx. **a)** The SPI timing diagram for AD9106. The SPI is a 4-wire interface that can write and read registers on AD9106, with MSB first [98]. **b)** The SPI timing diagram for the HPS of Altera Trasic ADC-SoC in receiving mode. It is also a 4-wire interface, and during transmit mode, no data are present (high impedance) on the serial master's "rxd" line [104]. **c)** The port connections between two boards' SPI interfaces.

Register Name	Address	Description
SPICONFIG	0x00	Reset entire register map
RAMUPDATE	0x1D	Update all SPI settings with new values
PAT_STATUS	0x1E	Enable memory SPI access and allows pattern generation
WAV2_1CONFIG	0x27	Select prestored waveform or values read from RAM
DAC1_DGAIN	0x35	Set digital gain of DAC1
DDS_TW32	0x3E	Set DDS tuning word MSB
DDS_TW1	0x3F	Set DDS tuning word LSB
DDS_CYC1	0x5F	Set number of sine wave cycles for DDS prestored waveform
DDS1_PW	0x43	Set phase offset for DAC1
PAT_TYPE	0x1F	Set pattern to repeat the number of times defined in DAC2_1PATx
PAT_TIMEBASE	0x28	Set number of DAC clock periods per PATTERN_PERIOD LSB and START_DELAYx LSB
PAT_PERIOD	0x29	Set pattern period
DAC2_1PATx	0x2B	Set number of DAC1 pattern repeat cycles
TRIG_TW_SEL	0x44	Set start delay to repeat for all patterns or only at the start of the first pattern
START_DLY1	0X5C	Set start delay of DAC1

Table 7.2: AD9106 register descriptions for sinusoidal waveform generation on DAC1

generator creates continuous waveform and to disable it, the user needs to define proper values in DAC2_1PATx (*i.e.*, 0x0101) and PAT_TYPE (*i.e.*, 0x0000). Sinusoids are generated using the DDS from the chip AD9106. The frequency is configured by writing to a 24-bit tuning word split into two registers (MSB and LSB), since each register only has 16-bit width. The value is controlled by the formula $TW = \frac{f}{f_{clk}} \times 2^{24}$, in which f is the target sinusoidal frequency and f_{clk} represents the DAC clock frequency from the on-board clock divider chip AD9514. The phase can be carefully adjusted in the register DDS1_PW, with a resolution of $360^{\circ}/(2^{16} - 1) = 0.005$ degree. The waveform amplitude is controlled by the DAC1_DGAIN register which is a 12-bit gain factor. In terms of waveform duration, this can be set by assigning a specified number of cycles for a set period. An example of sinusoidal hard pulse generation with defined timing controls is shown in Figure 7.8a). Prior to waveform generation, the RUN bit in the PAT_STATUS register needs to set to 1, and all new register values are updated by setting RAMUPDATE to 0x0001 [108]. These new register values are saved in a text file and loaded to AD9106 via SPI interfaces.

FPGA programming to drive the waveform generator

Once the board modifications and SPI configurations are set, the waveform is ready to be generated, as long as proper clock and trigger signals can be detected, see Figure 7.8b). Since

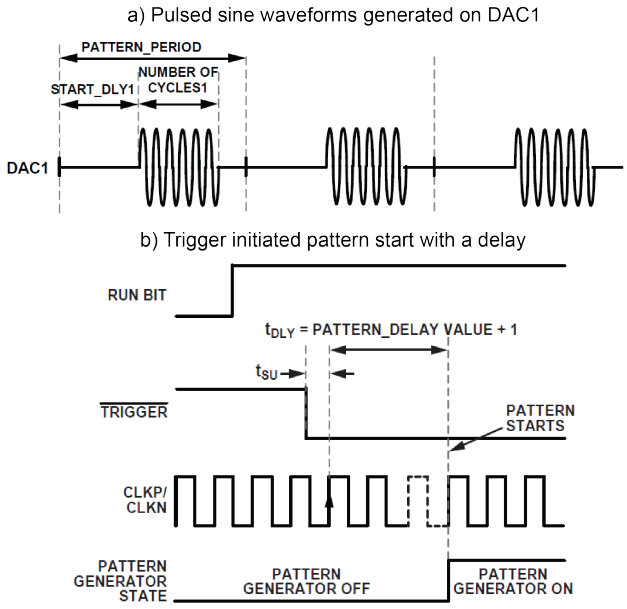

Figure 7.8: Waveform generation example on AD9106. **a)** An example of sine waveform generation using the on-board DDS with various given timing parameters. **b)** When a negative edge is detected on the trigger terminal while the RUN bit is set, pattern generation will begin after the delay specified in the PATTERN_DELAY register [98].

in current stage the pulse sequence design is controlled by the existing TMX MR console, it provides two initialization dummy signals: 1) a trigger signal to initialize the PTx system and waveform generation; and 2) 10 MHz reference clock which is used for the synchronization of the entire system. Therefore, the programming of Cyclone's FPGA part involves with two tasks.

Trigger signal: A direct wiring (essentially just connect the input and output directly) was made in the FPGA, which detected the input dummy square waveform initialization signal and output it directly as the trigger signal to initialize the waveform generation on chip AD9106. This direct wiring yields a fast response, and may be also used as a trigger signal to start the pulse sequence once the sequence design is controlled by FPGA in the future developments.

Clock upgrade: The generation of 9.28 MHz sine waveforms using a 10 MHz input clock will result in severe aliasing problem. To overcome this, the phase locked loops (PLLs) were used

to perform clock multiplication which upgraded the 10 MHz input clock to an in-sync clock with a frequency of 150 MHz. The exact setup of PLLs can be found in the document [106].

In the FPGA development, the generated trigger and clock outputs were also sent to the on-board LEDs, so the user can monitor the status of the PTx during an experiment. A screenshot of the FPGA configuration in Quartus Prime is shown in Figure 7.9.

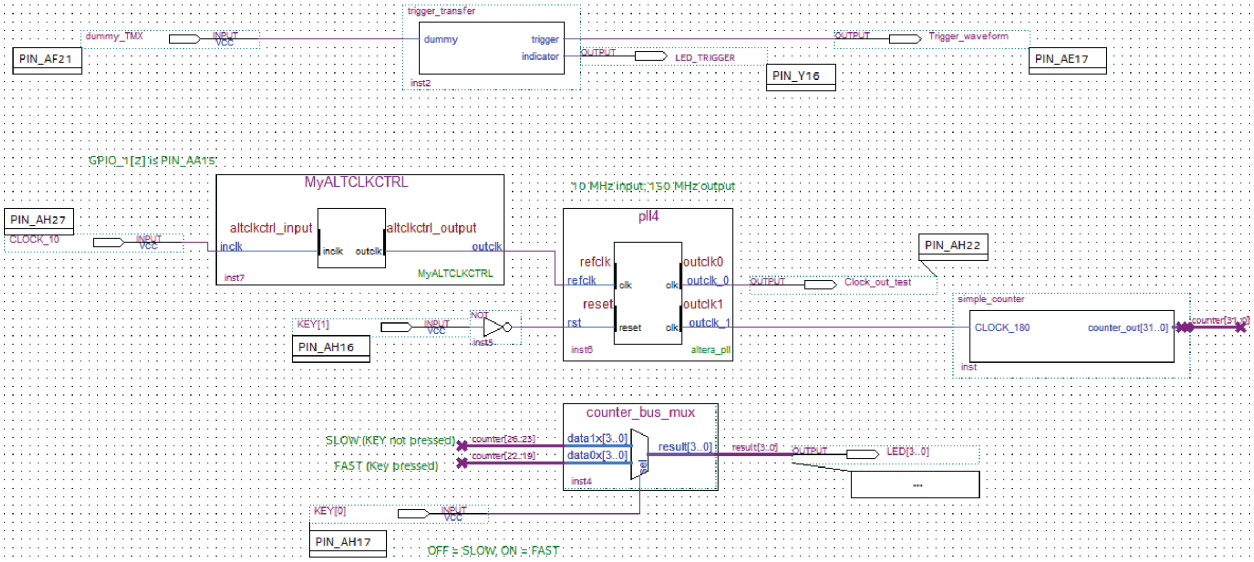

Figure 7.9: The screenshot of FPGA programming for the PTx in Quartus Prime Lite 18.1. The dummy initialization signal was directly wired to generate a corresponding trigger signal. Two identical upgraded clocks were generated using a PLL which converted a 10 MHz clock to 150 MHz. One clock output was used to drive the AD9106-EBZ while the other was wired to LEDs.

7.4.4 Waveform Bench Measurements

The PTx system was tested under two different configurations, denoting as Phase I and Phase II, which can be found in Figure 7.5. The Phase I configuration focused on the test of SPI communication and the proper data transfer for the control of AD9106-EBZ for waveform generation. In this test, no FPGA was used because all necessary driving signals (clock and trigger) were generated directly from the function generator (again, mimic TMX console for test purpose). In Phase II configuration, the FPGA was included, mainly because the generation of 9.28 MHz RF waveforms without aliasing needed an upgraded high frequency

in-sync clock, which can be produced by the PLL inside the FPGA.

Phase I: Bench measurements without FPGA

The SPI communication was first verified while both boards were powered on. Note that the AD9106-EBZ comes with no power DC adapter so it was supplied by a laboratory DC power supply (DW GPC-3030D). The SPI interfaces between two boards were linked by a ribbon cable which was also connected to a breadboard for bench measurements. Accessing Cyclone's HPS via the PuTTY terminal in the Ubuntu Linux OS, a text file containing all register values was loaded by the C program "write-SPI" using Linux commands. To test the functionality of SPI communication, a mixed domain oscilloscope (Tektronix MDO4054B-3) was used to monitor the state of 4-wire SPI interfaces for a single register writing. Six register values including amplitude and phase information on three different DAC channels were then written in a row to test the speed of SPI data transfer, as these register values need to be updated quickly between two adjacent refocusing RF pulses for the decoupling of three-coil set in TRASE MRI applications.

With all required register values loaded in the AD9106-EBZ, to evaluate the outcomes of all modifications made on the waveform generator, simple sine waveforms with varying durations, amplitudes and delays were generated without the use of FPGA. To drive the AD9106 chip, a function generator (Tektronix AFG3022, to take place of TMX console, for testing only) was implemented to create a 10 MHz reference clock (3.3V square pulse), and the trigger signal (3.3V, 10% duty cycle, 500 kHz, high impedance output). To actively decouple the three-coil set, three parallel RF pulses need to be generated with adjustable phases and magnitudes. Therefore, three hard pulses with identical durations but different gains (ratio of 4:2:1) and phases (0, 90 and 180 degrees) were generated at a low frequency $f = 78.125$ kHz. While keeping the same waveform parameters, the frequency was increased to $f = 1.25$ MHz (*i.e.*, 1/8 of the input 10 MHz ref clock) to assess the waveform distortions caused by the aliasing of DDS.

Phase II: Bench measurements with FPGA involved

The tests on FPGA were performed with the Verilog HDL program loaded to Cyclone's FPGA via JTAG chain first. In practice, the inputs for FPGA should be from existing MR TMX console, but for the purpose of bench measurements, identical signals (*e.g.*, dummy initialization signal and 10 MHz reference clock) can be generated with a function generator. During the test, a dummy trigger signal (3.3 V, 50% duty cycle, 500 kHz, high impedance output) was sent into the FPGA directly, generating a similar output which was used as the trigger signal to drive AD9106-EBZ. On the scope the response of such a direct wiring was analyzed on both rising and falling edges.

To avoid the aliasing issue while generating a higher frequency sine waveforms (*i.e.*, generate 9.28 MHz sinusoidal waveforms with a 10 MHz reference clock), the PLLs in FPGA was programmed to generate a 150 MHz in-sync clock with an input of a 10 MHz reference clock (3.3 V square pulse) from the function generator. This upgraded 150 MHz clock was directed to the AD9106-EBZ and used for replicating three parallel RF pulses with same parameters (*i.e.*, gains ratio of 4:2:1 and phases 0, 90 and 180 degrees) while at an ideal frequency f = 9.28 MHz. To examine the synchronization, the resulting waveforms were also compared with the original 10 MHz reference clock obtained from the function generator.

7.5 Results

7.5.1 Phase I Bench Measurements

Test of SPI communication

The SPI communication bench measurements are shown in Figure 7.10, in which Figure 7.10a) displays a single register writing while Figure 7.10b) demonstrates six registers data transfer including three amplitudes and three phases information for DAC1, DAC2 and DAC3. As can be seen in Figure 7.10a), when chip select line ($\overline{CS}$) was active low, 32 SPI

clocks (SCLK) were observed with the first 16 clocks giving 1-bit write command and 15-bit register address, and the rest 16 clocks corresponding to the actual value of the register. The time needed to write a single register was approximately 5 μs. In Figure 7.10b) it can be found that the chip select line had to jump back to the active low state before the next register could be written. This introduced a delay of nearly 12 μs, which was limited by the speed of the controller. However, this was fast enough because six register values were successfully updated within 80 μs, meeting the target of update time less than 100 μs.

Figure 7.10: Bench measurements for SPI communications between the waveform generator AD9106-EBZ and the controller Altera Terasic ADC-SoC. **a)** A singe register data transmission was recorded by the scope. While chip select line ($\overline{CS}$") was at low active state, in the first clock cycle, a digital '0' was given to the read/write bit ($R/\overline{W}$) on "SDIO" to activate the transmit mode, followed by a specification of the register address with 15-bit data. The actual register value was assigned by the next 16-bit data, making a total of 32 clock cycles. **b)** Following the same register writing protocol, data of six registers including three amplitudes and three phases were transfered, resulting in a total writing time of nearly 80 μs.

Test of waveform generation setup

In order to check the overall functionality of the PTx, I first tested the waveform generation without using the FPGA part, to avoid any unnecessary complexity. The function generator provided clock and trigger signals to the waveform generator, see Figure 7.11a). Under this experimental setup, three square sine waveforms with different durations, start delays, and amplitudes parameters, were first generated on DAC1 to DAC3, as shown in Figure 7.11b).

In Figure 7.11c), three parallel RF pulses with identical durations but different amplitudes (ratio of 4:2:1) and phases (0, 90, and 180 degree) were generated, representing a practical use of PTx to actively decouple three-coil set in TRASE MRI applications. Despite that accurate adjustments of amplitude and phase were achieved, the precision of pulse duration was limited to one cycle of the sine waveform, since only an integer number of sine wave cycles could be selected in the register, which resulted in inconsistent pulse stop times while the initial phases were set differently. Additionally, in Figure 7.11d) higher frequency (f = 1.25 MHz) sine waveforms were generated with all other register parameters kept the same. An aliasing issue was found in this case, as each sine waveform was represented by eight discrete values only, corresponding to 1/8 of the input 10 MHz clock.

7.5.2 Phase II Bench Measurements

After the success of Phase I, the control of FPGA was then added into the PTx to solve the aliasing problem. The function generator now acted as an MRI console providing dummy signals and 10 MHz reference clock. A fast response from Cyclone's FPGA to the square dummy signal was achieved, demonstrating delays of about 20 ns and 30 ns on the rising and falling edges, as shown in Figure 7.12. This completed PTx configuration was depicted in Figure 7.13a). Using the PLL of FPGA, a 150 MHz in-sync clock was generated with noticeable signal interference that was sensitive to the system cabling, see Figure 7.13b). The upgraded 150 MHz clock was then input to drive the waveform generator, producing three parallel rectangular-shape waveforms with adjustable amplitudes and phases that are needed to actively decouple 2D TRASE three-coil set, at a desired frequency $f = 9.28$ MHz. These waveforms were also synchronized to the original 10 MHz clock with a fixed overall phase shift, which is manageable in the MRI experiment.

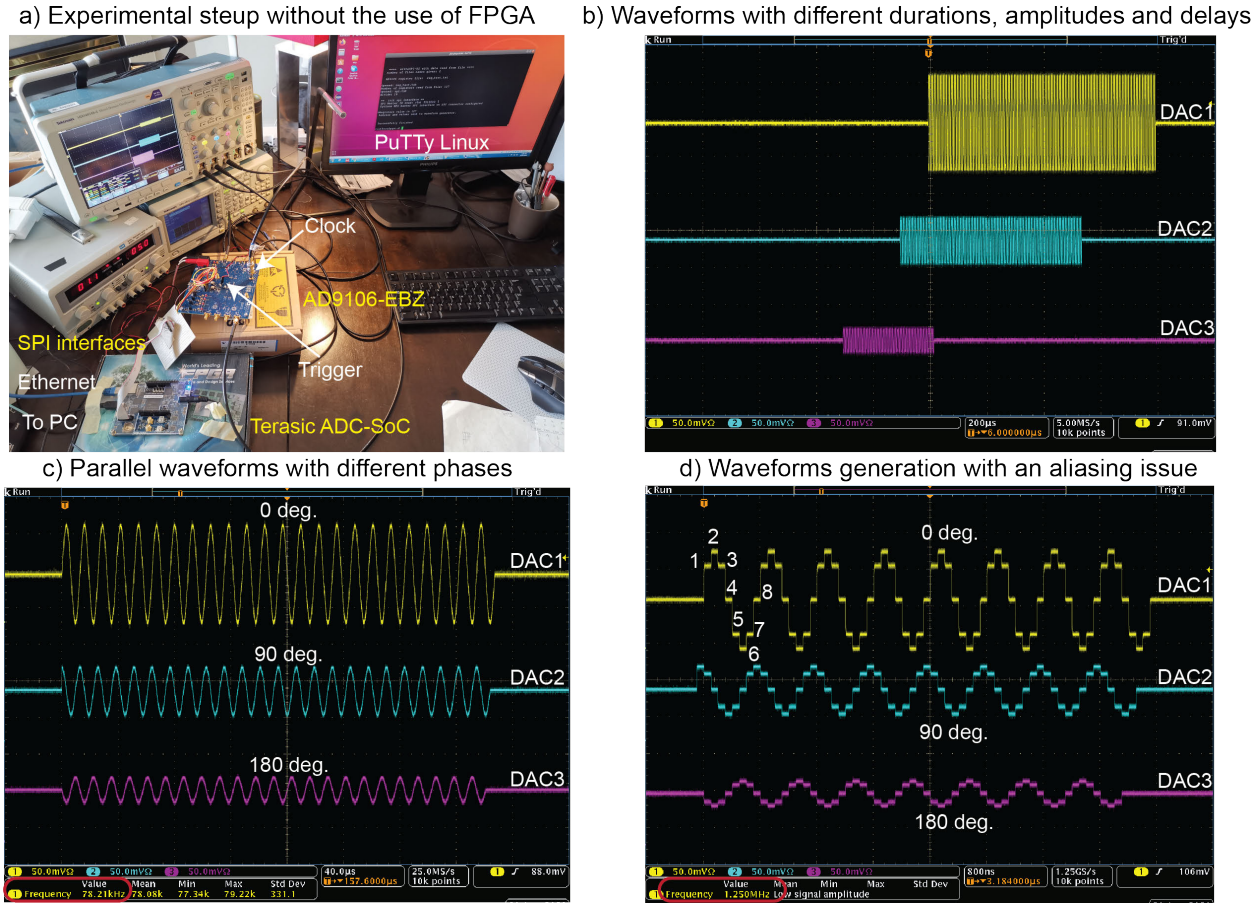

Figure 7.11: Waveform generation without the use of FPGA. **a)** The picture of experimental setup. A SPI communication was established by SPI interfaces between two boards. The clock (10 MHz) and trigger signals were provided by the function generator. The Cyclone's HPS on Terasic ADC-SoC was controlled via PuTTY on a virtual Linux (Ubuntu) system. **b)** The scope displays three sine waveform generations with different durations, amplitudes and delays, confirming the proper controls of the PTx without using the FPGA. **c)** A practical parallel waveform generations for active decoupling of the 2D TRASE three-coil set. Adjustable amplitudes (ratio of 4:2:1) and phases (0, 90 and 180 degree) were achieved at a frequency of $f = 78.125$ kHz. **d)** The same waveforms were produced with an increased frequency. Since the required frequency ($f = 1.25$ MHz) was 1/8 of the input 10 MHz clock, an aliasing issue was observed in the scope, with each sine waveform represented by only eight discrete values.

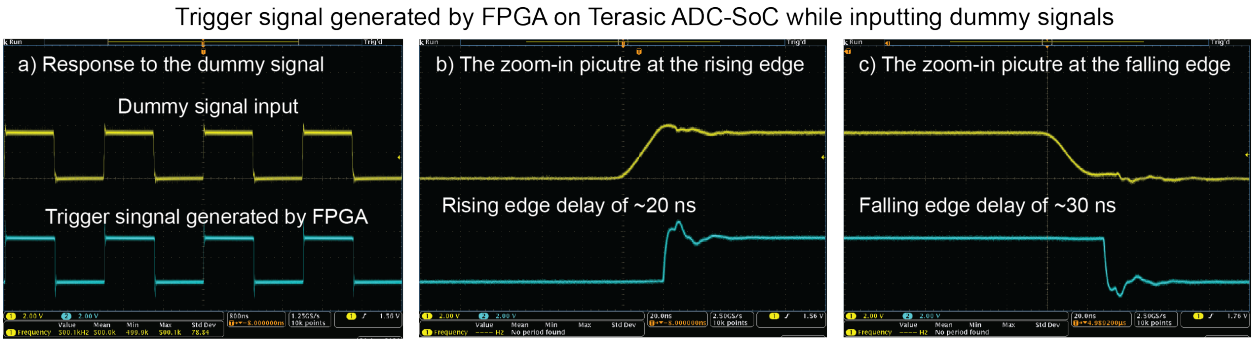

Figure 7.12: Generation of a trigger signal for the waveform generator using Cyclone's FPGA. **a)** A dummy signal was generated from a function generator and sent to the Cyclone's FPGA. The direct wiring program on FPGA yielded a quick response by producing a corresponding trigger signal that was used to drive the waveform generator. **b)** The zoom-in picture demonstrates a delay of 20 ns at the rising edge. **c)** A delay of 30 ns at the falling edge was found in the zoom-in picture.

7.6 Discussion

The geometrical decoupling technique requires mm-level positional adjustment, but is a crucial step for the decoupling of three-coil set. It avoids a significant current introduced back to the primary coil due to strong coupling, while a cancelling current is sent into the secondary coil. For example, in LTSpice simulation only 0.16% current increment was found in the primary coil TS1+RS1 while the secondary coil TS2+RS2 was driven simultaneously by $V2$, because two resonators were already weekly coupled (set by a low coupling coefficient $k_{12} = 0.052$) with regular solenoids attachments. Once geometric decoupling is achieved, on the network analyzer split resonance (three dips) no longer exist, so fine manual adjustments (tuning and matching) for each coil at the operating frequency $f = 9.28$ MHz can be conveniently achieved. The passive geometric decoupling and the PTx-based active decoupling approaches can be combined together to provide necessary isolations among three coils.

The PTx system functions as expected and meets all design targets. Specifically, SPI test results shown in Figure 7.10 confirms that RF waveform amplitudes and phases on three channels can be independently adjusted and updated within 80 μs, allowing a short echo train to be generated. The waveform generation results found in Figure 7.11 indicates that

a) Experimental steup using the PTx including HPS and FPGA on Terasic ADC-SoC, and AB9106-EBZ

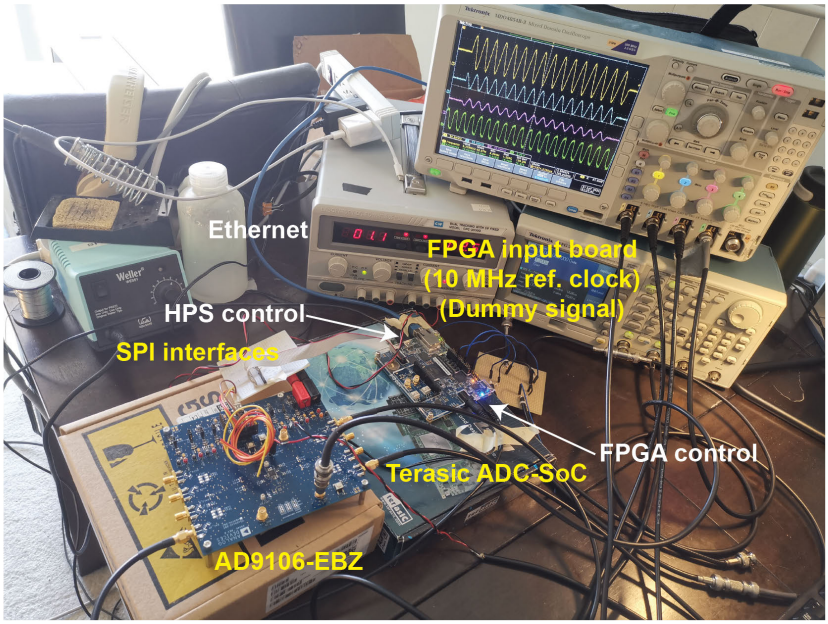

b) Clock frequency upgrade using the PLL on FPGA

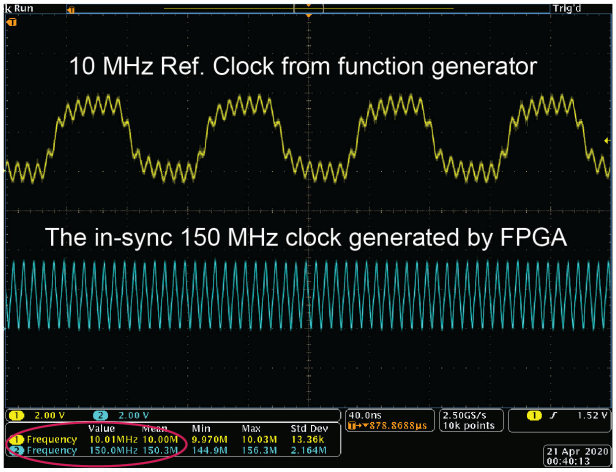

c) Parallel waveforms with different phases at f = 9.28MHz

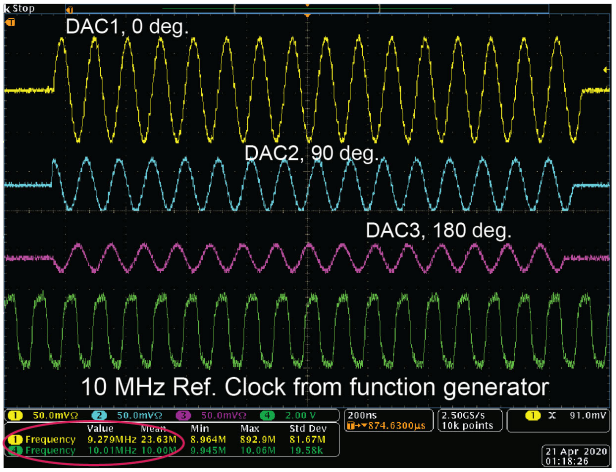

Figure 7.13: Waveform generation using the completed PTx including HPS and FPGA from Altera Terasic ADC-SoC and AD9106-EBZ. **a)** The picture of the completed PTx experimental setup. The Cyclone's HPS transfered register data to the AD9106-EBZ via SPI communications, while the FPGA part controlled trigger and upgraded clock signals. **b)** The scope screenshot shows that the PLL in FPGA was programmed to generate an in-sync upgraded clock in a frequency of 150 MHz, with an input 10 MHz clock from the function generator. Signal interference sensitive to the system cabling was found in the measurement. **c)** A practical parallel waveform generations for active decoupling of the 2D TRASE three-coil set using the PTx system. Adjustable amplitudes (ratio of 4:2:1) and phases (0, 90 and 180 degree) were achieved at a desirable frequency $f = 9.28$ MHz. All three produced sine waveforms were synchronized to the original 10 MHz reference clock (green), which was crucial for further MRI applications.

parallel rectangular pulses at a low frequency (*i.e.*, 78.125 kHz) can be generated with user-defined amplitudes, phases, and durations, demonstrating the proper functionality of the PTx system. However, an aliasing issue was found while the output frequency was at the same order of the input clock frequency (*i.e.*, 1.25 MHz vs. 10 MHz), although the waveform generator AD9106-EBZ can take up to GHz clock signals on AD9514 chip, and the chip AD9106 can use up to 180 MHz master clock on the DDS. This issue was addressed by Cyclone's FPGA which can be programed to produce fast response trigger signals (see Figure 7.12) and upgraded clocks (see Figure 7.13). With this completed PTx design, the frequency of three obtained RF hard pulses was successfully increased to 9.28 MHz without aliasing issue, while maintaining phase coherence with the original clock, as needed for TRASE MRI applications.

The chosen waveform generator chip AD9106 has fine tuning of phase (0.005 degree) and amplitude (12-bit DAC), and is a powerful device designed for waveform generation. The waveform duration was controlled by setting the number of waveform cycles, so the pulse duration accuracy is limited to one cycle, *e.g.*, for a 9.28 MHz sine waveform, the RF pulse duration resolution is 108 ns. Although only rectangular sine waveforms were generated in this work, other waveform shapes such as triangular, sawtooth and even arbitrary, can also be created by writing to different registers. Prior to 2D TRASE MR experiments, a calibration process is required to optimize the power, amplitude, phase and waveforms of the individual RF sources to each coil for a specific phantom. This is the next step needed to use the PTx system to drive the coil array, which has not been implemented yet. In the future work section in Chapter 8, a brief discussion will be given to this topic.

This PTx design introduces an inexpensive RF transmit system for low-field MRI. Not only it can actively decouple RF coil arrays, it can be also used in other applications including tailored RF pulses, RF power reduction, and even coil ringing mitigation which is more problematic for low-field MRI. Although not described in this chapter, the intercommunication between HPS and FPGA on the Cyclone SoC may be enabled to allow on-board

pulse sequence programming; the included high-speed DDR3 memory and ADC may be also employed to add a receiving capability with inherent clock synchronization, making a more powerful PTx system feasible in the future developments.

7.7 Conclusions

In this work the design of an inexpensive parallel transmit RF system is proposed. This system can generate four single-frequency waveforms with user-defined amplitudes, phases, durations, and is hoped to find many applications such as tailored RF pulses, active coil decoupling, and coil ringing mitigation in low-field MRI regimes. From circuitry simulations and bench measurements, the system shows great promise to add additional coil isolation for the previously described geometrically decoupled three-coil set. The combination of geometric and active decoupling approaches will provide necessary coil isolations required to obtain a clean 2D TRASE image. The system design is equipped with many unused powerful components including built-in intercommunication between HPS and FPGA, high-speed DDR3 memory and ADC, which all can be further exploited to develop a full-scale MRI RF system that features sequence design and RF transmission/receiving.

7.8 Acknowledgements

I would acknowledge my funding sources 1) Natural Sciences and Engineering Research Council of Canada, Grant/Award Number: RGPIN-2016-05183; 2) Alberta Graduate Excellence Scholarship (AGES), Alberta Student Aid; and 3) 75th Anniversary Award, University of Alberta, for the support of this work.

Chapter 8

Conclusions and Future Work

8.1 Summary of Findings

Magnetic resonance imaging provides very high quality diagnostic images for a large range of disease (in particular, cancer). Much work is being done to develop technologies that are robust, yet cost-effective, for delivering the highest quality for patient results. For MRI systems, innovative designs often feature novel magnetic fields and lower-cost magnets, or enhanced computational algorithms that yield better quality of images and patients results. Despite considerable improvements in magnetic resonance imaging (MRI) quality and speed, the underlying design philosophy remains remarkably unchanged compared to the first-generation MR scanners developed several decades ago. Currently, more than half of the world's population has no more than 1 MRI unit per 1 million people while over 90% of developing countries have no access to MRI due to extensive costs, bulkiness, complexity and geographical access limitations.

Undeniably, cost-effectiveness is an integral component in next revolutions in MRI health care. This doctoral research dissertation has attempted to develop novel RF and imaging technologies to expand the use of TRASE MRI towards a more clinically-relevant device. As outlined in Chapter Overview of the Thesis, previous RF coil array(s) were not efficient enough to encode short T_2 *in vivo* tissues, so the goal of this work is to design an efficient

TRASE RF coil to achieve short refocusing pules and fast echo train, which are important to obtain high resolution images for short T_2 objects. With such new coil design, multiple coils should be combined together with adequate decoupling techniques to accomplish multi-dimensional TRASE encoding.

In Chapter 4: a simple, compact, and reliable twisted solenoid phase gradient RF coil was proposed. At relatively low operating frequency, bench B_1 field measurements show great agreements (largest deviation 3.2%) with the Biot-Savart's calculations. By comparing with previously published designs of TRASE phase gradient encoding coils (most notably the rectangular Helmholtz-Maxwell coil array which was used to acquire *in vivo* human wrist images), this twisted solenoid coil, with a single current path, efficiently produces a large cylindrical volume of B_1 field for TRASE MRI encoding. Its cylindrical outer shape is particularly advantageous for cylindrical Halbach-style permanent magnets, which is the target low-field magnet being investigated. The large twisted solenoid phase gradient direction can be set to any transverse direction by rotating the coil about its cylindrical axis, leading to the further investigations of combining multiple such coils for high-resolution multi-dimensional TRASE encoding.

In Chapter 5: a pair of twisted solenoid TRASE coils was geometrically decoupled with specifically-designed regular solenoid attachments using *FastHenry2* simulator. In general, this geometric decoupling is a viable alternative to active switched solutions (*i.e.*, PIN diodes) for coil pairs with high inherent coupling, while introducing minimal B_1 field disturbances. Rapid echo MR encoding (a line of 128 k-space points collected within 80 ms) was performed using this twisted solenoid pair, resulting in proper imaging of short T_2 phantoms (T_2 of 17 to 35 ms). Additionally, compared with the 1D TRASE coil array (twisted + saddle) that was described in Chapter 4, this twisted solenoid pair encoded a double k-space range within the same acquisition time, obtaining a higher resolution image over a large usable imaging volume. Similarly, this phase gradient coil set is well suited to low B_0 field MRI magnets, such as Halbach arrays and bi-planar magnets.

In Chapter 6: to perform 2D TRASE encoding with the new coil design, a three-coil set consisting of twisted solenoid pair (as demonstrated in Chapter 5) and a saddle coil was proposed. These three coils independently generate $+X$, zero, and $+Y$ phase gradients, forming a triangle in k-space, a requirement for 2D TRASE experiment. Since the saddle coil is inherently decoupled with the solenoid coil, and the twisted solenoid pair can be geometrically decoupled using the attached regular solenoids (as described in Chapter 5), a geometric decoupling among three coils was established and verified by both S parameter measurements and individual 1D TRASE experiments. However, a noticeable imaging distortion was observed in the 2D TRASE experiments, where a certain portion of object was missing and not properly imaged. To narrow down the cause of such artifact, a Bloch simulation was performed using coil B_1 maps generated by Biot-Savart calculations. The simulations show that an unwanted flip angle contribution of 5% or higher from the secondary transmit coil(s) is sufficient to give rise to severe image artifacts in 2D TRASE MRI using this three-coil setup. The simulation results agree qualitatively with the experimental images, indicating that a range of 5% to 11% field contamination from secondary coil(s) may exist during the MR experiments. The 2D TRASE sequence involves with extensive use of RF pulses, hence, it is sensitive to coil interactions and can suffer from coil coupling that is not fully eliminated by geometric decoupling techniques. This is a crucial step for designers to understand the acceptable levels of isolation among TRASE transmit array systems. For a successful 2D TRASE MRI encoding, additional decoupling capacity needs to be added to the current three-coil setup.

In Chapter 7: to minimize the residual coupling which is unable to resolve by geometric decoupling technique, the idea of transmitting RF pulses into each coil in parallel to cancel induced currents in the secondary coil(s), was presented. This parallel transmit system method was first evaluated in a circuitry simulation using LTSpice, demonstrating a significant reduction of induced current (98.9%) in the secondary coil at the resonating frequency, provided that an RF input with fine tuned amplitude and phase, could be sent into the sec-

ondary coil simultaneously. Following this validation, the design of an inexpensive, low-field parallel transmit RF system was proposed using a waveform generator AD9106 chip and a controller Altera Terasic Cyclone V ADC-SoC. This system have been proved by bench measurements that is capable of generating four single-frequency waveforms with user-defined precise adjustments on amplitudes, phases and durations. The system's four channel outputs can be updated within 80 μs and be implemented as an active decoupling approach. This new system is expected to provide additional decoupling capacities that are required by the geometrically-decoupled three-coil set mentioned in Chapter 6. In addition, this new parallel RF transmit system design is believed to find many applications such as tailored RF pulses, active coil decoupling, and coil ringing mitigation in low-field MRI regimes.

8.2 Limitations

There are a number of limitations to the work presented in this thesis. The localization errors in B_1 field bench measurements were not estimated. The point-by-point B_1 measurement was performed using a pick-up surface coil that has a finite area of approximately 6 cm^2, and such quantification errors were not considered either. At relatively low operating frequency, the Biot-Savart calculation is good to model phase gradient generated by twisted solenoid coil. However, due to its limits on the quasi-static approximation, future full wave simulations may further increase the accuracy. Additionally, in both Biot-Savart B_1 field and *FastHenry2* inductance simulations, coil return wire was not included. Certain discrepancies between the measurements and simulations results are expected. For example, a 0.5 cm z shift difference was found between the theoretical and actual null position in the geometrically-decoupled twisted solenoid pair. Therefore, more accurate matching of simulated and physical geometry may help to resolve this inconsistency. In the design of decoupling regular solenoid attachments, the search procedure was limited to integer number of turns and same radius. Although this is convenient for coil former 3D printing and coil construction, this does not necessarily promise the best geometric decoupling condition. For

better geometric decoupling, one may loosen such criteria and search in a wider range. Additionally, this project does not consider other coupling effects such as capacitive, resistive, etc. In image reconstructions, a conventional Fourier Transform was employed, so image distortions caused by non-linear phase gradient strength and non-uniform B_1 magnitude which were commonly seen in twisted solenoids, were not corrected for. However, since the variation of the phase gradient is known from B_1 map, when necessary, the image can be better reconstructed using other algorithms such as regularized least squares.

8.3 Future Work

The research presented in this thesis can be applied to guide the fabrication of a lightweight, low-field, low-cost, yet high resolution MRI system. However, efforts can be made in different areas to further improve and expand its use.

8.3.1 Coil Length Optimization

The twisted solenoid coil design can be scaled up. For large imaging targets, this typically requires large space to accommodate its relatively long geometry, which might limit its implementation in certain applications. Additionally, the inductance of a twisted solenoid coil increases rapidly with physical dimensions. When a regular solenoid is attached for coil decoupling purpose, the coil inductance becomes even larger, which may self-resonate below the Larmor frequency. For future variants, it would be useful to study the design of the solenoid end turns to better control the coil length, while maintaining overall coil performance.

8.3.2 Developments on the RF Tx/Rx System

In Chapter 7, it is mentioned that a calibration process is required to optimize the power, amplitude, phase and waveforms on each coil, in order to minimize the induced current(s)

using the PTx system. But, currently such technique is not available. Future developments for this challenge using either an electrical or optical feedback approach to monitor the current inside each coil in real time, is needed.

Additionally, the current parallel transmit RF system uses the existing console for experiment initialization and data acquisition. However, the selected controller is equipped with ADC, so a receiving module can be configured. The inclusion of such receiving feature not only avoids the complicated clock synchronization between two systems, it also meets the target of designing a robust, low-field, low-cost MRI system. This will further expand its use in areas where siting and power are out-of-reach.

8.3.3 Rotating 2D TRASE Encoding using Single Twisted Solenoid pair

2D TRASE encoding needs at least three different phase gradient RF coils which require very delicate decoupling technologies (geometric and/or active decoupling), and more transmit channels. More importantly, in any three coils configuration, the achievable spatial resolution is expected to be 50% (two twisted + one saddle) or 13% (three twisted solenoids) lower than that of a pair of geometrically-decoupled twisted solenoids. One may try to develop four twisted solenoid coil array to achieve a high resolution 2D TRASE within the transverse plane, however, the effective decoupling among a four-coil array is expected to be challenging. As a remedy for this, a 2D radial TRASE encoding principle is proposed here by rotating either magnet, or patient and RF coil sets together. Keep patient and a pair of geometrically-decoupled twisted solenoid in position, rotating B_0 direction (magnet) in transverse plane can acquire different lines of k-space data, achieving 2D radial transverse plane encoding. All required technologies are ready for this proposed new MRI system. This geometry is advantageous for future plan of using light and cylindrical Halbach arrays permanent magnet for TRASE MRI.

8.3.4 Slice-selective 2D TRASE with Static B_0 Gradient

In this doctoral research, 2D TRASE encoding within the transverse plane is demonstrated using twisted solenoids design, but it cannot encode in the third dimension. The obstacles for making a pure 3D TRASE MRI system are multi-fold: TRASE data acquisition occurs discretely at each refocusing pulse such that pure 3D TRASE encoding is expected to be too slow for *in vivo* studies; Additionally, four B_1 fields with different phase gradients are least needed for 3D TRASE encoding, and to achieve high resolution 3D TRASE, the number of required different B_1 fields can be up to six. This results in complicated RF coil configuration, making the MRI system less reliable due to strong coil coupling, demanding switching efficiency, and requirement of excessive hardwares, etc.

A compromise for pure 3D TRASE would be slice-selective 2D TRASE, which is a widely accepted idea for clinical use. TRASE slice selection has been achieved by interleaving small flip-angle excitation pulses between refocusing pulses, but this multi-pulse technique tends to be a long process, where the duration is inversely proportional to slice width [20]. One potential solution for this would be applying TRASE in parallel with conventional encoding principles, as TRASE is just an alternative method of encoding k-space data. An idea of hybrid B_0 and B_1 encoding has been described in previous study for wrist imaging, where only in-plane 2D data were acquired with TRASE while the third dimension was encoded with ordinary B_0 phase encoding with the use of switched B_0 gradients [19]. Cooley et al. [12] proposed a portable MRI scanner prototype capable of utilizing TRASE for the third dimension encoding while achieving 2D MRI encoding based on generalized projections created by a "built-in" gradient field [11], *i.e.*, rotating spatial encoding magnetic field.

The spark for these work was to ask: "Is it possible to combine a real static B_0 gradient (built into the magnet) and 2D TRASE to make a slice-selective 2D TRASE regime?" This configuration is advantageous because it needs neither switched external imaging gradients nor mechanical magnet rotation. In this configuration, the popular axial plane acts as the

2D image plane, since the object is bounded in both directions, thus showing cross-sectional anatomy.

The idea of encoding MRI data with a static B_0 gradient is analogous to stray field imaging (STRAFI) which was first proposed in 1988 by Samoilenk et al [109]. The novelty of this method is that the sample was placed in an enormous static B_0 gradient, e.g. above 60 T/m typically, in the fringe field surrounding high field magnets [110]. The similarities between STRAFI and the proposed slice-selective TRASE are: 1) static B_0 gradient; 2) hard pulses echo train; 3) direct measure of echo intensity instead of readout encoding. The main difference between these two technologies, excluding different coils (phase gradient vs. uniform), is that TRASE uses spin echoes rather than solid echoes. Fortunately, the application of spin echoes to STRAFI has been demonstrated in the literature [111], where a considerably improved signal-to-noise ratio (SNR) was achieved. Another similar technique to the proposed slice-slective 2D TRASE is slant-slice imaging introduced by Epstein et al in 2006 [112]. It uses 2D multiple spin echo sequence in the presence of a static linear gradient G_z, and adjustable B_0 gradients in the x and y directions. It is considered to replace the switchable B_0 gradients by TRASE phase gradients, aiming at achieving 2D plane imaging perpendicular to the static B_0 gradient.

To make this CT-like MRI scanner, such B_0 gradient may be generated from the magnet design. Since TRASE is ideal for low-cost, low-field MRI, a particularly suitable magnet design is the Halbach cylinder [21] which can be compactly constructed and shimmed [113] to generate images of high quality [114], [115]. The application of TRASE within cylindrical Halbach magent arrays have been discussed [12], with optimization on magnet using genetic algorithms published recently[116]. The construction of a built-in static B_0 gradient has also been proposed [117] by rotating additional rings of permanent magnets so that deliberately scale the direction and strength of the static B_0 gradient is feasible. This new type of magnet generates B_0 gradients perpendicular to the axis of the Halbach cylinder, with adequate adjustments shown in the collaboration work from Dr. Tomanek's group, it is believed that

a desired static B_0 gradient can be made to fit the idea of 2D slice-selective TRASE.

8.4 Final Closing Remarks

In this concluding chapter, the major findings and limitations were highlighted. Several future research directions were also proposed, according to the latest results obtained from this doctoral work. Although it is a bit early to foresee these new TRASE RF designs to enter the market, it is confident to conclude that the hardware and software developed in this work lay the solid foundation for the design of a low-field, low-cost, clinically-useful TRASE MRI. With a goal of benefiting the provision of health care in remote regions (*e.g.*, rural locations and developing countries), more decent phantom images need to be obtained first, followed by human *in vivo* studies and clinical trials to be conducted next.

Bibliography

[1] F. Rabai and R. Ramani, "Chapter 31 - Magnetic Resonance Imaging: Anesthetic Implications," in *Essentials of Neuroanesthesia*, H. Prabhakar, Ed., Academic Press, 2017, pp. 519–532, ISBN: 978-0-12-805299-0. DOI: https://doi.org/10.1016/B978-0-12-805299-0.00031-2. [Online]. Available: http://www.sciencedirect.com/science/article/pii/B9780128052990000312.

[2] M. A. Bernstein, X. J. Zhou, and K. F. King, *Handbook of MRI pulse sequences*. Amsterdam ; Boston: Academic Press, 2004, xxii, 1017 p. ISBN: 0120928612 (alk. paper). [Online]. Available: //catalog.hathitrust.org/Record/004921404%20http://hdl.handle.net/2027/mdp.39015059184906.

[3] D. Hoult and R. Richards, "The signal-to-noise ratio of the nuclear magnetic resonance experiment," *Journal of Magnetic Resonance (1969)*, vol. 24, no. 1, pp. 71–85, 1976, ISSN: 0022-2364. DOI: https://doi.org/10.1016/0022-2364(76)90233-X. [Online]. Available: http://www.sciencedirect.com/science/article/pii/002223647690233X.

[4] D. Hoult, "The NMR receiver: A description and analysis of design," *Progress in Nuclear Magnetic Resonance Spectroscopy*, vol. 12, no. 1, pp. 41–77, Jan. 1978. DOI: 10.1016/0079-6565(78)80002-8. [Online]. Available: https://doi.org/10.1016/0079-6565(78)80002-8.

[5] J. P. Marques, F. F. J. Simonis, and A. G. Webb, "Low-field MRI: An MR physics perspective," *J Magn Reson Imaging*, 2019, ISSN: 1522-2586 (Electronic) 1053-1807 (Linking). DOI: 10.1002/jmri.26637. [Online]. Available: https://www.ncbi.nlm.nih.gov/pubmed/30637943.

[6] G. Sarty, A. Scott, K. Turek, P. Liszkowski, J. Sharp, and B. Tomanek, "Wrist Magnetic Resonance Imager: ISS - MRI Study Phase," International Space Station, Tech. Rep., 2014.

[7] L. L. Wald, P. C. McDaniel, T. Witzel, J. P. Stockmann, and C. Z. Cooley, "Low-cost and portable MRI," *J Magn Reson Imaging*, 2019, ISSN: 1522-2586 (Electronic) 1053-1807 (Linking). DOI: 10.1002/jmri.26942. [Online]. Available: https://www.ncbi.nlm.nih.gov/pubmed/31605435.

[8] S. Geethanath and J. Vaughan J. T., "Accessible magnetic resonance imaging: A review," *J Magn Reson Imaging*, 2019, ISSN: 1522-2586 (Electronic) 1053-1807 (Linking). DOI: 10.1002/jmri.26638. [Online]. Available: https://www.ncbi.nlm.nih.gov/pubmed/30637891%20https://onlinelibrary.wiley.com/doi/abs/10.1002/jmri.26638.

[9] G. I. Ogbole, A. O. Adeyomoye, A. Badu-Peprah, Y. Mensah, and D. A. Nzeh, "Survey of magnetic resonance imaging availability in West Africa," *Pan Afr Med J*, vol. 30, p. 240, 2018, ISSN: 1937-8688 (Electronic). DOI: 10.11604/pamj.2018.30.240.14000. [Online]. Available: https://www.ncbi.nlm.nih.gov/pubmed/30574259.

[10] M. Sarracanie, C. D. LaPierre, N. Salameh, D. E. Waddington, T. Witzel, and M. S. Rosen, "Low-cost High-performance MRI," *Sci Rep*, vol. 5, p. 15 177, 2015, ISSN: 2045-2322 (Electronic) 2045-2322 (Linking). DOI: 10.1038/srep15177. [Online]. Available: https://www.ncbi.nlm.nih.gov/pubmed/26469756.

[11] J. P. Stockmann, C. Z. Cooley, B. Guerin, M. S. Rosen, and L. L. Wald, "Transmit array spatial encoding (TRASE) using broadband WURST pulses for RF spatial encoding in inhomogeneous b0 fields," *Journal of Magnetic Resonance*, vol. 268, pp. 36–48, Jul. 2016. DOI: 10.1016/j.jmr.2016.04.005. [Online]. Available: https://doi.org/10.1016/j.jmr.2016.04.005.

[12] C. Z. Cooley, J. P. Stockmann, B. D. Armstrong, M. Sarracanie, M. H. Lev, M. S. Rosen, and L. L. Wald, "Two-dimensional imaging in a lightweight portable MRI scanner without gradient coils," *Magnetic Resonance in Medicine*, vol. 73, no. 2, pp. 872–883, Mar. 2014. DOI: 10.1002/mrm.25147. [Online]. Available: https://doi.org/10.1002/mrm.25147.

[13] H. Sun, S. Yong, and J. C. Sharp, "The twisted solenoid RF phase gradient transmit coil for TRASE imaging," *Journal of Magnetic Resonance*, vol. 299, pp. 135–150, 2019, ISSN: 10907807. DOI: 10.1016/j.jmr.2018.12.015.

[14] P. Bohidar, H. Sun, G. Sarty, and J. C. Sharp, "A Novel Approach to Investigate 1D TRASE MRI Pulse Sequence Performance in Imperfect B1 Fields," in *Proc. Intl. Soc. Mag. Reson. Med. 27 (2019)*, 2019.

[15] A. Purchase, T. Palasz, H. Sun, J. Sharp, and B. Tomanek, "A High Duty Cycle, Multi-channel, RF Power Amplier for High Resolution TRASE MRI," in *Proc. Intl. Soc. Mag. Reson. Med. 27 (2019)*, 2019.

[16] H. Sun, A. AlZubaidi, A. Purchase, and J. C. Sharp, "A geometrically decoupled, twisted solenoid single-axis gradient coil set for TRASE," *Magnetic Resonance in Medicine*, 2019, ISSN: 0740-3194 1522-2594. DOI: 10.1002/mrm.28003.

[17] E. Der, V. Volotovskyy, H. Sun, B. Tomanek, and J. C. Sharp, "Design of a high power PIN-diode controlled switchable RF transmit array for TRASE RF imaging," *Concepts in Magnetic Resonance Part B: Magnetic Resonance Engineering*, 2018, ISSN: 15525031. DOI: 10.1002/cmr.b.21365.

[18] S. Salajeghe, P. Babyn, and G. E. Sarty, "Composite pulses for RF phase encoded MRI: A simulation study," *Magnetic Resonance Imaging*, vol. 36, pp. 40–48, Feb. 2017. DOI: 10.1016/j.mri.2016.10.007. [Online]. Available: https://doi.org/10.1016/j.mri.2016.10.007.

[19] J. C. Sharp, S. B. King, Q. Deng, V. Volotovskyy, and B. Tomanek, "High-resolution MRI encoding using radiofrequency phase gradients," *NMR in Biomedicine*, vol. 26, no. 11, pp. 1602–1607, Sep. 2013. DOI: 10.1002/nbm.3023. [Online]. Available: https://doi.org/10.1002/nbm.3023.

[20] J. C. Sharp and S. B. King, "MRI using radiofrequency magnetic field phase gradients," *Magnetic Resonance in Medicine*, vol. 63, pp. 151–161, 2010. DOI: 10.1002/mrm.22188. [Online]. Available: https://doi.org/10.1002/mrm.22188.

[21] K. Halbach, "Design of permanent multipole magnets with oriented rare earth cobalt material," *Nuclear Instruments and Methods*, vol. 169, no. 1, pp. 1–10, 1980, ISSN: 0029-554X. DOI: https://doi.org/10.1016/0029-554X(80)90094-4. [Online]. Available: http://www.sciencedirect.com/science/article/pii/0029554X80900944.

[22] D. Hoult, "Rotating frame zeugmatography," *Journal of Magnetic Resonance (1969)*, vol. 33, no. 1, pp. 183–197, 1979, ISSN: 0022-2364. DOI: https://doi.org/10.1016/0022-2364(79)90202-6. [Online]. Available: http://www.sciencedirect.com/science/article/pii/0022236479902026.

[23] M. J. Blackledge, P. Styles, and G. K. Radda, "The elimination of transmitter-receiver phase-twist artifacts in the phase-modulated rotating-frame imaging experiment," *Journal of Magnetic Resonance (1969)*, vol. 79, no. 1, pp. 176–183, 1988, ISSN: 0022-2364. DOI: https://doi.org/10.1016/0022-2364(88)90336-8. [Online]. Available: http://www.sciencedirect.com/science/article/pii/0022236488903368.

[24] J. C. Sharp, Q. Deng, S. B. King, V. Volotovskyy, and B. Tomanek, "A 3-Axis Phase Gradient Array for RF Encoded MRI using the TRASE Method," *Proc. Intl. Soc. Mag. Reson. Med. 21 (2013)*, 2013.

[25] Q. Deng, S. B. King, V. Volotovskyy, B. Tomanek, and J. C. Sharp, "B1 transmit phase gradient coil for single-axis TRASE RF encoding," *Magnetic Resonance Imaging*, vol. 31, no. 6, pp. 891–899, Jul. 2013. DOI: 10.1016/j.mri.2013.03.017. [Online]. Available: https://doi.org/10.1016/j.mri.2013.03.017.

[26] F. Bloch, "Nuclear induction," *Physical Review*, vol. 70, no. 7-8, pp. 460–474, 1946, ISSN: 0031-899X. DOI: 10.1103/PhysRev.70.460.

[27] F. Bloch, W. W. Hansen, and P. Me, *The Nuclear Induction Experiment*. 1946, vol. 70, pp. 474–485. DOI: 10.1103/PhysRev.70.474.

[28] E. Haacke, R. Brown, M. Thompson, and R. Venkatesan, *Magnetic Resonance Imaging: Physical Principles and Sequence Design*. Wiley, 1999, ISBN: 9780471351283. [Online]. Available: https://books.google.ca/books?id=BnOvQgAACAAJ.

[29] E. L. Hahn, "Spin echoes," *Phys. Rev.*, vol. 80, pp. 580–594, 4 Nov. 1950. DOI: 10.1103/PhysRev.80.580. [Online]. Available: https://link.aps.org/doi/10.1103/PhysRev.80.580.

[30] R. H. Hashemi, W. G. Bradley, C. J. Lisanti, and I. Ovid Technologies, *MRI : The Basics*, English, 2nd ed. Philadelphia : Lippincott Williams & Wilkins, 2004, Formerly CIP, ISBN: 0781741572.

[31] D. Moratal, A. Vallés-Luch, L. Martí-Bonmatí, and M. Brummer, "K-space tutorial: An mri educational tool for a better understanding of k-space," *Biomedical imaging and intervention journal*, vol. 4, no. 1, e15–e15, 2008, ISSN: 1823-5530. DOI: 10.2349/biij.4.1.e15. [Online]. Available: https://pubmed.ncbi.nlm.nih.gov/21614308%20https://www.ncbi.nlm.nih.gov/pmc/articles/PMC3097694/.

[32] P. C. Lauterbur, "Image formation by induced local interactions: Examples employing nuclear magnetic resonance," *Nature*, vol. 242, no. 5394, pp. 190–191, 1973, ISSN: 1476-4687. DOI: 10.1038/242190a0. [Online]. Available: https://doi.org/10.1038/242190a0.

[33] Q. Qin, "Point spread functions of the T2 decay in k-space trajectories with long echo train," *Magn Reson Imaging*, vol. 30, no. 8, pp. 1134–42, 2012, ISSN: 1873-5894 (Electronic) 0730-725X (Linking). DOI: 10.1016/j.mri.2012.04.017. [Online]. Available: https://www.ncbi.nlm.nih.gov/pubmed/22817958.

[34] D. Schaefer, "SAR Measurement," *Proc. Intl. Soc. Mag. Reson. Med. (2009)*, Feb. 2009.

[35] J. C. Sharp, Q. Deng, S. B. King, V. Volotovskyy, and B. Tomanek, "High Resolution 2D Imaging without Gradients with Accelerated TRASE.," *16th Annual Meeting of the International Society of Magnetic Resonance in Medicine.*, 2008.

[36] R. Ludwig and P. Bretchko, *RF Circuit Design: Theory & Applications (2nd Edition)*. Upper Saddle River, NJ, USA: Prentice-Hall, Inc., 2007, ISBN: 0131471376.

[37] J. Mispelter, M. Lupu, and A. Briguet, *NMR Probeheads for Biophysical and Biomedical Experiments: Theoretical Principles and Practical Guidelines*. Imperial College Press, 2015, ISBN: 9781848166622. [Online]. Available: https://books.google.ca/books?id=u9vEbwAACAAJ.

[38] F. Caspers and P. Kowina, "RF Measurement Concepts," CERN in the Proceedings of the CAS-CERN Accelerator School: Advanced Accelerator Physics, Trondheim, Norway, 19-29 August 2013, Tech. Rep., 2014.

[39] F. W. Grover, *Inductance calculations: working formulas and tables*. Courier Corporation, 2004.

[40] M. Kamon, L. Silveira, C. Smithhisler, and J. White, "Fasthenry user's guide," 1996.

[41] M. R. Bendall, A. Connelly, and J. M. McKendry, "Elimination of coupling between cylindrical transmit coils and surface-receive coils for in vivo NMR," *Magnetic Resonance in Medicine*, vol. 3, no. 1, pp. 157–163, 1986. DOI: 10.1002/mrm.1910030124. eprint: https://onlinelibrary.wiley.com/doi/pdf/10.1002/mrm.1910030124. [Online]. Available: https://onlinelibrary.wiley.com/doi/abs/10.1002/mrm.1910030124.

[42] P.-J. Nacher, S. Kumaragamage, G. Tastevin, and C. P. Bidinosti, "A fast MOSFET RF switch for low-field NMR and MRI," *Journal of Magnetic Resonance*, vol. 310, p. 106 638, 2020, ISSN: 1090-7807. DOI: https://doi.org/10.1016/j.jmr.2019.106638. [Online]. Available: http://www.sciencedirect.com/science/article/pii/S1090780719302770.

[43] L. Quéval, "BSmag Toolbox User Manual, Tech. report, Dept. Elect. Eng., University of Applied Sciences Düsseldorf, Germany," Apr. 2015. [Online]. Available: http://www.lqueval.com.

[44] D. M. Peterson, "Impedance matching and baluns," in *eMagRes*. American Cancer Society, 2011, ISBN: 9780470034590. DOI: 10.1002/9780470034590.emrstm1112. eprint: https://onlinelibrary.wiley.com/doi/pdf/10.1002/9780470034590.emrstm1112. [Online]. Available: https://onlinelibrary.wiley.com/doi/abs/10.1002/9780470034590.emrstm1112.

[45] C. F. M. Carobbi and L. M. Millanta, "Analysis of the common-mode rejection in the measurement and generation of magnetic fields using loop probes," *IEEE Transactions on Instrumentation and Measurement*, vol. 53, pp. 514–523, 2004.

[46] C. H. Cunningham, J. M. Pauly, and K. S. Nayak, "Saturated double-angle method for rapid B1+ mapping," *Magnetic Resonance in Medicine: An Official Journal of the International Society for Magnetic Resonance in Medicine*, vol. 55, no. 6, pp. 1326–1333, 2006.

[47] S. Salajeghe, P. Babyn, J. C. Sharp, and G. E. Sarty, "Least squares reconstruction of non-linear RF phase encoded MR data," *Magnetic Resonance Imaging*, vol. 34, no. 7, pp. 951–963, Sep. 2016. DOI: 10.1016/j.mri.2016.04.010. [Online]. Available: https://doi.org/10.1016/j.mri.2016.04.010.

[48] C. Bidinosti, C. Liu, and S. King, "The intrinsic magnetic field symmetries of the spiral birdcage coil," in *Proc. Intl. Soc. Mag. Reson. Med*, vol. 18, 2010, p. 1509.

[49] T. Taves, L. Kasian, and S. King, "The SNR of spiral birdcage coils," 2004.

[50] J. Bellec, C.-Y. Liu, and S. B. King, "A Target Field Approach to the Design of RF Phase-Gradient Coils," *Proc. Intl. Soc. Mag. Reson. Med. 19 (2011)*, 2011.

[51] S. Wang, "Measurement of the magnetic field of an RF-encoding birdcage-coil design for magnetic resonance imaging," Master's thesis, University of Saskatchewan, Jun. 2016. [Online]. Available: http://hdl.handle.net/10388/7316.

[52] D. Alsop, T. Connick, and G. Mizsei, "A spiral volume coil for improved RF field homogeneity at high static magnetic field strength," *Magnetic Resonance in Medicine*, vol. 40, pp. 49–54, 1 1998.

[53] S. Yong, B. Tomanek, and J. C. Sharp, "The Twisted Solenoid RF Phase Gradient Transmit Coil for TRASE Imaging," *Proc. Intl. Soc. Mag. Reson. Med. 25 (2017) Honolulu, p. 4281*, 2017.

[54] C. Goodzeit, M. Ball, and R. Meinke, "The double-helix dipole - a novel approach to accelerator magnet design," *IEEE Transactions on Appiled Superconductivity*, vol. 13, no. 2, pp. 1365–1368, Jun. 2003. DOI: 10.1109/tasc.2003.812672. [Online]. Available: https://doi.org/10.1109/tasc.2003.812672.

[55] J. Alonso, A. Soleilhavoup, A. Wong, A. Guiga, and D. Sakellariou, "Double helix dipole design applied to magnetic resonance: A novel NMR coil," *Journal of Magnetic Resonance*, vol. 235, pp. 32–41, Oct. 2013. DOI: 10.1016/j.jmr.2013.07.004. [Online]. Available: https://doi.org/10.1016/j.jmr.2013.07.004.

[56] R. Meinke, C. Goodzeit, and M. Ball, "Modulated double-helix quadrupole magnets," *IEEE Transactions on Appiled Superconductivity*, vol. 13, no. 2, pp. 1369–1372, Jun. 2003. DOI: 10.1109/tasc.2003.812674. [Online]. Available: https://doi.org/10.1109/tasc.2003.812674.

[57] L. Queval and R. Gottkehaskamp, "Analytical field calculation of modulated double helical coils," *IEEE Transactions on Applied Superconductivity*, vol. 25, no. 6, pp. 1–7, Dec. 2015. DOI: 10.1109/tasc.2015.2477377. [Online]. Available: https://doi.org/10.1109/tasc.2015.2477377.

[58] B. Blasiak, V. Volotovskyy, C. Deng, and B. Tomanek, "An optimized solenoidal head radiofrequency coil for low-field magnetic resonance imaging," *Magnetic Resonance Imaging*, vol. 27, no. 9, pp. 1302–1308, Nov. 2009. DOI: 10.1016/j.mri.2009.05.018. [Online]. Available: https://doi.org/10.1016/j.mri.2009.05.018.

[59] D. M. Ginsberg and M. J. Melchner, "Optimum geometry of saddle shaped coils for generating a uniform magnetic field," *Review of Scientific Instruments*, vol. 41, no. 1, pp. 122–123, 1970, ISSN: 0034-6748 1089-7623. DOI: 10.1063/1.1684235.

[60] J. C. Sharp, D. Yin, R. H. Bernhardt, Q. Deng, A. E. Procca, R. L. Tyson, K. Lo, and B. Tomanek, "The integration of real and virtual magnetic resonance imaging experiments in a single instrument," *Review of Scientific Instruments*, vol. 80, no. 9, p. 093 709, Sep. 2009. DOI: 10.1063/1.3202410. [Online]. Available: https://doi.org/10.1063/1.3202410.

[61] H. Sun, A. Purchase, A. AlZubaidi, P. Bohidar, G. Sarty, B. Tomanek, and J. C. Sharp, "High Resolution TRASE by Rapid Echo Encoding with Twisted Solenoid RF Phase Gradient Coils," in *Proc. Intl. Soc. Mag. Reson. Med. 27 (2019)*, 2019.

[62] S. Su, M. X. Zou, and J. Murphy-Boesch, "Solenoidal array coils," *Magn Reson Med*, vol. 47, no. 4, pp. 794–9, 2002, ISSN: 0740-3194 (Print) 0740-3194 (Linking). [Online]. Available: https://www.ncbi.nlm.nih.gov/pubmed/11948742.

[63] L. Cohen and S. United, *An exact formula for the mutual inductance of coaxial solenoids*, ser. Bulletin of the Bureau of Standards ;v. 3, no. 2. [Washington, D.C.: U.S. Dept. of Commerce and Labor, Bureau of Standards : U.S. Govt. Print. Off., 1907, p. 295-303. [Online]. Available: //catalog.hathitrust.org/Record/009487514%20http://hdl.handle.net/2027/mdp.39015086557116.

[64] E. B. Rosa, L. Cohen, and S. United, *The mutual inductance of coaxial solenoids*, ser. Bulletin of the Bureau of Standards ;v. 3, no. 2. [Washington, D.C.: U.S. Dept. of Commerce and Labor, Bureau of Standards : U.S. Govt. Print. Off., 1907, p. 305-324. [Online]. Available: //catalog.hathitrust.org/Record/009487515%20http://hdl.handle.net/2027/mdp.39015086557124.

[65] H. B. Dwight and P. W. Sayles, "Mutual inductance of short concentric solenoids," *Journal of Mathematics and Physics*, vol. 9, no. 1-4, pp. 162–165, 1930, ISSN: 0097-1421. DOI: 10.1002/sapm193091162. [Online]. Available: https://doi.org/10.1002/sapm193091162.

[66] M. Caravaca, J. Abad, and J. D. Catalá, "Biot-savart law as a tool to calculate the matrix of inductances and the coupling coefficient of two coaxial solenoids with arbitrary cross sections," *International Journal of Electrical Engineering & Education*, vol. 52, no. 3, pp. 237–247, 2015, ISSN: 0020-7209 2050-4578. DOI: 10.1177/0020720915583862.

[67] L. Wu, K. Lu, and Y. Xia, "Mutual inductance calculation of two coaxial solenoid coils with iron core," *2018 21st International Conference on Electrical Machines and Systems (ICEMS)*, pp. 1804–1808, 2018.

[68] P. B. Roemer, W. A. Edelstein, C. E. Hayes, S. P. Souza, and O. M. Mueller, "The NMR phased array," *Magnetic Resonance in Medicine*, vol. 16, no. 2, pp. 192–225, 1990. DOI: doi:10.1002/mrm.1910160203. [Online]. Available: https://onlinelibrary.wiley.com/doi/abs/10.1002/mrm.1910160203.

[69] X. Song, W. Wang, B. Zhang, M. Lei, and S. Bao, "Digitalization decoupling method and its application to the phased array in MRI," *Progress in Natural Science*, vol. 13, no. 9, pp. 683–689, 2003. DOI: 10.1080/10020070312331344240. eprint: https://www.tandfonline.com/doi/pdf/10.1080/10020070312331344240. [Online]. Available: https://www.tandfonline.com/doi/abs/10.1080/10020070312331344240.

[70] M. A. Ohliger and D. K. Sodickson, "An introduction to coil array design for parallel MRI," *NMR Biomed*, vol. 19, no. 3, pp. 300–15, 2006, ISSN: 0952-3480 (Print) 0952-3480 (Linking). DOI: 10.1002/nbm.1046. [Online]. Available: https://www.ncbi.nlm.nih.gov/pubmed/16705631.

[71] S. Orzada, S. Maderwald, S. L. Göricke, N. Parohl, S. C. Ladd, M. E. Ladd, and H. H. Quick, "Design and comparison of two eight-channel transmit/receive radiofrequency arrays for in vivo rodent imaging on a 7 T human whole-body MRI system," *Medical Physics*, vol. 37, no. 5, pp. 2225–2232, 2010, ISSN: 0094-2405. DOI: 10.1118/1.3378478. [Online]. Available: https://doi.org/10.1118/1.3378478.

[72] Y. Duan, B. S. Peterson, F. Liu, and A. Kangarlu, "A Composite Decoupling Method for RF Transceiver Array Coils in MRI," in *Proc. Intl. Soc. Mag. Reson. Med.*, 2010.

[73] B. Wu, X. Zhang, P. Qu, and G. X. Shen, "Design of an inductively decoupled microstrip array at 9.4 T," *J Magn Reson*, vol. 182, no. 1, pp. 126–32, 2006, ISSN: 1090-7807 (Print) 1090-7807 (Linking). DOI: 10.1016/j.jmr.2006.04.013. [Online]. Available: https://www.ncbi.nlm.nih.gov/pubmed/16829145.

[74] B. Wu, P. Qu, C. Wang, J. Yuan, and G. X. Shen, "Interconnecting L/C components for decoupling and its application to low-field open MRI array," *Concepts in Magnetic Resonance Part B: Magnetic Resonance Engineering*, vol. 31B, no. 2, pp. 116–126, 2007, ISSN: 15525031 1552504X. DOI: 10.1002/cmr.b.20087.

[75] C. Von Morze, J. Tropp, S. Banerjee, D. Xu, K. Karpodinis, L. Carvajal, C. P. Hess, P. Mukherjee, S. Majumdar, and D. B. Vigneron, "An eight-channel, nonoverlapping phased array coil with capacitive decoupling for parallel MRI at 3 T," *Concepts in Magnetic Resonance Part B: Magnetic Resonance Engineering*, vol. 31B, no. 1, pp. 37–43, 2007, ISSN: 15525031 1552504X. DOI: 10.1002/cmr.b.20078.

[76] R. F. Lee, R. O. Giaquinto, and C. J. Hardy, "Coupling and decoupling theory and its application to the MRI phased array," *Magn Reson Med*, vol. 48, no. 1, pp. 203–13, 2002, ISSN: 0740-3194 (Print) 0740-3194 (Linking). DOI: 10.1002/mrm.10186. [Online]. Available: https://www.ncbi.nlm.nih.gov/pubmed/12111947.

[77] J. Jevtic, "Ladder networks for capacitive decoupling in phased-array coils," in *Proc. Intl. Soc. Mag. Reson. Med 9*, 2001.

[78] Y. Li, Z. Xie, Y. Pang, D. Vigneron, and X. Zhang, "ICE decoupling technique for RF coil arrary designs," *Med Phys*, vol. 38, no. 7, 2011. DOI: 10.1118/1.3598112].

[79] X. Yan, J. C. Gore, and W. A. Grissom, "New resonator geometries for ICE decoupling of loop arrays," *J Magn Reson*, vol. 277, pp. 59–67, 2017, ISSN: 1096-0856 (Electronic) 1090-7807 (Linking). DOI: 10.1016/j.jmr.2017.02.011. [Online]. Available: https://www.ncbi.nlm.nih.gov/pubmed/28236786.

[80] A. Özen, M. Bock, and E. Atalar, *Active decoupling of RF coils using a transmit array system*. 2015, vol. 28. DOI: 10.1007/s10334-015-0497-0.

[81] X. Yan, J. C. Gore, and W. A. Grissom, "Self-decoupled radiofrequency coils for magnetic resonance imaging," *Nat Commun*, vol. 9, no. 1, p. 3481, 2018, ISSN: 2041-1723 (Electronic) 2041-1723 (Linking). DOI: 10.1038/s41467-018-05585-8. [Online]. Available: https://www.ncbi.nlm.nih.gov/pubmed/30154408.

[82] S. C. Thierauf, "High-speed circuit board signal integrity, second edition," 2017, ISSN: 9781630814441 163081444X. [Online]. Available: http://www.books24x7.com/marc.asp?bookid=132761.

[83] P. Bohidar, H. Sun, G. E. Sarty, and J. C. Sharp, "TRASE 1D sequence performance in imperfect B1 fields," *Journal of Magnetic Resonance*, vol. 305, pp. 77–88, 2019, ISSN: 10907807. DOI: 10.1016/j.jmr.2019.06.005.

[84] A. R. Purchase, T. Pałasz, H. Sun, J. C. Sharp, and B. Tomanek, "A high duty-cycle, multi-channel, power amplifier for high-resolution radiofrequency encoded magnetic resonance imaging," *Magnetic Resonance Materials in Physics, Biology and Medicine*, 2019, ISSN: 0968-5243 1352-8661. DOI: 10.1007/s10334-019-00763-1.

[85] X. Zhu, B. Tomanek, and J. Sharp, "A pixel is an artifact: On the necessity of zero-filling in Fourier imaging," *Concepts in Magnetic Resonance Part A*, vol. 42A, no. 2, pp. 32–44, 2013, ISSN: 1552-5023. DOI: 10.1002/cmr.a.21256. [Online]. Available: https://doi.org/10.1002/cmr.a.21256.

[86] W. D. Rooney, G. Johnson, X. Li, E. R. Cohen, S. G. Kim, K. Ugurbil, and J. Springer C. S., "Magnetic field and tissue dependencies of human brain longitudinal 1H2O relaxation in vivo," *Magn Reson Med*, vol. 57, no. 2, pp. 308–18, 2007, ISSN: 0740-3194 (Print) 0740-3194 (Linking). DOI: 10.1002/mrm.21122. [Online]. Available: https://www.ncbi.nlm.nih.gov/pubmed/17260370.

[87] S. Li, Q. X. Yang, and M. B. Smith, "RF coil optimization: Evaluation of B1 field homogeneity using field histograms and finite element calculations," *Magnetic Resonance Imaging*, vol. 12, no. 7, pp. 1079–1087, 1994, ISSN: 0730-725X. DOI: https://doi.org/10.1016/0730-725X(94)91240-W. [Online]. Available: http://www.sciencedirect.com/science/article/pii/0730725X9491240W.

[88] P. Bohidar, G. Sarty, and J. C. Sharp, "The Effects of Coupled B1 Fields in B1 Encoded TRASE MRI – A Simulation Study," in *Proc. Intl. Soc. Mag. Reson. Med. 28 (2020)*, 2020.

[89] U. Katscher and P. Börnert, "Parallel RF transmission in MRI," *NMR in Biomedicine*, vol. 19, no. 3, pp. 393–400, 2006, ISSN: 0952-3480. DOI: 10.1002/nbm.1049. [Online]. Available: https://onlinelibrary.wiley.com/doi/abs/10.1002/nbm.1049.

[90] J. S. Hyde, A. Jesmanowicz, W. Froncisz, J. [Kneeland], T. M. Grist, and N. F. Campagna, "Parallel image acquisition from noninteracting local coils," *Journal of Magnetic Resonance (1969)*, vol. 70, no. 3, pp. 512–517, 1986, ISSN: 0022-2364. DOI: https://doi.org/10.1016/0022-2364(86)90146-0. [Online]. Available: http://www.sciencedirect.com/science/article/pii/0022236486901460.

[91] W. A. Grissom, L. Sacolick, and M. W. Vogel, "Improving high-field MRI using parallel excitation," *Imaging in Medicine*, vol. 2, no. 6, pp. 675–693, 2010, ISSN: 1755-5191.

[92] P. Röschmann, "Radiofrequency penetration and absorption in the human body: Limitations to high-field whole-body nuclear magnetic resonance imaging," *Medical Physics*, vol. 14, no. 6, pp. 922–931, 1987, ISSN: 0094-2405. DOI: 10.1118/1.595995. [Online]. Available: https://aapm.onlinelibrary.wiley.com/doi/abs/10.1118/1.595995.

[93] T. S. Ibrahim, Y.-K. Hue, and L. Tang, "Understanding and manipulating the RF fields at high field MRI," *NMR in Biomedicine: An International Journal Devoted to the Development and Application of Magnetic Resonance In vivo*, vol. 22, no. 9, pp. 927–936, 2009.

[94] F. Padormo, A. Beqiri, J. V. Hajnal, and S. J. Malik, "Parallel transmission for ultrahigh-field imaging," *NMR Biomed*, vol. 29, no. 9, pp. 1145–61, 2016, ISSN: 1099-1492 (Electronic) 0952-3480 (Linking). DOI: 10.1002/nbm.3313. [Online]. Available: https://www.ncbi.nlm.nih.gov/pubmed/25989904.

[95] B. Yang, P.-S. Wei, C. E. McElcheran, F. Tam, and S. J. Graham, "A Platform for 4-channel Parallel Transmission MRI at 3 T: Demonstration of Reduced Radiofrequency Heating in a Test Object Containing an Implanted Wire," *Journal of Medical and Biological Engineering*, vol. 39, no. 6, pp. 835–844, 2019, ISSN: 1609-0985.

[96] S. Orzada, K. Solbach, M. Gratz, S. Brunheim, T. M. Fiedler, S. Johst, A. K. Bitz, S. Shooshtary, A. Abuelhaija, M. N. Voelker, S. H. G. Rietsch, O. Kraff, S. Maderwald, M. Floser, M. Oehmigen, H. H. Quick, and M. E. Ladd, "A 32-channel parallel transmit system add-on for 7T MRI," *PLoS One*, vol. 14, no. 9, e0222452, 2019, ISSN: 1932-6203 (Electronic) 1932-6203 (Linking). DOI: 10.1371/journal.pone.0222452. [Online]. Available: https://www.ncbi.nlm.nih.gov/pubmed/31513637.

[97] Y. Eryaman, B. Akin, and E. Atalar, "Reduction of implant RF heating through modification of transmit coil electric field," *Magn Reson Med*, vol. 65, no. 5, pp. 1305–13, 2011, ISSN: 1522-2594 (Electronic) 0740-3194 (Linking). DOI: 10.1002/mrm.22724. [Online]. Available: https://www.ncbi.nlm.nih.gov/pubmed/21500259.

[98] *Analog Converter and Waveform Generator AD9106*, Rev.B, Analog Devices. [Online]. Available: https://www.analog.com/media/en/technical-documentation/data-sheets/ad9106.pdf.

[99] *AD9106 Evaluation Board Quick Start Guide*, Analog Devices. [Online]. Available: ftp://ftp.analog.com/pub/HSSP_SW/HSCDAC/Documents/AD9106/AD9106%20Evaluation%20Board%20Quick%20Start%20Guide.pdf.

[100] *AD9514 - 1.6 GHz Clock Distribution IC*, Rev.0, Analog Devices. [Online]. Available: https://www.analog.com/media/en/technical-documentation/data-sheets/AD9514.pdf.

[101] *ADC-SoC User Manual*, Version 1.0.1, Terasic, Oct. 2017. [Online]. Available: https://www.terasic.com.tw/cgi-bin/page/archive_download.pl?Language=English&No=1061&FID=2170285f16d7e05879607fccd2f31574.

[102] Y. Yu, "A Linear Transmit Design of Ultrasound System Based on AD9106," *Zhongguo yi liao qi xie za zhi = Chinese journal of medical instrumentation*, vol. 40, no. 5, pp. 344–346, Sep. 2016, ISSN: 1671-7104. [Online]. Available: http://europepmc.org/abstract/MED/29792629.

[103] L. Gong, G. Shen, S. Qiao, W. Liu, and Y. Yi, "A miniaturized phased high intensity focused ultrasound transducer-driven system with MR compatibility," in *2017 10th International Congress on Image and Signal Processing, BioMedical Engineering and Informatics (CISP-BMEI)*, Oct. 2017, pp. 1–5. DOI: 10.1109/CISP-BMEI.2017.8302248.

[104] *Cyclone V Hard Processor System Technical Reference Manual*, Intel. [Online]. Available: https://www.intel.com/content/dam/www/programmable/us/en/pdfs/literature/hb/cyclone-v/cv_54001.pdf.

[105] *Using Linux* on DE-series Boards*, Intel. [Online]. Available: ftp://ftp.intel.com/Pub/fpgaup/pub/Intel_Material/17.0/Tutorials/Linux_On_DE_Series_Boards.pdf.

[106] *Cyclone V Device Handbook*, Volume 1: Device Interfaces and Integration, Intel. [Online]. Available: https://www.intel.ca/content/dam/www/programmable/us/en/pdfs/literature/hb/cyclone-v/cv_5v2.pdf.

[107] *ARM DS-5 Eclipse for DS-5 User Guide*, ARM Limited or its affiliates, 2016. [Online]. Available: https://static.docs.arm.com/dui0480/u/DUI0480U_arm_ds5_eclipse_user_guide.pdf.

[108] J. Cochingco, "Design and implementation of a modularized ultrasound breast imaging system," Master's thesis, University of Manitoba, Mar. 2018.

[109] A. Samoilenko, D. Y. Artemov, and L. Sibeldina, "Formation of sensitive layer in experiments on NMR subsurface imaging of solids," *Jetp Lett*, vol. 47, no. 7, pp. 417–419, 1988.

[110] P. J. McDonald, "Stray field magnetic resonance imaging," *Progress in Nuclear Magnetic Resonance Spectroscopy*, vol. 30, no. 1, pp. 69–99, 1997, ISSN: 0079-6565. DOI: https://doi.org/10.1016/S0079-6565(96)01035-7. [Online]. Available: http://www.sciencedirect.com/science/article/pii/S0079656596010357.

[111] T. B. Benson and P. J. McDonald, "The application of spin echoes to stray-field imaging," *Journal of Magnetic Resonance, Series B*, vol. 109, no. 3, pp. 314–317, 1995, ISSN: 1064-1866. DOI: https://doi.org/10.1006/jmrb.1995.9989. [Online]. Available: http://www.sciencedirect.com/science/article/pii/S106418668579989X.

[112] C. L. Epstein and J. Magland, "A novel technique for imaging with inhomogeneous fields," *J Magn Reson*, vol. 183, no. 2, pp. 183–92, 2006, ISSN: 1090-7807 (Print) 1090-7807 (Linking). DOI: 10.1016/j.jmr.2006.08.012. [Online]. Available: https://www.ncbi.nlm.nih.gov/pubmed/16962800.

[113] A. J. Parker, W. Zia, C. W. Rehorn, and B. Blumich, "Shimming Halbach magnets utilizing genetic algorithms to profit from material imperfections," *J Magn Reson*, vol. 265, pp. 83–9, 2016, ISSN: 1096-0856 (Electronic) 1090-7807 (Linking). DOI: 10.1016/j.jmr.2016.01.014. [Online]. Available: https://www.ncbi.nlm.nih.gov/pubmed/26874333.

[114] E. Danieli, J. Mauler, J. Perlo, B. Blumich, and F. Casanova, "Mobile sensor for high resolution NMR spectroscopy and imaging," *J Magn Reson*, vol. 198, no. 1, pp. 80–7, 2009, ISSN: 1096-0856 (Electronic) 1090-7807 (Linking). DOI: 10.1016/j.jmr.2009.01.022. [Online]. Available: https://www.ncbi.nlm.nih.gov/pubmed/19217330.

[115] E. Danieli, J. Perlo, B. Blumich, and F. Casanova, "Small magnets for portable NMR spectrometers," *Angew Chem Int Ed Engl*, vol. 49, no. 24, pp. 4133–5, 2010, ISSN: 1521-3773 (Electronic) 1433-7851 (Linking). DOI: 10.1002/anie.201000221. [Online]. Available: https://www.ncbi.nlm.nih.gov/pubmed/20446281.

[116] C. Z. Cooley, M. W. Haskell, S. F. Cauley, C. Sappo, C. D. Lapierre, C. G. Ha, J. P. Stockmann, and L. L. Wald, "Design of Sparse Halbach Magnet Arrays for Portable MRI Using a Genetic Algorithm," *IEEE Transactions on Magnetics*, vol. 54, no. 1, pp. 1–12, 2018, ISSN: 0018-9464. DOI: 10.1109/TMAG.2017.2751001.

[117] P. Blümler, "Proposal for a permanent magnet system with a constant gradient mechanically adjustable in direction and strength," *Concepts in Magnetic Resonance Part B: Magnetic Resonance Engineering*, vol. 46, no. 1, pp. 41–48, 2016, ISSN: 15525031. DOI: 10.1002/cmr.b.21320.

[118] *AD9106-EBZ RevC Schematic*, Analog Devices, Oct. 2012. [Online]. Available: ftp://ftp.analog.com/pub/HSSP_SW/HSCDAC/Documents/AD9106/AD9106-EBZ%20RevC%20Schematic.pdf.

[119] *ADP1715 - CMOS Linear Regulator*, Analog Devices. [Online]. Available: https://www.analog.com/media/en/technical-documentation/data-sheets/ADP1715_1716.pdf.

Appendices

Appendices I - for Chapter 4

An Example C Code using Arduino Single Board Computer (Mega 2560) to Generate Two RFPA Enable (Gating) Signals

```
// Hongwei Sun
// This code takes a dummy pulse from input, as a sign to start generate gating pulses fr two RFAPs
// Note that the first 90 and 180 pulse are special
// Coil A and B will be repeatedly controlled by "for" loop

const
// RF page
int EXCITATION_PULSE_LEN = 200;          // Duration of 90 pulse (us)
int REFOCUS_PULSE_LEN = 200;         // Duration of 180 pulse (us)

// Timing page
int ECHO_TIME = 1000;      // Timing between two 180 pulses (us) or Echo spacing
int ECHOES = 128;


// Account for instability
int Ext_time_window = 10;
// Duration of extended timing window on both sides of each gating signal
int First_Pulse_Delay = 0;
// Observed delay for first pulse caused by Arduino board


// Set input/output channels

int Gating_input = 21;

int Gating_RFAP_A = 49;
// PORTL6

int Gating_RFAP_B = 37;
// PORTC1   https://www.arduino.cc/en/uploads/Main/arduino-mega2560-schematic.pdf


// Timing constant calcs
int Time_After_90 = (ECHO_TIME/2) - First_Pulse_Delay -
Ext_time_window - ((EXCITATION_PULSE_LEN + REFOCUS_PULSE_LEN)/2);

int Time_On = REFOCUS_PULSE_LEN +  Ext_time_window + Ext_time_window;
int Time_Off = ECHO_TIME - 2*Ext_time_window - ((REFOCUS_PULSE_LEN + REFOCUS_PULSE_LEN)/2);

void setup() {
// initialize outputs pins:
pinMode(Gating_input, INPUT_PULLUP);
attachInterrupt(digitalPinToInterrupt(Gating_input), Main, RISING);
//pinMode(Gating_RFAP_A,OUTPUT);
//pinMode(Gating_RFAP_B,OUTPUT);
// Set all pins in PORTL & PORTC to be outputs
DDRL = B11111111;
DDRC = B11111111;

}

void loop() {
}


void Main() {
detachInterrupt(digitalPinToInterrupt(Gating_input));
```

```
PORTL = 1; // PORTL = B00000001 set PORT-L Bit0 high
delayMicroseconds(EXCITATION_PULSE_LEN); //delayMicroseconds is accurate for above 3 us delay time
PORTL = 0; // PORTL = B00000000 set PORT-L Bit0 low
delayMicroseconds(Time_After_90);


// Below is repeated loop for A and B
for (int i = 0; i < ECHOES; i+=2){
// For coil A
PORTL = 1;
delayMicroseconds(Time_On);
PORTL = 0;
delayMicroseconds(Time_Off);

// For B coil
PORTC = 1;
delayMicroseconds(Time_On);
PORTC = 0;
delayMicroseconds(Time_Off);

//nop is 62.5 ns 0.1us = 100ns, so 4 nop for 0.25 us delay;
//asm("nop\n nop\n nop\n nop \n");  // 0.25 us nop
//asm("nop\n nop\n nop\n nop \n");  // 0.25 us nop
//asm("nop\n nop\n nop\n nop \n");  // 0.25 us nop
//asm("nop\n");  // 0.0625 us nop
}

delayMicroseconds(1000);
delayMicroseconds(1000);
delayMicroseconds(1000);
delayMicroseconds(1000);
delayMicroseconds(1000);
delayMicroseconds(1000);
delayMicroseconds(1000);
delayMicroseconds(1000);
delayMicroseconds(1000);
delayMicroseconds(1000);
delayMicroseconds(1000);
attachInterrupt(digitalPinToInterrupt(Gating_input), Main, RISING);
}
```

An Example MATLAB Code for Twisted Solenoid Field Calculation using BSMAG

```
%-------------------------------------------------------
%  AUTHOR:     Hongwei Sun (adapted from the code shared by L. Queval)
%  WHAT:       BSmag_1Dplot.m - Calculate numerically the magnetic field of a modulated helical coil (+ 1D plot).
%  REQUIRED:   BSmag Toolbox 20150407
%   (http://www.mathworks.com/matlabcentral/fileexchange/50434-biot-savart-magnetic-toolbox)
%-------------------------------------------------------

%Equations and explanation can be found in [1].
 %[1] L. Queval, R. Gottkehaskamp, "Analytical Field Calculation of Modulated Double Helical Coils,"
%IEEE Trans. on Applied
%Superconductivity, in press.

clear all, close all, clc

%% Fixed Parameters
%alpha     = 50;           % tilt angle [deg]
%alpha_rad = alpha*pi/180; %[rad]
n     = 2;              % coil multipole order. Fixed.
mu0   = 4*pi*1e-7;        % vacuum permeability
I1    = 1;               % current inner coil [A]
phi1 = 0;                % phase shift coil [rad] (rotates the coil pattern).

%% - Set Coil Geometric Parameters:
switch 4
case 1
% SET1 : Coil Parameters (Approx. to infinite)
a1_m    = 7.8/100.0;  % radius inner coil [m]
h_m     = 2.0/100.0;  % turn advance [m]
A_m     = 7.0/100.0;  % modulation inner coil [m]  was A_m = a1_m/tan(alpha_rad)
Nturns = 25;          %number of turns []

case 2
% SET2:
a1_m    = 7.8/100.0;  % radius inner coil [m]
h_m     = 1.0/100.0;  % turn advance [m]
A_m     = 7.0/100.0;  % modulation inner coil [m]  was A_m = a1_m/tan(alpha_rad)
Nturns = 4;           %number of turns []

case 3
% SET3:
a1_m    = 7.8/100.0;  % radius inner coil [m]
h_m     = 7.0/100.0;  % turn advance [m]
A_m     = 7.0/100.0;  % modulation inner coil [m]  was A_m = a1_m/tan(alpha_rad)
Nturns = 4;           %number of turns []
```

```
case 4
% SET4 (Optimal TW-solenoid coil geometry - Hongwei):
a2_m    = 6.0325/100.0;   % I.D of Acrylic tube
a1_m    = 7.8/100.0;  % radius of coil (cylin O.D + radius of wire) [m]
%a1_m    = a2_m;        % Not used for calc. just for wire pattern printing
A_m     = 5.5/100.0;  % modulation inner coil [m]  was A_m = a1_m/tan(alpha_rad)
h_m     = 3.0/100.0;  % turn advance [m]
Nturns = 10;          % number of turns [] , set even number


otherwise
disp('other value')
end

field_points     = 35;
radius_fraction = 0.8;

Radius_cm  = a1_m * 100.0;
A_cm       =  A_m * 100.0;
Advance_cm =  h_m * 100.0;
h_cm = h_m*100.0;
a1_cm = a1_m*100.0;
a2_cm = a1_m*100.0;

disp('---- 1D PLOTS ----')
%disp(['Coil Radius:   ', num2str(Radius_cm), 'cm'])
%disp(['Modulation:    ', num2str(A_cm),       'cm'])
%disp(['Turn Advance: ', num2str(Advance_cm),'cm'])
%disp(['Turns:',          num2str(Nturns) ])

%% Numerical integration with BSmag toolbox
Wire = BSmag_init(); % Initialize BSmag analysis

Wire = [];
Wire.Nfilament = 0; %Number of source filament

% PLOT X,Y,Z AXES
left = 300;
bottom = 300;
width = 800;
height = 500;
%figure(1, 'position',[left bottom width height]);
figure(1);
set(gcf,'position',[left bottom width height]);
hold on, grid on, box on, axis equal
subplot(1,3,1)
view(3), %axis tight
grid on;


%% CURRENT source points
theta   = -Nturns*pi : 2*pi/(360*2) : Nturns*pi;   %may be smaller than 1 deg;  was  2*pi/(360*64)
%theta   = 0 : 2*pi/(360*2) : 2*Nturns*pi;   %may be smaller than 1 deg;  was  2*pi/(360*64)

Gamma  = [a1_m*cos(theta') a1_m*sin(theta') A_m*sin(n*theta'+phi1) + h_m/2/pi*theta']; % x,y,z [m,m,m]
dGamma = 1e9; % filament max discretization step [m]

%[Wire] = BSmag_add_filament(Wire, Gamma1, I1, dGamma1);
n = Wire.Nfilament+1;
Wire.filament(n).Gamma = Gamma;
Wire.filament(n).I = I1;
Wire.filament(n).dGamma = dGamma;
Wire.Nfilament = n;
% PLOT WIRE
%plot3(Gamma(:,1),Gamma(:,2),Gamma(:,3),'.-r')
plot3(Gamma(:,1)*100.0,Gamma(:,2)*100.0,Gamma(:,3)*100.0,'.-r') % in coordinates of cm
axis equal; grid on;
xlabel('x [cm]'), ylabel('y [cm]'), zlabel('z [cm]')
title('(A) 3D View of Twisted Solenoid Coil')

%% Plot Current on a 2D Sheet of Paper
% flat paper is (x,y), on which we will plot (theta,Z)
% One direction on paper is axial (Z) direction
% The other is the angle theta
circum_cm = 2*pi* Radius_cm;
paperYcoord_cm = Gamma(:,3) .* 100.0;   % third column
paperXcoord_cm = (circum_cm/(2*pi)) * mod(theta', 2*pi);
subplot(2,3,2);
scatter(paperXcoord_cm, paperYcoord_cm, '.r');
grid on;
xlabel('Circumferential (cm)')
ylabel('Axial (cm)')
title('(B) WIRE PATTERN')
axis equal;
%axis([-cm cm 0.9 1.5])


%% FIELD points (to calculate)
rho_M           = linspace(-radius_fraction*a2_m, radius_fraction*a2_m, field_points);
theta_M         = 0; % was 45*(pi/180); % theta [m]
```

```
[RHO_M,THETA_M] = ndgrid( rho_M, theta_M );
Z_M             = zeros( length(rho_M), length(theta_M) ) ; % z [m]

% Cylindrical -> Cartesian transformation
%[X_M, Y_M, Z_M] = pol2cart(THETA_M, RHO_M, Z_M);
X_M = RHO_M .* cos(THETA_M);
Y_M = RHO_M .* sin(THETA_M) + 0.015;

subplot(1,3,1); hold on;
%plot3(X_M, Y_M, Z_M, 'k.'); % black dots plot
plot3(X_M*100.0, Y_M*100.0, Z_M*100.0, 'k.'); % black dots plot in coordinates of cm.
%BSmag_plot_field_points(Wire, X_M, Y_M, Z_M); % shows the field points plane

%% Biot-Savart Integration
[Wire, X,Y,Z, BX,BY,BZ] = BSmag_get_B(Wire, X_M, Y_M, Z_M);

% Cartesian (x,y,z) -> Cylindrical transformation (theta,rho,z) [Not Needed at the moment.]
%[thetaM,rM,zM ] = cart2pol(X,Y,Z);
%Br              =  BX.*cos(thetaM) + BY.*sin(thetaM);
%Bth             = -BX.*sin(thetaM) + BY.*cos(thetaM);
%normB           = sqrt(BX.^2 + BY.^2 + BZ.^2);

%% MRI

B1mag   = sqrt(BY.^2 + BZ.^2);   % because B0 is in the X-direction
normalizeTo = min(B1mag);  %  minimum
B1mag = B1mag./normalizeTo;

%B1phase = atan2d(BZ, BY);
B1phase = atan2d(-BY, BZ);

%% Plot B/|B|
subplot(1,3,1); hold on;
%quiver3(X,Y,Z, BX./normB, BY./normB, BZ./normB,'b')
%quiver3(X,Y,Z, BX.*0.0, BY, BZ,'b')
quiver3(X*100.0,Y*100.0,Z*100.0, BX.*0.0, BY, BZ,'b') % in coordinates of cm.

%% 1D Plot

cm = 0.5 + a1_m * 100;

% Plot B1 vs. x
subplot(2,3,3);
box on, grid on, hold on
plot(X.*100.0, B1mag, 'b')
plot([-Radius_cm -Radius_cm], [0.0 2.5], '--k')  % vertical line
plot([+Radius_cm +Radius_cm], [0.0 2.5], '--k')  % vertical line
xlabel('X [cm]')
ylabel('B1 (a.u.)')
title('(C) B1 Magnitude (a.u.)')
yticks([0.95:0.05:1.3])
axis([-cm cm 0.95 1.3])

% Plot B1phase vs. x
subplot(2,3,6);
box on, grid on, hold on
plot(X.*100.0, B1phase, 'b')
plot([-Radius_cm -Radius_cm], [-40 40], '--k')  % vertical line
plot([+Radius_cm +Radius_cm], [-40 40], '--k')  % vertical line
xlabel('X (cm)')
ylabel('B1 Phase (deg)')
title('(D) B1 PHASE (deg)')
yticks([-40:10:40])
axis([-cm +cm -40 40])
%% SAVE FIGURE
saveas(gcf,'MATLAB1','epsc')
saveas(gcf,'MATLAB1','png')
```

Appendices II - for Chapter 5

Supporting Information in Methods:

Distributed capacitors: To avoid potential RF propagation phase shifts within the long wire, in my construction coil windings were broken every 1.6 m by a fixed capacitor, corresponding to 1/20 wavelength in free-space at 9.28 MHz.

FastHenry2: *FastHenry2* is derived from *FastHenry*, an acceleration of the mesh formulation approach, solved by a generalized minimal residual algorithm. *FastHenry2* is a frequency-dependent software package for the solution of Maxwell equations and extraction of inductances and resistances of three-dimensional conductive structures under the magnetoquasistatic approximation. Since the operating frequency is relatively low (f = 9.28 MHz), in the simulation I assumed that every segment carries a uniform current so the skin effect was not considered. This was done by setting each straight-line current segment into only one filament, *i.e.*, the segment height (h), width (w), number of filaments in the height ($nhinc$) and width ($nwinc$) direction were all assigned a default value of 1.0.

3D Printing: Printing parameters were as follows: bed temperature = 60°C, extrusion temperature = 205°C, infill percentage= 20%, layer thickness= 0.175 mm, top/bottom thickness= 1 mm, shell thickness= 1 mm, printing speed= 100 mm/sec, and with a skirt adhesion profile to avoid any non-linearity and geometric distortion at edges.

An Example Python Code Making Readable Files for *FastHenry2* Simulation

```
# -*- coding: utf-8 -*-
"""
Created on Mon Nov 19 15:17:49 2018

@author: hongwei -
Note this python code needs input of coil geometry,
```

```
generated from MATLAB code in chapter 3's appendix
"""

import math
# Constants:
endline = '\n'


#----------######## Write Nodes ###########----------#
def WriteNodes(output, nodefirst, number_of_nodes, x_mm, y_mm, z_mm):
"""
COIL nodes are points in space
"""
nodenum = nodefirst
for n in range(number_of_nodes):
output.write("N%d \t x=%6.3f  y=%6.3f  z=%6.3f " % (nodenum, x_mm[n], y_mm[n], z_mm[n])  )
output.write(endline)
nodenum += 1
return

#----------######## Write Segments ###########----------#
def WriteSegments(output, nodefirst, number_of_nodes):
"""
Coil segments join nodes to make the wire path
"""
nodeNum = nodefirst
segments = []
for seg in range(number_of_nodes-1):
nodepair =("N"+`nodeNum`, "N"+`nodeNum+1`)
nodeNum += 1
segments.append(nodepair)
#--- Write segments to file
segnum = nodefirst - 1
for seg in segments:
segnum += 1
output.write("E" + `segnum` + " " + seg[0] + " " + seg[1] + endline)
return

#----------######## Read Wire Points ###########----------#
def Read_Twisted(data_filename, henry_filename):
"""twisted coil data from Hongwei Oct 2018 """

print "\n-------\nReading wire path from: ", data_filename
output = open(henry_filename, "w")
output.write("*---- TW Coil, Hongwei" + endline)
output.write(".units MM" + endline)
output.write(".default sigma=5.8e4" + endline)
output.write(".default nhinc=3" + endline)
output.write(".default nwinc=3" + endline)

# Get node coords from file
f = open(data_filename, "r")
lines = f.readlines()
number_of_nodes = len(lines)
print "number_of_nodes",number_of_nodes
x_mm = []
y_mm = []
z_mm = []
for line in lines[::stride]:
(x_cm, y_cm, z_cm) = line.split() #cm
x_mm.append(float(x_cm) * 10.0)
y_mm.append(float(y_cm) * 10.0)
z_mm.append(float(z_cm) * 10.0)

#-- Look at the ranges of the coordinates:
number_of_nodes = len(x_mm)
print "Nodes used:     ", number_of_nodes
print "x_mm_min:%8.2f mm,   max:%8.2f mm" % (min(x_mm), max(x_mm))
print "y_mm_min:%8.2f mm,   max:%8.2f mm" % (min(y_mm), max(y_mm))
print "z_mm_min:%8.2f mm,   max:%8.2f mm" % (min(z_mm), max(z_mm))

#       #--- Center the Coil Position in the Z-direction
#       z_middle_mm = ( min(z_mm) + max(z_mm))/2.0
#       print "z middle mm:", z_middle_mm
#       for n in range(number_of_nodes):
#               z_mm[n] = z_mm[n] - z_middle_mm
#       print "z_mm_min:%8.2f mm,   max:%8.2f mm" % (min(z_mm), max(z_mm))

#--- Output Nodes
output.write(endline)
output.write("*---- Nodes" + endline)
WriteNodes(output, 1, number_of_nodes, x_mm, y_mm, z_mm)

#---- Create segments, joining all the nodes
output.write("" + endline)
output.write("*---- Wire Segments" + endline)
output.write("*- wire width and height" + endline)
output.write(".default w = 1.0" + endline)
output.write(".default h = 1.0" + endline)
WriteSegments(output, 1, number_of_nodes)

#--- Write Stuff at end of file
```

```
output.write(endline)
output.write("*---- External Port(s)" + endline)
output.write(".external N1 N%d" % number_of_nodes + endline)
output.write(endline)
output.write("*---- Frequency" + endline)
output.write(".freq fmin=9.27e6 fmax=9.27e6 ndec=1" + endline)
output.write(endline)
output.write(".end" + endline)
output.close()
print "Wrote:",henry_filename
return (x_mm, y_mm, z_mm)

def Twisted_Mutual(nodesCoil1, nodesCoil2, henry_filename, deg, (x_shift_mm, y_shift_mm, z_shift_mm)):
"""
Mutual Inductance, from two lists of nodes
"""
print "\nMutual: -->",henry_filename
(x1_mm, y1_mm, z1_mm) = nodesCoil1[:]
(x2_mm, y2_mm, z2_mm) = nodesCoil2[:]
number_of_nodes1 = len(x1_mm)
number_of_nodes2 = len(x2_mm)

# ROTATE COIL 2
# x' = x cos(t) - y sin(t)
# y' = x sin(t) + y cos(t)
print "The 2nd COIL rotated by:", deg
rad = deg * (math.pi/180.0)
(COS, SIN) = ( math.cos(rad), math.sin(rad) )
for n in range(number_of_nodes2):
xtemp = x2_mm[n]
ytemp = y2_mm[n]
x2_mm[n] = xtemp*COS - ytemp*SIN
y2_mm[n] = xtemp*SIN + ytemp*COS

#--- Shift Coil 2 in any direction
print "The 2nd COIL shifted by: ",x_shift_mm, y_shift_mm, z_shift_mm
for n in range(number_of_nodes2):
x2_mm[n] += x_shift_mm
y2_mm[n] += y_shift_mm
z2_mm[n] += z_shift_mm

#-- Print the ranges of the coordinates:
print "\n First Coil:"
print "x1_mm Min:%8.2f mm,  Max:%8.2f mm" % (min(x1_mm), max(x1_mm))
print "y1_mm Min:%8.2f mm,  Max:%8.2f mm" % (min(y1_mm), max(y1_mm))
print "z1_mm Min:%8.2f mm,  Max:%8.2f mm" % (min(z1_mm), max(z1_mm))
print "\n Second Coil:"
print "x2_mm Min:%8.2f mm,  Max:%8.2f mm" % (min(x2_mm), max(x2_mm))
print "y2_mm Min:%8.2f mm,  Max:%8.2f mm" % (min(y2_mm), max(y2_mm))
print "z2_mm Min:%8.2f mm,  Max:%8.2f mm" % (min(z2_mm), max(z2_mm))

#--- OUTPUT TO HENRY FILE
henry_filename = henry_filename + '_' + str(deg) + 'DEG' ...
+ '_' + '(' + str(x_shift_mm) + ',' + str(y_shift_mm) + ',' + str(z_shift_mm) +').inp'
output = open(henry_filename, "w")
output.write("*---- TW " + endline)
output.write(".units MM" + endline)
output.write(".default sigma=5.8e4" + endline)
output.write(".default nhinc=1" + endline)
output.write(".default nwinc=1" + endline)

FirstNode1 = 1
FirstNode2 = 100001
WriteNodes(output, FirstNode1, number_of_nodes1, x1_mm, y1_mm, z1_mm)
WriteNodes(output, FirstNode2, number_of_nodes2, x2_mm, y2_mm, z2_mm)

#---- Create segments, joining all the nodes
output.write("" + endline)
output.write("*---- Wire Segments" + endline)
output.write("*- wire width and height" + endline)
output.write(".default w = 1.0" + endline)
output.write(".default h = 1.0" + endline)
WriteSegments(output, FirstNode1, number_of_nodes1)
WriteSegments(output, FirstNode2, number_of_nodes2)

#--- Write Stuff at end of file
output.write(endline)
output.write("*---- External Port(s)" + endline)
LastNode1 = FirstNode1 + number_of_nodes1 - 1
LastNode2 = FirstNode2 + number_of_nodes2 - 1
output.write(".external N%d N%d" % (FirstNode1, LastNode1) + endline)
output.write(".external N%d N%d" % (FirstNode2, LastNode2) + endline)
output.write(endline)

output.write("*---- Frequency" + endline)
output.write(".freq fmin=9.27e6 fmax=9.27e6 ndec=1" + endline)
output.write(endline)
output.write(".end" + endline)
output.close()
print "Wrote:",henry_filename
return
```

```
#==== CODE BEGINS HERE ====#
print "\n\n----- Program to generate input files for the Fast Henry Inductance Calc Program ----"
#SquareLoopJCS1()

stride = 1  # jumps some of the input data. Dont need so many points to define coil.


nodesTW1 = Read_Twisted("TW-1-coil-coords.txt", "TW1.inp")
nodesTW2 = Read_Twisted("TW-2-coil-coords.txt", "TW2.inp")

x_shift_mm = 0.0 # Shift entire coil along x, to mimic my in/out adjustments
y_shift_mm = 0.0 # Shift entire coil along y, to mimic my in/out adjustments
z_shift_mm = +50.0 # Shift entire coil along z, to mimic my in/out adjustments
rot_Phi_deg = 45.0 # Rotate the second coil by rot_Phi_deg, to mimic the second coil rotation

#Twisted_Mutual(nodesTW1, nodesTW3, "TW13", rot_Phi_deg, ( x_shift_mm, y_shift_mm, z_shift_mm))
```

Appendices III - Chapter 6

Simulated B_1 field Maps Due To Coil Interactions

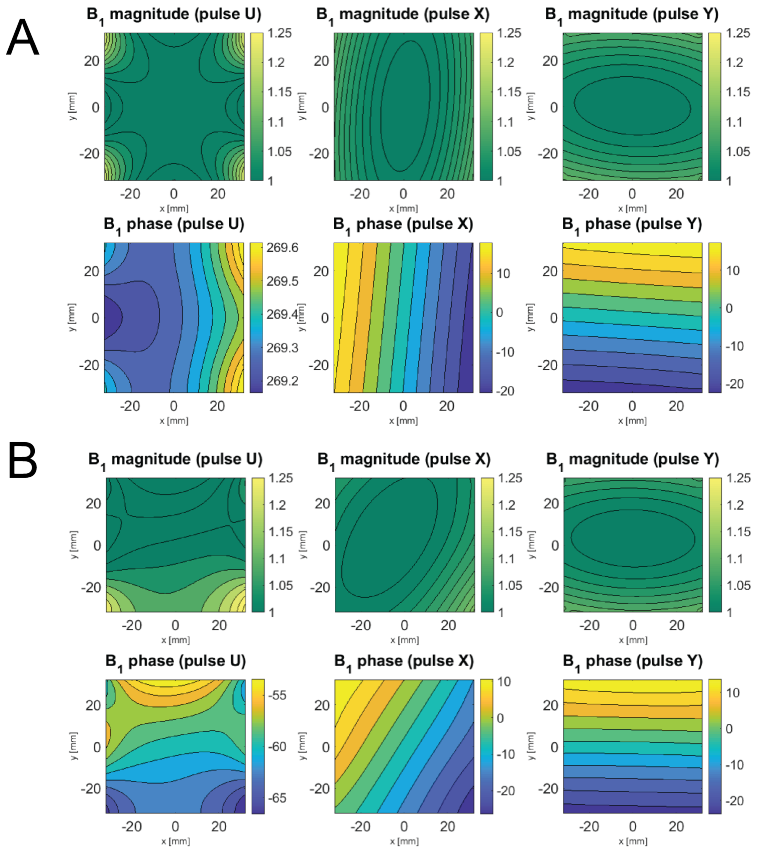

Figure Append-1: B_1 field magnitude (normalized) and phase contour maps (generated from Biot-Savart simulations) of the three-coil geometry used in the 2D TRASE MR imaging, over a FOV of 64mm x 64mm for $|B_1|$ contributions from the primary coil: (A) 100% (no coupling) and (B) 78% (interaction from each secondary coil is 11%). Here, U, X and Y represents different coils generating coil origins at the k-space center, on X, and Y axes, respectively. In panel (B), as the B_1 field interactions from the secondary (un-driven) coils is larger, the B_1 field perturbations appear more dominant (as compared to panel (A)). The induced phase gradient in pulse U and the shift in the B_1 phase gradient direction of pulse X in panel (B) is visually distinguishable in their phase contour maps. The loss in the $|B_1|$ homogeneity of pulse U can also be observed in its magnitude contour map of panel (B). Note that the magnitude and phase contour maps are shown in distinct color schemes for clarity. Images courtesy from Bohidar [88].

Appendices IV - for Chapter 7

AD9106-EBZ Board Modifications

In the following sections, three different modifications on AD9106-EBZ will be introduced. These changes are necessary for the proposed parallel transmit system design, and should be performed before the combination of AD9106-EBZ and Altera Terasic Cyclone ADC-SoC controller.

Change clock divider setup

AD9106-EBZ is equipped with an on-board clock divider (AD9514) [100]. This chip takes 0 - 1.6 GHz differential external clock input, and generates modified clock signal as the clock input for AD9106. The modification is a divide number set by users. On board AD9106-EBZ, the default setup divides the input clock by 8. The AD9514 operation is determined by the combination of logic levels present at the setup pins. The four logic levels are referred to as 0, 1/3, 2/3 and 1. These numbers represent the fraction of the Vs voltage that defines the logic levels. On board AD9106-EBZ, logic numbers for S0-S10 are controlled by resistors. The resistors schematic [118] for default AD9106-EBZ board is shown in Figure Append-2 a). Note that DNI means do not include on board for default setup. S0, S3, S4, S7, S8 are not connected, hence their values are zero. Referring to the S9 and S10 setup maps in Figure Append-2 b) and c), it can be found the divide number of 1 is achieved while S9 = 0 and S10 = 0 (only "OUT0" is used in this project). This corresponds to resistor change summarized in Table Append-1.

Disable PIC UBS interface

The 0 ohm resistors at XJP1, XJP3, XJP4, and XJP5 needs to be removed in order to disable the SPI connections to the on-board PIC processor (USB interface). In the mean time, XP3 6-hole through hole section is needed for the communication between SoC board

a) The resistors schematic for default AD9106-EBZ board

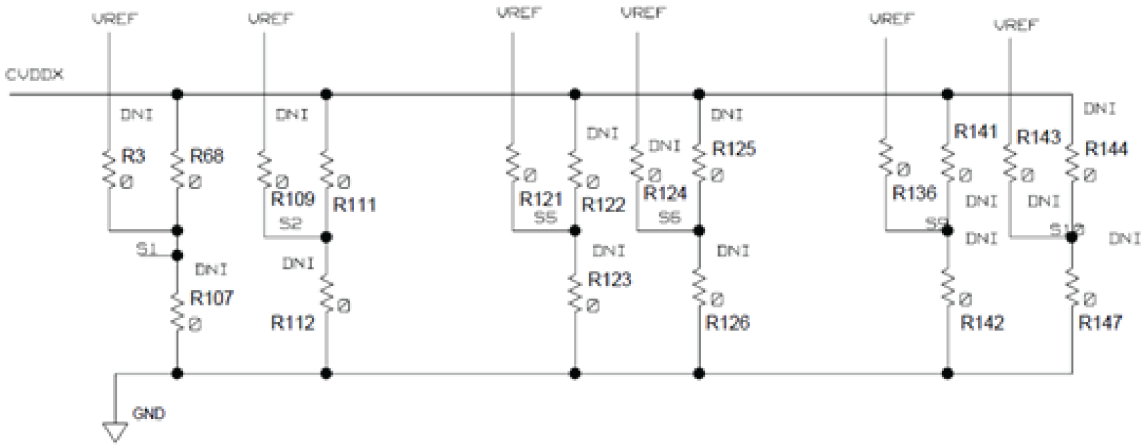

b) AD9514 output divide setup map

S9	S10	S2 ≠ 2/3 OUT0 Divide (Duty Cycle[1])	S2 = 2/3 OUT2 Divide (Duty Cycle[1])
0	0	1	7 (43%)
1/3	0	2 (50%)	11 (45%)
2/3	0	3 (33%)	13 (46%)
1	0	4 (50%)	14 (50%)
0	1/3	5 (40%)	17 (47%)
1/3	1/3	6 (50%)	19 (47%)
2/3	1/3	8 (50%)	20 (50%)
1	1/3	9 (44%)	21 (48%)
0	2/3	10 (50%)	22 (50%)
1/3	2/3	12 (50%)	23 (48%)
2/3	2/3	15 (47%)	25 (48%)
1	2/3	16 (50%)	26 (50%)
0	1	18 (50%)	27 (48%)
1/3	1	24 (50%)	28 (50%)
2/3	1	30 (50%)	29 (48%)
1	1	32 (50%)	31 (48%)

c) Examples of divide number

	S9			S10		
÷2	1/3			0		
	R142 open	R136 open	R141 open	R147 0Ω	R143 open	R144 open
÷4	1			0		
	open	open	0Ω	0Ω	open	open
÷8	2/3			1/3		
	open	0Ω	open	open	open	open
÷16	1			2/3		
	open	open	0Ω	open	0Ω	open

Figure Append-2: The resistor schematics and setup maps on AD9106-EBZ for the clock divide number [100], [118]. **a)** The resistors schematic for default AD9106-EBZ. It has 11 digital states from S0 to S10. By changing the resistor setup, different logical values 0, 1/3, 2/3, and 1 can be assigned. **b)** AD9514 clock divider output setup. In this project, only OUT0 was used, so both S9 and S10 need to be set to 0, in order to make the divide number to be 1. **c)** Examples of how to change resistors setups to give different logical values on S9 and S10.

S9	R142	R136	R141	Logic Value	Condition
	open	0 ohm	open	2/3	Default
	0 ohm	open	open	0	New Setup
S10	R147	R143	R144	Logic Value	Condition
	open	open	open	1/3	Default
	0 ohm	open	open	0	New Setup

Table Append-1: The resistors setup needed to change the divide number from 8 to 1 on the clock chip AD9514.

and AD9106-EBZ, see in Figure Append-3.

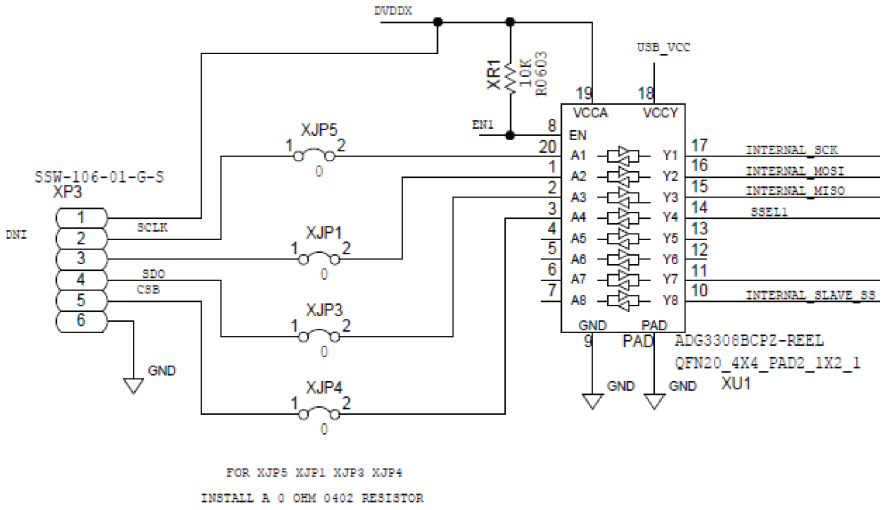

Figure Append-3: Internal SPI connection on the AD9106-EBZ evaluation board via USB interface [118]. This USB interface was disabled and replaced by a through-hole pin head.

Board power and trigger

As depicted in Figure Append-4, the power controls lines DVDD_CTRL, CVDD_CTRL, and AVDD_CTRL are connected to pull-up resistors, resulting in high logic input to the ADG733 Triple SPDT Switch. This further connects the ADJ_DVDD, ADJ_CVDD, and ADJ_AVDD lines to 15.8kΩ resistors which are used in the ADP1715 Linear Regulator to yield an output voltage of 1.8V (VOUT = 0.8(1+R1/R2) where R1 = 20kΩ and R2 = 15.8kΩ, based on ADP1715 datasheet [119]). When the CTRL lines are low, the ADJ lines would all switch to connect the 6.34kΩ resistor instead, resulting in VOUT = 3.3V. The AD9106 needs 3.3V power supply, so the resistors R27, R29 and R40 were removed and the CTRL lines were

grounded to provide an high input logic to the ADG733 and produce 3.3V supply [108].

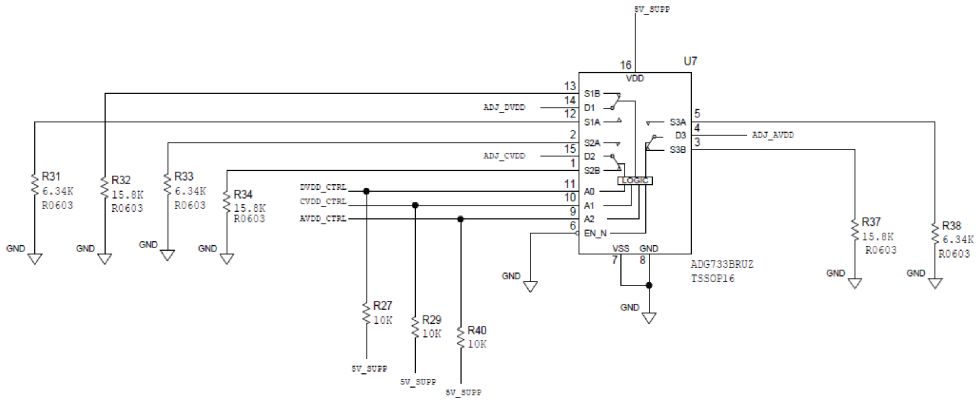

Figure Append-4: Voltage switching controls on the AD9106-EBZ evaluation board [118].

An Example SPI Configuration C Code

A write-SPI.c code is attached here to configure the SPI interfaces between two boards using National Semiconductor Microwire protocol [104].

```
/*
* target:  Terasic ADC-SoC board
*
1) Set up SPI communication from Terasic board (as SPI master using HPS)
- using some parameters from spi.txt

2) Send data to waveform generation board
- read register addresses and data from file
- send data over SPI interface in (addr, data) pairs

Usage:   ./writeSPI spi.txt reg.txt

HS Jan 2020 - to load all register values in one shot
*/

#include <stdio.h>
#include <unistd.h>
#include <fcntl.h>
#include <sys/mman.h>
#include "hwlib.h"
#include "socal/socal.h"
#include "socal/hps.h"
#include "socal/alt_gpio.h"
#include "hps_spi_registers.h"

int read_register_file(char *reg_file, uint32_t AD_reg_addr[], uint32_t AD_reg_data[]) {
// read file with (address, value) pairs for registers

FILE *fp;
int lineNum = 0;
int nreg    = 0;

// look for file with (address, value) pairs for registers
fp = fopen(reg_file, "r");
if (fp == NULL) {
printf("Could not open: %s",reg_file);
printf(" ...quitting\n\n");
return 0;
}

else {
printf("Opened: %s\n",reg_file);
lineNum = 0;
while (fscanf(fp, "%X %X", &AD_reg_addr[lineNum], &AD_reg_data[lineNum]) > 0) {
//  printf("Line %d: %04X  %04X\n", lineNum, word1[lineNum], word2[lineNum] );
```

```
lineNum++;
}
nreg = lineNum;
printf("Number of registers read from file: %d\n",lineNum);
fclose(fp);
}

return nreg;
}

int read_spi_file(char *spi_file) {

FILE *fp;
int baud_div=128;
//int gap_us;
char someText[200];

// look for file with (address, value) pairs for registers
fp = fopen(spi_file, "r");
if (fp == NULL) {
printf("Could not open: %s",spi_file);
printf(" ...quitting\n\n");
return 0;
}

else {
printf("Opened: %s\n",spi_file);

fscanf(fp,"%s %d", someText, &baud_div);
printf(   "%s %d\n", someText, baud_div);

//       fscanf(fp, "%s %d", someText, &gap_us);
//       printf("Line %s %d\n", someText, gap_us );

fclose(fp);
}

return baud_div;
}

int init_spi_interface(void *virtual_base, int baud_divider){

uint32_t my_addr, my_data;
uint32_t id_register;

printf("\n ==  init spi interface ==\r\n");
//printf (" HW_REGS_BASE (0x)%8X \n", HW_REGS_BASE);
//printf (" HW_REGS_SPAN (0x)%8X \n", HW_REGS_SPAN);
//printf (" HW_REGS_MASK (0x)%8X \n", HW_REGS_MASK);
//printf (" \n");

//printf("\n == GPIO base addresses ==\r\n");
//printf (" aGPIO0 (0x)%8X \n", aGPIO0);
//printf (" aGPIO1 (0x)%8X \n", aGPIO1);
//printf (" aGPIO2 (0x)%8X \n", aGPIO2);
//printf (" \n");
//printf (" HPS_LTC_GPIO (0x)%8X \n", HPS_LTC_GPIO); // will this work? NO

// HS - alt_setvits_word: set specified bit value to 1 for a specified register
// HS - alt_clrbits_word: set specified bit value to 0 for a specified register
// HS - alt_write_word: write a value into a specified register
// HS - alt_read_word: read a value from a specified register

alt_setbits_word( ( virtual_base + ( (uint32_t)( GPIO1_DIRECTION_ADDR ) & (uint32_t)(HW_REGS_MASK))), USER_IO_DIR);
alt_setbits_word( ( virtual_base + ( (uint32_t)( GPIO1_DIRECTION_ADDR ) & (uint32_t)(HW_REGS_MASK))), USER_IO_DIR);
alt_clrbits_word( ( virtual_base + ( (uint32_t)(GPIO1_WRITE_ADDR)       & (uint32_t)(HW_REGS_MASK))), BIT_11);
// alt_setbits_word( ( virtual_base + ( (uint32_t)(GPIO1_WRITE_ADDR)       & (uint32_t)(HW_REGS_MASK))), BIT_11);
//printf("  clrbits   \n");



// Disable (write zero to enable register)
my_addr = SPIM | spienr;
my_data = 0x0;
alt_write_word( (virtual_base + (my_addr & (uint32_t)(HW_REGS_MASK))), my_data );
//printf (" SPIM - spienr address (0x)%8X \n", my_addr);

// Read from SPI interface - contains peripherals identification code
my_addr = SPIM | idr;
id_register = alt_read_word( (virtual_base + (my_addr & (uint32_t)(HW_REGS_MASK) )));
//printf (" SPIM - idr address (0x)%8X \n", my_addr);
printf (" SPI Master ID read: (0x)%8X \n", id_register);


//---- Initialize SPI control registers:


// 16 bit transfer
my_addr = (SPIM | ctrlr0);
my_data = 0xF;
alt_write_word((virtual_base + (my_addr & (uint32_t)(HW_REGS_MASK))), my_data);
my_addr = (SPIM | ctrlr1);
```

```
my_data = 0x0;
alt_write_word((virtual_base + (my_addr & (uint32_t)(HW_REGS_MASK))), my_data);

// this is the clock divisor.
my_addr = (SPIM | baudr);
my_data = baud_divider;
alt_write_word((virtual_base + (my_addr & (uint32_t)(HW_REGS_MASK))), my_data);

// tx fifo threshold level register - default value
my_addr = (SPIM | txftlr);
my_data = 0x0;
alt_write_word((virtual_base + (my_addr & (uint32_t)(HW_REGS_MASK))), my_data);
// Rx tx fifo threshold level register - default value -
my_addr = (SPIM | rxftlr);
my_data = 0x0;
alt_write_word((virtual_base + (my_addr & (uint32_t)(HW_REGS_MASK))), my_data);

// interrupt mask register - all disabled
my_addr = (SPIM | imr);
my_data = 0x0;
alt_write_word((virtual_base + (my_addr & (uint32_t)(HW_REGS_MASK))), my_data);
// Slave Enable - activate.
my_addr = (SPIM | ser);
my_data = 0x1;
alt_write_word( (virtual_base + (my_addr & (uint32_t)(HW_REGS_MASK))), my_data );



//-------------------------Protocol change here----------------

my_addr = (SPIM | mwcr);
my_data = 0x0;
alt_write_word((virtual_base + (my_addr & (uint32_t)(HW_REGS_MASK))), my_data);

// For HS version, if we want to use microwire, we need to write
// 16 bit transfer still, but active frf in ctrlr0 to choose national semi microwire protocol.
my_addr = (SPIM | ctrlr0);
my_data = 0xF02F;
alt_write_word((virtual_base + (my_addr & (uint32_t)(HW_REGS_MASK))), my_data);
//mwcr fields, disable handshaking interface, SPI Master transmits data, non-sequential transfer
my_addr = (SPIM | mwcr);
my_data = 0x2;
alt_write_word((virtual_base + (my_addr & (uint32_t)(HW_REGS_MASK))), my_data);


// Finally enable the interface
// Now Enable (write 1 to enable register)
my_addr = (SPIM | spienr);
my_data = 0x1;
alt_write_word( (virtual_base + (my_addr & (uint32_t)(HW_REGS_MASK))), my_data );

printf(" Cyclone HPS master SPI interface on LTC connector configured\n\n");
return 0;
}

int send_to_AD9106(void *virtual_base, int nRegisters, int baud_divisor, uint32_t AD_reg_addr[], AD_reg_data[]){

uint32_t interface_addr;
//uint32_t my_addr, my_data;
//uint32_t AD_reg_addr[128];
//uint32_t AD_reg_data[128];
int reg;
int delay, count;
//nRegisters=128;

//AD_reg_addr[0] = 0xAAAA;
//AD_reg_data[0] = 0x0001;

//======== USE THE SPI INTERFACE TO SEND DATA ========//
// [1] send data to initialize the waveform generation board
interface_addr = (SPIM | dr); //data line now.

printf("nRegisters value is %d \n", nRegisters);

for(reg=0; reg<nRegisters; reg++){

alt_write_word( (virtual_base + (interface_addr & (uint32_t)(HW_REGS_MASK))), AD_reg_addr[reg]);
alt_write_word( (virtual_base + (interface_addr & (uint32_t)(HW_REGS_MASK))), AD_reg_data[reg]);

// HS updated: Version 2- Best edition 2020-01-20

for (delay=0; delay<1500; delay++)  // - working delay of 12 us between two reg values, cannot go lower..
{
count++;
}

}


printf(" Address and values sent to waveform generator.\n\n");
return 0;
}
```

```
// Format of giving command-line arguments in C
int main(int numArgs, char *argument[]) {

void *virtual_base; // a generic pointer
int fd, nreg;
int baud_divisor;
char *reg_file;
char *spi_file;
uint32_t word1[200], word2[200];

printf("\n\n\n   =====  writeSPI-HS with data read from file ====\r\n");

printf("  number of files names given: %d \n\n", numArgs-1);
if (numArgs != 3){
printf("    Expects:  writeSPI <spi.txt> <reg.txt> \r\n");
return 0;
}
spi_file = argument[1];
reg_file = argument[2];

printf("  AD9106 register file:  %s \n",reg_file);
printf("\n");

// map the address space for the HPS registers into user space so we can interact with them.
// map in the entire CSR span of the HPS since we want to access various registers within that span
if( ( fd = open( "/dev/mem", ( O_RDWR | O_SYNC ) ) ) == -1 ) {
printf( "ERROR: could not open \"/dev/mem\"...\n" );
return( 1 ); }
virtual_base = mmap( NULL, HW_REGS_SPAN, ( PROT_READ | PROT_WRITE ), MAP_SHARED, fd, HW_REGS_BASE );
if( virtual_base == MAP_FAILED ) {
printf( "ERROR: mmap() failed...\n" );
close( fd );
return( 1 ); }

nreg = read_register_file(reg_file, word1, word2); // return number of reg. lines

baud_divisor = read_spi_file(spi_file); //

init_spi_interface(virtual_base, baud_divisor);

send_to_AD9106(virtual_base, nreg, baud_divisor, word1, word2);

//--------------
// clean up our hps memory mapping and exit
if( munmap( virtual_base, HW_REGS_SPAN ) != 0 ) {
printf( "ERROR: munmap() failed...\n" );
close( fd );
return( 1 );
}
printf("\n Successfully finished\n\n");
close( fd );


return( 0 );
}
```